

8636(FC)

Examiner's copy

JNCASR
620.44 P03



Band Model Computation of Near-surface Longwave Fluxes

A Thesis
Submitted for the Degree of
Doctor of Philosophy
in the Faculty of Engineering

by
Saji Varghese



Engineering Mechanics Unit
Jawaharlal Nehru Centre for Advanced Scientific Research
Bangalore – 560 064, India

June 2003

DECLARATION

I hereby declare that the matter embodied in the thesis entitled “**Band Model Computation of Near-surface Longwave Fluxes**” is the result of investigations carried out by me at the Engineering Mechanics Unit, Jawaharlal Nehru Centre for Advanced Scientific Research, Bangalore, India under the supervision of Prof. Roddam Narasimha and that it has not been submitted elsewhere for the award of any degree or diploma.

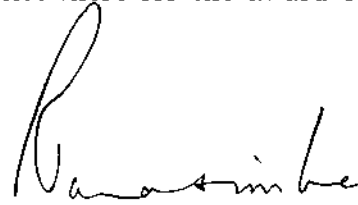
In keeping with the general practice in reporting scientific observations, due acknowledgement has been made whenever the work described is based on the findings of other investigators.



Saji Varghese

CERTIFICATE

I hereby certify that the matter embodied in this thesis entitled “**Band Model Computation of Near-surface Longwave Fluxes**” has been carried out by Mr. Saji Varghese at the Engineering Mechanics Unit, Jawaharlal Nehru Centre for Advanced Scientific Research, Bangalore, India under my supervision and that it has not been submitted elsewhere for the award of any degree or diploma.



Prof. Roddam Narasimha
(Research Supervisor)

Dedicated to Prof. Roddam Narasimha on his 70th birthday.

Abstract

Infrared radiation plays a key role in the determination of the near-surface thermal environment, especially during night. A small error in the relatively large fluxes can lead to appreciable errors in the estimated cooling rates near the surface where the radiative calculations have to be over thin atmospheric layers (Tjemkes and Duynkerke, 1989).

The objectives of the present work are to study longwave radiative transfer near the ground in different bands for arbitrary surface emissivities, to generate a code which provides precise estimates of fluxes and cooling rates near the surface and to simulate the Ramdas layer using a band model. Most previous studies on near-surface radiative transfer use a broadband flux emissivity approach (see for e.g., Coantic and Seguin, 1971; Vasudeva Murthy, Srinivasan and Narasimha, 1993). This is sufficiently accurate for many applications, but cannot provide an estimate of the contribution of different longwave bands to radiative cooling, which would be important when one considers the effect of different constituents of atmospheric air or needs to use band-dependent surface emissivities. This drawback of flux emissivity schemes can be overcome by band models.

The present work takes as its starting point the very useful code developed by Chou, Ridgway and Yan (1993). This code is based on a band model that comprises 11 bands for water vapour and 5 bands for CO₂ absorption, using an appropriate one-

parameter scaling approximation in each case. Totally there are 62 sub-bands. The Planck-weighted diffuse transmittance is then reduced to a function depending only on the scaled absorber amount. This transmittance is then fitted with an exponential sum in each of the bands (11 in total).

One difficulty experienced with the Chou code is that, when it is used for near-surface computations, the evaluation of fluxes and cooling rates near the surface is not only insufficiently precise but also highly oscillatory (see Figure 2.1). The reason for this is that in the Chou code the integrals are evaluated using a numerical scheme that is unstable near the surface, because of a sharp boundary layer there caused by the huge absorption coefficients in some bands. In fact, evaluating integrals of functions that have large gradients in special regions requires special care. The present work is directed towards tackling this issue.

The main departure of the present code from Chou's rests on the recognition that, if the transmission functions are given by exponential sums, then the corresponding flux integral can be evaluated by solving an ordinary differential equation (ODE). To illustrate this idea, consider evaluating the integral

$$y(z) = \int_0^z e^{-(z-x)/\delta} dx; \quad (0.1)$$

then y satisfies the ODE

$$\begin{cases} \frac{dy}{dz} = \delta^{-1}(\delta - y); & z > 0, \\ y(0) = 0. \end{cases} \quad (0.2)$$

Now evaluating the integral by quadrature causes problems if δ is small, because of a thin layer of large gradient in the integrand near $x = z$. But the equivalent ODE can be solved very efficiently using readily available software that not only incorporates adaptive gridding but also generates solutions to a given user-specified tolerance. It is known that uniform grids are not only highly inefficient but are often incapable

of solving singularly perturbed ODE's such as (0.2)(see e.g., Farrel *et al.*, 2000). A preliminary account of this work has appeared in Varghese *et al.* (2001).

Our proposal here is to reformulate the flux integrals as solutions of certain ordinary differential equations. There are two main reasons for adopting this approach. The first is that the exponential sum-fit proposed facilitates it, because each band integral will be the sum of several sub-integrals with an exponential kernel. This means that the derivative of those integrals can be expressed in terms of the integral itself. Secondly the absorption coefficients k_j^i in the exponentials can be extremely large in certain bands, and so result in a thin radiative sub-layer near the surface, generally extending to heights of less than a centimetre and characterised by extremely sharp temperature gradients.

The longwave spectrum is divided into 11 bands in Chou's model. The spectrally integrated flux in band j is denoted by

$$F_j^{\uparrow\downarrow} = \int_{\nu_j}^{\nu_{j+1}} F_{\nu}^{\uparrow\downarrow} d\nu$$

where ν_j and ν_{j+1} are the starting and ending wave numbers of band j .

The ODE's satisfied by $F_{ji}^{\uparrow\downarrow}$ are

$$\begin{cases} \frac{dF_{ji}^{\downarrow}}{dz} = -A_j^i [c_i^j \pi B_j(T) - F_{ji}^{\downarrow}], \\ F_{ji}^{\downarrow}(\infty) = 0; \end{cases} \quad (0.3)$$

$$\begin{cases} \frac{dF_{ji}^{\uparrow}}{dz} = A_j^i [c_i^j \pi B_j(T) - F_{ji}^{\uparrow}], \\ F_{ji}^{\uparrow}(0) = c_i^j [\varepsilon_g \pi B_j(T_g) + (1 - \varepsilon_g) F_j^{\downarrow}(0)]. \end{cases} \quad (0.4)$$

Here A_j^i is the scaled absorber amount in each sub-band, c_i^j is a constant, B_j the Planck function in each band, T the temperature and ε_g the ground emissivity.

To solve (0.3,4) we use the code of Sommeijer *et al.* (1998). This code is based on the explicit Runge-Kutta formulae of the Chebyshev type proposed by

Van der Houwen and Sommeijer (see the above reference). These formulae have good stability bounds and are ideal for large mildly stiff systems because of their explicit nature. The code is written in such a way that it automatically selects, at each vertical level z , the most efficient stable formula as well as the most efficient step size.

The code output was verified using exact solutions. Apart from serving to verify the code, these solutions also address the crucial z -test that Ellingson *et al.* (1991) suggest. The results were further verified using the ICRCCM results and the line-by-line results of Clough *et al.* (1992). As the present radiation code has no restriction on the number of grid points and yields fluxes accurate to a prescribed tolerance limit, it consequently also provides cooling rates to a desired accuracy. The computing times for executing the current program are comparable (for given accuracy) to those demanded by other standard current codes.

Figure 4.3 shows the results of a study carried out to understand the influence of ground emissivity on cooling rates (including both line and continuum contributions) across the longwave spectrum in the entire atmosphere (surface to 100 km). It is seen that a decrease in ϵ_g from 1.0 to 0.8 increases the surface cooling rate from 4.47 to 37.5 K/d, and that the effect of lower values of surface emissivity extends to a height of almost 1 km. This confirms the estimates made by Ragothaman *et al.* (2001), using the flux emissivity scheme, of the unsuspectedly large extent of the influence of surface conditions on radiative cooling.

An analysis of spectral distribution shows that, when the surface is not radiatively black, the major contributions to near-surface cooling rates (due to water vapour) come from the two wave number bands $340\text{--}540\text{ cm}^{-1}$ and $1215\text{--}1380\text{ cm}^{-1}$ (located on either side of the atmospheric window) in which both absorption and radiative flux are significantly high. The identity of the bands contributing most to the cooling rate depends on a balance between flux and absorption; if either is too low little cooling occurs. As altitude increases and temperature falls, the flux spectrum

peaks at longer wavelengths, where absorption still remains significant; consequently the contribution to cooling also moves to the longer waves.

Furthermore the present code was used to simulate the Ramdas layer. The lifted temperature minimum (LTM) formed was weak in intensity and height due to low radiative slip generated by the band model. A detailed study was carried out to investigate the difference in radiative slip temperature produced by the present band model and the flux emissivity scheme.

The present code enables us to investigate in considerable detail the spectral energetics of longwave radiative transfer that result in the extremely high cooling rates observed near ground. This should be of use in exploring the basic problem of interaction between radiation and turbulence on the one hand, and (with the inclusion of effects of vegetation) the elucidation of the meteorological conditions that influence the health of agricultural crops - in particular the occurrence and possible control of frost.

Acknowledgements

Words are few to express my gratitude to Prof. Roddam Narasimha, fondly known among students as RN. A pleasant mannered multifaceted genius with expertise in science, technology, literature, history, arts, national security and so forth has been a great source of inspiration and motivation to me. Apart from guiding me in my research, he has influenced in getting the best out of me. His thought provoking discussions, openness to ideas and dynamism, made me feel at ease and helped me develop the researcher in me. His teachings, I shall cherish forever.

Dr. Vasudeva Murthy, an unassuming, down to earth person is more of a friend than a teacher. He has contributed in several ways in developing my research skills. His patience, approachability and unflagging encouragement helped me get going. I thank him for the financial support through the NMLITI project supported by the Department of Science and Technology.

I express my great indebtedness to both RN and Vasudeva Murthy for their critical reviews of my work.

I am thankful to Dr. Ming-Dah Chou, Radiation Branch, Goddard Space Flight Centre, NASA, for providing a recent version of his code and other useful scientific literature and to Prof. J. Srinivasan (CAOS) for some useful discussions in the initial stages of my work. Special thanks to the Chairman of SERC for providing me with computational facilities where all my computations were done.

A special mention to Nagarathna and Mariammal who have assisted me greatly in various ways.

I am grateful to Sivakumar for training me in developing computational skills and for the useful academic and non-academic discussions we had and for keeping my spirits up at times of difficulties. My heartfelt gratitude to Reena (MCBL) and Vasudevan (Cambridge) for staying by me through thick and thin. Thanks to Joseph for ingraining in me a love for the Scripture and instilling academic discussions.

I am thankful to Sivettan, Subbu, Kunji Sir for taking me a step closer to nature and teaching me how to appreciate it - I can never forget the several adventurous treks we had in the Western Ghats which were quite refreshing physically and mentally. They have always been concerned about my well-being.

I take this opportunity to thank Prof. Rama Govindarajan (JNC) for all the moral support and encouragement she has given. Special thanks to N. Vinod for his help in academic and non-academic matters. Many thanks to Bannaiah for helping me in administrative work.

There are others who have supported me every step of the way: Srinidhi, Veena, Vinita and Divya from CES; Sameen, Manoj, Gautam, Pattu, Sudhi, Sachin, John, Jayalakshmi, Lakshmi and Pushpa from JNC; Pappan and Anil from SSCU; Rama, Sriram and Anil from Aero, Sunil Thomas from New York and Sasi Kumar from SERC - I am blessed to have friends like you.

My friends at TIFR gave me constant company and never had I a dull moment; thanks to Harish, Prachi, Rahul, Sabu, Siddarth, Sivaji and Srinath. Of course, Desaiah, Hariettan, Mahakud, Nirmala, Pramila, Shekar, Unni, Veena, Vishwanathan at TIFR have helped me a great deal.

I thank my family - Appachen, Ammachy, Pappa, Mummy, Sindhu, Sajeev, Sherry, Ricky, Vinod uncle and Thomas uncle for their love and support.

Words are few to thank my wife, Merry, who has stood by me at all times.

A reseacher on Ants, she has always been keen to know the details of my research. I am also thankful to her for correcting some of the typographical errors in this thesis.

There are many fine people who have selflessly enriched me in ways beyond measure. I thank them all.

Above all, I thank the Almighty for teaching me His ways.

Contents

Abstract	i
Acknowledgements	vii
List of Figures	xv
List of Tables	xxi
1 Introduction	1
1.1 Near-surface Thermal Environment	3
1.1.1 Ramdas Layer	4
1.1.2 The VSN Theory	5
1.2 Radiation Models	6
1.2.1 Line-by-line Model	7
1.2.2 Narrow Band Model	8
1.2.3 Wide Band Models	10
1.2.4 Flux Emissivity Model	11
1.3 Objectives	12
1.4 Previous Work	12
1.4.1 Surface Emissivity	17

2	Formulation of Model and Methodology of Implementation	21
2.1	Preliminary Numerical Experiments	21
2.2	Background	25
2.3	Chou's One-parameter Scaling Approximation of Absorption Coefficient	27
2.3	Present Approach	33
3	Verification and Validation	39
3.1	Testing Radiation Schemes	39
3.2	Vertical Resolution	41
3.3	Some Exact Solutions	43
3.4	Resolution Requirements	45
4	Spectral and Net Cooling Rates	53
4.1	Spectral Density of Cooling Rate at Different Altitudes	53
4.2	Source-wise Decomposition of Cooling Rate	74
4.5	Discussion	78
4.6	Carbon dioxide	82
5	Temperature Slip at the Surface	87
5.1	Introduction	87
5.2	Survey of Earlier Work on Radiative Slip and Cooling Rates near the Surface	93
5.3	Sensitivity Study of Cooling Rate from Present Model	98
6	Simulation of Lifted Temperature Minimum with the Present Code	113
6.1	VSN Model	113
6.6	Validation of Code for Time Evolution	116
6.6.1	Validation of Radiation Code	116
6.6.2	Validation of Diffusion Code	117

6.2 Simulation with the Present Band Model	119
7 Conclusions	137
A Calculation of Transmission Function	141
B Derivation of Flux Equations	143
C Computation of Blackbody Fraction	145
C.1 Lawson's Method	145
D Unit Conversion	147
D.1 Conversion of atm.cm to kgm^{-2}	147
D.2 Conversion of ppmv to kgm^{-3}	148
E Comparison of Cooling Rates for Broadband Flux Emissivity and Band Models in an Isothermal Atmosphere with a Discontinuity at the Surface	149
E.1 Flux emissivity	149
E.2 Band emissivity	150
E.3 Discussion	150
References	165

List of Figures

2.1	Oscillations in cooling rate near the surface, using Chou's (1993) code with 771 layers; isothermal atmosphere, water vapour line absorption only, $\varepsilon_g = 1.0$	23
2.2	Oscillations in cooling rate near the surface, using Chou's (1993) code with 771 layers; isothermal atmosphere, water vapour line absorption only, $\varepsilon_g = 0.8$	24
3.1	Effect of prescribed tolerance on performance parameters of present code; isothermal atmosphere.	46
3.2	Comparison of computed cooling rates for an isothermal atmosphere with $\varepsilon_g = 0.8$, water vapour line absorption only.	49
3.3	Comparison of cooling rates for an isothermal atmosphere with $\varepsilon_g = 0.8$, water vapour line absorption only, for present, Chou and exact.	50
3.4	Comparison of present results for upward, downward and net flux, with results presented by Clough <i>et al.</i> (1992) using two different codes, FASCODE and GLA. MLS atmosphere with water vapour absorption only.	51
4.1	Input profiles of pressure, temperature and humidity in the MLS atmosphere.	55
4.2	Effect of ground emissivity on cooling rates computed by present code; MLS atmosphere, water vapour absorption only.	56
4.3	Influence of change in ground emissivity from 1.0 to 0.8 on spectral distribution of cooling rate for MLS atmosphere from surface to 100 km, water vapour absorption only.	58

4.4	Influence of change in ground emissivity from 1.0 to 0.8 on spectral distribution of cooling rate for MLS atmosphere from surface to 1 m, water vapour absorption only.	59
4.5	Influence of ground emissivity in spectral distribution of upward flux; MLS atmosphere, water vapour absorption only.	60
4.6	Spectral distribution of cooling rate at five levels for $\varepsilon_g = 1.0$ and $\varepsilon_g = 0.8$, showing also the gross cooling rate at each level; water vapour absorption only.	61
4.7	Normalised spectral cooling rate distribution of MLS atmosphere for various heights with $\varepsilon_g = 1.0$, water vapour absorption only.	62
4.8	Normalised spectral cooling rate distribution of MLS atmosphere for various heights with $\varepsilon_g = 0.8$, water vapour absorption only.	63
4.9	Spectral distribution of cooling rate, blackbody radiation and transmission function (joined circles) at four different levels for MLS atmosphere, water vapour absorption only.	64
4.10	Effect of ground emissivity on cooling rates computed by present code from 1 km to 100 km; MLS atmosphere, water vapour absorption only.	66
4.11	Percentage-wise cooling rate contributions from different bands upto heights of 20 km; MLS atmosphere, water vapour absorption only.	67
4.12	Percentage-wise cooling rate contributions from different bands upto heights of 10 km; MLS atmosphere, water vapour absorption only.	68
4.13	Percentage-wise cooling rate contributions from different bands upto heights of 5 km; MLS atmosphere, water vapour absorption only.	69
4.14	Percentage-wise cooling rate contributions from different bands upto heights of 1 km; MLS atmosphere, water vapour absorption only.	70
4.15	Percentage-wise cooling rate contributions from different bands upto heights of 100 m; MLS atmosphere, water vapour absorption only.	71
4.16	Percentage-wise cooling rate contributions from different bands upto heights of 10 m; MLS atmosphere, water vapour absorption only.	72
4.17	Percentage-wise cooling rate contributions from different bands upto heights of 1 m; MLS atmosphere, water vapour absorption only.	73
4.18	Cooling due to air-emission at four different levels for MLS atmosphere, water vapour absorption only.	76
4.19	Cooling due to ground-emission at four different levels for MLS atmosphere; water vapour absorption only.	77

4.20	Difference in cooling due to ground-reflection at four different levels, with emissivities $\varepsilon_g = 1.0$ and $\varepsilon_g = 0.8$; MLS atmosphere, water vapour absorption only.	78
4.21	Difference in cooling due to ground-emission and air-emission at eight different levels, with $\varepsilon_g = 0.8$; MLS atmosphere, water vapour absorption only.	79
4.22	Differential between $\varepsilon_g = 1.0$ and $\varepsilon_g = 0.8$, of the difference of the ground-emission and ground-reflection cooling terms ; MLS atmosphere, water vapour absorption only.	80
4.23	Variation of surface cooling rate with change in surface emissivity for MLS atmosphere.	82
4.24	Difference in cooling rate due to CO ₂ (300 ppmv) with $\varepsilon_g = 1.0$ and 0.8; MLS atmosphere.	85
4.25	Net cooling rate due to water vapour and CO ₂ (300 ppmv) with $\varepsilon_g = 1.0$ and 0.8; MLS atmosphere.	86
5.1	Components of cooling in the atmosphere	88
5.2	Variation of air temperature with height for different grid resolutions near the surface; pure radiation.	91
5.3	Variation of air temperature just above the surface for different grid resolutions.	92
5.4	Variation of temperature slip with grid resolution for $\varepsilon_g = 0.8$	99
5.5	Variation of surface cooling rate with prescribed temperature slip.	101
5.6	Variation of SCR/ ΔT with ground emissivity.	102
5.7	Variation of cooling rate with height for different temperature slip and ground emissivity.	103
5.8	Spectral distribution of cooling rate for an isothermal atmosphere (300 K) with temperature slip of 3 K.	104
5.9	Spectral distribution of cooling rate for an isothermal atmosphere (300 K) with temperature slip of 2 K.	105
5.10	Spectral distribution of cooling rate for MLS atmosphere with temperature slip of 2 K.	106
5.11	Spectral distribution of cooling rate for MLS atmosphere with temperature slip of 3 K.	107
5.12	Variation of ground flux with height in an isothermal atmosphere (300 K) for ground temperatures 300 K and 297 K.	108

5.13	Difference in ground flux gradient (with and without temperature slip), ground temperatures being 300 K and 297 K.	109
5.14	Spectral distribution of difference in ground emission gradient (with and without slip) for different heights, $T = T_0 - \Gamma z$	110
6.1	Error in the radiation code for an exact solution at $t = 5$ h.	117
6.2	Variation of error in the radiation code upto a height of 1 km with an exact solution, $t = 5$ h.	118
6.3	Error in diffusion code for an exact solution after 10^6 time steps.	120
6.4	Temperature slip evolution for $\varepsilon_g = 0.8$ and $\beta = 0.0$ K hr ^{-1/2}	121
6.5	Temperature slip evolution for $\varepsilon_g = 0.8$ and $\beta = 2.0$ K hr ^{-1/2}	122
6.6	Temperature profile for a height a 25 m; pure radiation, $\varepsilon_g = 0.8$ and $\beta = 0.0$ K hr ^{-1/2}	123
6.7	Cooling rate profile for a height a 25 m; pure radiation, $\varepsilon_g = 0.8$ and $\beta = 0.0$ K hr ^{-1/2}	124
6.8	Temperature profile for a height a 1 m; pure radiation, $\varepsilon_g = 0.8$ and $\beta = 0.0$ K hr ^{-1/2}	125
6.9	Cooling rate profile for a height a 1 m; pure radiation, $\varepsilon_g = 0.8$ and $\beta = 0.0$ K hr ^{-1/2}	126
6.10	Temperature profiles at different time intervals for a height a 25 m; isothermal atmosphere, pure radiation, $\varepsilon_g = 0.8$ and $\beta = 0.0$ K hr ^{-1/2}	127
6.11	Cooling rate profiles at different time intervals for a height a 25 m; isothermal atmosphere, pure radiation, $\varepsilon_g = 0.8$ and $\beta = 0.0$ K hr ^{-1/2}	128
6.12	Temperature profiles at different time intervals for a height a 1 m; isothermal atmosphere, pure radiation, $\varepsilon_g = 0.8$ and $\beta = 0.0$ K hr ^{-1/2}	129
6.13	Cooling rate profiles at different time intervals for a height a 1 m; isothermal atmosphere, pure radiation, $\varepsilon_g = 0.8$ and $\beta = 0.0$ K hr ^{-1/2}	130
6.14	Temperature profile at $t = 1$ hr and upto 25 m with $\varepsilon_g = 0.8$ and $\beta = 0$ K hr ^{-1/2} for both radiation and diffusion.	131
6.15	Cooling rate profile at $t = 1$ hr and upto 25 m with $\varepsilon_g = 0.8$ and $\beta = 0$ K hr ^{-1/2} for both radiation and diffusion.	132
6.16	Temperature profile at $t = 1$ hr and upto 1 m with $\varepsilon_g = 0.8$ and $\beta = 0$ K hr ^{-1/2} for both radiation and diffusion.	133
6.17	Cooling rate profile profile at $t = 1$ hr and upto 1 m with $\varepsilon_g = 0.8$ and $\beta = 0$ K hr ^{-1/2} for both radiation and diffusion.	134

6.18	Temperature profiles at $t = 1$ hr and upto 10 m with $\varepsilon_g = 0.8$ and $\beta = 0$ and $2 \text{ K hr}^{-1/2}$ with pure radiation and with radiation and diffusion.	135
E.1	Vertical variation of emissivity with present band model upto 1 km.	151
E.2	Vertical variation of emissivity with present band model upto 100 km.	152
E.3	Vertical variation of emissivity with flux emissivity model upto 1 km.	154
E.4	Vertical variation of emissivity with flux emissivity model upto 100 km.	155
E.5	Vertical variation of cooling rates with flux emissivity scheme and present band model for $\varepsilon_g = 1.0$ and 0.8 upto 1 km; $T_0 = T_{g0} = 300 \text{ K}$.	159
E.6	Vertical variation of cooling rates with flux emissivity scheme and present band model for $\varepsilon_g = 1.0$ and 0.8 upto 1 m; $T_0 = T_{g0} = 300 \text{ K}$.	160
E.7	Variation of surface cooling rate with different ground temperatures for flux emissivity scheme and band model, $\varepsilon_g = 0.8$.	161
E.8	Variation of cooling rate with different ground temperatures for flux emissivity scheme and band model; $\varepsilon_g = 0.8$.	162
E.9	Variation of cooling rate with different ground temperatures for flux emissivity scheme and band model; $\varepsilon_g = 1.0$.	163

List of Tables

2.1	Values of radiation code parameters for water vapour line absorption.	32
2.2	Spectral bands, its width and the major absorbers in each band. . . .	33
3.1	Comparison of surface downward and upward fluxes (Wm^{-2}) in an isothermal atmosphere for $\varepsilon_g=1.0$	45
3.2	Variation of surface downward flux with change in grid resolution near the surface.	48
3.3	Grid resolution at various height bands in present code.	48
3.4	Comparison of upwelling and downwelling radiative fluxes at the surface and tropopause for an MLS atmosphere with and without continuum and $\varepsilon_g=1.0$. The units are in Wm^{-2}	52
4.1	Values of radiation code parameters for carbon dioxide absorption. . .	83
4.2	Comparison of upwelling and downwelling radiative fluxes at the surface and tropopause for an isothermal atmosphere at 300 K and 300 ppmv of CO_2 only.	84
5.1	Comparison of temperature slip obtained from flux emissivity model by VSN and present model for $\varepsilon_g = 0.8$ and different β	90
5.2	Near-surface cooling rates observed/simulated.	97
E.1	Values for band emissivity at 100 km, its gradient at the surface and the product of blackbody fraction and gradient of emissivity at the surface from the present code.	156
E.2	Values for cooling rate at the surface with band model and flux emissivity model for different ground temperatures; $\varepsilon_g = 0.8$, isothermal atmosphere.	157

Chapter 1

Introduction

Almost all the energy that drives the earth's atmosphere and ocean currents originates from the sun. More than 80% of the energy absorbed by the atmosphere is through radiative transfer. The land and ocean surfaces absorb 44% of the incoming solar flux while 26% of it is absorbed by the atmosphere (Hartmann, 1994). Different components of energy in the atmosphere are in balance over a period of time and so maintain overall thermal equilibrium. Vertical transfers of radiant energy involved in this balance determine the thermal structure and characteristics of the different layers in the atmosphere. Geographical differences in radiation are compensated for in part by horizontal transfers of energy. This energy transfer is accomplished by the general circulation, both in the atmosphere and the oceans, which in turn are driven by non-uniform distribution of heating. Radiative processes are the only means by which the earth and atmosphere exchange energy with space. Thus, a better understanding of weather and climate processes requires a detailed study of radiative processes and radiative balance of the earth-atmosphere system.

Infrared radiation not only plays a key role in determining the weather and climate but also the near-surface thermal environment, especially during night. Several workers (Ramdas and Malurkar, 1932; Ramanathan and Ramdas, 1935; Lake, 1956; Goody, 1964; Coantic and Seguin, 1971; Kondratyev, 1972) have pointed out the importance of accurate computation of near-surface radiative fluxes as the accuracy of

these parameters are crucial in the study of remote sensing, agricultural meteorology and atmospheric modelling studies. A small error in the relatively large fluxes can lead to appreciable errors in the estimated cooling rates, especially near the surface where the radiative calculations have to be over thin atmospheric layers (Tjemkes and Duynkerke, 1989; Quinet and Vanderborght, 1996). For instance, an error of 10^{-4} Wm^{-2} in the net radiative flux could produce a cooling rate error of 3.6 K/d in a thin layer of $\Delta z = 5$ mm with air density of 1.2 kgm^{-3} and specific heat at constant pressure of $1000 \text{ Jkg}^{-1}\text{K}^{-1}$ (see cooling rate equation in Section 2.3).

The vertical variation of radiative fluxes in the surface layer is 10-15% of the surface values (Eliseyev, Paramonova, Privalov and Utina, 2001). Usual experimental error in the estimation of radiative fluxes is of the same order as this variation. This experimental error increases as the atmospheric layers become thinner near the ground. Depending on the stratification of the near-surface layers, the radiative flux values could change with time and altitude and cooling rates range upto tens of K/h near the surface. As one gets closer to the surface, measuring the radiative fluxes accurately is a difficult task.

We may illustrate these conclusions by considering the direct measurements of radiative flux divergence carried out by Eliseyev *et al.* (2001) in North Kazakhstan dry steppe in August 1981, based on an optical-acoustic method using a specially designed spectrophone. The observation site was a plain and covered by thin grass. Measurements were taken from 5:00 h to 22:00 h local time under light cloudiness. Sunrise and sunset were at 5:00 h and 19:00 h respectively. Upwelling and downwelling fluxes were measured at 0.1, 0.5, 2 and 6 m. During mid-day hours a maximum heating rate of 30 K/h (720 K/d) was recorded. Episodic measurements on some days revealed a heating rate of 50 K/hr (1200 K/d) at a height of 2 cm above the ground. This is cited just as an example of the high heating/cooling rates that could prevail near the surface although several other studies (e.g. Tjemkes and Duynkerke,

1989) have confirmed such high rates by observation/simulation. However there is no mention of surface emissivity in the findings reported. A detailed account of high cooling rates near the surface is given in Section 5.2.

The importance of fast and accurate long-wave radiation parameterization in atmospheric models for weather and climate studies has been stressed by several authors (see e.g., Ellingson, Ellis and Fels, 1991). In these models, calculations of longwave fluxes take a third or more of the total computing time (Chou and Suarez, 1994).

1.1 Near-surface Thermal Environment

The nocturnal distribution of air temperature, especially within the boundary layer, is an important subject of study in agricultural and boundary layer meteorology. The air layers close to the surface affect the formation of fog and frost, which are important factors in agricultural meteorology. At much greater heights, upto the order of hundreds of metres, there occur temperature inversions which influence the dispersion of pollutants and aerosols in the atmosphere. The dynamical and thermodynamical aspects of the nocturnal boundary layer are yet to be well understood (Garratt, 1992). The stable boundary layer that develops contiguous with the earth's surface on calm clear nights is characterised by a positive lapse rate. This stable layer begins to establish itself soon after sunset, continues to grow till early morning, and generally dissipates itself after sunrise when a thermally convective atmosphere starts developing near the ground. Radiative cooling, shear-generated turbulence and horizontal advection are considered to be responsible for the growth of the nocturnal boundary layer, while winds may modify its structure (Garratt, 1992).

The relative importance of the different modes of energy transfer depends on the local conditions that prevail in the atmosphere and the properties of the

underlying surface such as ground cooling rate and emissivity (see e.g., Vasudeva Murthy, Srinivasan and Narasimha, 1993, hereafter VSN). Theoretical studies of the temperature distribution of air have to take into account this relative importance in the simplification of the various models (VSN, Ragothaman, Narasimha, Vasudeva Murthy, 2001, 2002; Garratt and Brost, 1981). However, it can be said that, at any given time, the temperature distribution is in general the result of an interplay of these different mechanisms.

1.1.1 Ramdas Layer

One such interaction results in a singular temperature distribution known as the lifted or raised minimum reported first by Ramdas and Atmanathan (1932). The phenomenon is that the air layer within a metre or less from the ground gets cooler than the ground by a few degrees at night. The conditions under which such observations were made were reported to be calm winds, clear skies, and bare soil. In the absence of wind, the lifted minimum is sustained almost till sunrise, as reported by Ramdas and others. The air layer close to the ground where this phenomenon occurs has been termed the Ramdas layer by Narasimha (1994).

The prevailing view at the time of Ramdas's report was that during night, the lowest temperature must be at ground. This view was based on near-surface temperature observations that generally stopped at screen height (1.22 m), and therefore could not detect the presence of the lifted minimum which was reported to occur below 1 m. The first reports of such a lifted temperature minimum (LTM) were received with considerable surprise and skepticism. It was initially thought that the reported observations could have been the result of instrumentation errors. Another explanation given was that the LTM could be due to advection. However, further work by Ramdas and his co-workers showed that the LTM does arise in the absence of advection (Ramanathan and Ramdas, 1935). A further reason for the skepticism

was a puzzling aspect of the phenomenon, namely that it was not destroyed by the Rayleigh-Bénard instability that is expected to develop when a cooler layer of air overlies a warm layer. VSN have shown, by a detailed analysis, that such an instability may not arise as the critical Rayleigh number (Ra_c) for onset of Rayleigh-Bénard thermal convection can go up by a factor of 10–150 under the conditions of interest because of the stabilising effect of radiative transport.

The careful observations of Raschke (1954), Lake (1956), and Oke (1987) have confirmed the existence of the LTM beyond doubt. A comprehensive theory of the LTM has been proposed by VSN. A short description of their model will be given in the next Section. Narasimha (1994) provides an extensive account of the early history of studies of the phenomenon.

1.1.2 The VSN Theory

A theory based on the energy balance between radiation, conduction and convection was formulated by VSN to describe near-surface nocturnal temperature distributions. It was shown that the lifted minimum is the result of smearing by molecular conduction of the radiative slip in temperature that occurs on calm clear nights. This smearing is similar to that by viscosity of the slip velocity that is encountered in low-density gas dynamics. VSN also showed that there is no need to assume the presence of haze or other particulate matter to explain LTM, as had been done by Zdunkowski (1966).

Another striking difference between the theory of Zdunkowski (1966) and the VSN theory is that the former considers values of thermal diffusivity lower than the molecular value by factors of upto 18. This assumption of unrealistically low diffusivities (as molecular transport cannot be suppressed) was considered a serious flaw in the theory by VSN. The VSN model predicted a lifted minimum for values of ground emissivity not too close to unity and for low values of ground cooling rates.

These two parameters, which were earlier ignored in most studies, were highlighted by the model as the most significant in the problem. A heuristic argument was provided to show how the LTM can be sustained, as the Rayleigh-Bénard instability can be appreciably delayed (i.e., there is a considerable increase in the critical Rayleigh number) due to radiative stabilisation.

Thus, the value of their model in simulating the LTM under suitable conditions in the atmosphere and ground was established by VSN. The results of the simulation were shown to be in reasonably good agreement with observations and the sensitivity of the phenomenon to the various parameters was demonstrated. Recently, Ragothaman *et al.* (2001) have studied the dynamical behaviour of the lifted minimum temperature when the surface emissivity is not too close to unity. Their study showed that LTM can appear shortly after sunset, but its subsequent evolution, depending on the ground cooling rate, can lead to monotonic growth, near-steady state, or growth followed by collapse. On the basis of numerical simulations of the evolution of nocturnal inversion carried out by them, Ragothaman *et al.* (2002) suggested that both the depth and the intensity of the nocturnal temperature inversion depend on surface emissivity and ground cooling rates, especially under calm conditions.

1.2 Radiation Models

Due to the many complexities involved in the direct evaluation of radiative fluxes, radiation models are generally parameterized and approximations are made depending on the problem on hand. For instance, for use in climate models, accuracy is compromised to a certain extent by the demand for speed and simplicity. It is important to have radiation codes which can accurately compute the radiative fluxes, taking account of the fact that the transmission function/absorption coefficient (k_ν) of atmospheric air at any frequency (ν) is a wild function of frequency and depends

in general on both pressure (p) and temperature (T).

In radiation modelling studies, the atmosphere is generally assumed to be a plane, parallel, horizontally homogeneous medium in local thermal equilibrium. The next few sub-sections discuss different methods of making radiation calculations.

1.2.1 Line-by-line Model

This is a computer-intensive technique where k_ν is resolved over very small intervals in wavelength (10^{-4}cm to 10^{-2}cm). The dependence of k_ν on frequency, and the varying strength and shape of each spectral line throughout the spectrum, make the task of computing the fluxes very difficult (Ellingson *et al.*, 1991). The method involves the integration of the contributions of each spectral line, and hence its name.

The technique is accurate owing to its ability to resolve a large number of spectral lines (of order 10^5), but it is not appropriate for routine calculations in climate models or GCMs (General Circulation Models) as it is computationally very expensive. Line-by-line models however represent the best available benchmarks, as their accuracy depends only on the basic spectroscopic properties of the attenuating gases in the atmosphere.

Such models usually do not include the effects of lines beyond a given distance from the line centres because of uncertainties in line shape. Thus they usually take adequate account of the effects of local lines, but not of the cumulative effects of strong distant lines (Ellingson *et al.*, 1991). This is not a major problem for gases like CO_2 where the effects of distant lines are not considerable. But for water vapour the effects of the distant lines may dominate the effects of the local lines in regions of weak absorption. Hence modellers are forced to add an additional absorption coefficient known as continuum absorption (Ellingson *et al.*, 1991).

1.2.2 Narrow Band Model

In band models, the absorption properties of lines, with parameters such as line strength, separation and position, are averaged over certain prescribed bands, and appropriate transmission functions are expressed in terms of pseudo line parameters such as mean line intensity, mean half-width and mean line spacing. Integration over frequency (ν) is replaced by a summation over the finite number of bands or spectral intervals that span the long-wave absorption spectrum.

A spectral line at a certain spectral position is fully characterised by its strength (the intensity or integrated absorption coefficient), its line half-width, and knowledge of the broadening mechanism. But a vibration-rotation band, of the kind that is present in the water vapour absorption spectrum, has many closely spaced spectral lines that may overlap considerably. While the absorption coefficient for individual lines may simply be added to give the absorption coefficient of a certain band at any spectral position, the resulting function tends to oscillate violently across the band unless the lines overlap strongly. This tendency makes heat transfer calculations difficult, if the exact relationship is to be used in spectral integration for total intensity or radiative flux.

The spectrum of the radiation, given say by the Planck function, does not vary appreciably over the spectral range of a few lines, considering that adjacent lines are very closely spaced (Modest, 1993). The local radiation intensity can also be expected to be relatively smooth since it is due to emission from all locations in the medium and is further smoothed by absorption and scattering. Therefore, if one can assume the spectral variation of absorption coefficient and emissivity to be relatively smooth over the band, it makes spectral integration of radiative fluxes feasible.

To find spectrally averaged or "narrow band" values of the absorption coefficient and the emissivity, some information must be available on the spacing of

individual lines within the group and on their relative strengths. In the *Elsasser* model equally spaced lines of equal intensity are considered, while in the *statistical* model spectral lines are assumed to have random spacing and/or intensity. Both models will predict the same narrow band parameters for optically thin situations. Under intermediate conditions, the Elsasser model always predicts a higher emissivity/absorptivity than the statistical model, since regular spacing always results in less overlap, and hence the statistical model is better.

In another approach to band modelling, scaling to the atmosphere is done with the use of the Curtis-Godson approximation (Goody, 1964), which defines a temperature-scaled amount of the absorber at a definable mean pressure. Chou and Arking (1980) use a different method in their band model where the band absorption coefficient is determined from line-by-line calculations. This method is the k -distribution technique applied to problems with the use of a one-parameter scaling approximation. This is the method which is adopted in the present model. The method is discussed in detail in Chapter 2. Closely related to this method is the sum of exponentials technique discussed by Lacis and Hansen (1974). The advantages of the k -distribution method over the analytical band model are that the actual distribution of k_ν is employed, the frequency integration is performed accurately for homogeneous paths, and the form of frequency-averaged transmissivity allows a radiation model to be extended to include multiple scattering (Ellingson *et al.*, 1991). Another type of narrow band model uses empirical function fits to a small range of observations or calculations (Selby, Shettle and Mc Clatchey, 1976; Kneizys, Shettle, Abreu, Chetwynd, Anderson, Gallery, Selby and Clough, 1988).

In their calculations of a nocturnal boundary layer, Tjemkes and Duynkerke (1989) used a narrow-band model in which the infrared spectrum between 3.6 and 100 μm is divided into 178 bands, and solved the transfer equations given by Rodgers and Walshaw (1966) for the mean upward and downward fluxes in each of the bands.

The solution extends over a domain limited at the top by the location where the wind is set equal to the geostrophic value. The 'surface' level in the model is within the vegetation layer, and has a temperature different from that of the surface itself; the differential is calculated using a scheme proposed by Holtslag and De Bruin (1988).

The band model method is constrained by the need to define spectral intervals that are narrow enough to treat the Planck function as constant across each one of them. The model is also restricted by the fact that for broad spectral intervals the transmission function is no longer exponential in character, thus making it difficult to fit a pure exponential to the mean transmission (Stephens, 1984).

1.2.3 Wide Band Models

In these models the approach to the transmission-absorption problem is through the use of spectroscopic observations and line-by-line or narrow band model calculations over large band widths or even the entire spectrum. One method related to this approach is the flux emissivity scheme in which an attempt is made to perform the entire spectral integration separately for each absorber. A detailed description of this method is presented in the next Section.

Another wide band model approach is called the perturbation technique. This method was first proposed by Curtis (1956) and applied by Rodgers (1967). It is useful to precompute the transmissivity for those constituents that do not change and are weakly dependent on temperature variations along the atmospheric path. Fels and Schwarzkopf (1981) extended this idea by computing the integrated absorptivities for the 15 μm band of CO_2 with a line-by-line integration for a standard pressure grid. The major limitations of this approach include the necessity for large computer storage compared with the emissivity approach, the difficulty in accurately accounting for overlap with other absorbers, and the difficulty in accounting for a varying absorber concentration.

A technique related to the perturbation technique is the table look-up technique. In this approach, the pressure increments of atmospheric layers are fixed, except perhaps for the layer closest to the surface. The water vapour, carbon dioxide and ozone transmissivities are precomputed for a wide range of temperature and absorber amounts in each layer. When an actual sounding is used, the data are interpolated to the model grid and the necessary absorber amounts are calculated through interpolation of the precomputed data. Chou and Arking (1980) and Chou and Peng (1983) have developed such a technique for water vapour and carbon dioxide. We shall return to these methods in Chapter 2.

1.2.4 Flux Emissivity Model

The essence of the flux emissivity approach for the calculation of infrared fluxes and heating rates is to use the temperature directly in terms of the Stefan-Boltzmann law instead of the Planck function (Liou, 1992). Eliminating the number of spectral intervals required to evaluate the broadband longwave fluxes and cooling rates has several practical advantages including the obvious one of removing once and for all the frequency integral in the longwave flux equations. This is done as follows. A function is first derived by integrating the absorption over frequency and weighting it in some way with the Planck function (Stephens, 1984). This "integrated" absorption is then expressed in terms of only one parameter, namely the optical path length.

Atmospheric applications of this approach date at least to Elsasser (1942), and modifications and improvements are discussed by Ramanathan (1976). This approach is appealing in climate studies because the integrated absorption for the active gases may be measured over a wide range of variables in the laboratory, and because the calculations may be performed rapidly on the computer. The primary difficulties with this approach are accurately accounting for inhomogeneous paths and for overlap with other active gases.

1.3 Objectives

The objectives of the present thesis are:

- (i) to study the longwave radiative transfer near the ground in different bands for arbitrary ground emissivities,
- (ii) to generate a band model which provides accurate estimates of fluxes and cooling rates near the surface for use in general circulation models, remote sensing and agricultural meteorology and
- (iii) to simulate the Ramdas layer for a detailed spectral analysis of the phenomenon.

1.4 Previous Work

Most previous studies of near-surface radiative transfer use a broadband flux emissivity approach (Coantic and Seguin, 1971; Coantic and Simonin, 1984; André, De Moor, Lacarrere, Therry and du Vachat, 1978; Garratt and Brost, 1981; Estournel and Guedalia, 1985; VSN; Narasimha, 1997; Ragothaman *et al.*, 2001, 2002). This is sufficiently accurate for many applications, but cannot provide an estimate of the contribution of different infrared wave bands to radiative cooling, which would be important when one considers the effect of different constituents of atmospheric air or needs to use band-dependent surface emissivities

The importance of ground emissivity ε_g and its effects on the near-surface cooling rates for a small departure of its value from unity has been shown by VSN in their study of the Ramdas layer.

One of the objectives of meteorological remote sensing is to assess the temperature-humidity distribution of the surface-atmosphere system. Quantitative estimates of these parameters are based upon the numerical solution of the radiative transfer equation wherein contributions to the measured radiance from the observed system are modelled. The model must account for emissions from both the earth's sur-

face and the atmosphere. Plokhenko and Menzel (2000) demonstrate the importance of accounting for the variations of surface emissivity in meteorological remote sensing so as to improve the defined temperature-humidity profiles when using infrared spectral measurements. They show three effects due to the inclusion of emissivity in the solution of the inverse problem: (i) Even small emissivity variations cause measurable changes in infrared radiance. (ii) Modern satellite meteorological remote sensing instruments are very sensitive, with a relative accuracy of approximately 0.2 K. Disregarding the spectral, angular or spatial variations of emissivity in the radiative transfer model magnifies the errors by at least a factor of 3–5. (iii) The different kinds of surface cover, with different surface optical properties and extremely high spatial and temporal variations, restrict the use of *a priori* estimates of the surface effects. Therefore, the direct evaluation of emissivity is a simpler and more effective approach for modelling. Emissivity errors distort derived atmospheric parameters, primarily in the lower atmosphere.

The detection of unusual weather events and quasi-weather phenomena often poses challenging problems. As the usual spectral bands available on weather satellites are not designed to look at these phenomena, differencing an optimal combination of bands helps in the detection of some of these features. Detailed knowledge of the characteristics of various spectra helps in the process of choosing the right bands (Hillger and Ellrod, 2000).

The atmospheric emission of longwave radiation to the surface constitutes a significant component of the surface energy balance (Allan, 2000). Clear-sky downward longwave fluxes appear to be an important amplifier of greenhouse gas-forced surface warming due to water vapour feedback (Ramanathan, 1981). Wild, Ohmura, Gilgen and Roeckner (1995) made comparisons of surface downward fluxes simulated by a climate model with both surface observations and also radiative transfer calculations using radiosonde profiles as input data. Model surface downwelling fluxes

tended to be underestimated by 5 Wm^{-2} in comparison with radiative transfer scheme calculations and by 10 Wm^{-2} when compared with surface radiation observations. A similar result was found by Garratt and Prata (1996), who compared all-sky surface downwelling fluxes simulated by four climate models with observations over continental surfaces. They argued that the model underestimate in downwelling fluxes was caused by underestimates in near surface temperatures. The bias was less apparent in a subsequent study (Garratt *et al.*, 1998), and satellite-derived surface downwelling flux was greater than observed mean global values. Recently, Wild, Ohmura, Gilgen, Roeckner, Giorgetta and Morcrette (1998) argued that climate models generally underestimate surface downwelling fluxes and that realistic hydrological cycles were simulated only because the same models overestimated the surface absorbed radiation.

Validation of model-estimated surface fluxes is limited by the available observational network. The accuracy of ground-based radiometers is about $\pm 10 \text{ Wm}^{-2}$ (e.g., Weller and Anderson, 1996). Also surface network of radiometres is spatially limited and confined almost exclusively to land-based regions (Garratt and Prata, 1996). Using the method of inferring surface radiative fluxes from the satellite radiances at the top of the atmosphere, Gupta (1989) and Rossow and Xhang (1995) found differences in model-observation all-sky surface downward longwave fluxes to be large; this is unsurprising considering that the radiative fluxes are dependent mainly on near-surface conditions, which are the most difficult variables to derive remotely from satellite (Allan, 2000). Temperature and humidity fields near the surface are very important in determining the surface downward radiative fluxes (e.g., Zhao, 1994), and an accurate estimation of these terms is required for a robust simulation (Allan, 2000).

Although the atmosphere immediately above the surface is assumed to have a temperature directly dependent on the surface skin temperature, observations

show that this is not the case (see Allan, 2000). In some observations at a height of 2.6 m above ground, it was found that they were less than skin temperature by 1.5 K, and this discrepancy may account for much of the overestimation of simulated surface longwave downward fluxes in comparison with the observations (Allan, 2000). Coarse spatial and temporal resolutions may not represent the local atmospheric conditions and this may affect the simulations of radiative fluxes. The differences between surface and screen-height temperatures have been discussed by Ragothaman *et al.* (2001) through their numerical simulations based on the flux emissivity scheme.

There is great need for more accurate radiation calculations in the climate models as climate problems are sensitive to small changes in radiation quantities (Warner and Ellingson, 2000). Calculations from different radiation models used in climate calculations disagree with one another, and with more detailed models, at levels significant to many climate problems. A 10 Wm^{-2} change in net flux at the surface is on the average about 3% of the surface downwelling longwave flux, and if continued for a year could lead to a 1 degree change in the sea surface temperature. Therefore, the usually accepted 5–10% uncertainties in radiation calculations are not sufficient for many climate studies.

Emanuel and Zivkovic-Rothman (1999) questioned the adequacy of vertical grids currently used in many GCM studies, pointing out that, since the scale-height for water vapour in the atmosphere is around 3 km, models require vertical resolutions somewhat finer than this to represent the water vapour profile correctly. They found that degrading the vertical resolution of their column model from 25 to 100 mb greatly reduced the sensitivity of the water vapour profile to changes in the microphysical parameterization. Coarse vertical resolution could result in excessive diffusion of water vapour as a result of the implicit diffusion operating in the horizontal and (especially) vertical advection schemes (Tompkins and Emanuel, 2000). They argue that limitations on computing resources necessitate compromises in terms of

resolution and complexity of parameterization schemes when operating any numerical model. However, there has been a tendency to use increasing computer resources to improve the horizontal resolution of climate models, or to increase the complexity of subgrid-scale parameterization, while relatively little attention has been paid to the effect of vertical resolution (Tompkins and Emanuel, 2000).

Tompkins and Emanuel (2000) also show the futility of using an accurate cloud and convective scheme in a GCM if the vertical resolution is not adequate, as many physical processes are temperature-dependent and are restricted to thin layers, and stress the importance of considering the nature of physical processes when selecting vertical resolution. In their study of the effect of vertical resolution on the tropical radiative-convective equilibrium profiles of two single column models, they find sensitivity to increased vertical resolution; both models converged at a uniform vertical resolution of around 20–25 mb (\approx 200–250 m). They also stress that the 25 mb convergence limit only provides a lower bound on the resolution required in GCMs and sensitivities differ depending on the the models/parameterizations selected. Further tests revealed that the variability was reduced considerably when the boundary layer was resolved.

In the case of radiative transfer parameterization, most of the models use a total of less than 30 layers for the entire atmosphere. But it should be noted that the scale length of the physical processes occurring close to the surface are of the order of centimetres or less, so high resolution, certainly near the surface, is also important for radiative calculations.

All these arguments point to the sensitivity to the radiative fluxes in different applications and the need for accurate radiation calculations.

1.4.1 Surface Emissivity

Emissivity of a material is defined as the ratio of the radiance it emits to the blackbody radiance at the same temperature. The earth's surface imposes boundary conditions on the problem of radiative transfer in the atmosphere, by its reflectance in the solar spectrum and its emissivity in the longwave region. The spectral region 8–14 μm is a region of relative transparency (window region) of the atmosphere; therefore the value of the emissivity in this spectral interval plays a major role in surface radiative cooling (Lenoble, 1993).

Accurately characterising surface emissivity is important for determining the longwave radiation leaving the surface and for retrieving surface temperature by remote sensing measurements (Wan and Dozier, 1996; Kahle and Alley 1992; Kealy and Hook, 1993). Calculation of longwave surface energy budgets which are derived from data collected by remote sensing instruments aboard aircraft and satellites depends on the knowledge of surface emissivity.

Accurate in-situ measurements of surface emissivity are difficult to obtain as many parameters influence emissivity including surface temperature, soil moisture, composition and surface properties, some of which are highly variable quantities and are difficult to measure. Moreover, the spatial coverage for the available field measurements are insufficient for global studies. Remote sensing from satellites, which could be used to retrieve surface emissivities, requires concurrent temperature measurement on ground and good knowledge of atmospheric absorption and scattering. Thus, high quality surface emissivity data have not been readily available for global applications (Wilber, Kratz and Gupta, 1999). As a result, many remote sensing and climate modelling efforts have assumed the surface to radiate as a blackbody ($\epsilon_g=1.0$).

Measurements (Salisbury and D'Aria, 1992) of spectral reflectances of sur-

face materials show that surface emissivities deviate considerably from unity, both spectrally (upto 0.56) and integrated over the broadband. Assuming surface emissivity to be unity can lead to significant errors in surface temperature retrievals in longwave surface budgets and climate studies (Wilber *et al.*, 1999; Plokhenko and Menzel, 2000).

Surface emissivity of the ocean varies with viewing angle and sea state. But at near-nadir viewing angles, both spectral and broadband emissivity are nearly constant with respect to sea state (Wilber *et al.*, 1999). The emissivity also depends on seasonal effects, surface types, composition and properties. Computations carried out by Wilber *et al.* (1999) with a longwave model with a constant surface emissivity of unity and with spatially varying emissivity data showed a maximum difference in the net longwave fluxes of 6 Wm^{-2} over the Sahara desert and Arabian peninsula (both classified as barren) and open shrubland in Australia.

According to Weng, Yan and Grody (2001), satellite observations using microwave radiometres operating near the window regions are strongly affected by surface emissivity and the measurements obtained over land are not directly utilized in numerical weather prediction models because of uncertainties in estimating the emissivity. They have developed a microwave land emissivity model to quantify the land emissivity over various surface conditions. The lowest mean emissivities determined for bare soil, short grass and powder snow were respectively 0.75, 0.92 and 0.74.

Thus, it is clear that the surface emissivity has a vital role in determining the near-surface thermal environment. It is very important in the science of remote-sensing, agricultural meteorology and climate modelling. VSN has established the role played by surface emissivity in sustaining the Ramdas layer. In this thesis, a new code for computing infrared fluxes is presented. In Chapter 2, the formulation of the longwave radiation band model and methodology of implementation are described.

Details of verification and validation of the new code are presented in Chapter 3, followed by Chapter 4 which includes the present results on spectral as well as net cooling rates. In Chapter 5, previous studies related to radiative slip and some results associated with it are presented. Results and discussion on the simulated LTM with the new code are presented in Chapter 6. Summary of the present work and scope for future studies are included in Chapter 7.

Chapter 2

Formulation of Model and Methodology of Implementation

As part of a continuing programme on understanding the nocturnal near-surface thermal environment (VSN; Narasimha 1997; Ragothaman *et al.*, 2001, 2002), an attempt was made to understand in detail the role played by longwave radiation near the surface and its significance to radiative cooling in different infrared wave bands, as such a programme is not feasible in the VSN model which uses a flux-emissivity scheme for radiation calculations¹. Therefore a new infrared radiation model based on the work of Chou, Ridgway and Yan (1993) is developed as the currently available longwave radiation codes did not resolve the vertical distribution adequately and accurately. A new numerical approach is adopted to solve this very common vertical resolution problem. This Chapter describes the preliminary experiments carried out in this regard, the parameterization used and the present approach to the solution of the problem.

2.1 Preliminary Numerical Experiments

The present work takes as its starting point the very useful code developed by Chou *et al.* (1993) which was easily available, fast, and has performed well in comparison with

¹The contents of Chapters 2-4 are largely taken from a paper to appear in *Journal of Atmospheric Sciences*, 2003.

line-by-line models. This code has a medium sized band model for water vapour and CO₂ absorption using a one-parameter scaling approximation. The Planck-weighted diffuse transmittance is then reduced to a function depending only upon the scaled absorber amount. This transmittance is then fitted with an exponential sum in each of the bands (11 in total). By this method Chou *et al.* (1993) can calculate the flux integrals very rapidly compared to commonly used band models because the evaluation of each transmission function requires only n exponential operations for each value of k (absorption coefficient) where n is the number of atmospheric layers, whereas it would require $n^2/2$ operations in a conventional band model. Also the coefficients for the exponential sum fit are given recursively, which makes the evaluation even faster. These considerable advantages of the Chou code are utilized in the further development reported here.

Preliminary experiments were carried out with the band model of Chou *et al.* (1993, but using the 1997 version of the code). This code has performed well in inter-comparison tests (Ellingson *et al.*, 1991) and agrees satisfactorily with line-by-line computations over the pressure range from 0 to nearly 1000 mb. In the computations performed by Chou *et al.* (1993) the number of layers used was 75, with the lowest grid point being at 990 mb or at approximately 240 m from the surface. However the code permits more layers, and at the time the present work was initiated there was no *a priori* reason to suspect the performance of the model or the code near the surface. Calculations were therefore carried out with the number of mesh points going up to the maximum permitted by the code, namely 780 layers, in order to obtain the high resolution required near the surface. (With 780 layers the lowest grid point is 5 mm above the ground; such fine resolution is necessary in near-surface radiative flux calculations, as it is well known that lapse rates near the ground can be as much as three orders of magnitude greater than the adiabatic value, e.g. Ramdas and Malurkar, 1932.)

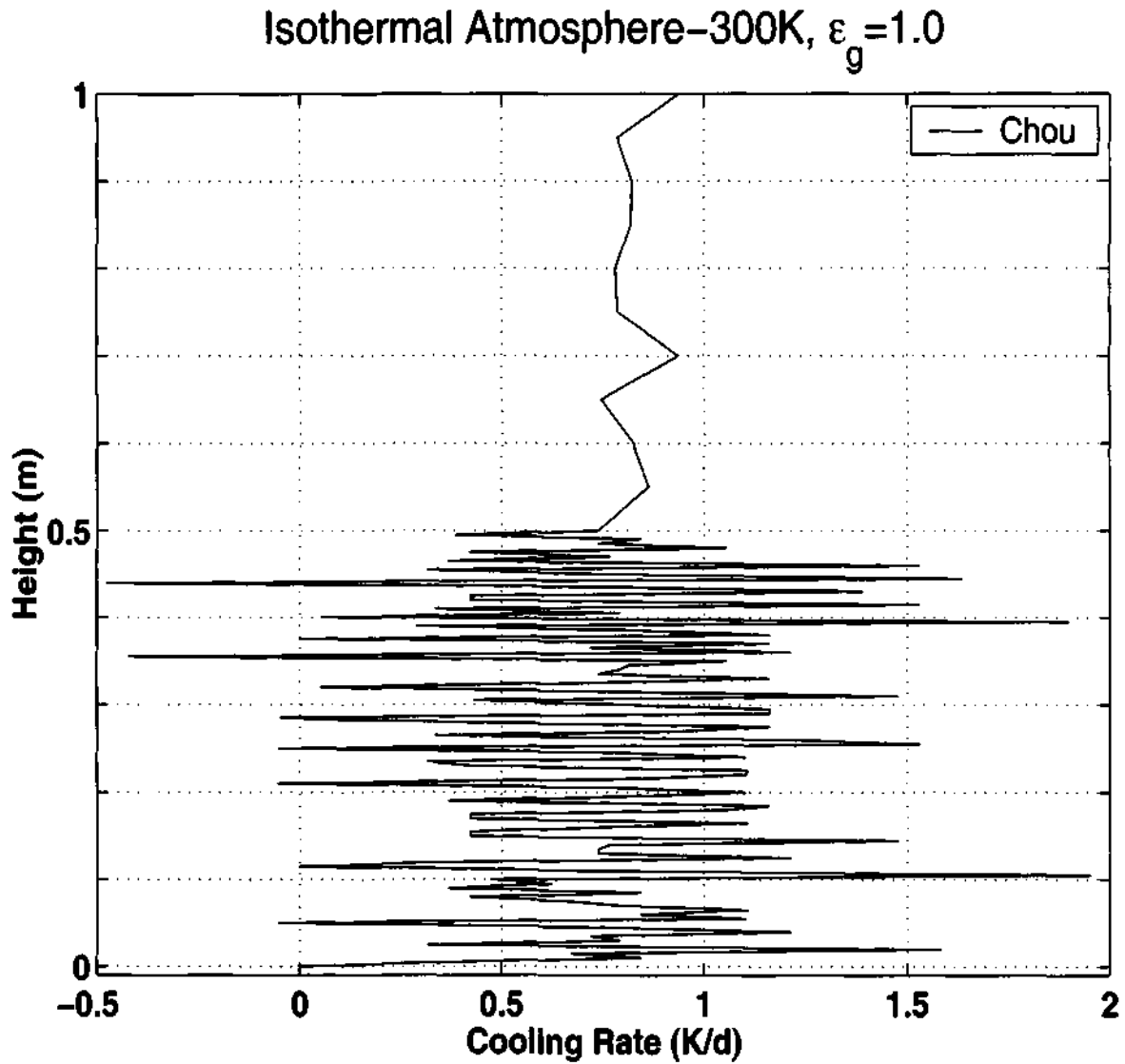


Figure 2.1: Oscillations in cooling rate near the surface, using Chou's (1993) code with 771 layers; isothermal atmosphere, water vapour line absorption only, $\varepsilon_g = 1.0$.

One difficulty we experienced with the Chou code when we used it for near-surface computations – for which it was not really designed – was that the evaluation of fluxes and cooling rates near the surface was not only insufficiently precise but also highly oscillatory. Indeed, code output showed unacceptable oscillations whose amplitude increased with increase in vertical resolution (Figures 2.1 and 2.2). Zhong

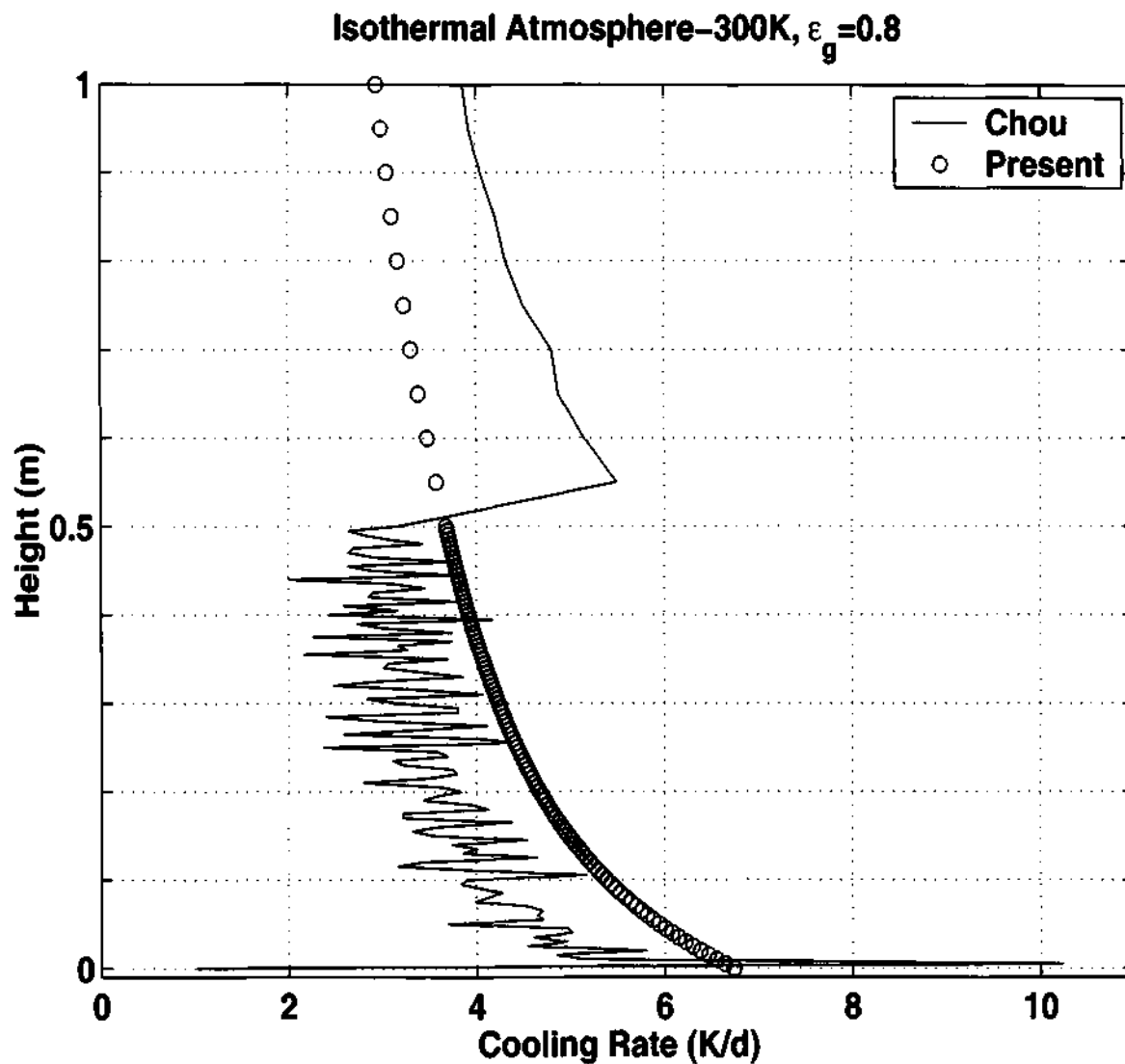


Figure 2.2: Oscillations in cooling rate near the surface, using Chou's (1993) code with 771 layers; isothermal atmosphere, water vapour line absorption only, $\varepsilon_g = 0.8$.

and Haigh (1995) also report that increasing the vertical resolution increased the errors in computed cooling rates with the ECMWF (European Centre for Medium Range Weather Forecasts) longwave radiation code. The problem therefore seems to be of fairly wide occurrence. (Since June 2000 (Morcrette, Mlawer, Iacono and Clough, 2001), the ECMWF long-wave radiation code has been replaced by a cor-

related k -distribution radiative transfer model, RRTM (Rapid Radiative Transfer Model) (Mlawer, Taubman, Brown, Iacono and Clough, 1997); however we are not aware of any cooling rate error analysis with the new code. But it is to be noted that the efficiency (which is defined as a measure of accuracy of the desired output and the time which the code takes for execution) of RRTM depends linearly on the number of levels used to discretise the atmospheric profiles while the ECMWF long-wave scheme, based on an emissivity method, displays a quadratic dependence (Morcrette, Clough, Mlawer and Iacono, 1998)).

2.2 Background

The reason for the oscillations shown in Figures 2.1–2 is that in the Chou code the integrals are evaluated using a numerical scheme that is unstable near the surface, because of a sharp boundary layer there (as will be explained in the next paragraph) caused by the huge absorption coefficients in some bands. In fact, evaluating integrals of functions that have large gradients in special regions requires special care. The present work is directed towards tackling this issue.

The main departure of the present code from Chou's rests on the recognition that, if the transmission functions are given by exponential sums, then the corresponding flux integral can be evaluated by solving an ordinary differential equation (ODE). To illustrate this idea, consider evaluating the integral

$$y(z) = \int_0^z e^{-(z-x)/\delta} dx; \quad (2.1)$$

then y satisfies the ODE

$$\begin{cases} \frac{dy}{dz} = \delta^{-1}(\delta - y); & z > 0, \\ y(0) = 0. \end{cases} \quad (2.2)$$

Now evaluating the integral by quadrature causes problems if δ is small, because of a thin layer of large gradients in the integrand near $x = z$. But the equivalent ODE can be solved very efficiently using readily available software packages that not only incorporate adaptive gridding (automatic step-size selection) but also generate solutions to a given user-specified tolerance. It is known that uniform grids are not only highly inefficient but are often incapable of solving singularly perturbed ODE's such as (1.2)(see e.g., Farrel, Hegarty, Miller, O'Riordan and Shishkin, 2000). In fact Shishkin (1997) has shown theoretically that if a singularly perturbed heat equation were to be discretized on a uniform mesh, then the error (i.e. the difference between the exact and numerical solutions) will not go to zero even if the mesh size tends to zero. Such a phenomenon has also been computationally demonstrated by Sundaresan, Nagarajan, Deshpande and Narasimha (1999) in their computation of lid-driven cavity flow at high Reynolds number (see Fedoseyev, 2001 on this point).

In summary the parameterization of Chou *et al.* (1993) provides a speed-up over conventional band models (e.g., Chou, 1991); we enhance it further by evaluating the flux integrals more precisely, especially very close to the surface, using the ODE strategy mentioned above. This is possible mainly due to the exponential structure of the transmission functions.

Compared to the method of Tjemkes and Duynkerke (1989), the present code has the advantages that it uses fewer bands without loss of accuracy, and goes all the way right from the surface to a height of 100 km.

A preliminary account of this work has appeared in Varghese, Vasudeva Murthy and Narasimha (2001). All the calculations for the results presented have been carried out on COMPAQ Alpha Server ES40 in double precision.

As a first step, only water vapour is considered (which includes both line and continuum absorption) in the parameterization described in the next Section. However it is to be noted that carbon dioxide absorption is parameterized in the same

way as that of water vapour line absorption and therefore it does not complicate the model further. Details related to inclusion of CO₂ are dealt with in Section 4.4.

2.3 Chou's One-parameter Scaling Approximation of Absorption Coefficient

Chou and his co-workers have demonstrated that, as the absorption in regions near a line-centre saturates quickly, an accurate treatment of it in such regions is not critical for infrared radiative transfer calculations. Following this argument, Chou *et al.* (1993) proposed the one-parameter scaling based on the shape of the wings of a line which is given by

$$k_\nu(p, T) = k_\nu(p_r, T_r)(p/p_r)^m f(T, T_r) \quad (2.3)$$

for the absorption coefficient k_ν at frequency ν ; here p, T are pressure and temperature at level z , while p_r, T_r are respective reference values and f is a scaling factor for temperature. The absorption coefficient is thus scaled up from its value at a reference pressure and temperature. The exponent m is a positive number typically close to but less than unity. For water vapour, p_r, T_r are chosen respectively to be 500 mb and 250 K which are characteristic of the middle regions of the troposphere. The diffuse transmittance of an atmospheric layer at level z with water vapour absorber amount u is

$$\tau_\nu(u) = 2 \int_0^1 \exp \left[\frac{-k_\nu(p_r, T_r)u}{\mu} \right] \mu d\mu, \quad (2.4)$$

where μ is the cosine of the angle between the beam and the vertical and

$$u(z) = \int_0^z (p(z')/p_r)^m f(T(z'), T_r) \rho_w(z') dz', \quad (2.5)$$

ρ_w being the density of water vapour.

To include the water vapour continuum effect, a scaled absorber amount

$$w = eu \exp \left[1800 \left\{ \frac{1}{T} - \frac{1}{296} \right\} \right] \quad (2.6)$$

is used by Chou. Here e is the water vapour partial pressure in atmospheres. Equation (2.6) is in accord with the observation that the continuum absorption increases with increasing water vapour partial pressure but with decreasing temperature. The absorption coefficients were computed from the analytical representation given by Robert, Selby and Biberman (1976) which is fitted to the laboratory data of D.E. Burch. They have carried out a detailed analysis of several long path-length transmission measurements in the 8–12 μm atmospheric window in order to determine the extinction coefficients due to the water vapour continuum. For path lengths ranging from 10 km to 50 km, failure to incorporate this parameterization can lead to errors in the computed transmission ranging from factors of 2 to more than 10,000. We follow this parameterization because of its excellent performance in inter-comparison tests (Ellingson *et al.*, 1991), although the water vapour continuum model of Clough, Iacono and Moncet (1992), which includes contributions from foreign continuum and a modified self-continuum, is claimed to be more accurate (Clough and Iacono, 1995).

The upwelling and downwelling radiative fluxes at frequency ν are given respectively by

$$F_{\nu}^{\uparrow}(u) = G_{\nu} + \int_0^u \pi B_{\nu}(T') \frac{d\tau_{\nu}}{du'} (u - u') du' \quad (2.7)$$

$$F_{\nu}^{\downarrow}(u) = - \int_u^{u_{\infty}} \pi B_{\nu}(T') \frac{d\tau_{\nu}}{du'} (u' - u) du' \quad (2.8)$$

where $B_{\nu}(T)$ is the Planck function

$$B_{\nu}(T) = \frac{2h\nu^3}{c^2 \exp[(h\nu/KT) - 1]} \quad (2.9)$$

in standard notation, K being the Boltzmann constant. Following Paltridge and Platt (1976), the term G_{ν} in (2.7), representing the contributions of radiation emitted by

the surface and the reflected component of the downwelling radiation received at the surface, is taken to be

$$G_\nu = [\varepsilon_g \pi B_\nu(T_g) + (1 - \varepsilon_g) F_\nu^\downarrow(0)] \tau_\nu, \quad (2.10)$$

the first term being the flux emission from the surface and the second the reflected component of the downwelling flux at the surface. Here ε_g is the emissivity of the surface and T_g is the ground temperature. Strictly speaking ε_g is also a function of the frequency ν , but we shall assume it to be a constant in the present work for the sake of simplicity and because of lack of data; the present code however permits incorporation of a functional dependence on ν for ε_g if the requisite information should become available.

The infrared spectrum is divided into 11 bands in Chou's model. The spectrally integrated flux in band j is denoted by

$$F_j^{\uparrow\downarrow} = \int_{\nu_j}^{\nu_{j+1}} F_\nu^{\uparrow\downarrow} d\nu$$

where ν_j and ν_{j+1} are the starting and ending wave-numbers of the spectral band j . From (2.8), the down flux in band j is

$$F_j^\downarrow = - \int_u^{u_\infty} \int_{\nu_j}^{\nu_{j+1}} \pi B_\nu(T') \tau'_\nu(u' - u) d\nu du'$$

where $\tau'_\nu(u)$ is the derivative of the transmittance function τ_ν with respect to u . The above double integral can be reduced to the single integral

$$F_j^\downarrow = - \int_u^{u_\infty} \pi B_j(T') \tau'_j(u' - u) du' \quad (2.11)$$

by defining

$$B_j(T') \equiv \int_{\nu_j}^{\nu_{j+1}} B_\nu(T') d\nu, \quad \tau_j(u) \equiv \frac{1}{B_j(T')} \int_{\nu_j}^{\nu_{j+1}} B_\nu(T') \tau_\nu(u) d\nu. \quad (2.12)$$

620.44
P03

Note that τ_j is a function of p and T also, the temperature dependence appearing both through B_ν and τ_ν . However Chou and Suarez (1994) have demonstrated that it suffices to consider the temperature dependence only in $B_\nu(T')$, and that the argument in τ_ν can be replaced by an appropriate constant reference value T_0 (taken by them to be 250 K). With this assumption (which we shall presently assess), the fluxes in band j can be written as

$$F_j^\uparrow = G_j - \int_0^u \pi B_j(T') \tau_j'(u - u') du', \quad (2.13)$$

$$F_j^\downarrow = - \int_u^{u_\infty} \pi B_j(T') \tau_j'(u - u') du', \quad (2.14)$$

$$G_j \equiv [\varepsilon_g \pi B_j(T_g) + (1 - \varepsilon_g) F_j^\downarrow(0)] \tau_j(u), \quad (2.15)$$

where we have found it useful to introduce the approximation

$$\int_{\nu_j}^{\nu_{j+1}} F_\nu^\downarrow(0) \tau_\nu(u) d\nu \approx F_j^\downarrow(0) \tau_j(u). \quad (2.16)$$

This approximation has the advantage of avoiding the use of another transmittance

$$\hat{\tau}_j(u) = \frac{\int_{\nu_j}^{\nu_{j+1}} F_\nu^\downarrow(0) \tau_\nu(u) d\nu}{F_j^\downarrow(0)};$$

more precisely the approximation made here is that

$$\frac{\int_{\nu_j}^{\nu_{j+1}} F_\nu^\downarrow(0) \tau_\nu(u) d\nu}{F_j^\downarrow(0)} \approx \frac{\int_{\nu_j}^{\nu_{j+1}} B_\nu(T_0) \tau_\nu(u) d\nu}{\int_{\nu_j}^{\nu_{j+1}} B_\nu(T_0)}. \quad (2.17)$$

We have found that this approximation, which is roughly equivalent to assuming that $F_\nu^\downarrow(0)$ is Planckian as in (2.12), does not introduce any significant error (see Appendix A).

Chou and Arking (1980) have shown that the diffuse transmittance $2E_3(k_\nu u)$ (e.g., see Liou, 1980) can be satisfactorily approximated by $\exp(-dk_\nu u)$ where d

($\approx 5/3$) is called the diffusivity factor. Comparing the cooling rates obtained from line-by-line calculations with and without the diffuse approximation, Chou *et al.* (1993) report that the error induced by this approximation is less than $0.05^\circ\text{C}/\text{day}$. Based on this approximation, an exponential sum fit was made to the transmission function in band j , writing

$$\tau_j(u) = \sum_{i=1}^{m_j} c_i^j \tau_j^i; \quad \tau_j^i = \exp(-dk_j^i u_j), \quad (2.18)$$

where

$$\frac{du_j}{dz} = (p/p_r)^m f_j(T, T_r) \rho_w, \quad (2.19)$$

$$f_j(T, T_r) = 1 + a_j(T - T_r) + b_j(T - T_r)^2, \quad (2.20)$$

and the coefficients c_i^j (derived from line-by-line calculations) satisfy

$$\sum_{i=1}^{m_j} c_i^j = 1.$$

Table 2.1 (reproduced from Chou *et al.*, 1993, 2001) gives the values of k_j^i , c_i^j , a_j and b_j for the 11 bands considered.

When multiple absorbing species are present in a band, the total diffuse transmittance is approximated by multiplying together the individual transmittances. For example, when the effect of carbon dioxide is also taken into account (see Section 4.4) we write

$$\tau_j(u) = \tau_j^{\text{wv}}(u) \cdot \tau_j^{\text{CO}_2}(u),$$

where $\tau_j^{\text{wv}}(u)$ and $\tau_j^{\text{CO}_2}(u)$ are the transmittances for water vapour and carbon dioxide respectively in band j .

Given the temperature distribution as a function of z , the integrals in (2.13,14) can be evaluated from a quadrature rule. It is not clear what kind of quadrature was used in Chou *et al.* (1993) to calculate the fluxes, but it seems

Units of μk are in cm^2/g , μ is the diffusivity factor.

Spectral Range μ	Band (cm^{-1})										
	1	2	3	4	5	6	7	8	9	10	11
0-340		340-540	540-620	620-720	720-800	800-980	980-1100	1100-1215	1215-1380	1380-1900	1900-3000
k	2.96×10	4.17×10^{-1}	1.33×10^{-2}	1.33×10^{-2}	1.33×10^{-2}	5.25×10^{-4}	5.25×10^{-4}	5.25×10^{-4}	4.72×10^{-2}	1.32	5.25×10^{-4}
n	6	6	8	8	8	6	6	8	9	6	16
c_1	0.2747	0.1521	0.1782	0.0923	0.0000	0.4654	0.5543	0.5955	0.1958	0.0740	0.1437
c_2	0.2717	0.3974	0.0593	0.1675	0.1083	0.2991	0.2723	0.2693	0.3469	0.1636	0.2197
c_3	0.2752	0.1778	0.0215	0.0923	0.1581	0.1343	0.1131	0.0953	0.3147	0.4174	0.3185
c_4	0.1177	0.1826	0.0068	0.0187	0.0455	0.0646	0.0443	0.0335	0.1013	0.1783	0.2351
c_5	0.0352	0.0374	0.0022	0.0178	0.0274	0.0226	0.0160	0.0064	0.0365	0.1101	0.0647
c_6	0.0255	0.0527	0.0000	0.0000	0.0041	0.0140	0.0000	0.0000	0.0048	0.0566	0.0183
a	0.0021	0.0140	0.0149	0.0199	0.0231	0.0302	0.0307	0.0195	0.0152	0.0008	0.0096
b	-1.01×10^{-5}	5.57×10^{-6}	6.2×10^{-5}	5.57×10^{-5}	1.70×10^{-4}	2.96×10^{-4}	2.86×10^{-4}	1.108×10^{-4}	7.608×10^{-5}	-3.52×10^{-6}	1.64×10^{-5}
m	1.0	1.0	1.0	1.0	1.0	1.0	1.0	0.77	0.5	1.0	1.0

From Chou *et al.* (1993, 2001).

Table 2.1: Values of radiation code parameters for water vapour line absorption.

Band	Spectral Range (cm^{-1})	Absorber
1	0–340	H ₂ O line
2	340–540	H ₂ O line
3	540–620	H ₂ O line and continuum, CO ₂
4	620–720	H ₂ O line and continuum, CO ₂
5	720–800	H ₂ O line and continuum, CO ₂
6	800–980	H ₂ O line and continuum, CO ₂
7	980–1100	H ₂ O line and continuum, CO ₂
8	1100–1215	H ₂ O line and continuum
9	1215–1380	H ₂ O line and continuum
10	1380–1900	H ₂ O line
11	1900–3000	H ₂ O line

Table 2.2: Spectral bands, its width and the major absorbers in each band.

evident that the oscillations seen in the cooling rates reported in Section 2.1 must be due to the numerics associated with the quadrature.

For computing thermal infrared fluxes, the spectrum is divided into 11 bands. Table 2.2 shows the spectral ranges for these 11 bands, together with the absorbers involved in each band. The water vapour line absorption covers the entire infrared spectrum, while the water vapour continuum absorption is included in the 540–1380 cm^{-1} spectral region. The absorption due to CO₂ is included in the 540–800 cm^{-1} region.

2.3 Present Approach

Our proposal here is to reformulate the flux integrals (2.13,14) as solutions of certain ordinary differential equations. There are two main reasons for adopting this

approach. The first is that the exponential sum-fit proposed in (2.18) facilitates it, because each band integral will be the sum of several sub-integrals with an exponential kernel. This means that the derivative of each of those integrals can be expressed in terms of the integral itself. This is not the case with other broad-band emissivity formulations because the kernel is logarithmic (e.g., see VSN). Secondly the absorption coefficient k_j^i in the exponentials (3.16) can be extremely large (see Table 2.1), and so result in a thin radiative sub-layer near the surface, generally extending to heights of the order of a centimetre or less and characterised by extremely sharp temperature gradients (of the order of several degrees per cm).

The second reason requires some further discussion. Contributions to the integrals come mainly from the large near-surface values, and this is why high resolution is needed there to evaluate the integrals accurately. However, the high resolution, which involves the use of a large number of grid points, usually leads to round-off error propagation and subsequently to possibly violent numerical instabilities. On the other hand when k_j^i is not large we do not require high resolution. To incorporate this kind of adaptivity it is convenient to convert the integrals into ODEs whenever possible (as it is in the present case, because of the exponential sum fitting that gives rise to exponential kernels), and then to solve them numerically with an appropriate ODE code.

This procedure is extremely efficient because present-day ODE solution codes have reached a mature capability stage, i.e., the output from the code can be quantified very well in terms of both confidence and accuracy (Oberkampf and Blottner, 1998). Note that, in the radiation problem under consideration, we have several parameters like the factor δ in the example (2.2) presented in Section 2.2; these take the form of k_j^i , some of them varying over several orders of magnitude. In order to have a method which will automatically take into account this variation in δ we need mesh adaptivity. The direct evaluation of the integral using numerical

quadrature poses problems (like the oscillations seen in Figures 2.1 and 2.2) because of the sharp variation of the integrand near the upper limit z (when $\delta \ll 1$) in the example (2.1,2). On the other hand the ODE can be numerically solved accurately for both small and moderate values of δ using a modern stiff solution code. As we shall explain below, such a code incorporates adaptivity in an efficient manner.

Accordingly, instead of evaluating the integrals using numerical quadrature, we solve here the equivalent ODEs by a readily available code that contains strategies to control error by adapting the time-stepping procedure. To derive the ODEs corresponding to the integrals (2.13,14), we first note from (2.18) that

$$\tau_j'(u) = -d \sum_{i=1}^{m_j} c_i^j k_j^i \tau_j^i, \quad (2.21)$$

where the prime denotes derivative with respect to u . Using (2.21) in (2.14) we can write

$$F_j^\downarrow = \sum_{i=1}^{m_j} F_{ji}^\downarrow \quad (2.22)$$

with

$$F_{ji}^\downarrow = dc_i^j k_j^i \int_{u_j}^{u_\infty} \pi B_j(T') \tau_j^i(u_j' - u_j) du_j'. \quad (2.23)$$

In a similar way we can decompose F_j^\uparrow and G_j as

$$F_j^\uparrow = \sum_{i=1}^{m_j} F_{ji}^\uparrow, \quad G_j = \sum_{i=1}^{m_j} G_{ji} \quad (2.24)$$

where

$$F_{ji}^\uparrow = G_{ji} + dc_i^j k_j^i \int_0^{u_j} \pi B_j(T') \tau_j^i(u_j - u_j') du_j', \quad (2.25)$$

$$G_{ji} = [\varepsilon_g \pi B_j(T_g) + (1 - \varepsilon_g) F_j^\downarrow(0)] c_i^j \tau_i^j(u). \quad (2.26)$$

Setting

$$A_j^i = dk_j^i (p/p_r)^m f_j(T, T_r) \rho_w \quad (2.27)$$

we can easily show (Appendix B) that the ODE's satisfied by $F^{\uparrow\downarrow}$ are

$$\begin{cases} \frac{dF_{ji}^{\downarrow}}{dz} = -A_j^i [c_i^j \pi B_j(T) - F_{ji}^{\downarrow}], \\ F_{ji}^{\downarrow}(\infty) = 0; \end{cases} \quad (2.28)$$

$$\begin{cases} \frac{dF_{ji}^{\uparrow}}{dz} = A_j^i [c_i^j \pi B_j(T) - F_{ji}^{\uparrow}], \\ F_{ji}^{\uparrow}(0) = c_i^j [\varepsilon_g \pi B_j(T_g) + (1 - \varepsilon_g) F_j^{\downarrow}(0)]. \end{cases} \quad (2.29)$$

For computational purposes we need to impose the top boundary condition in (2.28) at a finite but large height $z = L$. Therefore, instead of (2.28) we shall consider

$$\begin{cases} \frac{dF_{ji}^{\downarrow}}{dz} = -A_j^i [c_i^j \pi B_j(T) - F_{ji}^{\downarrow}]; \quad z \in (0, L), \\ F_{ji}^{\downarrow}(L) \text{ as prescribed.} \end{cases} \quad (2.30)$$

The cooling rate is given by

$$\frac{1}{\rho_a c_p} \sum_{j=1}^{11} \left[\frac{dF_j^{\uparrow}}{dz} - \frac{dF_j^{\downarrow}}{dz} \right]$$

where F_j^{\uparrow} and F_j^{\downarrow} are defined in (2.22) and (2.24), ρ_a is the density of air and c_p is the specific heat of air at constant pressure.

Now F_{ji}^{\downarrow} is prescribed by assuming in (2.23) that the temperature for z greater than L is a constant (say) T_{∞} and evaluating the resulting expression to get

$$F_{ji}^{\downarrow}(L) = c_i^j \pi B_j(T_{\infty}) \left[1 - \tau_i^j \{u_j(z = \infty) - u_j(z = L)\} \right]$$

In our calculations, we have chosen $L = 100$ km and consequently the results were totally insensitive to T_{∞} .

To solve (2.29,30) we use the code of Sommeijer, Shampine and Verwer (1998). This code is based on the explicit Runge-Kutta formulae of the Chebyshev type proposed by Van der Houwen and Sommeijer (see the above reference). These

formulae have good stability bounds and are ideal for large mildly stiff systems because of their explicit nature. The code is written in such a way that it automatically selects, at each vertical level z , the most efficient stable formula as well as the most efficient step size. Furthermore, it is possible to evaluate the formulae in just a few vectors of storage, making the code not only very fast but also simple to use. For more details we refer again to Sommeijer *et al.* (1998).

Details of the evaluation of black body fraction $B_j(T)$ in (2.12) are given in Appendix C.

Having discussed the formulation of the model and methodology of implementation, let us see how the code is verified and validated.

Chapter 3

Verification and Validation

The present code is first verified with an exact solution and then validated against benchmark results from the ICRCCM (Intercomparison of Radiation Codes for use in Climate Models) project (Ellingson *et al.*, 1991).

3.1 Testing Radiation Schemes

A rigorous comparison of radiation calculations with observations is a highly demanding enterprise (Ellingson *et al.*, 1991). The input data needed for a radiation scheme include the surface properties, solar elevation and the vertical profiles of temperature, absorbing gas concentrations, cloud fraction, cloud liquid and ice water content and aerosols. It is a difficult task to measure these with satisfactory accuracy (Raisanen, 1996). The measurement of radiative fluxes and heating rates is another problem. While the radiative heating rate profile can at least in principle be inferred from aircraft measurements (Slingo, Brown and Wrench, 1982), such measurements are necessarily very limited in their spatial and temporal extent. Thus the accuracy of radiation measurements continues to be a matter of concern (Ellingson and Wiscombe, 1996).

Due to observational difficulties, the usual practice when attempting to assess the accuracy of radiation schemes has been to compare their results with those

of schemes with fewer approximations, in particular line-by-line models. This approach was employed extensively in the ICRCCM project (Ellingson and Fouqart, 1991; Ellingson *et al.*, 1991; Fouqart, Bonnel and Ramaswamy, 1991). But due to the uncertainties remaining, for example in the water vapour continuum in the longwave region, even the line-by-line results serve only as a relative rather than an absolute benchmark (Ellingson *et al.*, 1991).

A single column experiment with a radiation scheme consists of performing the calculations for one atmospheric column with predefined vertical profiles of the quantities affecting radiative transfer. There exist reference results for many standardized test cases. In the ICRCCM project, more than 50 such cases were defined both for longwave (Ellingson *et al.*, 1991) and shortwave (Fouqart *et al.*, 1991) calculations, including both idealised and more realistic atmospheric situations. These test cases have been computed with many radiation schemes, ranging from wide band schemes typically used in GCMs to somewhat more accurate narrow band schemes, and, in some cases, to highly detailed line-by-line models. The results obtained in the ICRCCM comparison form a useful database for the validation of radiation schemes.

However, even though the consideration of only a small number of cases is sufficient for a careful analysis of the results, it is also a significant disadvantage. As the number of different possible atmospheric profiles is strictly speaking infinite, it is open to question how representative a view can be obtained by considering only a few or even a few dozens of columns. Similarly the results of only a few cases will not necessarily give a reasonable estimate of the maximum errors associated with a given simplification in radiation calculations.

Baer, Arsky, Charney, and Ellingson (1996) have carried out numerical experiments to study the impact of variability of input data on different longwave radiative heating parameterizations used in GCMs. They find that the shape of a given heating rate profile depends strongly on the depth of the model layers over which

the average conditions are determined. For clear sky conditions, seven algorithms were tested with a diverse range of input data taken from different geographic locations and seasons and with various distributions of vertical levels. Results indicated that heating rate profiles generated by the algorithms were similar, with a maximum difference of 0.5 K/d. It is to be noted that the maximum number of vertical layers chosen in their experiments was just 30. They used profiles of pressure, temperature, humidity and other variables from Mc Clatchey, Fenn, Selby, Volz, and Garing (1971) and Phillips, Susskind, and Mc Millin (1988) as input data.

3.2 Vertical Resolution

In the ICRCCM comparison (Ellingson *et al.*, 1991), unsatisfactory methods for performing the integration over altitude were identified as a major source of error in longwave clear-sky calculations. All numerical models considered in ICRCCM represent the atmosphere as a pile of discrete layers. The atmospheric profiles considered have mostly been idealised, and the role of vertical resolution in different parts of the column has not been studied in detail (Rodgers and Walshaw, 1966; Morcrette and Foucart, 1985; Ridgway, Harshvardhan and Arking, 1991). Rodgers and Walshaw (1966), testing a narrow band model for rather smooth sounding profiles, found differences in cooling rates of only 0.01–0.03 K/d when changing from a grid with 25 layers to one with 13 layers. Morcrette and Foucart (1985), testing their narrow band model for the Mc Clatchey *et al.* (1971) standard atmospheres, conclude that with their vertical integration method, 40 layers (20 in the troposphere and 20 in the stratosphere) would be needed to get a proper representation of radiative fluxes at the surface, the tropopause level and at the top of the atmosphere, and to keep errors in total longwave divergence within 2 Wm^{-2} . They also find that layers with equal pressure thickness yield a good representation of cooling rates in the troposphere,

whereas in the stratosphere it was preferable to keep the change in the logarithm of pressure across layers approximately constant.

In some cases, improper vertical discretization leads to problems like overestimation of surface temperature inversion, excessive warming of the tropopause and loss in detail in the humidity profile (Raisanen, 1999). The use of denser grid in certain radiation schemes produces insignificant changes in longwave fluxes due to convergence problems. This affects the results at high vertical resolution (Raisanen, 1999).

Some studies on vertical resolution made by Raisanen (1999), using the ECMWF radiation code (Morcrette, 1989, 1991) and another from Deutscher Wetterdienst (DWD) developed by Ritter and Geleyn (1992), show that the downward longwave flux at the surface is sensitive to the resolution close to the surface. This is because the major part of the thermal radiation reaching the surface originates from the humid layers close to the ground. The upward longwave flux at the top of the atmosphere (TOA) depended to some extent on the resolution in all parts of the column, but usually most on the upper tropospheric resolution. The upper tropospheric resolution also plays an important role in the net longwave flux at the tropopause.

Large errors will result if too coarse a vertical resolution is used in regions where there are also large variations in the Planck function, B_ν . In other words, vertical resolution depends on the variation of temperature as B_ν is a strong function of T (Ellingson *et al.*, 1991). Thus vertical resolution has to be fixed according to the application. Use of data sets with steep temperature gradients close to the surface produced large errors in the net longwave flux at the surface (Raisanen, 1999). This is attributed by him to the discretization error.

Poor resolution near the surface during inversion conditions leads to error in downward longwave fluxes (Raisanen, 1999). This is related to the overestimation of the thickness of the inversion at coarse resolution, and hence the underestimation

of emission from the lowest layer. The downward flux reaching the surface originates from the lowest few 100 m (Swinbank, 1964). Similar problems may occur during day time where lapse rate changes from super adiabatic near the ground to dry adiabatic higher up. A typical negative difference in temperature of a few degrees between the surface and 2 m induces strong radiative cooling in the lowest metres above the surface and thus helps to maintain the surface inversion (Raisanen, 1999).

The need for high accuracy in the computation of fluxes in the stratosphere, especially in the tropics, has been pointed out by Olaguer, Yang and Tung (1992). Hence an adequate resolution in the vertical is required not only in the boundary layer but also throughout the entire atmosphere where physical processes are important.

The problem of discretization and vertical resolution are automatically taken care of in the present formulation due to the novel numerical approach adopted here.

3.3 Some Exact Solutions

To test the code we construct some exact solutions in this Section. Apart from serving to verify the code, these solutions also address the crucial z -test that Ellingson *et al.* (1991) suggest: “A trivial but important result to check is a model’s output for an isothermal atmosphere. Although the importance of these type tests are known to many modellers, it appears that they are not always done in practice.” We construct here a new exact solution that allows for a surface that is not radiatively black (i.e. $\varepsilon_g \neq 1$).

We therefore consider an (artificial) isothermal atmosphere

$$T(z) \equiv T_1. \quad (3.1)$$

Furthermore it is convenient to set $m = 0$ in (2.19). Consequently (2.27) simplifies to

$$A_j^i = a_j^i \rho_w \quad (3.2)$$

where

$$a_j^i = dk_j^i f(T_1, T_r) \quad (3.3)$$

is a constant. In analogy with (2.1) and (2.2), where the solution was

$$y = (y_0 - \delta)e^{-z/\delta} + \delta, \quad (3.4)$$

we can write

$$F_{ji}^\uparrow = [F_{ji}^\uparrow(0) - \epsilon_j c_i^j \sigma T_1^4] e^{-A_j^i} + \epsilon_j c_i^j \sigma T_1^4 \quad (3.5)$$

where ϵ_j is the black body fraction defined in Appendix C. Under these conditions, (2.29,30) can be easily solved to yield

$$F_{ji}^\uparrow = \epsilon_j c_i^j \sigma T_1^4 - (1 - \epsilon_g) [\epsilon_j c_i^j \sigma T_1^4 - c_i^j F_j^\downarrow(0)] \tau_j^i(z), \quad (3.6)$$

$$F_{ji}^\downarrow = F_{ji}^\downarrow(L) \tau_j^i(u_L - u) + \epsilon_j c_i^j \sigma T_1^4 [1 - \tau_j^i(L - z)], \quad (3.7)$$

where c_i^j is defined in (2.18) and given in Table 2.1. Note that this is different from the expression of Ellingson *et al.* (1991), in that the upward fluxes here are not constant as we have taken into account the non-black ($\epsilon_g \neq 1$) effects of the surface as well. For large k_j^i , we note that τ_j^i (see (2.18)) will have a large gradient at $z = 0$. Also $[a_i^j \rho_{w_0}]^{-1}$ is a length scale defined for the j th band. Physically, this length scale would determine the height of the analogue (for each band) of what VSN have called the 'emissivity sublayer' that occurs close to the surface.

We emphasize here that the approximations (3.1)–(3.2) are introduced only to verify the code; for validation with other temperature profiles corresponding to different atmospheres we remove these assumptions. Nevertheless the exact solutions illustrate the effects of a non-black ground, in particular the associated strong cooling rates.

A comparison of downward and upward fluxes at the surface for $\epsilon_g=1.0$ is made in Table 3.1. The comparisons are made against results of Chou, ICRCM and

Table 3.1: Comparison of surface downward and upward fluxes (Wm^{-2}) in an isothermal atmosphere for $\epsilon_g=1.0$.

Downward flux	Chou	ICRCCM	Present	Exact
Without continuum	327.55	327.58	325.72	325.72
With continuum	413.17	411.78	412.97	
Upward flux				
Without continuum	459.39	459.88	459.09	459.09
With continuum	459.39	459.82	459.09	

exact solution. It is to be noted that the results for the exact solution assume only line absorption (without continuum). The present result agree fairly well with others.

3.4 Resolution Requirements

A typical result for the variation in the error in the downward flux at the surface and at 100 m for different prescribed tolerance levels is shown in Figure 3.1. This shows the flexible capability of the present numerics to cope with the different accuracies that may be demanded in different applications.

The computing times for executing the current program are comparable (for given accuracy) to those demanded by other standard current codes (such as e.g. that of Chou *et al.*, 1993). For example, the CPU time taken by the present

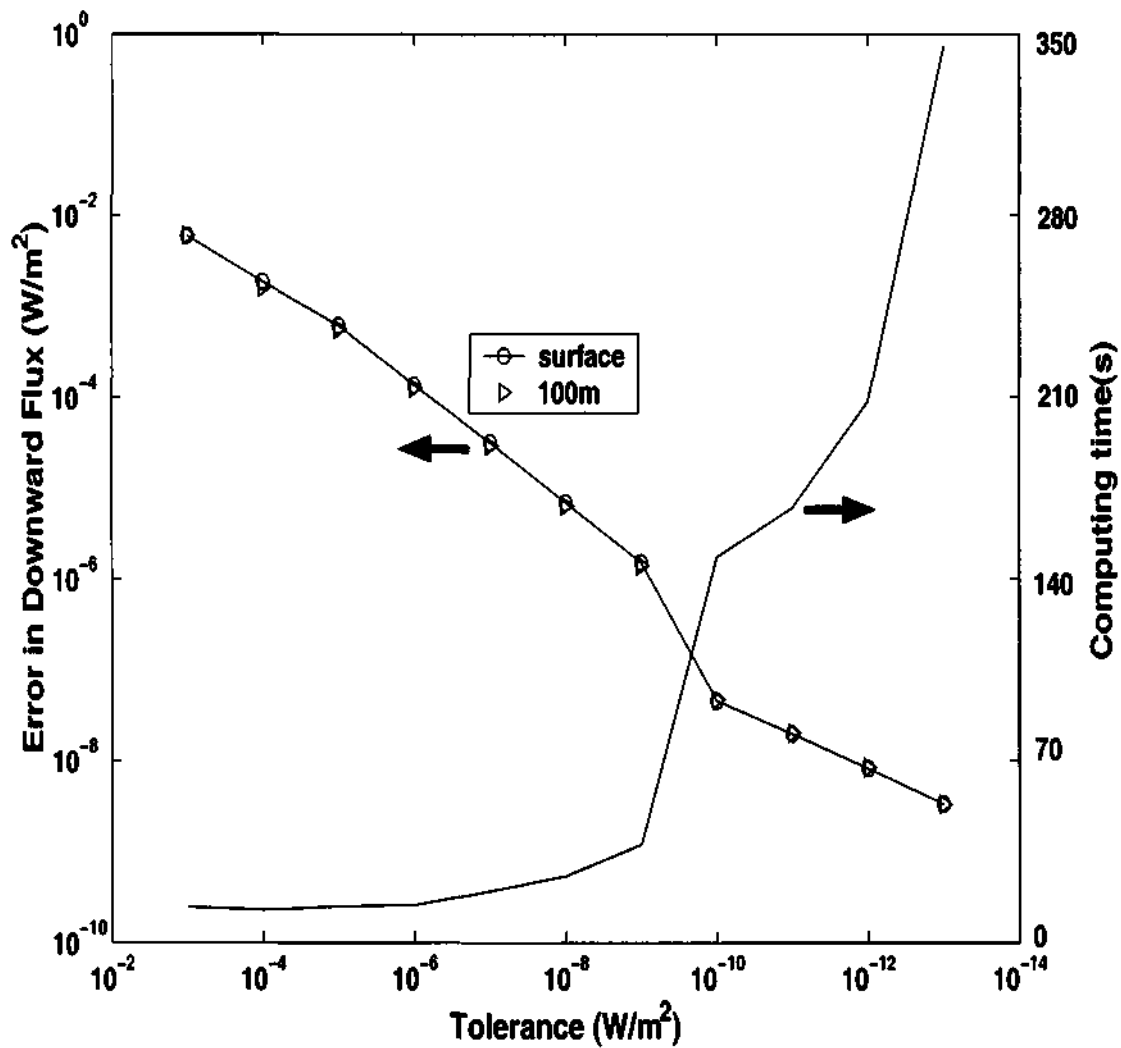


Figure 3.1: Effect of prescribed tolerance on performance parameters of present code; isothermal atmosphere.

code and the Chou code were 2.82 s and 3.18 s respectively for identical input data sets. The time taken by the present code for various tolerance levels is also shown in Figure 3.1. In the tolerance limit ranging from 10^{-3} to $10^{-9} Wm^{-2}$ the time taken for execution of the code hardly varies, but when the tolerance limit is further reduced the execution time shoots up very rapidly. Figure 3.1 suggests that an acceptable

tolerance level to prescribe is 10^{-6} Wm^{-2} , the figure that has therefore been adopted in all the computations reported here.

We first verify the code by comparing it with the exact solution given in the previous Section and results from Chou's code. Figure 3.2 shows the variation of cooling rate with height (up to 100 km) for $\varepsilon_g = 0.8$ in an isothermal atmosphere at 300 K, using line absorption only. Figure 3.3 shows the same results for heights upto 1 m and 1000m. The exact solution and computational results from the present code agree very well at all levels, so the z -test is found positive and thus provides strong verification for the code. Figures 3.2 and 3.3 also present the cooling rates from the code of Chou *et al.* (1993) which agrees with the exact solution from approximately 100 m and above.

As the present radiation code has no restriction on the number of grid points and yields fluxes accurate to a prescribed tolerance limit, it consequently also provides cooling rates to a desired accuracy. For the exact solution reported here, cooling rates have been computed over the entire atmosphere (surface to 100 km), using a total of 771 grid points with the resolution in different layers as shown in Table 3.2. A maximum of only 771 grid points could be used in Chou's code and hence the same number of grid points was used in the computations performed to make appropriate comparison of the results. The prescribed tolerance limit is 10^{-6} Wm^{-2} . It was concluded that a resolution of 5 mm was sufficient for the grid points close to the surface to simulate the cooling rate accurately as further refinement of the grid near the surface did not change the results. Table 3.2 shows the variation of surface downward flux near the surface with change in grid resolution near the surface.

Table 3.3 shows the grid resolution used at various heights in the present code.

A final validation of this code comes from a comparison with the results

Table 3.2: Variation of surface downward flux with change in grid resolution near the surface.

Grid Resolution z (m)	Downward Flux at $z = 0$ (Wm^{-2})
0.001	333.0546794
0.005	333.0546794
0.01	333.0546786
0.05	333.0546781
0.01	333.0546781

Table 3.3: Grid resolution at various height bands in present code.

Height z (m)	No. of grid points	Resolution Δz
0 - 0.5	100	5 mm
0.5 - 5.5	100	5 cm
5.5 - 55.5	100	50 cm
55.5 - 555.5	100	5 m
555.5 - 10555.5	100	100 m
10555.5 - 100,000	271	331.276 m

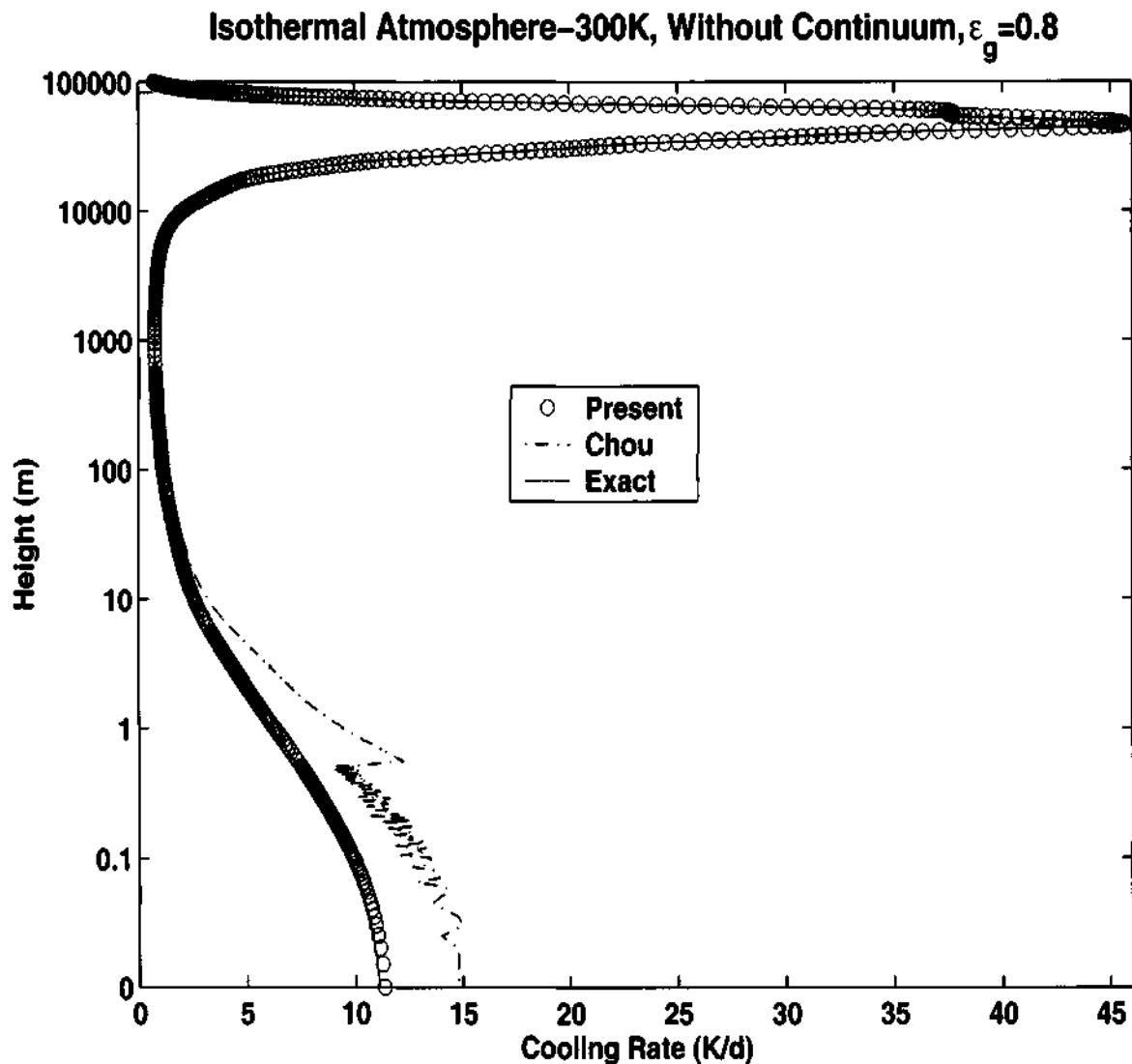


Figure 3.2: Comparison of computed cooling rates for an isothermal atmosphere with $\epsilon_g = 0.8$, water vapour line absorption only.

of Clough, Iacono and Moncet (1992) who present a line-by-line integration with a water vapour continuum model. The results for the fluxes from the present code are compared with those from Clough *et al.* (1992) in Figure 3.4 and Table 3.4. It will be seen from the Figure that on the scale of the diagram the results from either of the two codes used by Clough *et al.* (1992) and the present code are virtually indis-

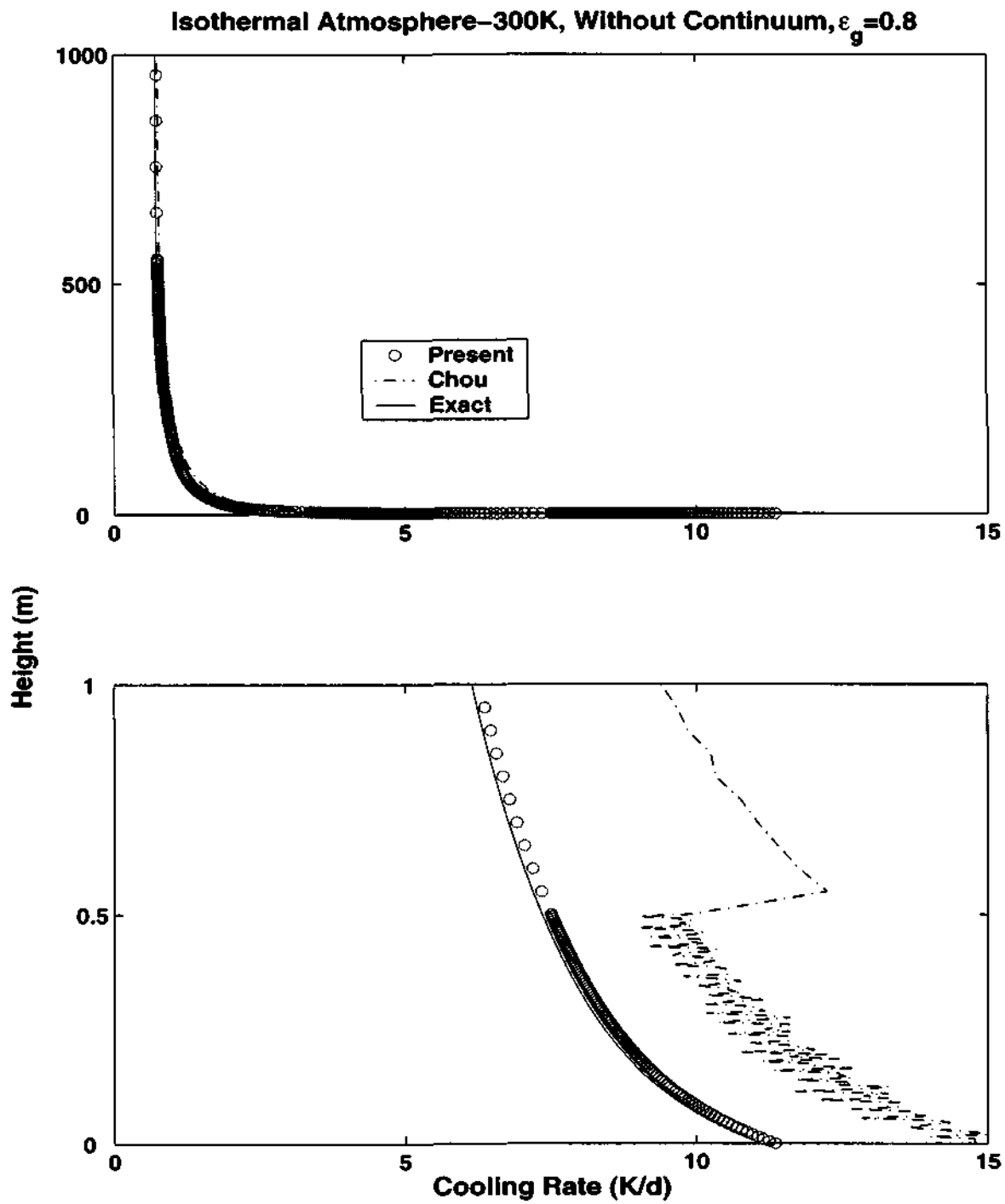


Figure 3.3: Comparison of cooling rates for an isothermal atmosphere with $\epsilon_g = 0.8$, water vapour line absorption only, for present, Chou and exact.

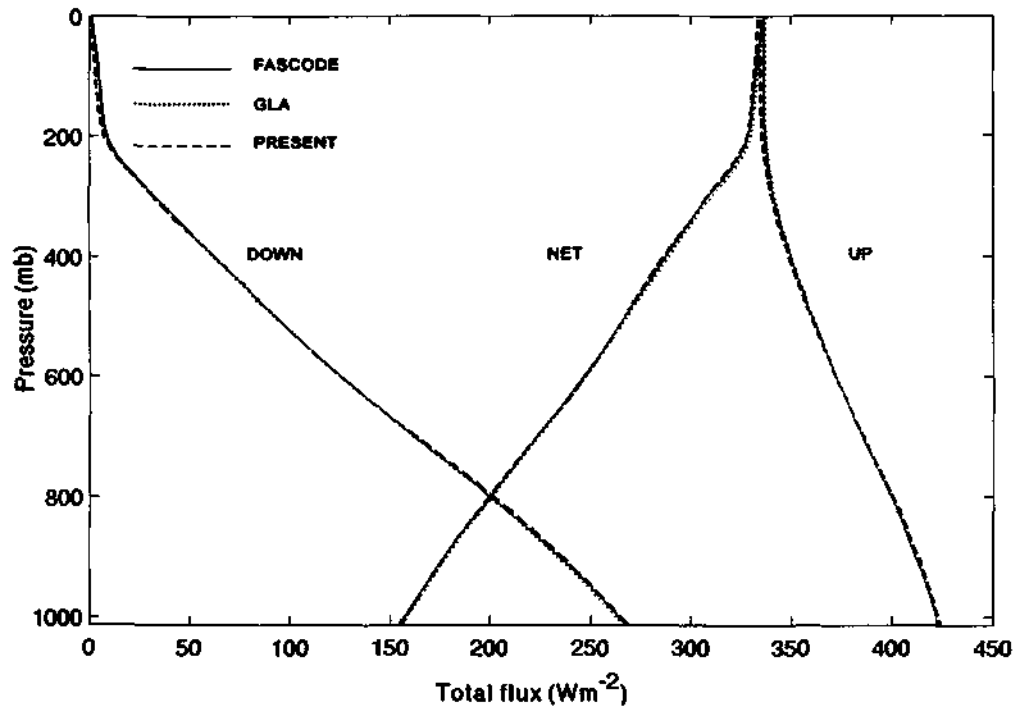


Figure 3.4: Comparison of present results for upward, downward and net flux, with results presented by Clough *et al.* (1992) using two different codes, FASCODE and GLA. MLS atmosphere with water vapour absorption only.

tinguishable. The two concerned codes are respectively one based on the FASCODE (Fast Atmospheric Signature Code) model, developed by Clough, Kneizys, Shettle and Anderson (1985), and another designated as GLA, based on the Goddard Laboratory for Atmospheres model. Table 3.4 shows that the fluxes, without the water vapour continuum, are in excellent agreement at both surface and tropopause, and with the continuum reveal small differences at the tropopause. The latter differences are probably attributable to the different parameterizations for continuum (CKD in the work of Clough *et al.* (1992) and Roberts *et al.* (1976) in the present work). MLS data profiles have been used for which details are given in the next Chapter.

Table 3.4: Comparison of upwelling and downwelling radiative fluxes at the surface and tropopause for an MLS atmosphere with and without continuum and $\varepsilon_g=1.0$. The units are in Wm^{-2} .

	Surface		Tropopause	
	up	down	up	down
Without continuum				
Clough <i>et al.</i> (1992)	423.5	269.0	335.8	6.9
Present	423.6	268.9	335.2	5.9
With continuum				
Clough <i>et al.</i> (1992)	423.3	333.8	321.3	7.4
Present	423.6	333.0	328.0	5.9

Thus the present code has been thoroughly verified, validated and an optimum resolution for grids to be used near the surface determined for near-surface infrared radiation computations.

The next Chapter provides results of net and spectral fluxes/cooling rates from some of the numerical experiments carried out here.

Chapter 4

Spectral and Net Cooling Rates

In this Chapter a detailed analysis of the spectral and net cooling rate is made for MLS conditions with arbitrary emissivities, followed by an illustration of the effect of carbon dioxide in atmospheric cooling rates.

4.1 Spectral Density of Cooling Rate at Different Altitudes

We now present results of a study carried out to understand the influence of ground emissivity on cooling rates across the infrared spectrum in the atmosphere all the way from surface to 100 km. Two cases, namely $\varepsilon_g = 1.0$ and 0.8 , are compared. Although the value of ε_g for most natural surfaces like snow, water and vegetation are close to unity (Wilber *et al.*, 1999), a value of 0.8 for bare soil is not uncommon. See for instance Paltridge and Platt (1976), Becker, Ngai and Stoll (1981), Garratt and Brost (1981) and Moriyami and Arai (1995). Also (as already mentioned in VSN) most of these compilations refer to vertical emissivities appropriate to remote measurements by vertically oriented radiometers on spacecraft. The quantity relevant to us is the global or flux emissivity which may be much less. Work on engineering surfaces has established that the global (also called hemispherical) emissivity is much less than the normal emissivity (see for e.g., Siegel and Howell, 2002, Chapter 2). Although no

corresponding result is available for natural surfaces, a similar factor will presumably apply. More work is of course needed to establish these arguments. But our main aim in taking $\varepsilon_g = 0.8$ is to highlight the dramatic differences in near surface cooling rates when the emissivity is less than unity.

For purposes of illustration, we adopt the mid-latitude summer atmosphere (MLS; Ellingson *et al.*, 1991). The reason for choosing this atmosphere was that the profile was easily available, and that it has been chosen by several researchers (e.g., Chou *et al.*, 1993, Clough *et al.*, 1992) to test their models; hence those results are available for comparison with the results from our code. Figure 4.1 shows the input profiles of pressure, temperature and humidity in the MLS atmosphere.

Figure 4.2 shows the results for this atmosphere, including both line and continuum contributions. The ordinate has been plotted on a quasi-logarithmic scale, following Narasimha (1983), using the expression $y = \log_{10}(1 + az)$, where z is the height (m) and a is an arbitrary constant which is here taken as 100. (This scale is linear near the origin but becomes asymptotically logarithmic at large z , and has the advantage of permitting explicit display of the $z = 0$ point.) It is seen that a decrease in ε_g from 1.0 to 0.8 increases the surface cooling rate from 4.47 to 37.54 K/day and that the effect of surface emissivity extends to a height of almost 1 km. This confirms the estimates made by Ragothaman *et al.* (2001), using the flux emissivity scheme, of the unsuspectedly large extent of the influence of surface conditions on radiative cooling.

Figure 4.3 and 4.4 show the cooling rate spectrum for clear-sky MLS conditions. Once again, it is seen that the difference between $\varepsilon_g = 1.0$ and 0.8, i.e. the ground emissivity effect, is generally observed all the way up to about 1 km (see Figure 4.2 also), but it is dramatically large near the surface which is seen clearly in Figure 4.4. Band 2 (wave-number range 340–540 cm^{-1} , or wavelength range 29.4 to 18.5 μm) is the single largest contributor to near-surface cooling ($> 50 \times 10^{-3}$ Kcm/d),

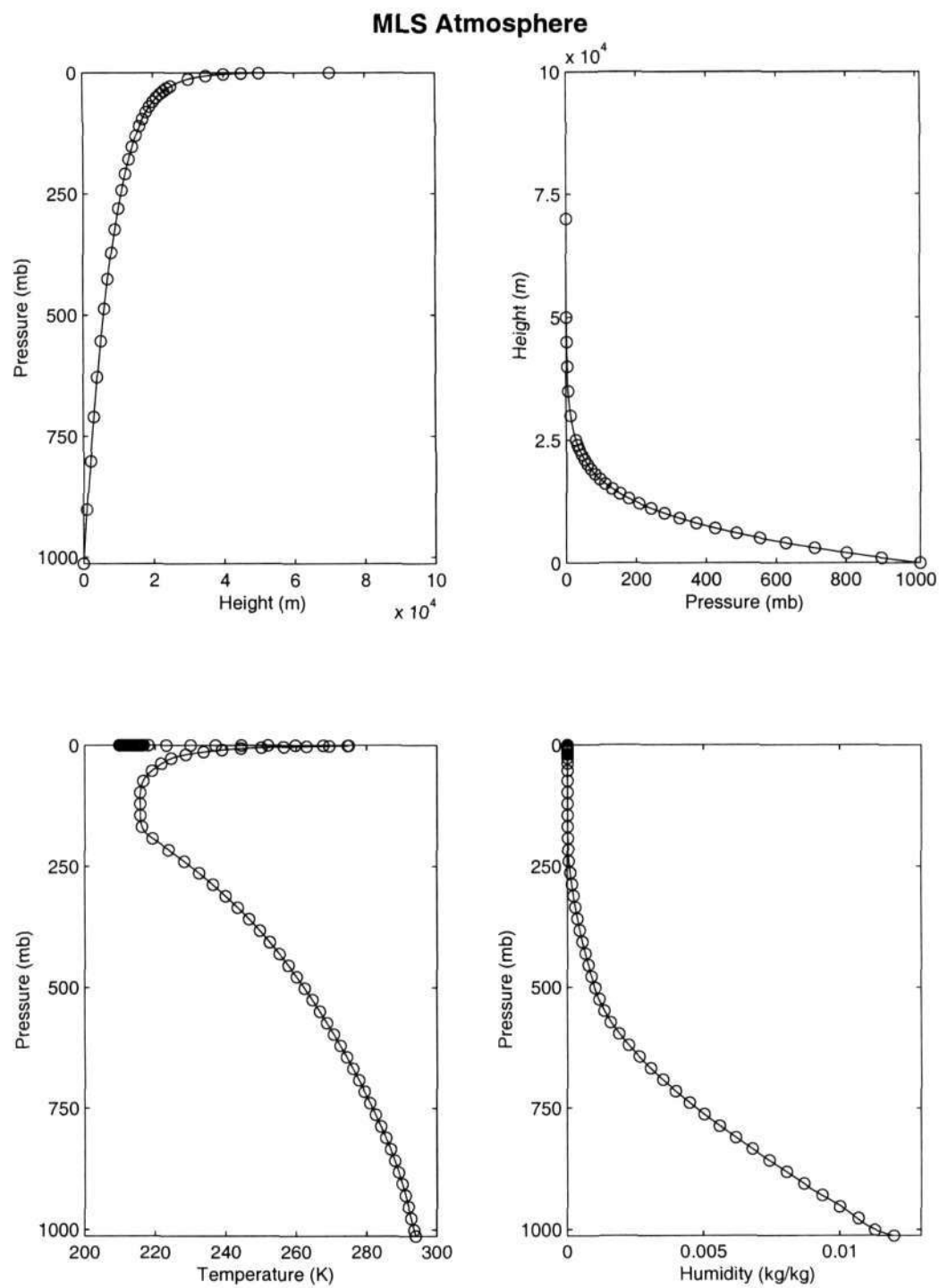


Figure 4.1: Input profiles of pressure, temperature and humidity in the MLS atmosphere.

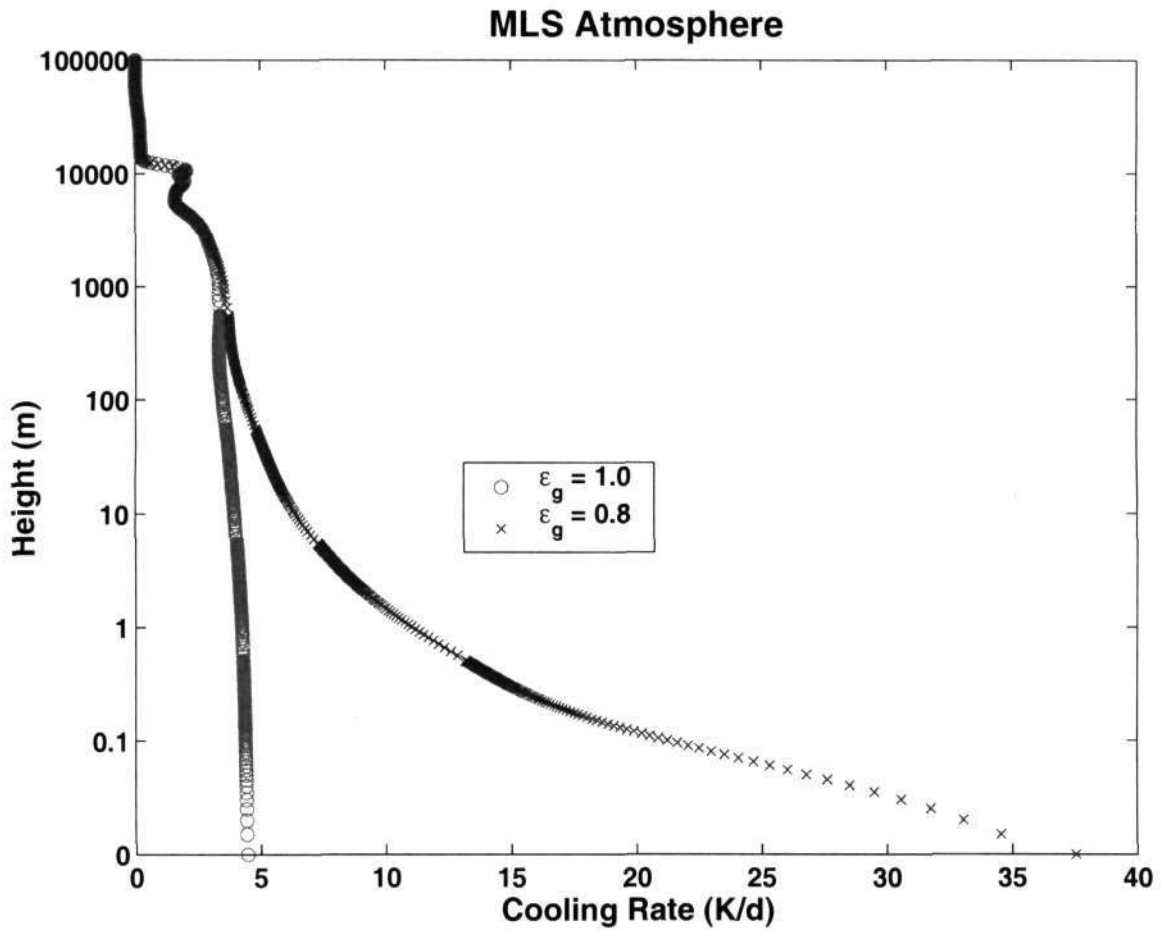


Figure 4.2: Effect of ground emissivity on cooling rates computed by present code; MLS atmosphere, water vapour absorption only.

followed closely by band 9 ($1215\text{--}1380\text{ cm}^{-1}$, 8.2 to $7.2\text{ }\mu\text{m}$, contribution 45×10^{-3} Kcm/d); note that these bands are on either side of the atmospheric window region ($8\text{ }\mu\text{m}$ – $12\text{ }\mu\text{m}$). The cooling in these two bands is approximately 50 times higher than that in the weakest band. There is a strong gradient of the cooling rate over the first few centimetres above the surface. A scale length for the height of this layer has been defined in Section 3.3. This constitutes what VSN have called the emissivity sublayer. The gradient rapidly decreases with height, and at higher levels (100 m – 1

km) it is the window region that contributes most to the cooling, as can be seen from Figure 4.6.

To understand further the basic mechanisms underlying the drastic changes in near-surface cooling rate indicated by the present calculations when ground emissivity is less than unity, we first note that they can in principle be due to changes in either the fluxes themselves or the flux *gradients* or both. In order to investigate these factors, we now explore the spectral distribution of the fluxes and the cooling rates, presented in Figures 4.5–9 and 4.11–22. Note that the ordinate in many of these diagrams (Figures 4.5–4.9 and 4.18–4.22) is the average spectral density in each band, obtained by dividing the total contribution from the band by its width, so that the area within each band is directly proportional to the contribution from that band.

For a given temperature distribution there can be no difference in the downward flux between $\varepsilon_g = 1.0$ and 0.8, so we may confine our attention to the upward flux. Figure 4.5 shows the spectral distribution of the upward fluxes at the surface for the MLS atmosphere, in the two cases $\varepsilon_g = 0.8$ and 1.0. In general the upward flux exhibits only small differences: the largest is in band 6 (where the flux at $\varepsilon_g = 0.8$ differs by less than 10% of the value of 0.34 Wcm/m^2 at $\varepsilon_g = 1.0$). The differences are even less significant at higher altitudes, and drop to 0.065 Wcm/m^2 at $z = 10 \text{ km}$.

The computed differences in cooling rates must therefore be largely attributed to changes in the flux *gradients*, which determine the cooling rate. That this is so is demonstrated in Figure 4.6 which replots the data of Figure 4.3 in more quantitative terms at selected heights for both $\varepsilon_g = 1.0$ and 0.8; the total cooling rate is also shown along-side. It is immediately clear that the highest contributions to the surface cooling rate at $\varepsilon_g = 0.8$ come from bands 2 and 9; the values here, respectively 13.6 and 7.78 K/d, are 42 and 31 times higher than at $\varepsilon_g = 1.0$. (The spectral density of the cooling rate in the same bands is 68.0×10^{-3} and 47.2×10^{-3}

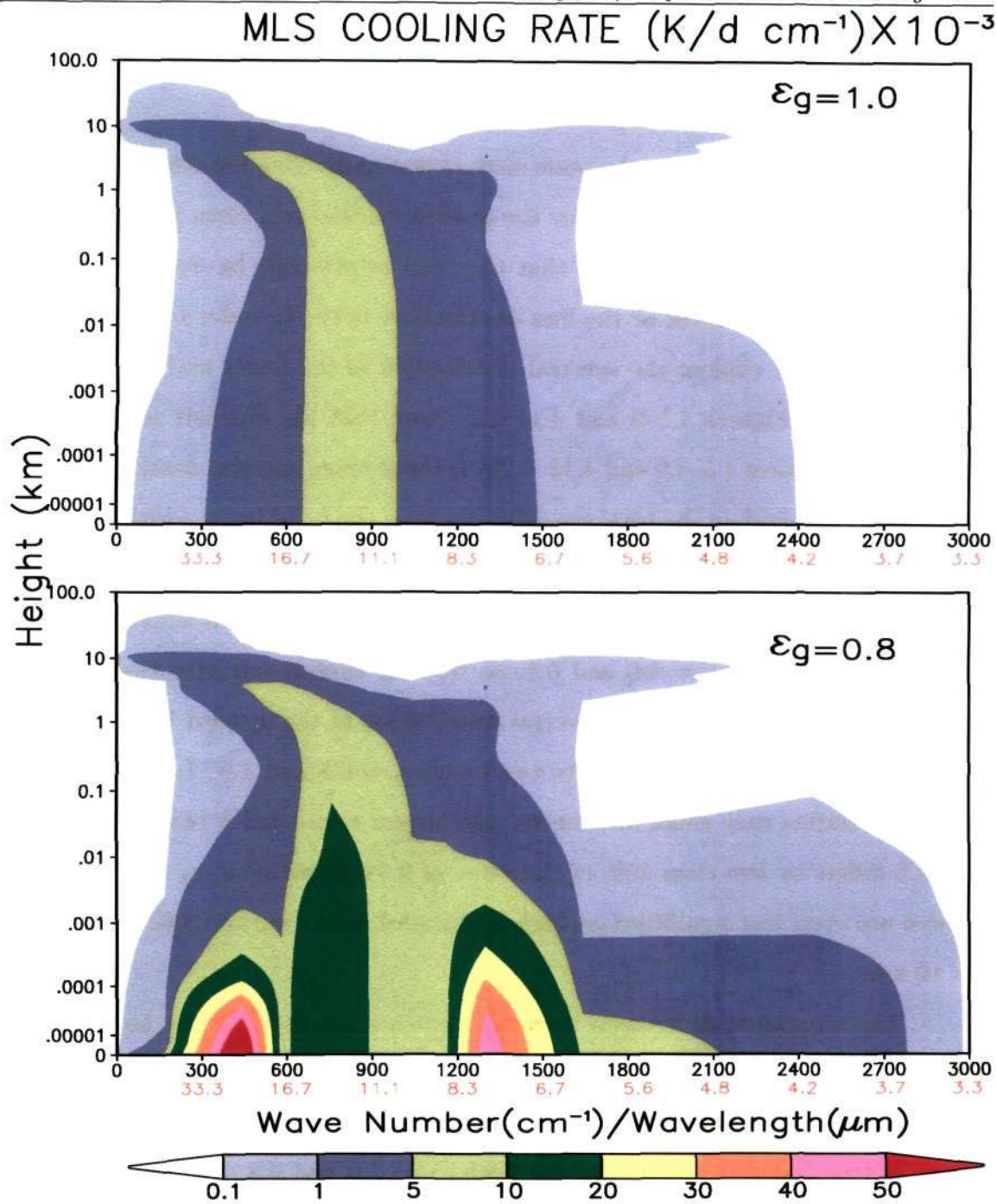


Figure 4.3: Influence of change in ground emissivity from 1.0 to 0.8 on spectral distribution of cooling rate for MLS atmosphere from surface to 100 km, water vapour absorption only.

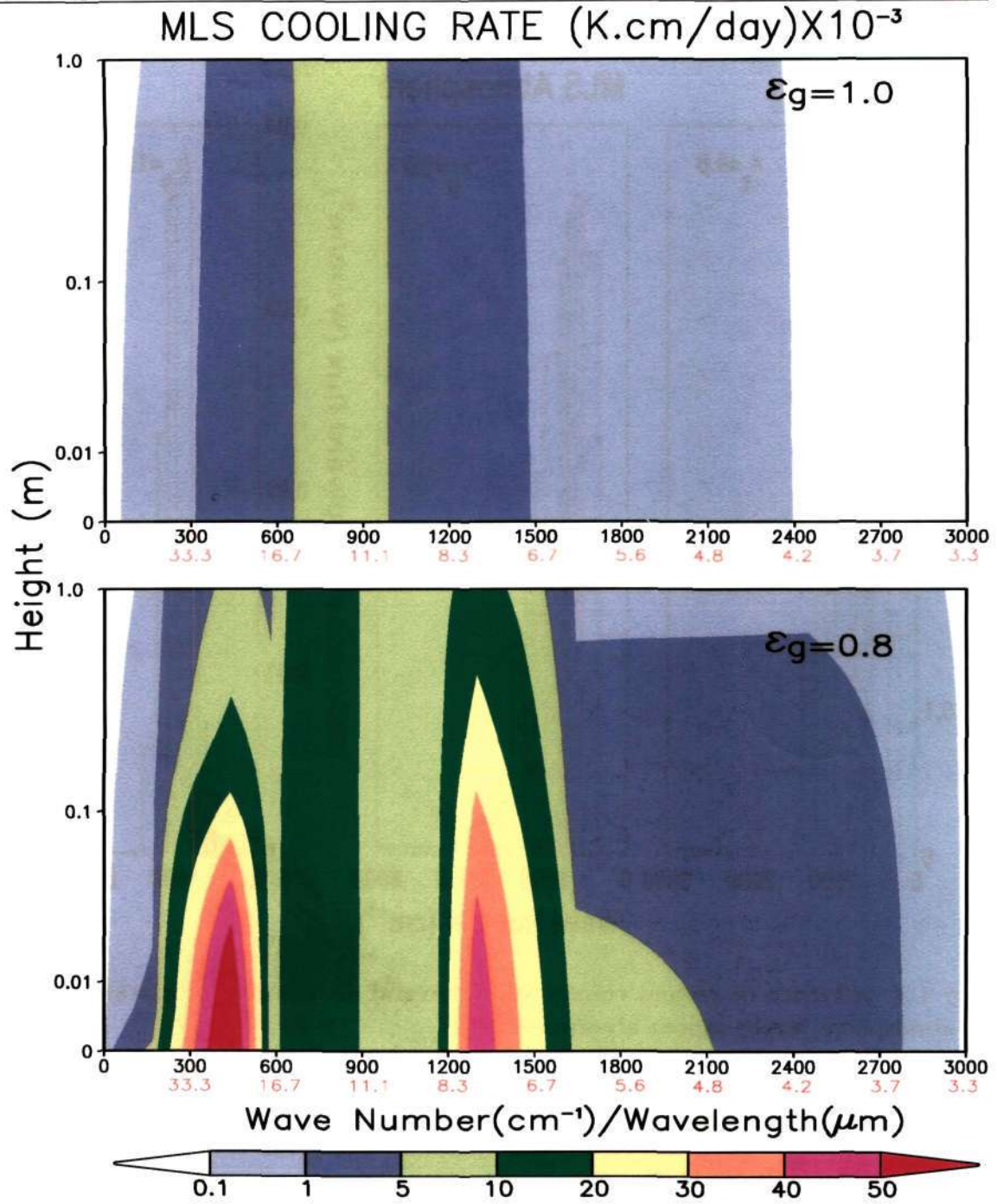


Figure 4.4: Influence of change in ground emissivity from 1.0 to 0.8 on spectral distribution of cooling rate for MLS atmosphere from surface to 1 m, water vapour absorption only.

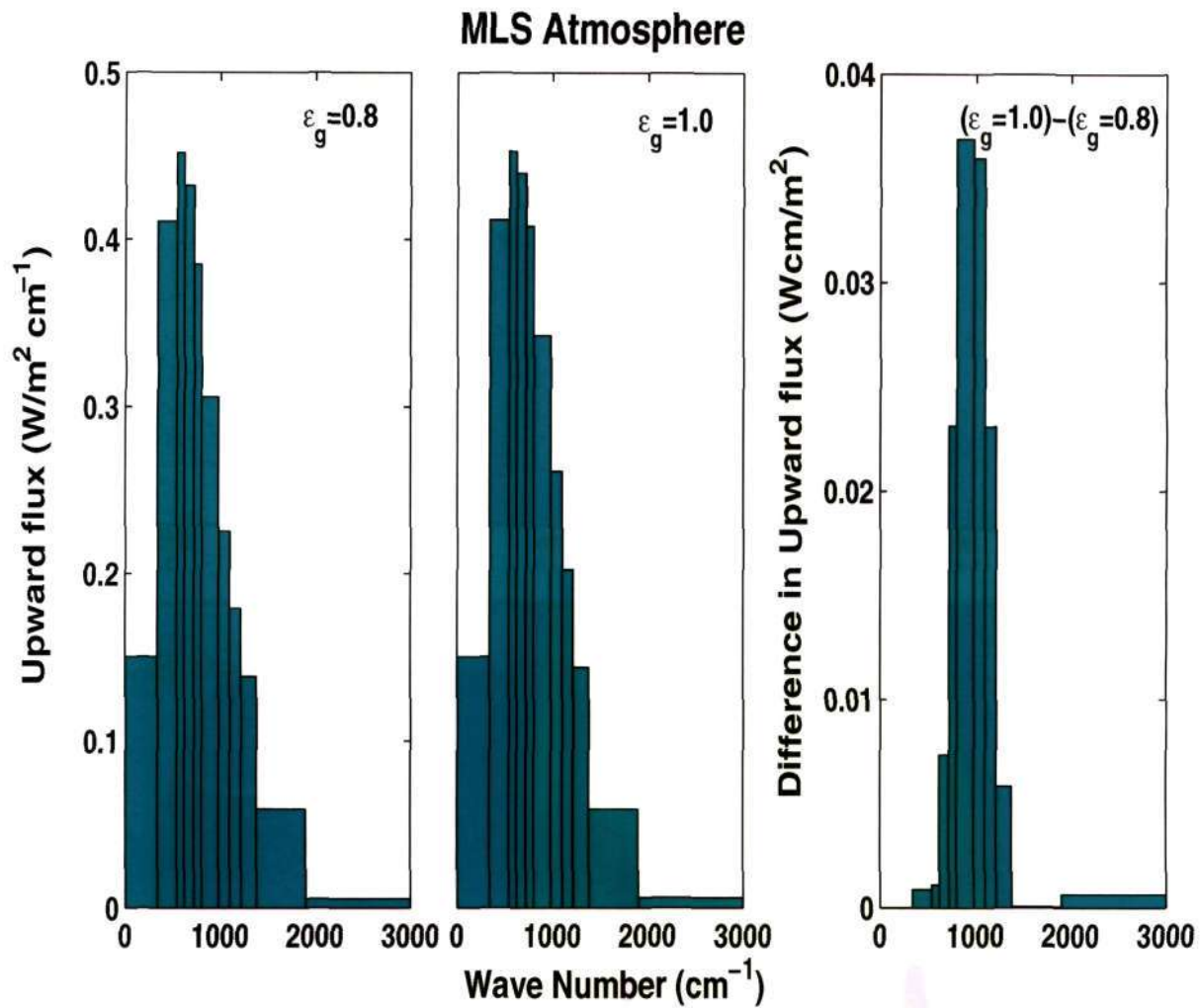


Figure 4.5: Influence of ground emissivity in spectral distribution of upward flux; MLS atmosphere, water vapour absorption only.

Kcm/d at the surface, higher than at $\epsilon_g = 1.0$ by the same factors as above.) This confirms the earlier conclusion from the discussion on Figures 4.3 and 4.4. Note that, when $\epsilon_g = 1.0$, the spectral distribution of the cooling rate remains largely similar till a height of about 1 km, being centred around bands 4 to 6, but at 10 km the contributions to cooling rate shift to longer waves. This is clearly seen in Figures 4.7 and 4.8 which show the normalised cooling rates for different levels for $\epsilon_g = 1.0$ and

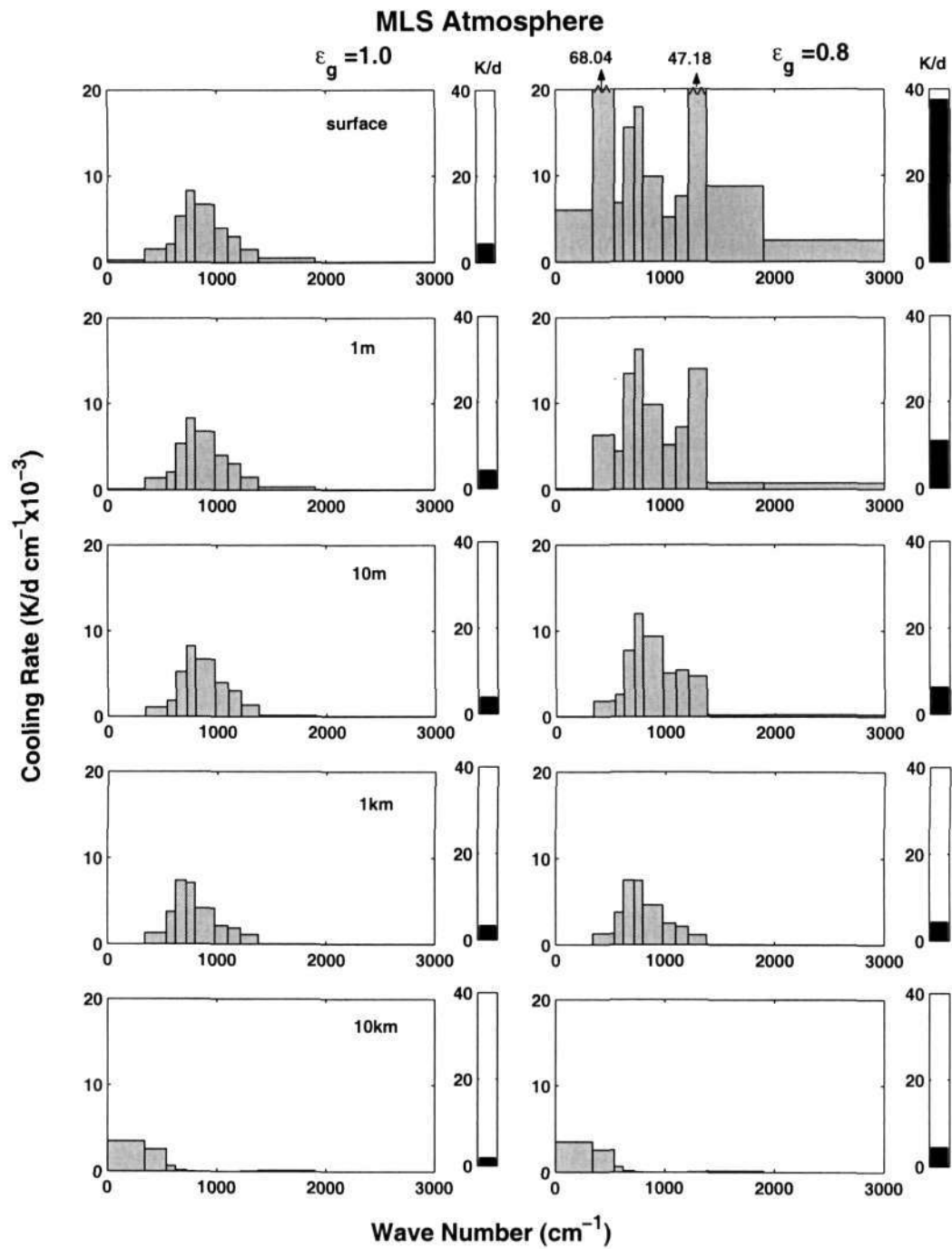


Figure 4.6: Spectral distribution of cooling rate at five levels for $\epsilon_g = 1.0$ and $\epsilon_g = 0.8$, showing also the gross cooling rate at each level; water vapour absorption only.

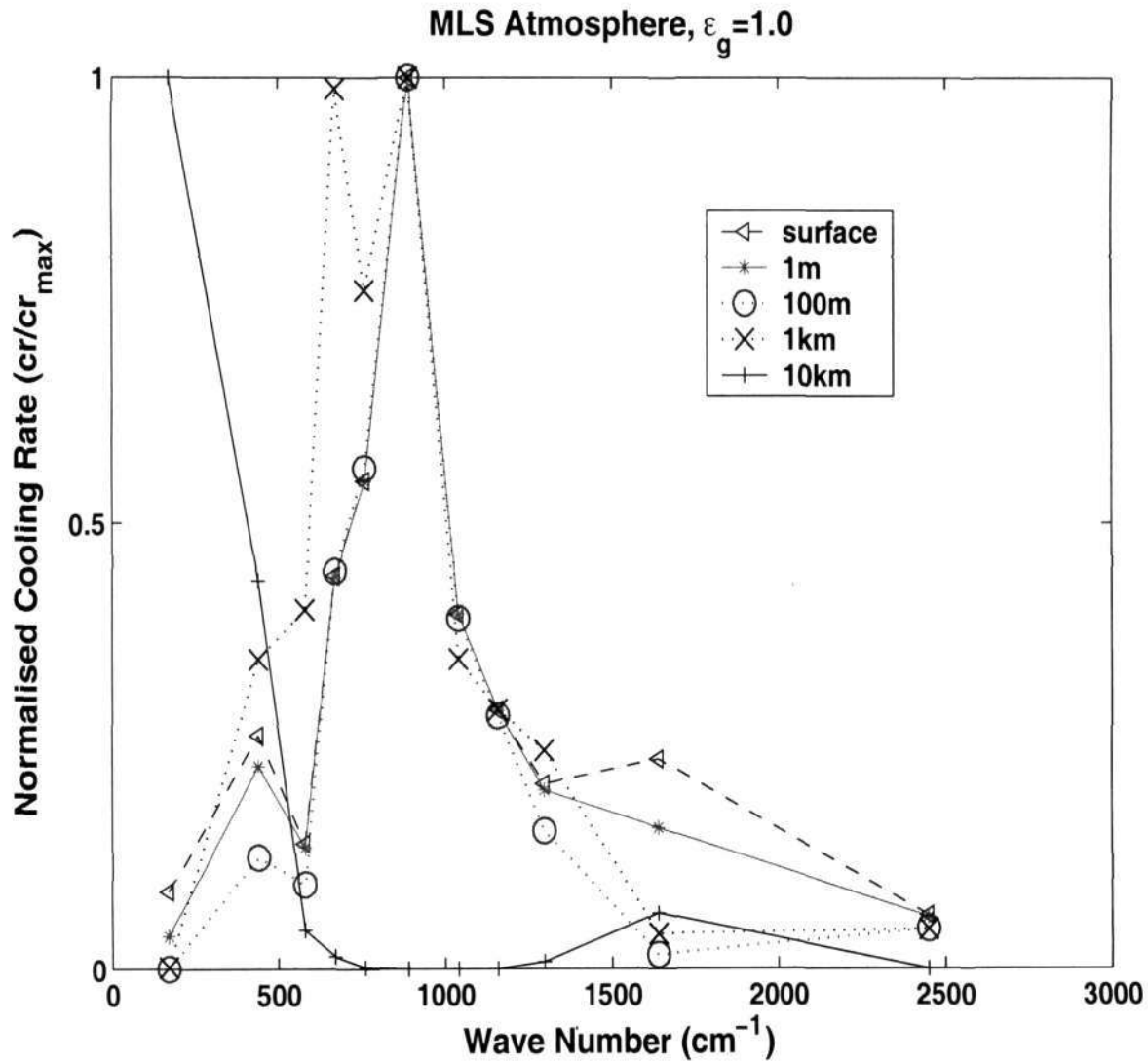


Figure 4.7: Normalised spectral cooling rate distribution of MLS atmosphere for various heights with $\varepsilon_g = 1.0$, water vapour absorption only.

0.8 respectively. With $\varepsilon_g = 0.8$, there are spectacularly high cooling rates at bands 2 and 9 at the surface; by $z = 1$ m there is already a remarkable change, the greatest spectral density now being in band 5 ($720\text{--}800\text{cm}^{-1}$, or wavelength range $13.89\text{--}12.5\ \mu\text{m}$), although bands 2 and 9 continue to be prominent. Beyond 10 m the shape of the cooling rate spectral distribution remains roughly similar at both $\varepsilon_g = 0.8$ and

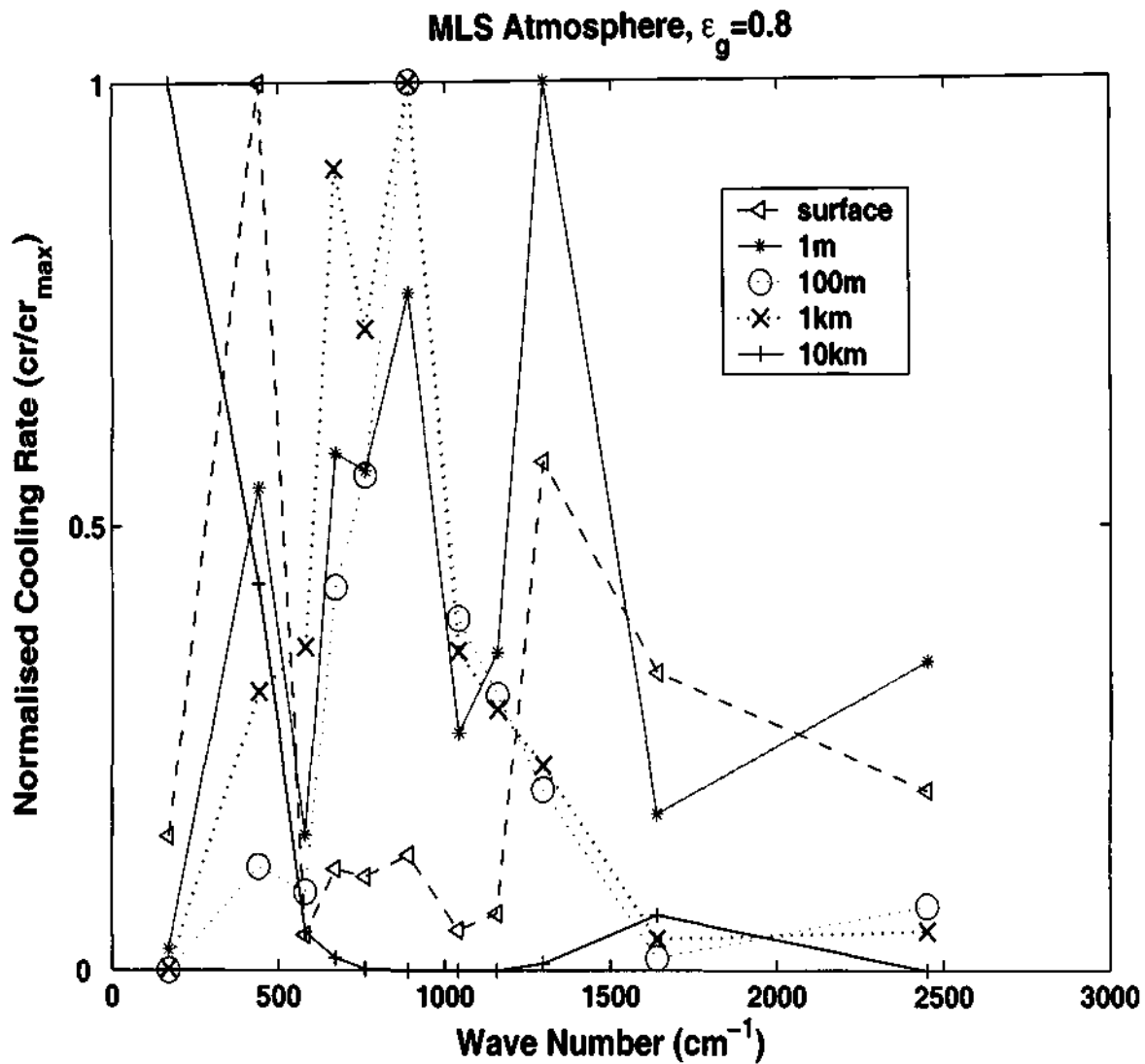


Figure 4.8: Normalised spectral cooling rate distribution of MLS atmosphere for various heights with $\epsilon_g = 0.8$, water vapour absorption only.

1.0, although the magnitudes are higher at the lower emissivity.

To understand why different bands play major roles at different heights, we display in Figure 4.9 the spectral density of the cooling rate (Kcm/day) at $\epsilon_g = 0.8$ along with the spectrum of black body radiation as well as the transmission function at four selected heights, $z = 0, 1 \text{ m}, 10 \text{ m}$ and 10 km . (The details of the transmission

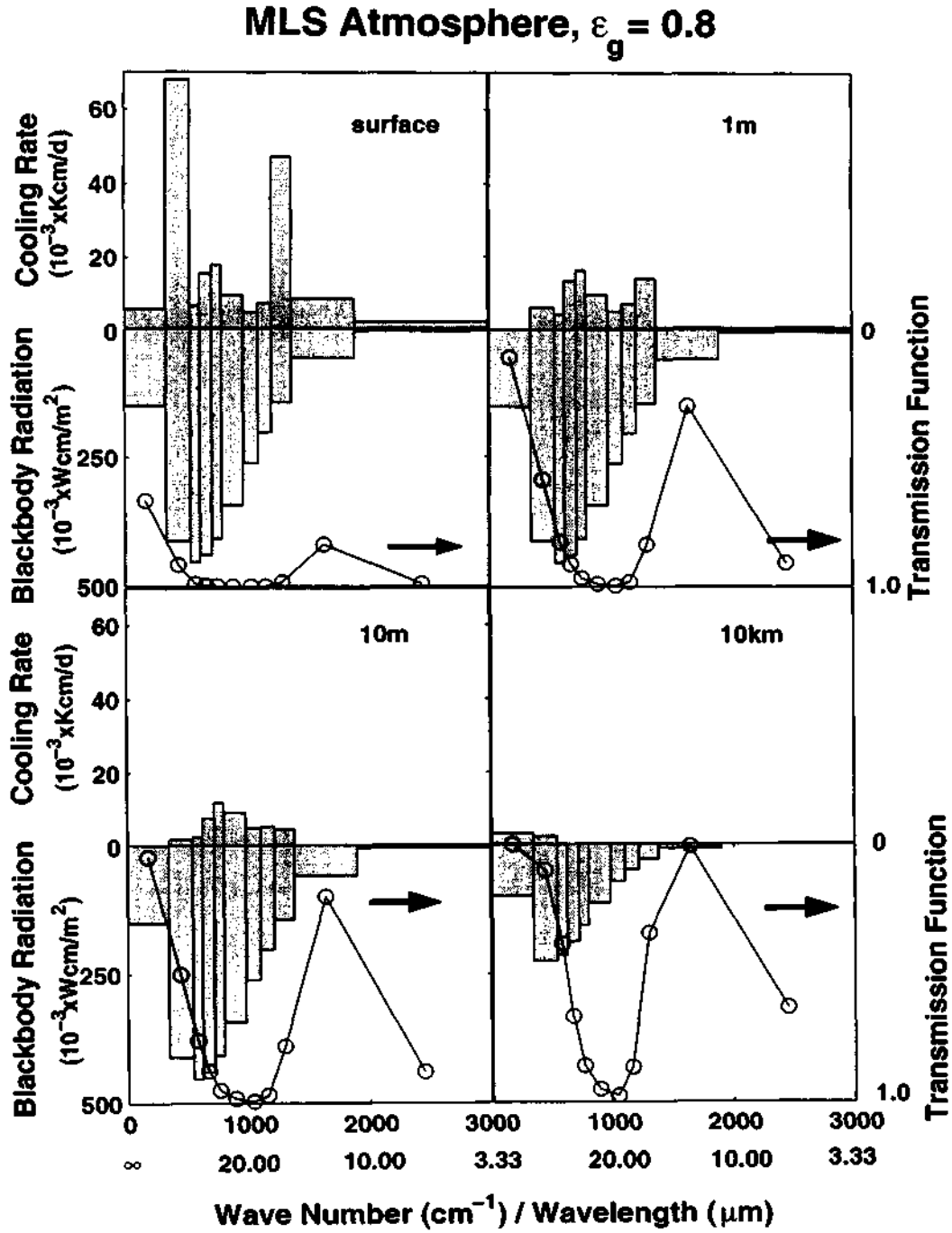


Figure 4.9: Spectral distribution of cooling rate, blackbody radiation and transmission function (joined circles) at four different levels for MLS atmosphere, water vapor absorption only.

function are given in Chapter 2, (2.18–20).) Near the surface, the lowest values of the transmission function occur in bands 1 and 10, but the ground radiation in these bands is small. In bands 2 and 9, on the other hand, the transmission function is lower (0.58 and 0.84) but the radiation flux is higher (411.6×10^{-3} and 143.9×10^{-3} Wcm/m²). The spectral density of radiation is highest around bands 3–5, but here the transmission is nearly unity, and there is little absorption. It is therefore clear that bands 2 and 9 play a special role because they have sufficient absorption at frequencies where the ground radiation flux is significant; it is the *combination* of these two factors that results in the dramatically high cooling rates. We may note that band 2 is in the rotation spectrum of the H₂O molecule, and band 9 in the rotation–vibration spectrum at the edge of the continuum-window.

Similar reasons operate at greater heights. By $z = 10$ m absorption in bands 2 and 9 has saturated, and the contribution to the cooling rate comes from around band 5. At $z = 10$ km the air temperature is lower and the radiation spectrum has shifted to lower wave-numbers; so has the absorption, which is also higher at lower wave-numbers. The net result is that the cooling now comes from bands 1 and 2, as may be seen from Figure 4.9.

Let us briefly recapitulate the present findings on the longwave radiative cooling rate. First of all, the surface cooling rate is sensitive to the ground emissivity, going up from nearly 5 K/d at $\varepsilon_g = 1.0$ to nearly 40 K/d at $\varepsilon_g = 0.8$ in the MLS atmosphere. The effect of the surface emissivity drops with height, becoming totally negligible only at and beyond heights of order 1 km (see Figure 4.10).

The spectral distribution of the cooling rate varies with altitude and ground emissivity. At $\varepsilon_g = 1.0$, the largest contributions to the cooling rate come from bands 4, 5, 6 (wave-number 620 to 980 cm⁻¹, wavelength 16.1 to 10.2 μm) upto $z = 1$ km, but the contributing bands slowly shift to longer waves as altitude increases. This shift becomes substantial at higher altitudes; e.g. at 10 km bands 1 and 2 (wave-

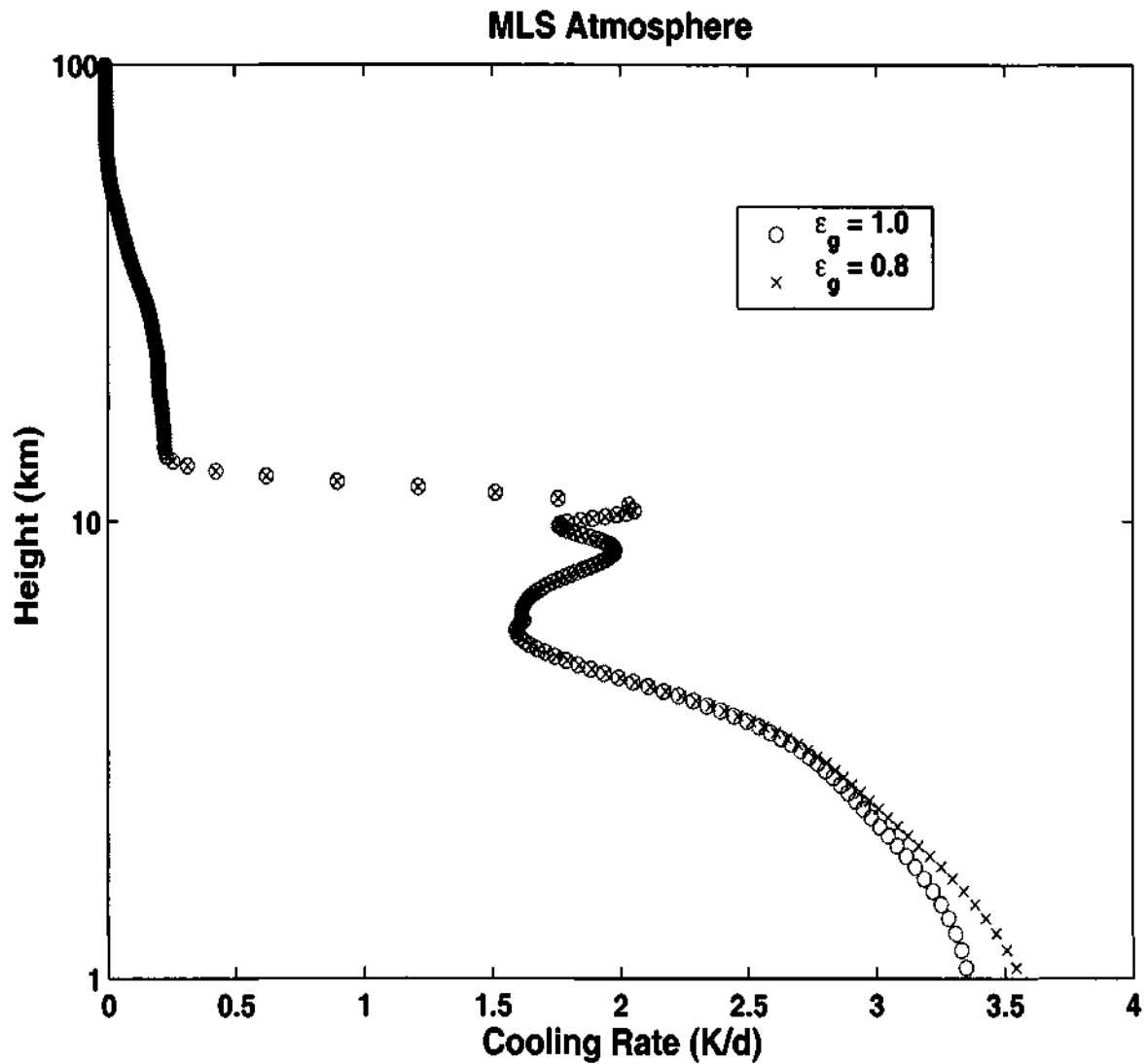


Figure 4.10: Effect of ground emissivity on cooling rates computed by present code from 1 km to 100 km; MLS atmosphere, water vapour absorption only.

number below 540 cm^{-1} , wavelength greater than $18.5 \mu\text{m}$) play the major role. Figures 4.11–17 show the percentage-wise contributions from different bands upto heights of 20 km, 10 km, 5km, 1km, 100 m, 10 m and 1 m for emissivities $\epsilon_g = 1.0$ and $\epsilon_g = 0.8$.

At $\epsilon_g = 0.8$ the picture is quite different. The biggest contributions near

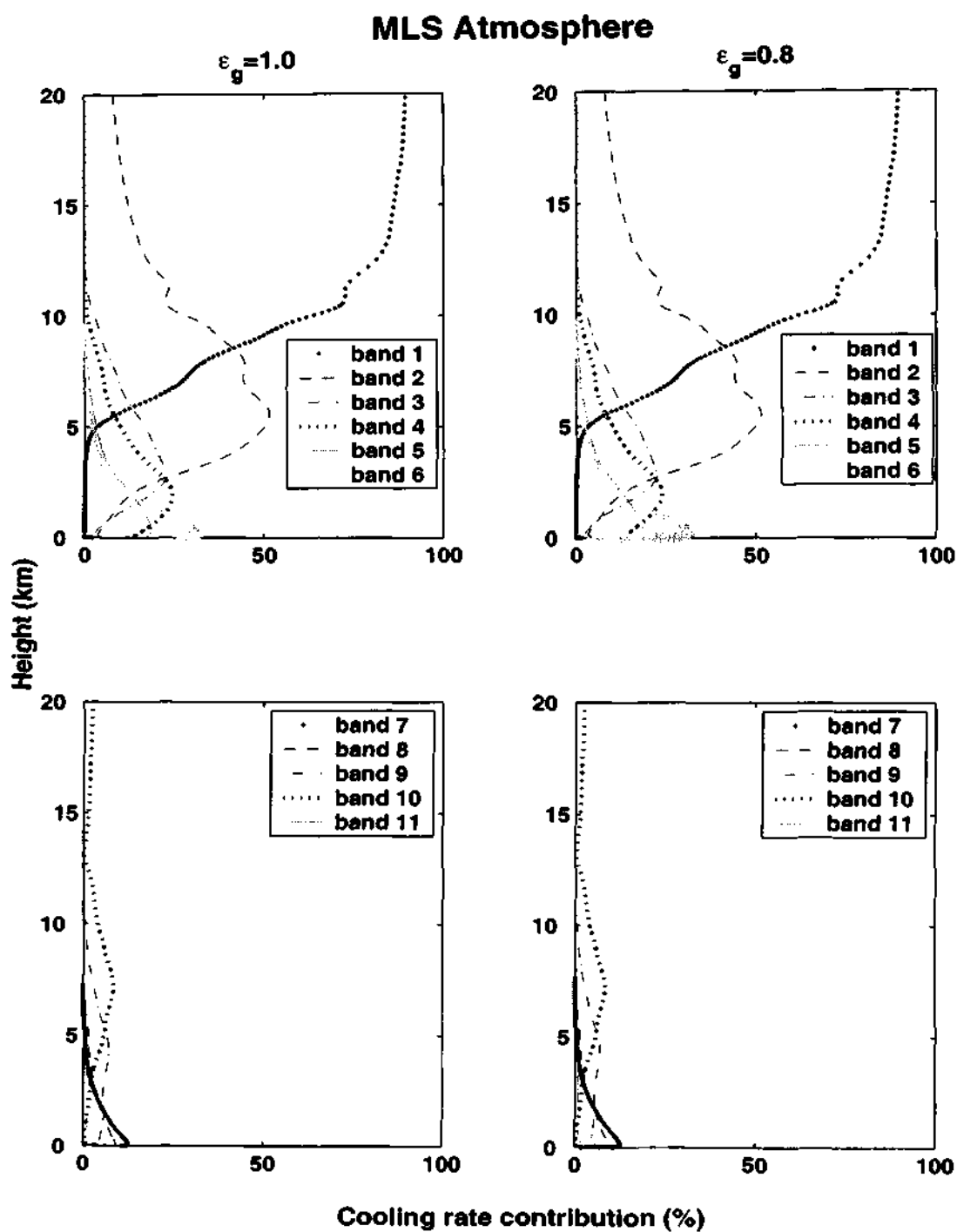


Figure 4.11: Percentage-wise cooling rate contributions from different bands up to heights of 20 km; MLS atmosphere, water vapour absorption only.

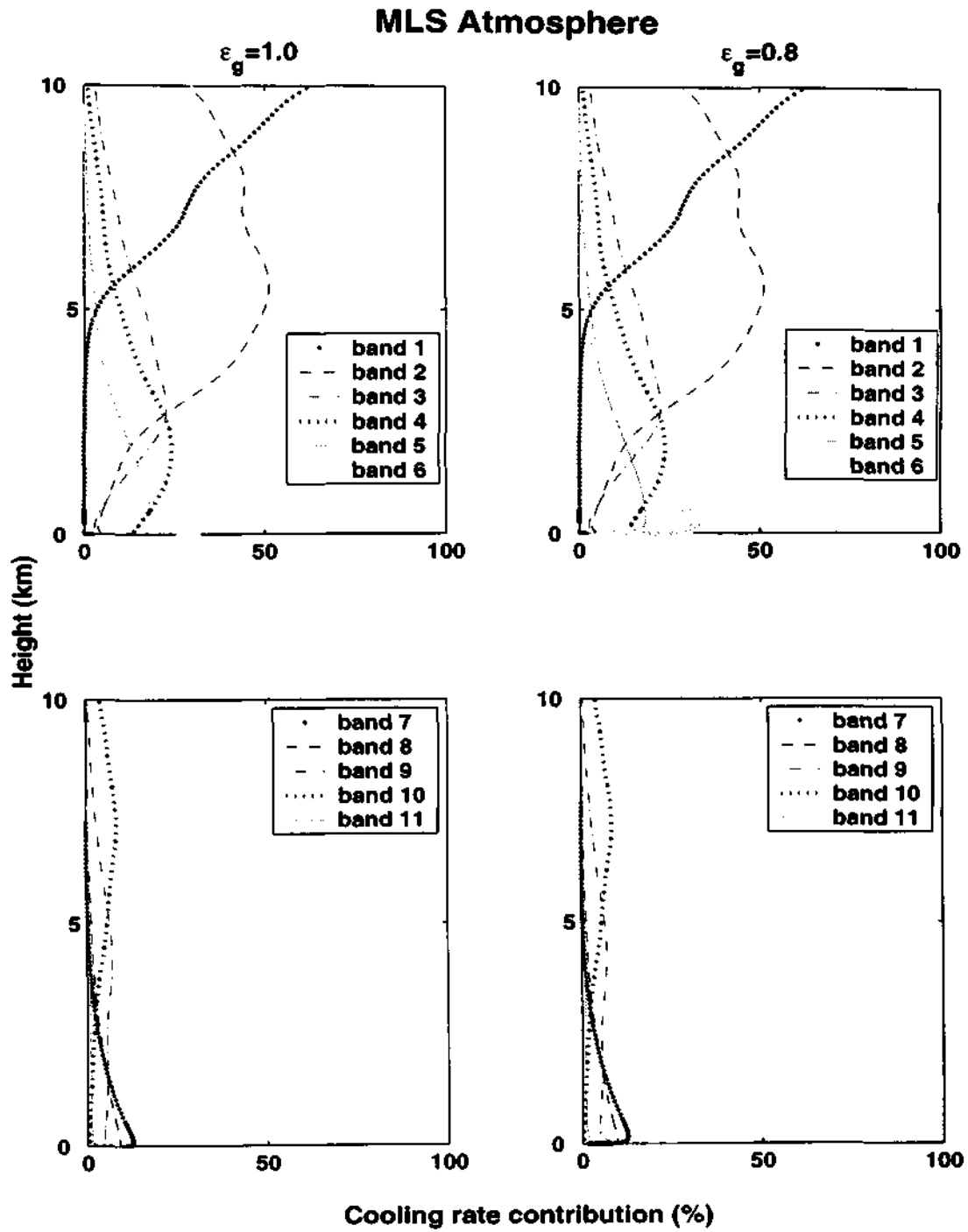


Figure 4.12: Percentage-wise cooling rate contributions from different bands upto heights of 10 km; MLS atmosphere, water vapour absorption only.

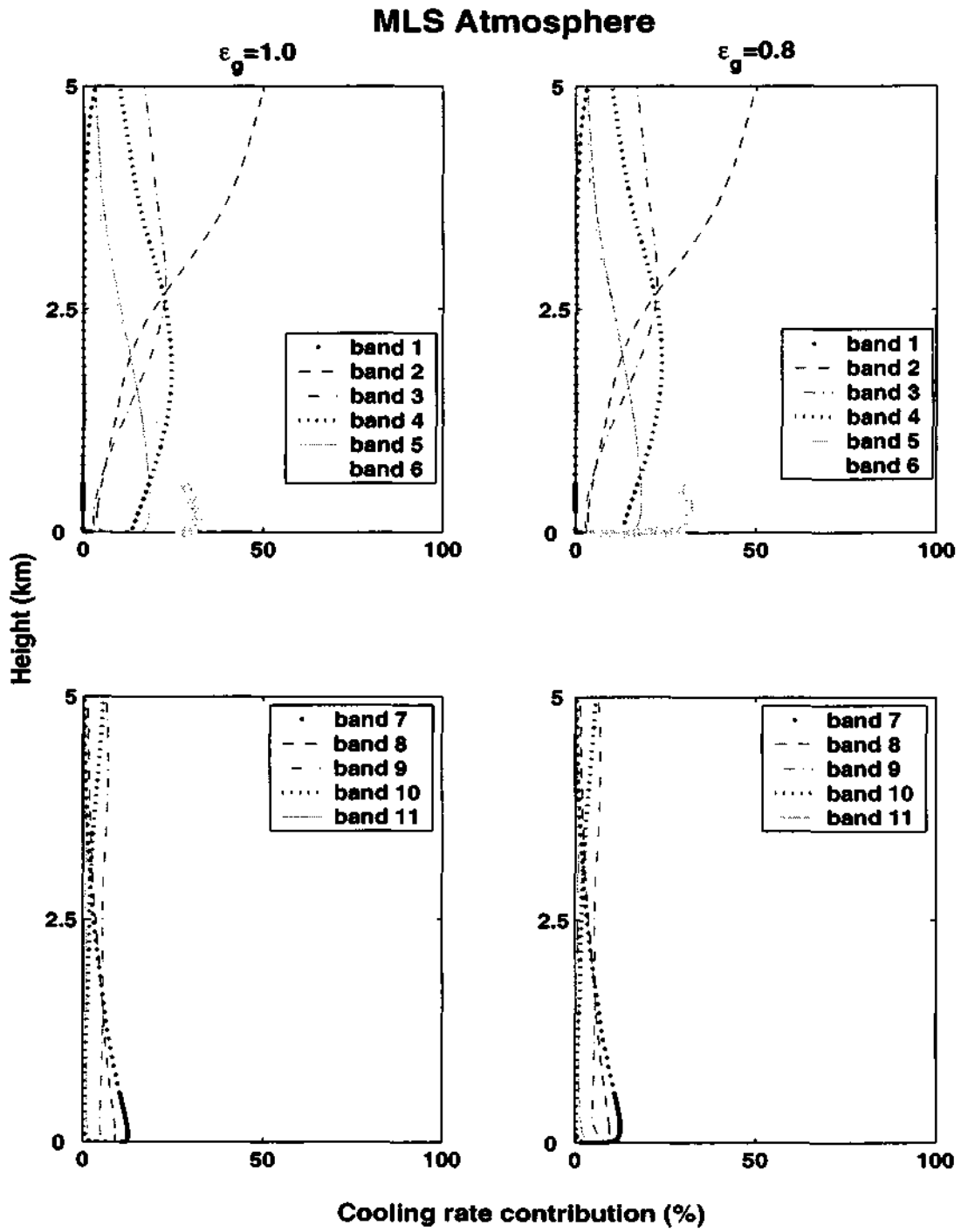


Figure 4.13: Percentage-wise cooling rate contributions from different bands upto heights of 5 km; MLS atmosphere, water vapour absorption only.

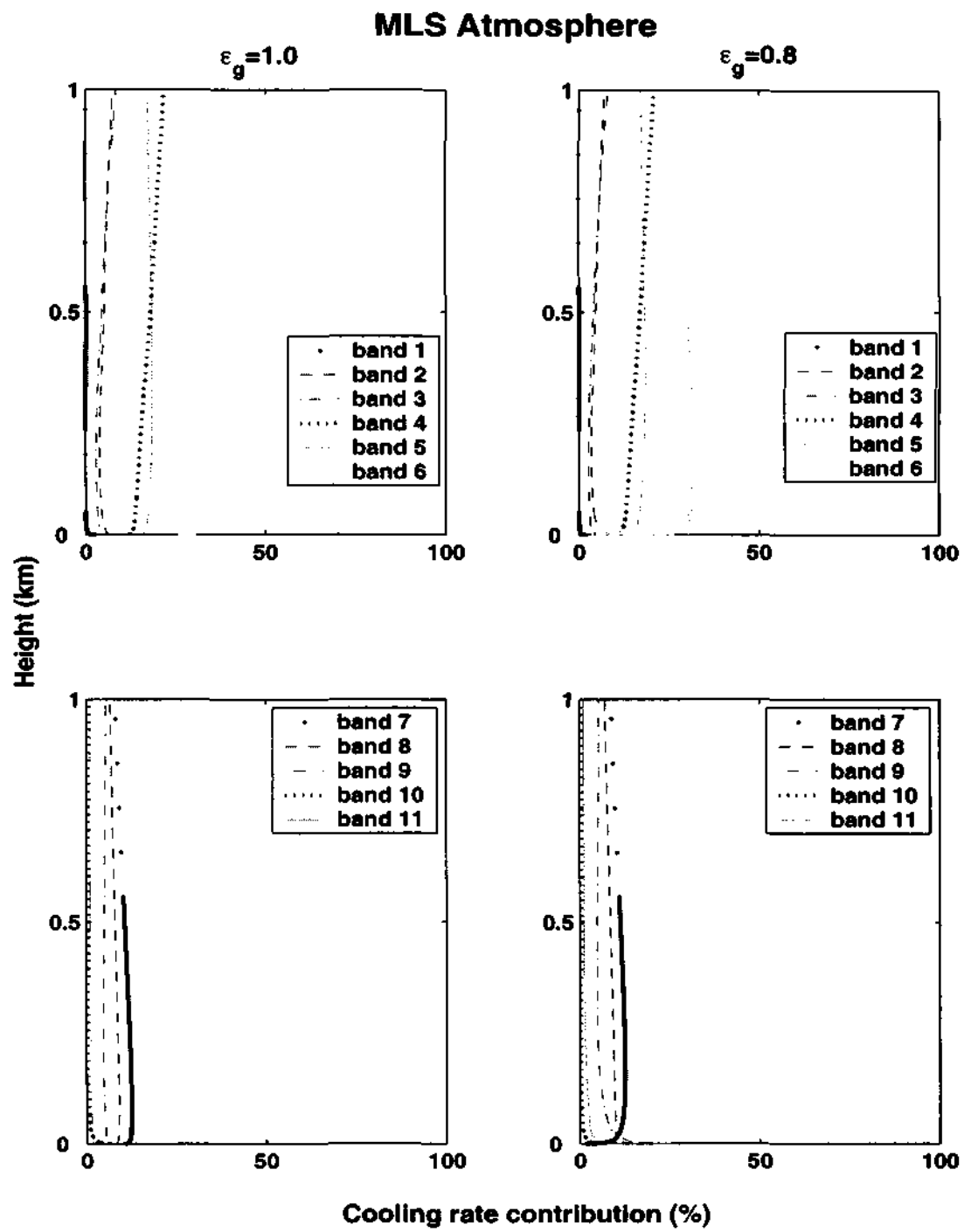


Figure 4.14: Percentage-wise cooling rate contributions from different bands upto heights of 1 km; MLS atmosphere, water vapour absorption only.

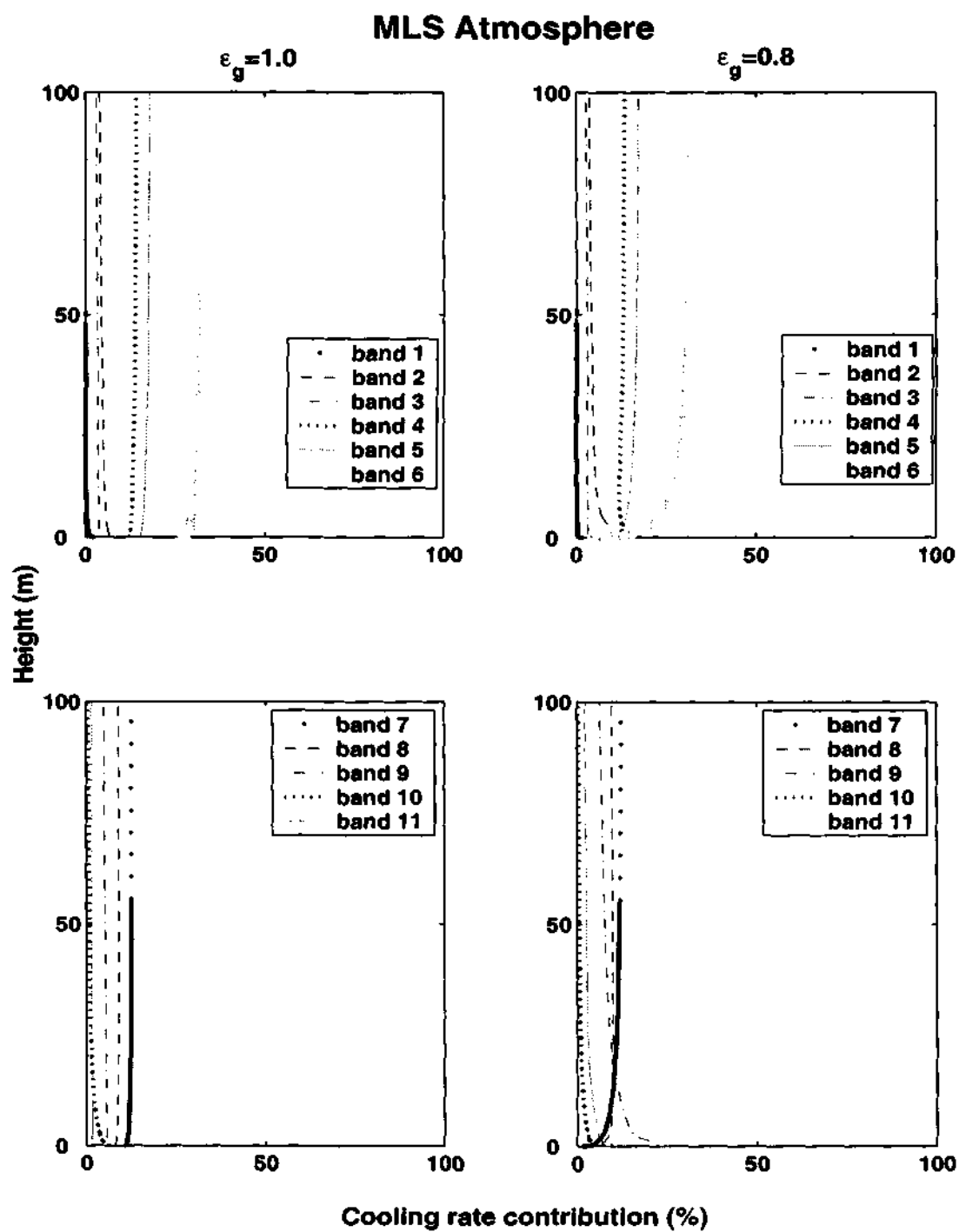


Figure 4.15: Percentage-wise cooling rate contributions from different bands up to heights of 100 m; MLS atmosphere, water vapour absorption only.

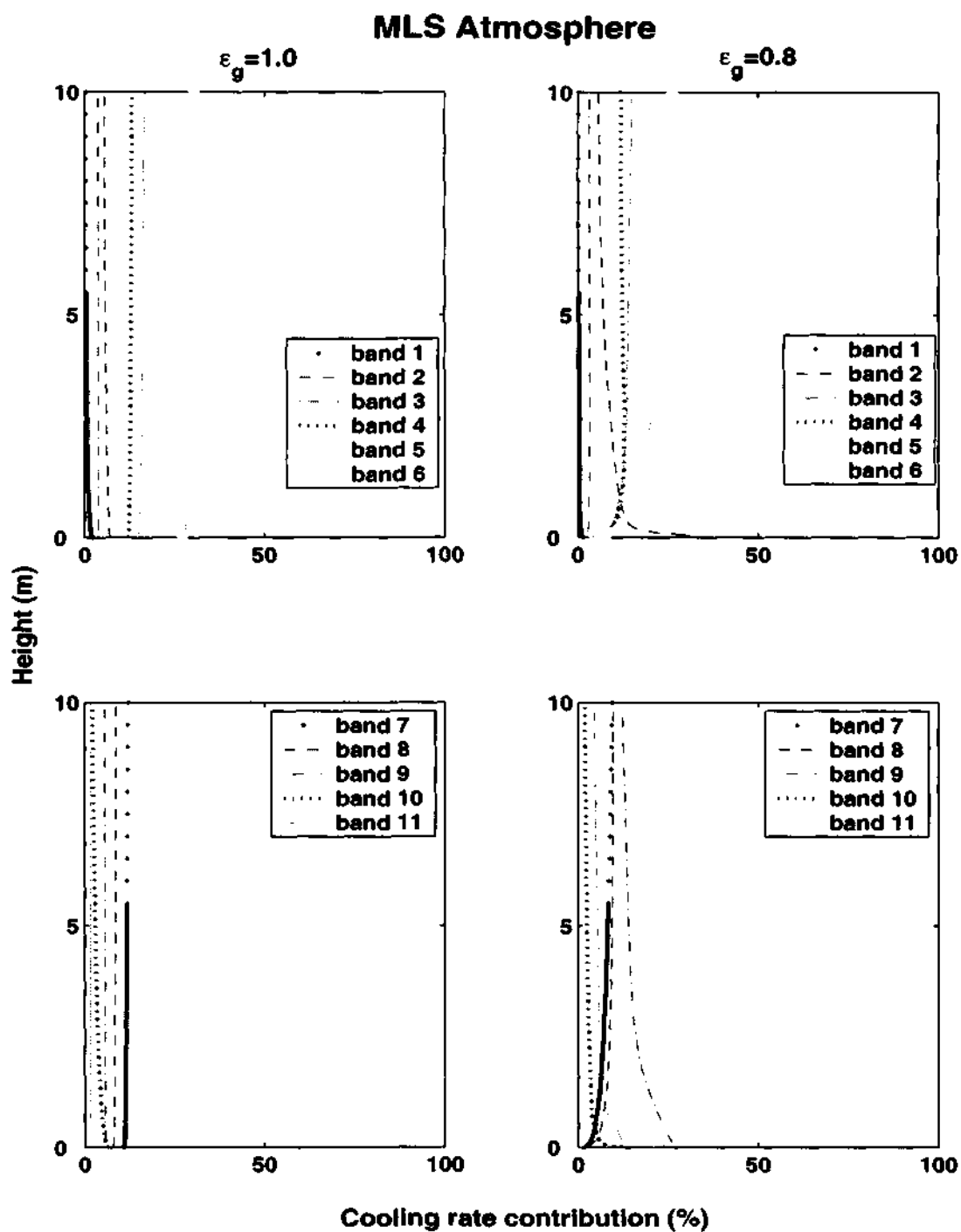


Figure 4.16: Percentage-wise cooling rate contributions from different bands upto heights of 10 m; MLS atmosphere, water vapour absorption only.

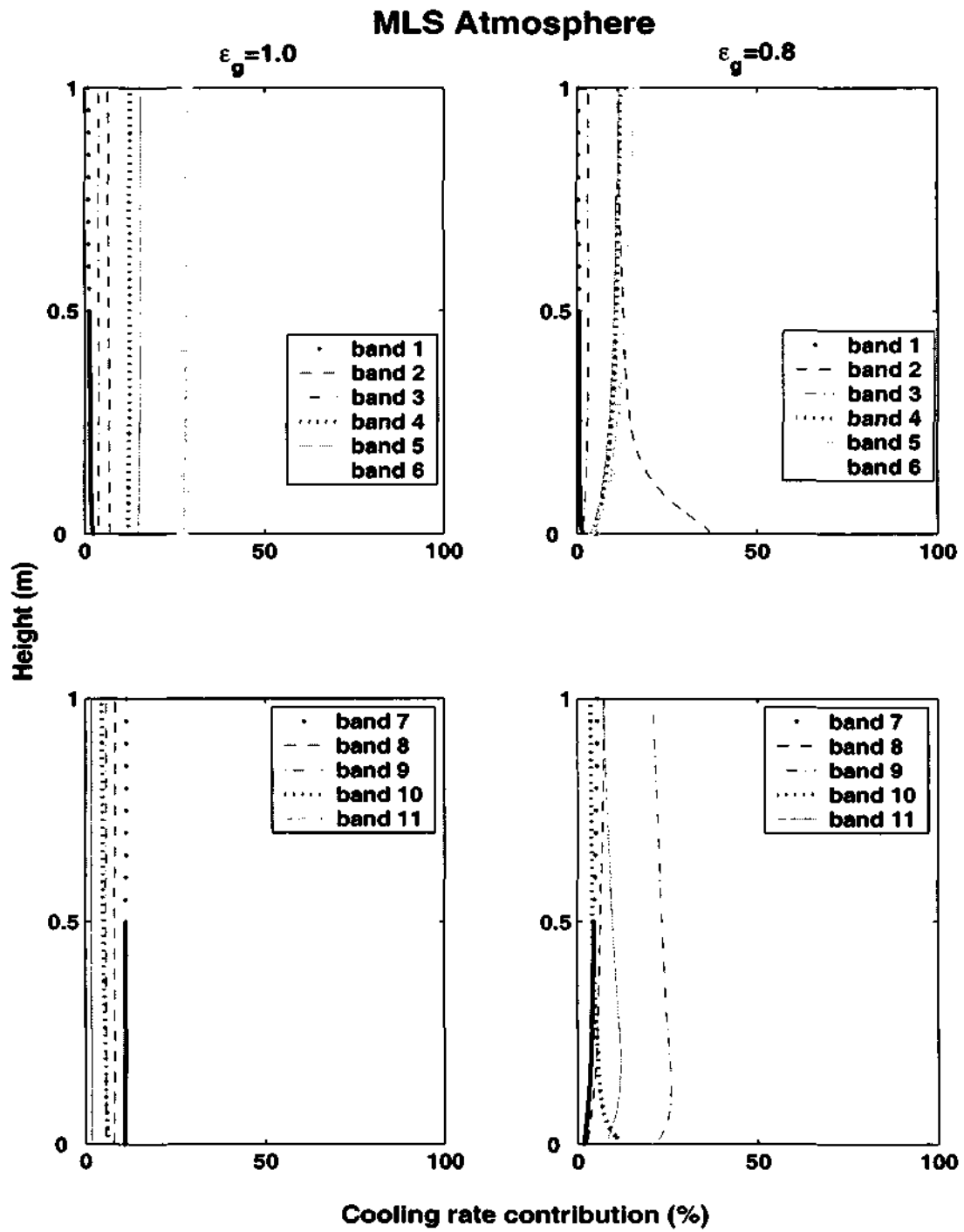


Figure 4.17: Percentage-wise cooling rate contributions from different bands upto heights of 1 m; MLS atmosphere, water vapour absorption only.

the surface are now bands 2 and 9 (wave-number 340 to 540 cm^{-1} , wavelength 29.4 to 18.5 μm and 1215 to 1380 cm^{-1} , 8.2 to 7.2 μm), on either side of the atmospheric window. From 10 m on, however, the spectral distribution begins to resemble that at $\varepsilon_g = 1.0$, although the total cooling rate remains noticeably higher upto $z = 1$ km.

The identity of the bands contributing most to the cooling rate depends on a balance between flux and absorption; if either is too low little cooling occurs. As altitude increases and temperature falls, the flux spectrum peaks at longer wavelengths, where absorption still remains significant; consequently the contribution to cooling also moves to the longer waves.

4.2 Source-wise Decomposition of Cooling Rate

To understand the energetics of near-surface longwave cooling, we first recall (from Section 4.1) that the downwelling flux F^\downarrow plays no significant role, as its gradient in z near the surface is negligible. The upwelling flux can be conveniently decomposed into three parts,

$$F_{ji}^\uparrow = F_{ji \text{ ae}}^\uparrow + F_{ji \text{ ge}}^\uparrow + F_{ji \text{ gr}}^\uparrow, \quad (4.1)$$

where

$$F_{ji \text{ ae}}^\uparrow = d c_i^j k_i^j \int_0^u \pi B_j(T^i) \tau_j^i (u - u') du', \quad (4.2a)$$

$$F_{ji \text{ ge}}^\uparrow = \varepsilon_g \pi B_j(T_g) c_i^j \tau_i^j(u), \quad (4.2b)$$

$$F_{ji \text{ gr}}^\uparrow = (1 - \varepsilon_g) F_j^\downarrow(0) c_i^j \tau_i^j(u). \quad (4.2c)$$

These terms may respectively be called the fluxes due to air emission, ground emission and ground reflection; note that each of these includes the appropriate transmission factor.

The cooling depends on the z -derivative of the flux; we find it convenient to write

$$C_{ji} = \frac{d}{dz} F_{ji}^\uparrow = C_{ji \text{ ae}} + \varepsilon_g C_{ji \text{ ge}}^{(1)} + (1 - \varepsilon_g) C_{ji \text{ gr}}^{(0)}, \quad (4.3)$$

decomposing C_{ji} also into three components and showing explicitly the dependence on ε_g (where the superscripts denote the value of ε_g). Thus $C_{ji \text{ ge}}^{(1)}$ is the cooling due to ground emission at $\varepsilon_g = 1$ and $C_{ji \text{ gr}}^{(0)}$ is that due to ground reflection at $\varepsilon_g = 0$; note that C_{ae} is independent of ε_g .

Figure 4.18 shows C_{ae} , at the surface and at heights of $z = 1, 10, 100$ m. The contributions here are much larger than the cooling rates shown in Figure 4.6 at $\varepsilon_g = 0.8$, and even more so than those at $\varepsilon_g = 1.0$; furthermore they are largest in bands 1, 2, 9 and 10, on either side of the atmospheric window. However they are not affected by a change in ε_g , and so will not be able to explain its effect.

To illustrate the dependence of cooling on ε_g , we consider the two cases $\varepsilon_g = 1.0$ and $\varepsilon_g = 0.8$, and note that

$$C_{ji}^{(1)} = C_{ji \text{ ae}} + C_{ji \text{ ge}}^{(1)}, \quad (4.4a)$$

$$C_{ji}^{(0.8)} = C_{ji \text{ ae}} + 0.8 C_{ji \text{ ge}}^{(1)} + 0.2 C_{ji \text{ gr}}^{(0)}. \quad (4.4b)$$

The difference between the two cases is therefore

$$\Delta C_{ji} \equiv C_{ji}^{(0.8)} - C_{ji}^{(1)} = -0.2 C_{ji \text{ ge}}^{(1)} + 0.2 C_{ji \text{ gr}}^{(0)}; \quad (4.5)$$

We first show in Figure 4.19 the ground emission term in (4.4a). Because of the linearity in ε_g , each of the gradients at $\varepsilon_g = 0.8$ and 1.0 may be obtained simply by multiplying the cooling rate shown in Figure 4.19 by ε_g . The contributions to cooling rate are once again largest in bands 1, 2, 9 and 10 at the lower altitudes, but by $z = 100$ m the contributions come from bands 2, 3 and 4. Compared to the values seen in Figure 4.6, the cooling rate shown in Figure 4.19 is substantial.

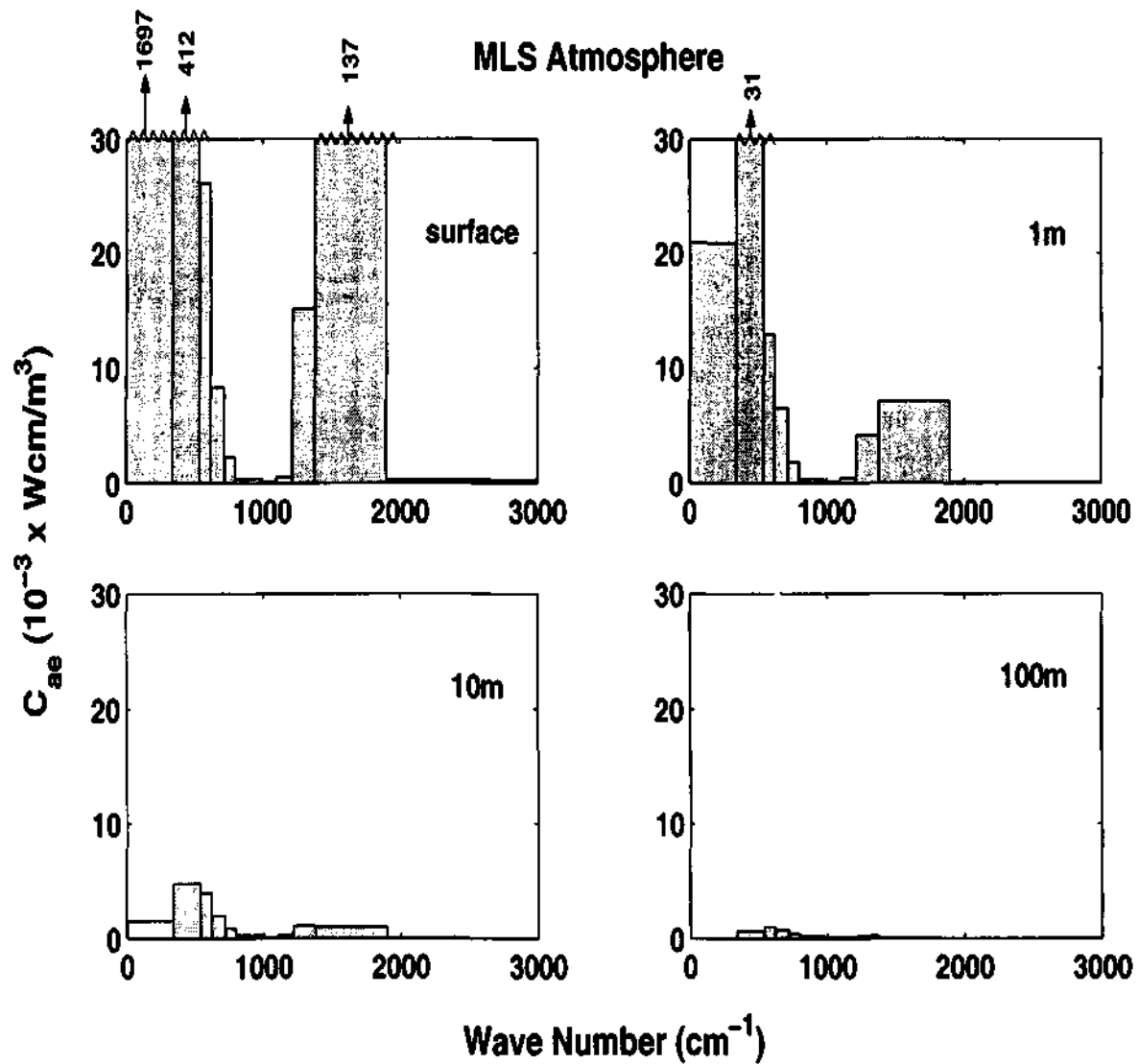


Figure 4.18: Cooling due to air-emission at four different levels for MLS atmosphere, water vapour absorption only.

Next, Figure 4.20 shows the ground reflection term in (4.5). Interestingly, it is immediately seen that the differentials in the gradient of F_{gr}^{\uparrow} ($\Delta C_{ji\ gr}$) closely match 0.2 times those of F_{ge}^{\uparrow} (C_{ge}) displayed in Figure 4.19. In fact, in the case of $\varepsilon_g=1.0$, the ground emission term (4.2b) is almost completely cancelled (see Figure 4.20) out by the air emission term (4.2a) (Figure 4.18).

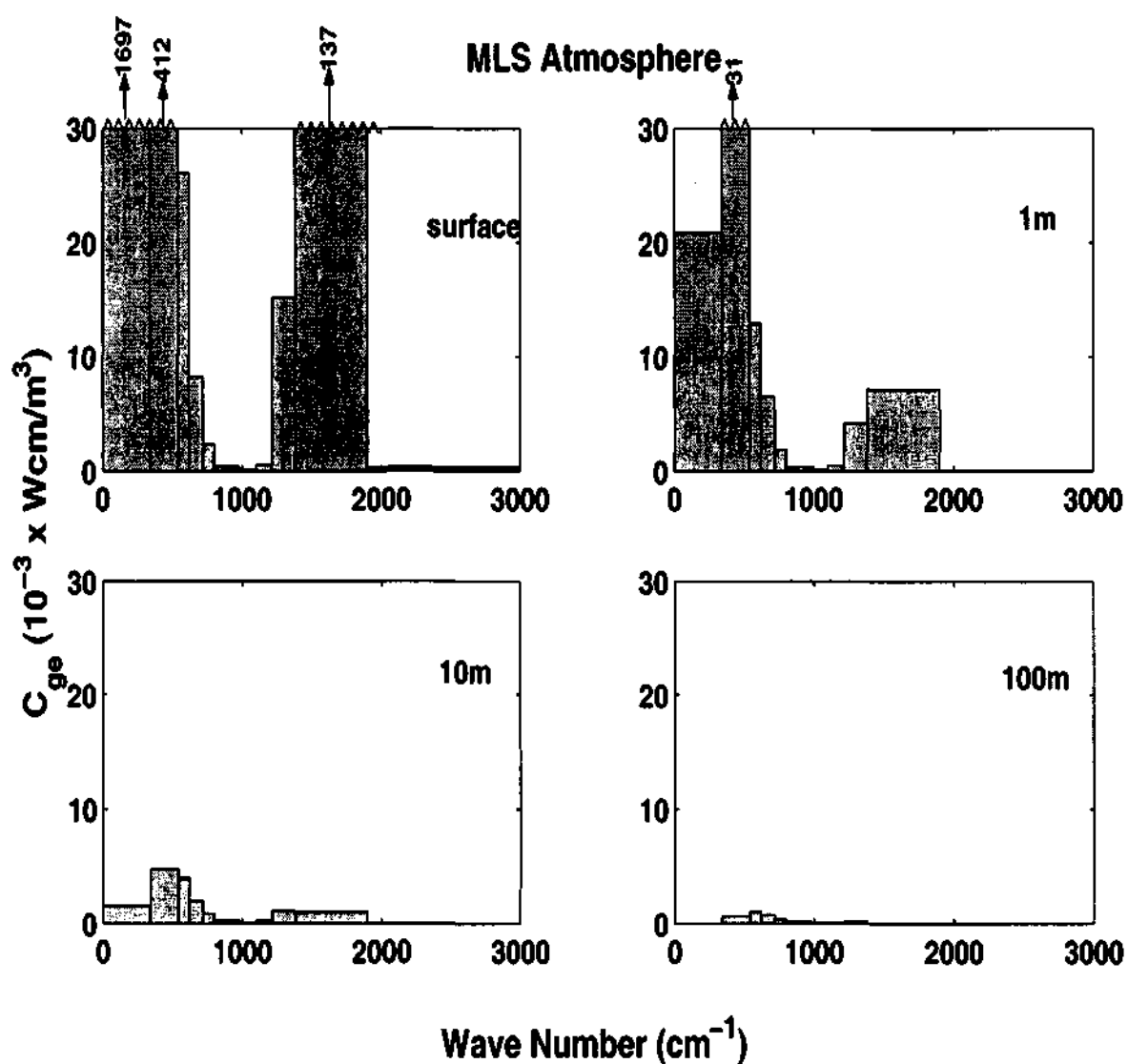


Figure 4.19: Cooling due to ground-emission at four different levels for MLS atmosphere; water vapour absorption only.

Finally, we show the contribution of both ground terms together, as a differential between values at the two emissivities, in Figure 4.21. It is clear that bands 2 and 9 play the major role in determining the high cooling rates at $\epsilon_g = 0.8$.

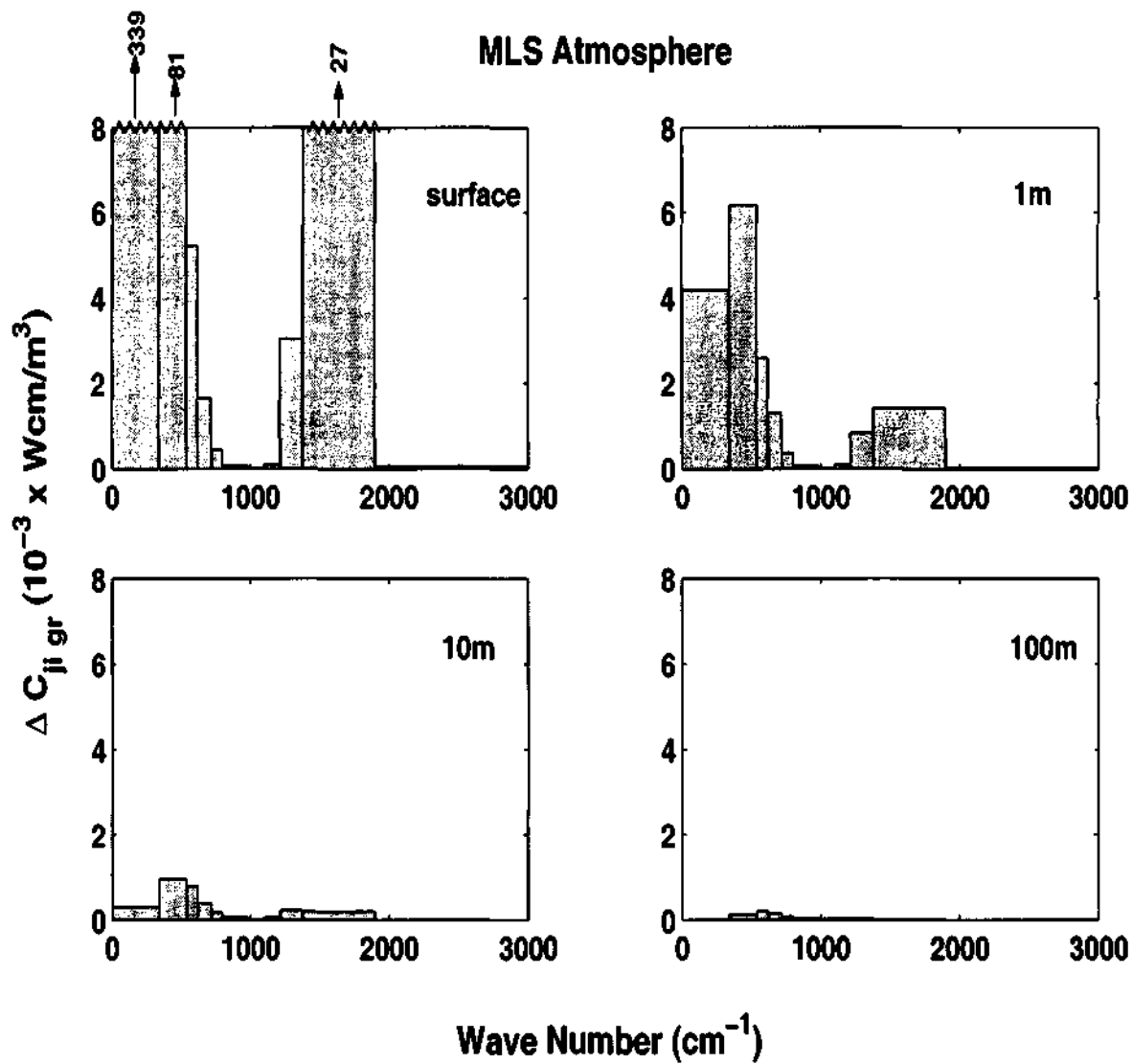


Figure 4.20: Difference in cooling due to ground-reflection at four different levels, with emissivities $\epsilon_g = 1.0$ and $\epsilon_g = 0.8$; MLS atmosphere, water vapour absorption only.

4.5 Discussion

The explanation for the dramatically high surface cooling rates, as it emerges from the above analysis, is thus the following. When $\epsilon_g = 1.0$, the large gradients of air emission and ground emission nearly cancel each other out, leaving a relatively small

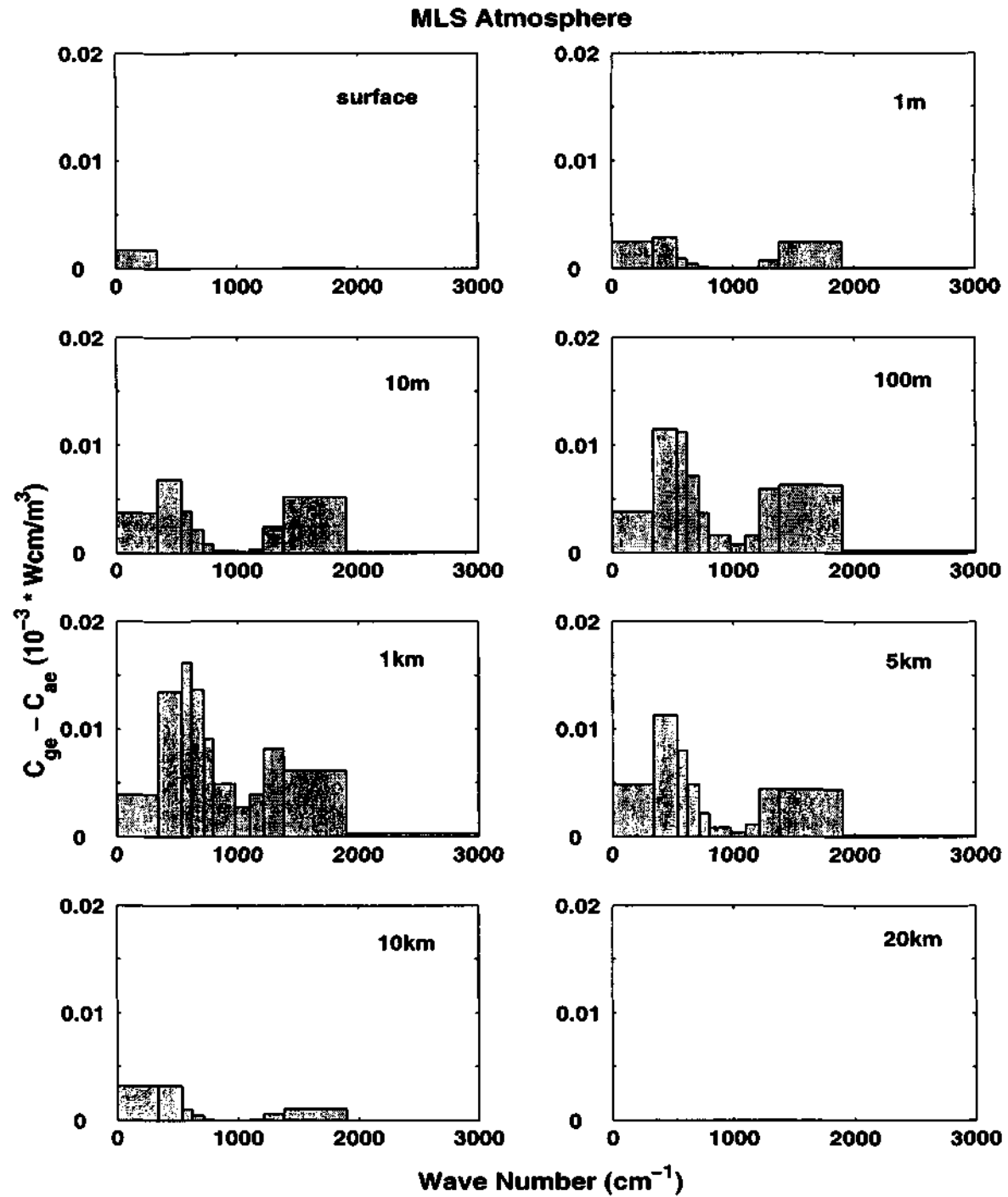


Figure 4.21: Difference in cooling due to ground-emission and air-emission at eight different levels, with $\varepsilon_g = 0.8$; MLS atmosphere, water vapour absorption only.

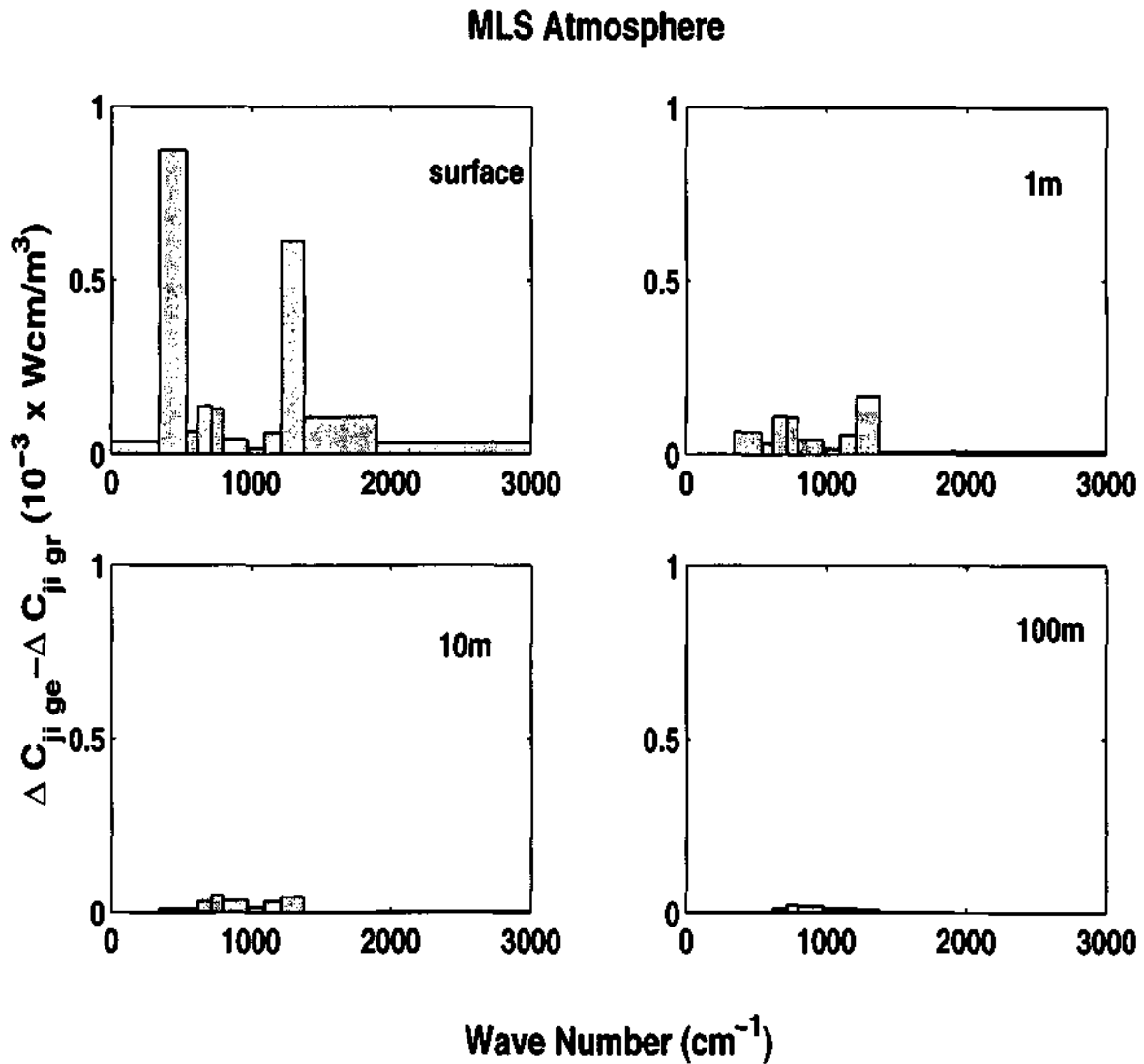


Figure 4.22: Differential between $\epsilon_g = 1.0$ and $\epsilon_g = 0.8$, of the difference of the ground-emission and ground-reflection cooling terms ; MLS atmosphere, water vapour absorption only.

cooling rate which receives dominant contributions from bands 4 to 6. At $\epsilon_g = 0.8$ the ground emission is lower relative to the value at $\epsilon_g = 1.0$, so the balance that prevailed between air and ground emission at $\epsilon_g = 1.0$ is lost; but in addition the ground reflection is a substantial contributor to the cooling. Thus the predominant

cause of the higher cooling when ground is not radiatively black is lower ground emission and higher ground reflection.

Figures 4.19–22 confirm that the high surface cooling rates, when ground emissivity is below unity, are to be attributed chiefly to absorption in bands on either side of the atmospheric window. It follows that emissivities in these bands can play a crucial role in determining the near-surface longwave radiative environment, and the spectral dependence of emissivity merits careful investigation.

Clough *et al.* (1992) conclude from their study that the spectral cooling at high altitudes in the MLS atmosphere (considering water vapour only) arises from the strongly absorbing regions of the water vapour spectrum; in the lower atmosphere, the weaker regions play the dominant role. This result broadly agrees with our own conclusion at altitudes greater than a few km, as can be seen from Figure 4.6. Below about $z = 1$ km, as we have seen, the contribution to the cooling rate depends strongly on the ground emissivity. Although no specific statement is made about ε_g by Clough *et al.* (1992), it appears as if they take $\varepsilon_g = 1$, so the contribution to the upward flux from the component of the downward flux reflected from ground, C_{gr} in our notation, is presumably not taken into account. However our work shows that this contribution plays an important role in near-surface cooling when $\varepsilon_g < 1$. Clough *et al.* (1992) do note that “in the spectral regions for which the atmosphere is not opaque, 800–1200 cm^{-1} and 2100–3000 cm^{-1} for water vapour, there will be a contribution from the Earth’s surface”; from the present computations this conclusion is generally true, but only above 10 m when $\varepsilon_g = 0.8$.

We finally show, in Figure 4.23, the dependence of the surface cooling rate on surface emissivity in the MLS atmosphere. It is seen that the cooling rate increases linearly with $(1 - \varepsilon_g)$.

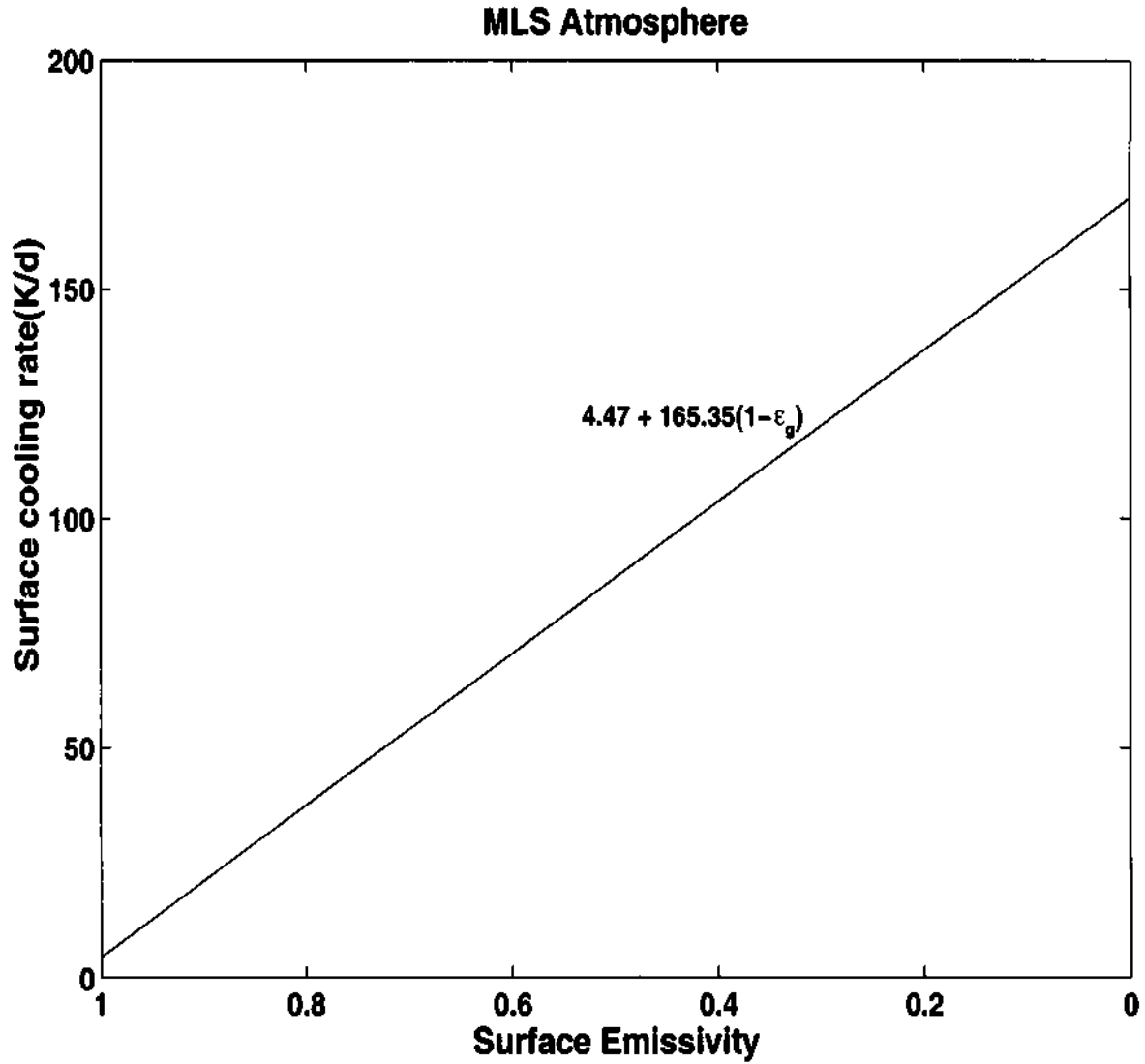


Figure 4.23: Variation of surface cooling rate with change in surface emissivity for MLS atmosphere.

4.6 Carbon dioxide

The effect of other atmospheric constituents on longwave radiative transfer can be handled by the present code in exactly the same way as described above for water vapour. We illustrate this by considering carbon dioxide (CO_2), the second most

important green house gas in the atmosphere. For CO₂, the diffuse transmittance is computed in a way very similar to that of water vapour line absorption, where the absorption coefficient is scaled from its value at reference pressure and temperature (see equations 2.3, 2.18–2.20). The values of the constants associated with the CO₂ transmission functions are again taken from Chou *et al.* (1993, 2001) and shown in Table 4.1.

	Band (cm ⁻¹)				
	3	4	5	6	7
Spectral Range	540–620	620–720	720–800	800–980	980–1100
μk	2.656×10^{-5}	2.656×10^{-3}	2.656×10^{-5}	3.187×10^{-7}	3.187×10^{-7}
n	8	8	8	5	5
c_1	0.2673	0.1970	0.1784	0.1216	0.0687
c_2	0.2201	0.3528	0.2432	0.2436	0.1480
c_3	0.2106	0.3056	0.3086	0.2498	0.1951
c_4	0.2409	0.0861	0.1983	0.2622	0.3344
c_5	0.0196	0.0434	0.0424	0.0781	0.1720
c_6	0.0415	0.0151	0.0291	0.0427	0.0818
a	0.0179	0.0042	0.0184	3.5775×10^{-2}	3.4268×10^{-2}
b	1.07×10^{-4}	2.0×10^{-5}	1.12×10^{-4}	4.05×10^{-4}	3.74×10^{-4}
m	0.5	0.85	0.5	0.0	0.0

From Chou *et al.* (1993, 2001), units of μk are in (cm.atm)⁻¹, μ is the diffusivity factor.

Table 4.1: Values of radiation code parameters for carbon dioxide absorption.

CO₂ is mainly absorbed in the 15 μm (540–800 cm⁻¹) band. In Chou's model, this band has been divided into central and wing regions (540–620 cm⁻¹, 620–720 cm⁻¹ and 720–800 cm⁻¹, constituting in all three sub-bands). Two other weak CO₂ absorption bands (800–980 cm⁻¹ and 980–1100 cm⁻¹) are located in the water vapour window region. Altogether, there are five CO₂ bands.

When absorption involves water vapour line, water vapour continuum and carbon dioxide, the total diffuse transmittance for individual bands is given by

$$\tau = \tau^{\text{wl}} \cdot \tau^{\text{wc}} \cdot \tau^{\text{CO}_2},$$

the product of the respective transmittances.

The rest of the calculations are carried out by exactly the same way as described above in Sections 2.3 and 3.3.

Table 4.2: Comparison of upwelling and downwelling radiative fluxes at the surface and tropopause for an isothermal atmosphere at 300 K and 300 ppmv of CO₂ only. The units are in Wm⁻².

	Surface		Tropopause	
	up	down	up	down
ICRCCM	458.85	90.16	458.86	52.91
Present	458.96	89.52	458.96	55.05

Table 4.2 shows a brief comparison of present results for the fluxes with ICRCCM results for an isothermal atmosphere at 300 K with 300 ppmv of CO₂ only. Both results are in good agreement (generally better than 1%), the largest difference

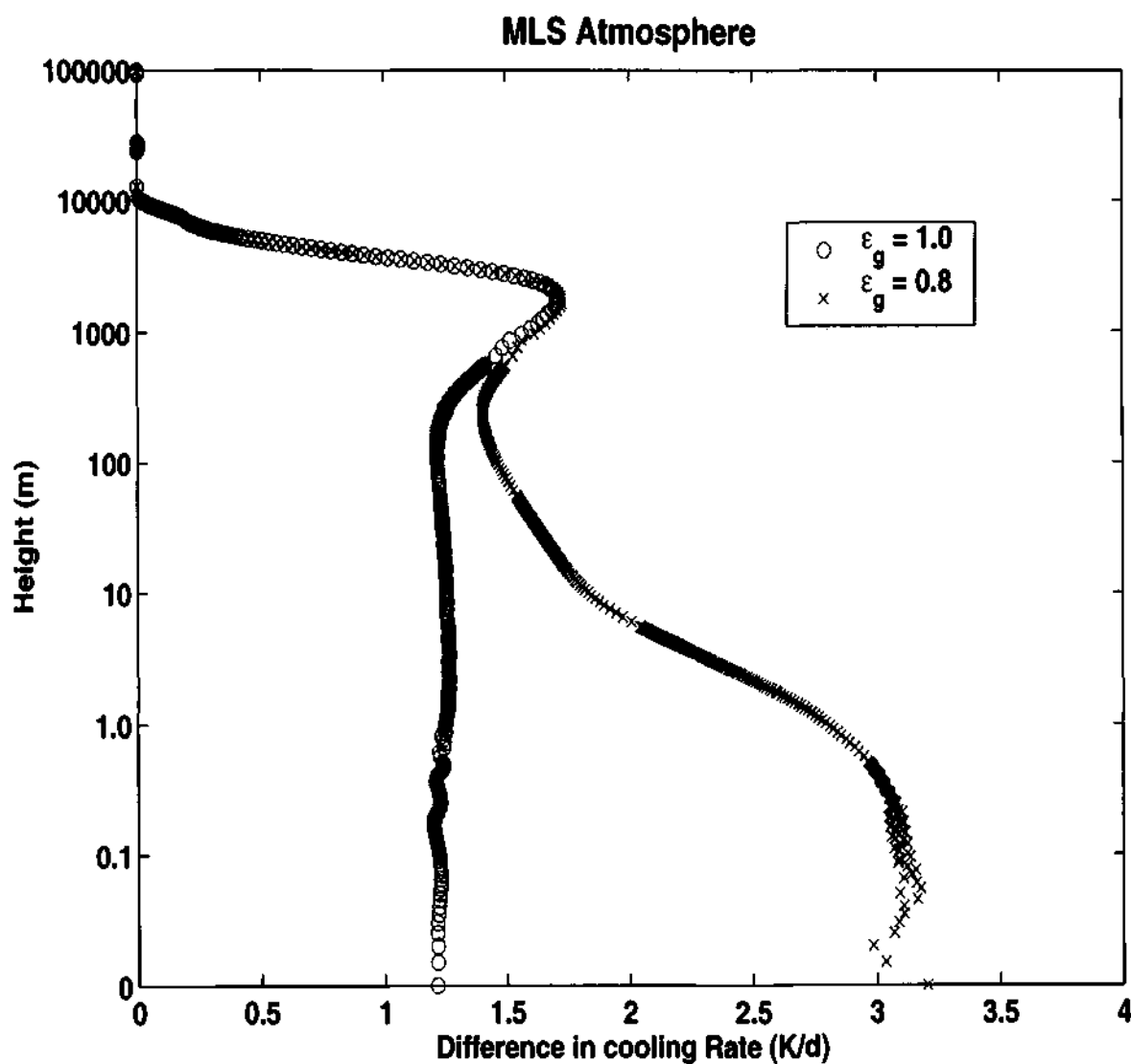


Figure 4.24: Difference in cooling rate due to CO₂ (300 ppmv) with $\epsilon_g = 1.0$ and 0.8; MLS atmosphere.

being about 3 Wm^{-2} in the down-flux at the tropopause. The relation between ppmv and density of carbon dioxide (in kgm^{-3}) is explained in Appendix D.

Figure 4.24 shows the difference in cooling rates with and without inclusion of CO₂. The addition of CO₂ results in a general decrease in the cooling rate everywhere in the atmosphere. At the surface the differences are appreciable, being

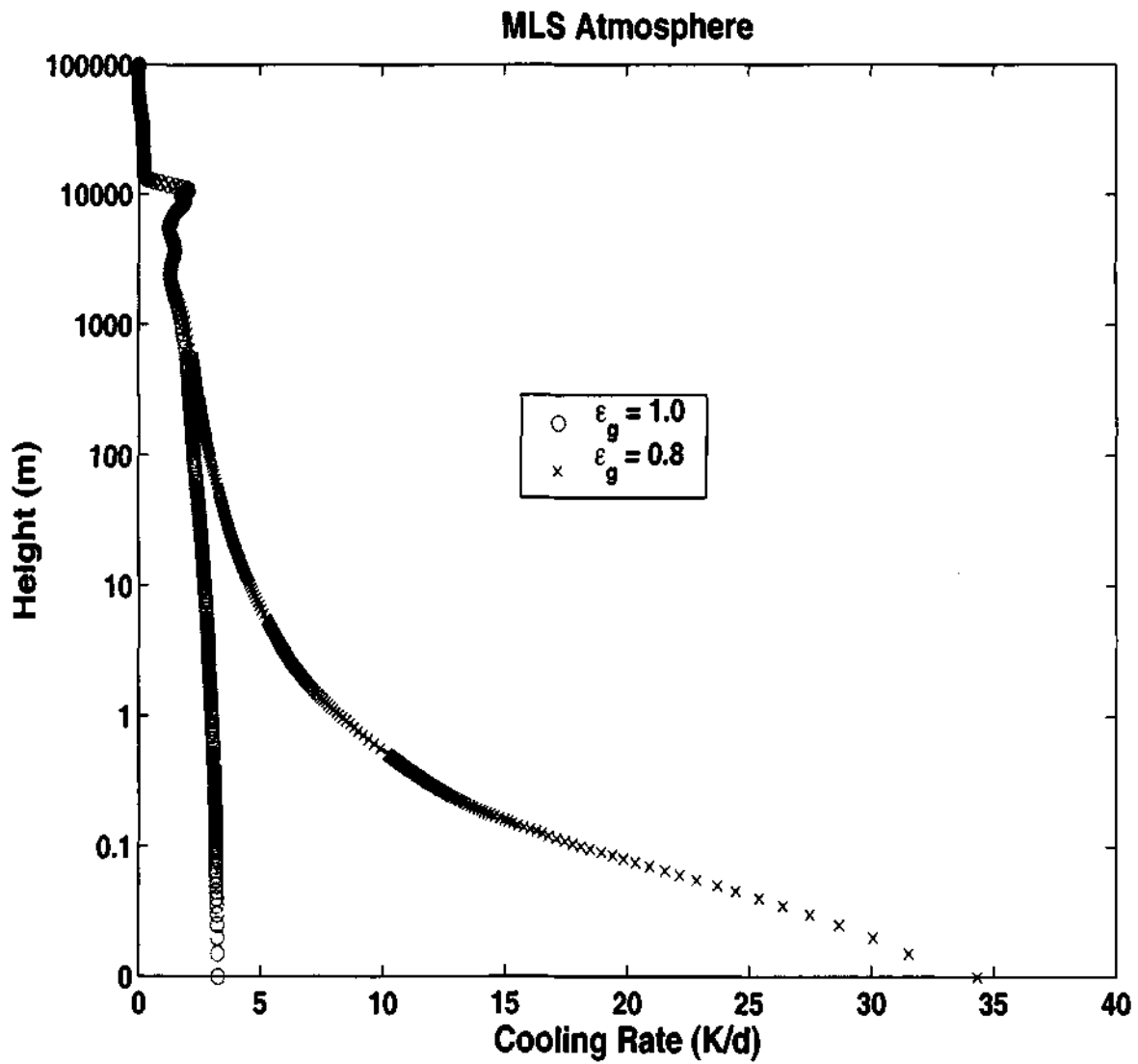


Figure 4.25: Net cooling rate due to water vapour and CO₂ (300 ppmv) with $\epsilon_g = 1.0$ and 0.8; MLS atmosphere.

3.2 K/d and 1.21 K/d for ground emissivity of 0.8 and 1.0 respectively. Figure 4.25 shows the net cooling in the entire atmosphere when both water vapour and carbon dioxide are included.

Chapter 5

Temperature Slip at the Surface

5.1 Introduction

We shall now show below that ground temperature is the most important parameter in the computation of near-surface infrared cooling rate. Cooling rates cannot be estimated accurately without knowing ground temperature. Most longwave radiation codes cannot independently retrieve the ground temperature and hence are incomplete. In other words the models stop their computations just above ground. Therefore to estimate the near-surface cooling accurately it is imperative that we either prescribe T_g (say from observation) or compute it taking account of the heat transfer within the soil or through some independent model. It is clear that this issue has not been addressed by researchers adequately. In this Chapter we show that near-surface cooling rates are very sensitive to ground temperature, using the present code with prescribed ground temperatures.

Morcrette *et al.* (1986), in the longwave radiation code developed for ECMWF, make allowance for a discontinuity at the surface in the formulation for the upward flux. However, they do not discuss the physics involved in the appearance of such a discontinuity, nor do they describe any procedure by which the ground temperature could be determined. In their simulation studies of the nocturnal boundary layer (NBL), Tjemkes and Duynkerke (1989) include a temperature discontinuity at

the ground based on a scheme proposed by Holtslag and De Bruin (1988). Here the surface temperature is related to the temperature just above the vegetation level, through a model. In this model, the surface level is within the vegetation layer. Therefore this formulation does not represent the actual temperature discontinuity at the ground-air interface on bare soil. This model is described in some detail in the next Section.

Radiative cooling at any level z is due to exchange of infrared radiation between the level z and

- (i) space ($z = \infty$),
- (ii) ground ($z = 0$) and
- (iii) other levels ($z = z'$),

as shown in Figure 5.1. The first mechanism (cooling to space term) is believed to be

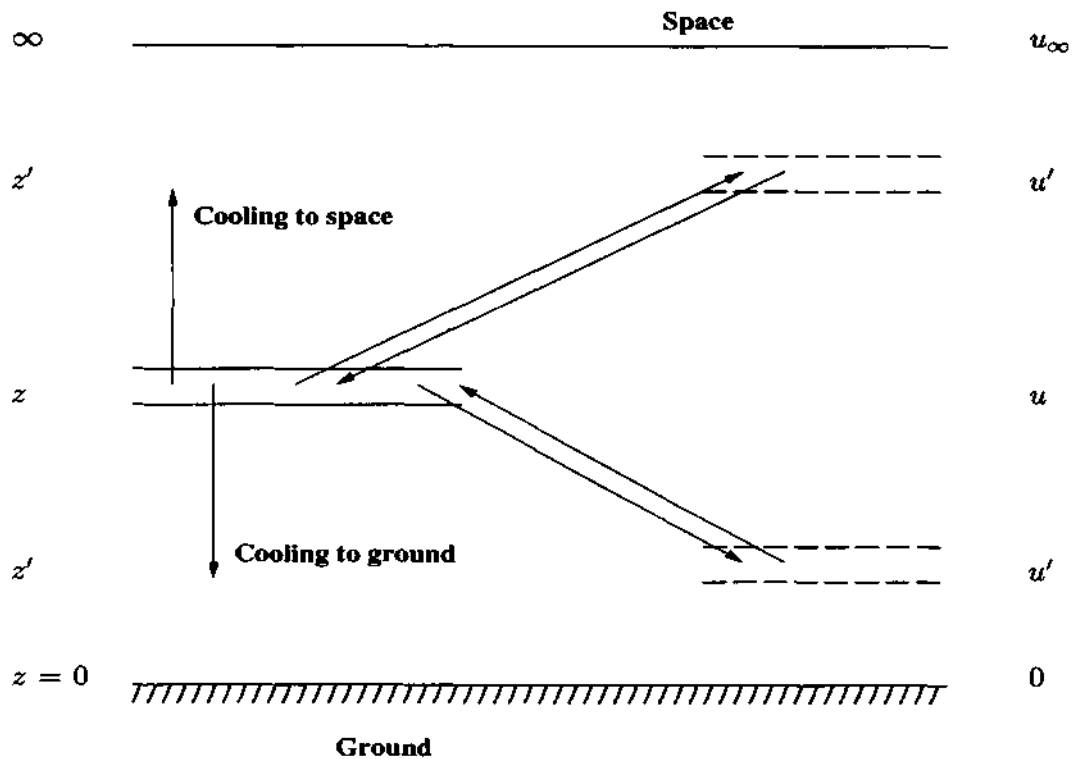


Figure 5.1: Components of cooling in the atmosphere

dominant (Rodgers and Walshaw, 1966). However, whether this is true even in the lowest layers of the atmosphere under calm conditions is not known.

VSN have studied the dominant role played by radiation in the lifted minimum phenomenon using a flux emissivity model. In the computation of the evolution of the temperature profile carried out by them for the case of pure radiation, the following initial/boundary conditions were assumed:

$$T(z, 0) = 300 - \Gamma z \quad (5.1)$$

$$T_g(t) = 300 - \beta\sqrt{t}, \quad (5.2)$$

with $\varepsilon_g = 0.9$, $\beta = 2 \text{ Kh}^{-1/2}$, adiabatic lapse rate $\Gamma = 0.0098 \text{ K/m}$, and surface humidity $q_0 = 0.01$. After 1 hour following sunset, a discontinuity of +3.4 K (plus sign indicates ground is warmer) was obtained. This discontinuity is also called radiative or temperature slip which is defined as the difference in temperature between the ground and the air just above,

$$\Delta T = T_g - T(0+). \quad (5.3)$$

The temperatures at and just above the ground were respectively 298 K and 294.6 K. VSN also confirmed that the discontinuity was genuine and not a numerical artifact by refining the spatial resolution near the surface down to 1 mm.

Now, the role of radiation (alone) with the present model, for different values of ground emissivity ε_g and ground cooling rate β , are examined with the initial/boundary conditions (5.1,2) (see Figure 5.2 and 5.3). The temperature slip obtained after one hour with $\varepsilon_g = 0.8$, $\beta = 0 \text{ Kh}^{-1/2}$ is +0.25 K, which is 6.75 K lower than the one obtained from the flux emissivity model. As in the case of VSN, the spatial mesh was refined to 0.0001 mm to make sure that the temperature slip was not an artifact. Table 5.1 shows a comparison of the values of the temperature slip obtained with different ε_g and β . Clearly the differences between VSN and the present code are substantial.

Table 5.1: Comparison of temperature slip obtained from flux emissivity model by VSN and present model for $\varepsilon_g = 0.8$ and different β .

$\varepsilon_g = 0.8$		
β	Present	VSN
0.0	0.25	7.0
2.0	-0.25	6.6

Kondo (1971) has computed the evolution of radiation temperature profiles near ground but the specific influence of the above mentioned parameters (ε_g and β) on the profiles was not studied; his major objective was to stress the fact that the effect of radiation on transfer problems in the surface layer cannot be ignored. The existence of a discontinuity for the temperature profile with radiation alone at the ground was also shown, but in his case the radiative slip was negative. According to him, radiative slip is caused because of the vastly different radiative properties of ground and air (see e.g., Su, 1973). Discontinuities in temperature gradient and in temperature itself are totally consistent with radiative transfer theory for an atmospheric model with layers of different radiative properties (Su, 1973).

There are many challenges and difficulties in the understanding of the radiative slip or discontinuity at the air-surface interface. According to Duynkerke (1999), it is typically impossible to measure the radiative flux divergence in the lower metres of the atmosphere. Eliseyev *et al.* (2001) explain the errors associated with making direct measurements of the radiative fluxes near the surface, and devise a

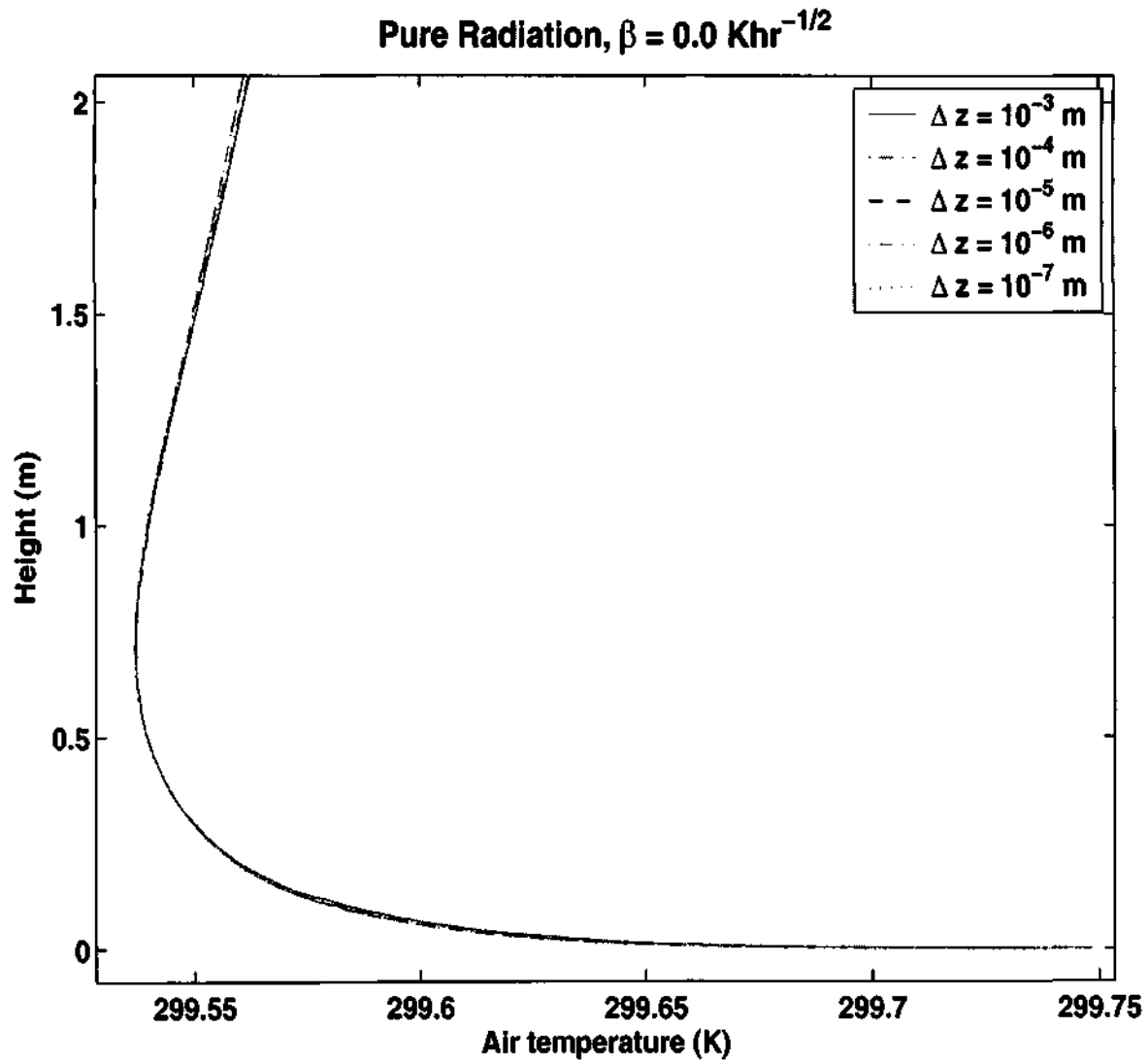


Figure 5.2: Variation of air temperature with height for different grid resolutions near the surface; pure radiation.

novel method to measure the cooling rates directly based on acoustics. Because of these difficulties, there have been only two or three measurements of temperature slip (direct or indirect) at the air-ground interface.

It is clear that the effect of ground temperature on radiation is responsible for the temperature slip near the surface. In the next Section results from previous

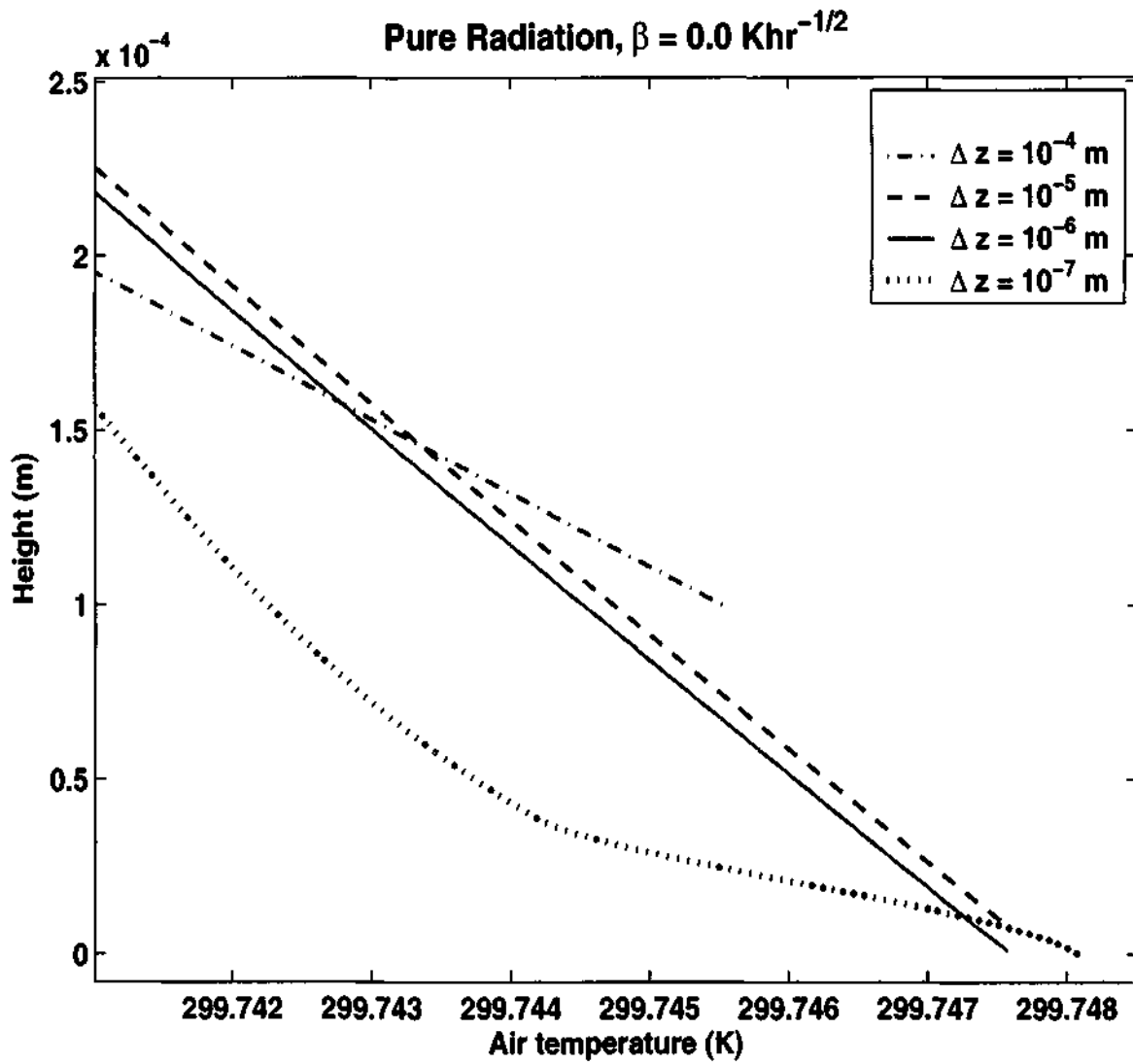


Figure 5.3: Variation of air temperature just above the surface for different grid resolutions.

studies related to temperature slip and near-surface cooling rates are presented.

5.2 Survey of Earlier Work on Radiative Slip and Cooling Rates near the Surface

Thomas and Stamnes (1999) study a simple model of energy balance in the case of radiative equilibrium, based on the facts that the surface is heated by incoming solar radiation and by downwelling infrared radiation from the atmosphere. The atmosphere is heated by infrared radiation, emitted by both the surface and by surrounding atmospheric layers. The atmosphere is assumed to be gray. The following boundary conditions are used:

- (i) a black surface of temperature T_g underlying a slab atmosphere of infrared optical depth u , and
- (ii) zero incoming infrared radiation from space.

No grass or vegetation is considered above the soil.

It is found that under these conditions a discontinuity results between the air immediately above the surface and the surface itself. The relative temperature change over the interface between the air and the surface is

$$\Delta T/T_g = [T_g - T(0+)]/T_g = 1 - \left[\frac{1+u}{2+u} \right]^{1/4}. \quad (5.4)$$

The value of this relative jump is $\sim 16\%$ for optically thin media, and decreases to zero as $u \rightarrow \infty$. This peculiarity arises from the fact that the surface is heated by radiation from both the Sun and the atmosphere, whereas the overlying layer is heated only by the neighbouring regions including the surface. Conservation of energy across the interface leads to a surface that is hotter than the immediately overlying atmosphere. Equation (5.4) implies that ΔT varies from about 40.6 K at $u = 0$ to 21.0 K at $u = 2$ and 15 K at $u = 4$. The value of T_g used by the author is not provided.

The radiative equilibrium expression (5.4) for the temperature slip ignores the possibility of fluid dynamical heat transport across the interface. According to

Thomas and Stamnes (1999), in the real world, convection tends to erase the discontinuity extremely quickly but does not necessarily eliminate it.

The boundary layer, the thin atmospheric layer located adjacent to the earth's surface and influenced by the surface and friction, develops over land during the night to a state of stability (leading to a stable boundary layer or SBL). The structure and evolution of this SBL is determined by infrared radiation, condensation and evaporation (fog), gravity waves and advection. Duynkerke (1999) studied the role played by radiation and turbulent mixing in the structure and evolution of the clear sky SBL, focusing on the direct effect of the radiative cooling just near and above the boundary layer and "close" to the surface, using both observational data and calculation. It is to be noted that the observation site was covered with vegetation. He found that, under stable conditions, the temperature jump (vegetation temperature minus upper soil temperature measured at a depth of 0 cm) can become as large as 10 K during night; here vegetation temperature is defined as the temperature just above the grass, whose height is stated to be "several centimetres"; no more precise value is given. This large temperature jump has a pronounced influence on the infrared radiative flux and cooling rate.

In the simulation of longwave radiative cooling in the lowest metres of SBL, Duynkerke (1999) uses a flux-emissivity model assuming ground emissivity to be 1.0 and a logarithmic initial temperature profile. For a temperature slip of 7 K, cooling rate obtained was 84 K/d at 1 m and approximately 252 K/d "near" the surface. He remarks that observed cooling rates are the order of 24 K/d (under unstable conditions) and this low value is due to the heating due to turbulence in the lowermost metres of the atmosphere during the night which cancels most of the infrared cooling. Duynkerke (1999) states that "these results seem rather controversial, although the same conclusions were reached by Rider and Robinson (1951), Funk (1960) and Elliot (1964)".

Tjemkes and Duynkerke (1989) tested an SBL model against night observations of the clear SBL made at the Cabauw meteorological tower (Nieuwstadt, 1984). The longwave radiation (3.6 to 100 μm) was calculated using a narrow band model with 178 spectral bands. In the prognostic simulation which followed, a high cooling rate of up to 100 K/d was achieved due to the temperature discontinuity. To relate the surface temperature (T_s) with the temperature (T_0) just above the vegetation level (z_0), Tjemkes and Duynkerke used an equation proposed by Holtslag and De Bruin (1988);

$$\frac{T_0 - T_s}{\theta_*} = c_v + \frac{u_0}{u_*}, \quad (5.5)$$

where, T_0 is the temperature at $z = z_0$, c_v and u_0 are empirical constants with values of 10 and 4.2 ms^{-1} respectively, and u_* is the frictional velocity. Their results are in correspondence with the computations made by Garratt and Brost (1981) but disagree with those of Estournel and Guedalia (1985). Garratt and Brost used a surface emissivity of 0.8 and 1.0 and obtained a cooling rate of approximately 72 K/d and 17 K/d respectively at 2 m level. They get a strong radiative cooling in a layer “close” to the surface. Estournel and Guedalia, who do not include a temperature discontinuity at the surface and use $\varepsilon_g = 1.0$, do not obtain strong radiative cooling near the surface.

Salerno and Gianotti (1995) introduced a thin transition layer (TTL) between the soil and the surface layer (SL) to provide the bottom boundary condition for temperature $T = T(t, z)$ in their model for the evolution of the temperature profile in the boundary layer in rural areas. The surface temperature controls the evolution of the profile. They note that “models of thermal balance at the ground always take surface temperature into account. Hence there is a sort of discontinuity between the temperature at the ground surface and at the bottom of the surface layer”. In the TTL, the conductive effect is in some way retained together with the turbulent trans-

fer to avoid an abrupt step jump from the ground surface to the SL. Simpler methods such as interpolation cannot be used as the phenomena are not linear. The depth of this layer was assumed to be independent of surface characteristics. According to them, the prediction of surface temperature is difficult as it is dependent on the specific site characteristics. Their model applies to bare soil.

Eliseyev *et al.* (2001) observe a radiative heating rate of 960-1200 K/d in mid-day hours at a height of 2 cm in field studies of heat flux divergence in the atmospheric surface layer in North Kazakhstan. Funk (1960) measured radiative flux divergence near the ground at night where a maximum cooling rate of approximately 290 K/d (average of 0.5–1.5m) was observed. Funk (1961) notes that “usual assumption of $T(0^+) = T_g$ is in general certainly incorrect, the reason being that T_g is an equivalent temperature and in principle only identical to the surface temperature if the underlying surface is both uniform in temperature and black, both of which conditions are rarely fulfilled. There is good experimental evidence showing T_g to be generally unequal to $T(0^+)$. Yamamoto and Kondo (1959) come to a similar conclusion.”

Table 5.2 shows the cooling rates observed/simulated near the surface and temperature slip used by different researchers in their computations.

It is now clear from the Table that nocturnal cooling rates at the surface and just above can be of the order of hundreds of K/d. The main contributory causes for these high cooling rates could be the temperature jump (slip) which exists near the ground-air interface. We shall examine this point in the next Section. Moreover it has been established beyond doubt by observation that such high cooling rates and temperature slips can actually occur during the night and are not artifacts of observation.

5.2. Survey of Earlier Work on Radiative Slip and Cooling Rates near the Surface97

Table 5.2: Near-surface cooling rates observed/simulated.

Authors	Height $z(\text{m})$	Time	Cooling rate (K/d)	Remarks
Funk, 1960	average of observations at 0.5-1.5	night	290	observation
Garratt and Brost, 1981	2.0	night	72	$\varepsilon_g = 0.8$ emissivity model
	2.0	night	17	$\varepsilon_g = 1.0$ Initial cooling rate, emissivity model
Tjemkes and Duynderke, 1989	near the surface	night	~ 100	$\varepsilon_g = 1.0$ narrow band model ΔT not specified
Duynderke, 1999	near the surface	night	252	$\varepsilon_g = 1.0$ emissivity model $\Delta T = 7 \text{ K}$
	1.0	night	84	$\varepsilon_g = 1.0$ emissivity model $\Delta T = 7 \text{ K}$
VSN, 1993	surface	night	~ 1700	$\varepsilon_g = 0.8$ emissivity model isothermal atmosphere
Raisanen, 1996	0.3	night	24.2	$\Delta T = -3 \text{ K}$
	0.3		12.7	
	0.3		31	
	surface layer		53	
Eliseyev <i>et al.</i> , 2001	0.02	mid-day	960-1200	observation
Ha and Mahrt, 2003	near the surface	early evening	144	observation
		night	42	model study

5.3 Sensitivity Study of Cooling Rate from Present Model

It is essential to conduct sensitivity tests on the grid resolution to obtain accurate results for radiative slip and cooling rates from the present model. Therefore, as a first step, grid resolution tests were carried out. This was followed by numerical experiments with various values of temperature slip in different atmospheres to study the sensitivity of near-surface cooling rates to change in ground temperature. Several numerical tests were carried out to accomplish this. In all these tests the following initial profiles were assumed:

$$q = q_0 \exp(-z/h_w)$$

$$\text{Case 1: } T = T_0$$

$$\text{Case 2: } T = T_0 - \Gamma z.$$

Here q is the specific humidity and q_0 is its value at the surface, taken to be 0.01. Γ is the adiabatic lapse rate and h_w is the scale height of water vapour (taken as 2 km).

Figure 5.4 shows the variation of temperature slip (which was determined from equation 5.3) at $t = 1$ h after sunset for different grid resolutions near the surface. Δz also represents the height of the first grid point (0+) from the surface. We take $\varepsilon_g = 0.8$ and ground cooling rate parameter $\beta = 0 \text{ K hr}^{-1/2}$. In this calculation, a constant lapse rate of 9.8 K/km (Case 2) was assumed. There is a decrease in slip until the grid resolution Δz is 10^{-4} m, and thereafter it is more or less constant. The difference in slip obtained for the maximum and minimum resolution is just 0.011 K. Therefore a minimum grid resolution of 10^{-3} m very near the surface is suggested for this model. A slip of 0.25 K and -0.25 K are produced at $\beta = 0$ and $2 \text{ K hr}^{-1/2}$ respectively as already cited in Table 5.1.

At this point it would be appropriate to compare the value of the slip from the flux emissivity and the present models. Before further discussion, we shall briefly

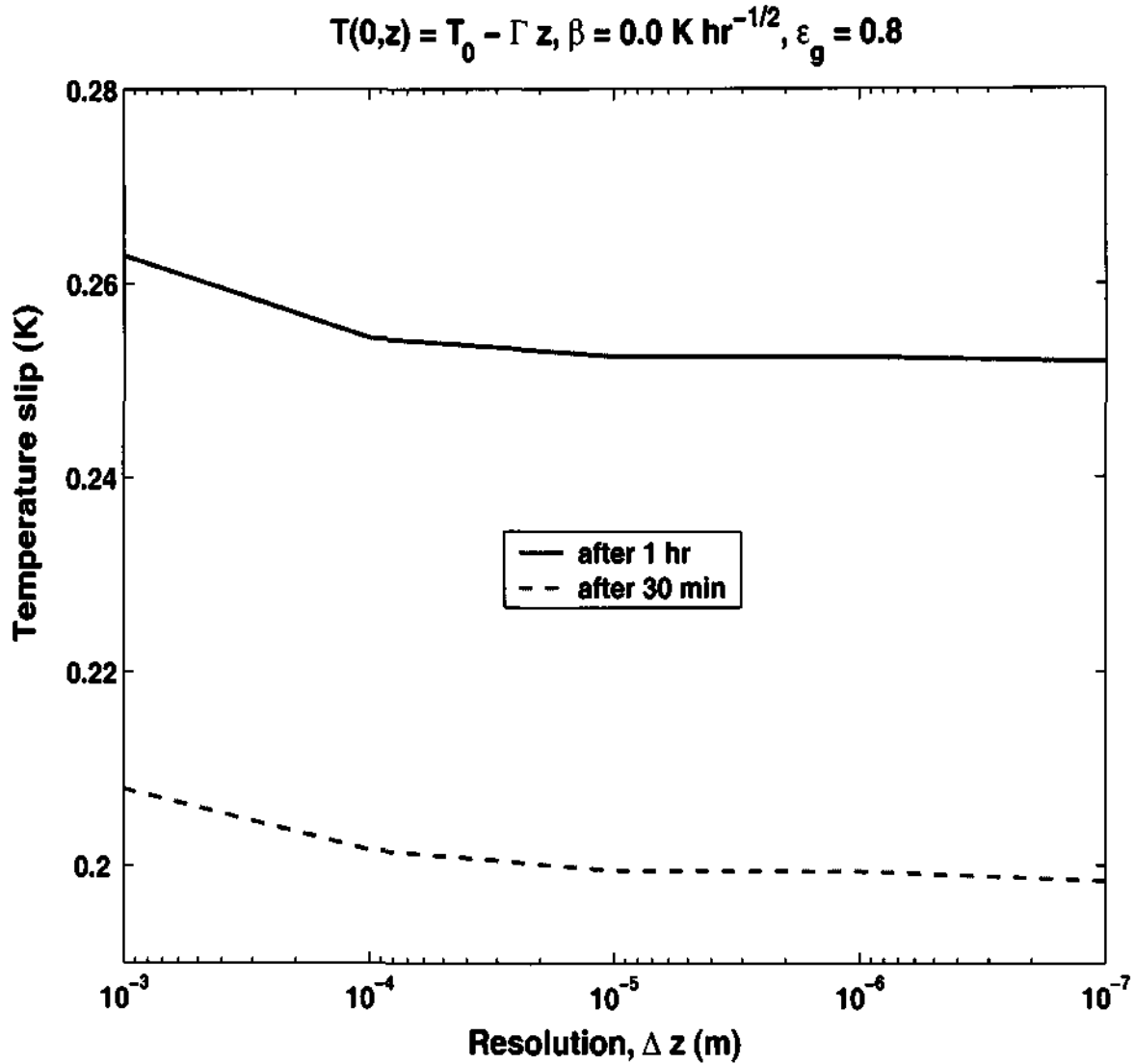


Figure 5.4: Variation of temperature slip with grid resolution for $\varepsilon_g = 0.8$.

recollect the details of the flux emissivity model explained in Chapter 1. This is a simple model for longwave radiation which assumes the absorption coefficient to be a function of optical path length only, unlike more sophisticated models (e.g., the present band model) where it is a function of pressure, temperature, wave number and optical path length. The flux emissivity model used by VSN is that of Liou and

Ou (1981), which is described in detail in the next Chapter (equation 6.9). This model is basically derived by making a fit to laboratory data while band models are validated against line-by-line models.

We can see that there is a difference of 6.75 K in slip with $\varepsilon_g = 0.8$ and $\beta = 0$ between the two models. It therefore appears that $T(0+)$ is estimated differently in the two models. Tests with T_g prescribed should illuminate the problem (see Appendix E). We shall therefore first study how sensitive the cooling rate is to changes in ground temperature.

With the present model, variation of surface cooling rate with ground temperature for an isothermal atmosphere ($T_0 = 300$ K) for $\varepsilon_g = 0.8$ and 1.0 is shown in Figure 5.5. In this case a black surface ($\varepsilon_g = 1.0$) produces larger cooling/heating rate compared to $\varepsilon_g = 0.8$ for the corresponding ground temperature. For a departure of 5 K from the ground temperature of 300 K, the cooling or heating produced is more than 6000 K/d. It is to be noted that the flux emissivity model by VSN model produces a surface cooling rate of 1728 K/d for an isothermal atmosphere at $\varepsilon_g = 0.8$. The corresponding ground temperature for the present model is 297.0 K to produce the same cooling rate for an isothermal atmosphere (300 K). This shows the sensitivity of cooling rates to ground temperature. Figure 5.6 shows the variation of $SCR/\Delta T$ (ratio of surface cooling rate to temperature slip) with ground emissivity. Again the range of variation of $SCR/\Delta T$ ($0-600$ d⁻¹) is larger for $\varepsilon_g = 1.0$ than for 0.8.

Figure 5.7 shows the variation of cooling rate with altitude for an isothermal atmosphere (300 K) with the present code for different ground temperatures (297, 298 and 300 K) and varying ground emissivity. For a ground temperature of 298 K, the increase in cooling is 146 times the value of cooling rate when T_g is 300 K with $\varepsilon_g = 0.8$ and 1458 times for $\varepsilon_g = 1.0$ at the surface. The cooling rates for this case are respectively 1042 K/d and 1294 K/d. In all cases where the ground temperature

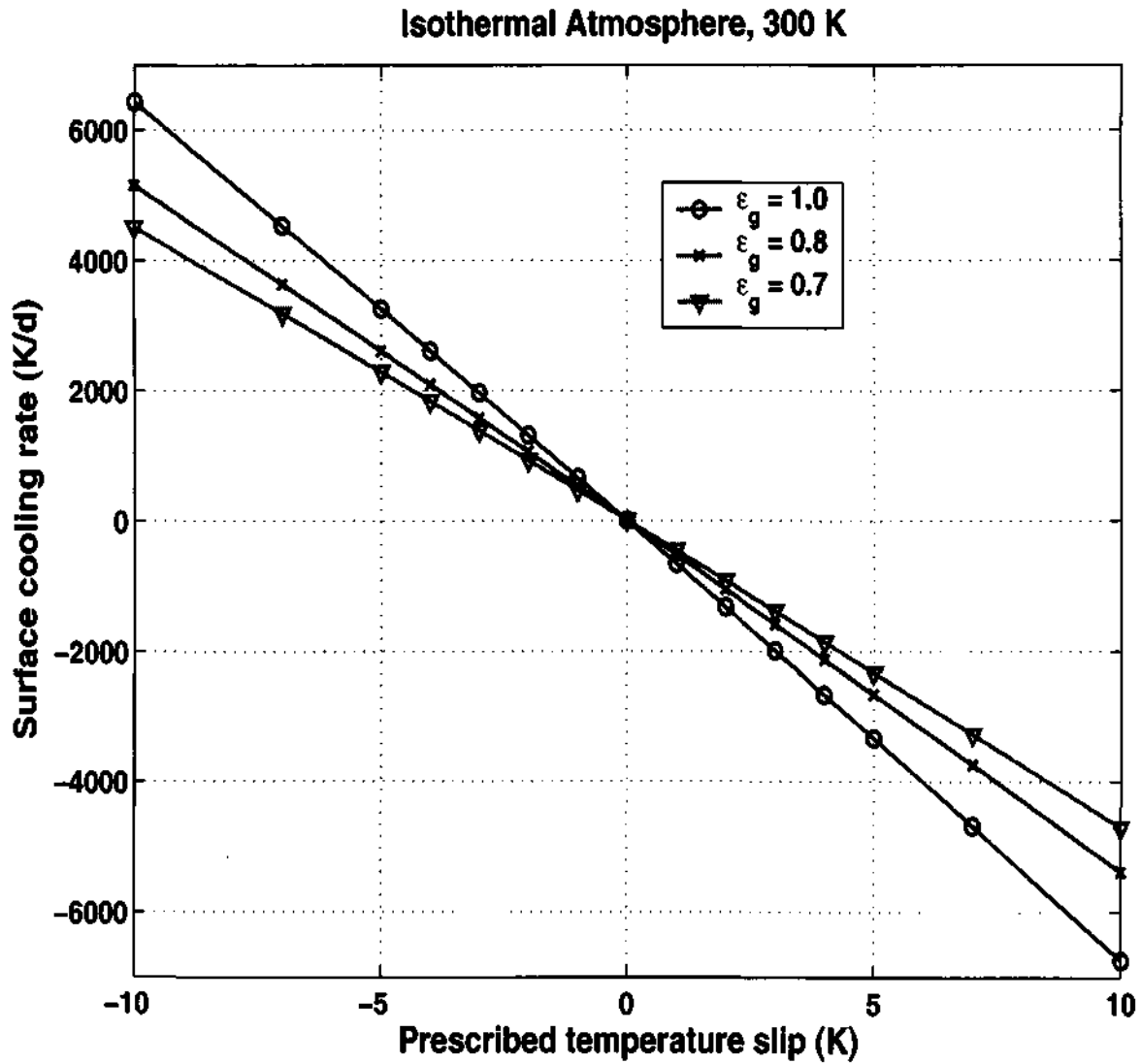


Figure 5.5: Variation of surface cooling rate with prescribed temperature slip.

is less than 300 K, cooling rates are high for $\epsilon_g = 1.0$ compared to $\epsilon_g = 0.8$. From Figure 5.7 the effect of the small variation in ground temperature is seen only upto around 100 m, after which the atmospheric cooling is not affected considerably.

Figures 5.8 and 5.9 show the variation of spectral cooling rate with altitude for the same isothermal atmosphere (300 K) with $T_g = 297$ K and 298 K respectively. As seen in Figure 5.7, the cooling rates are not substantially altered after 100 m. It

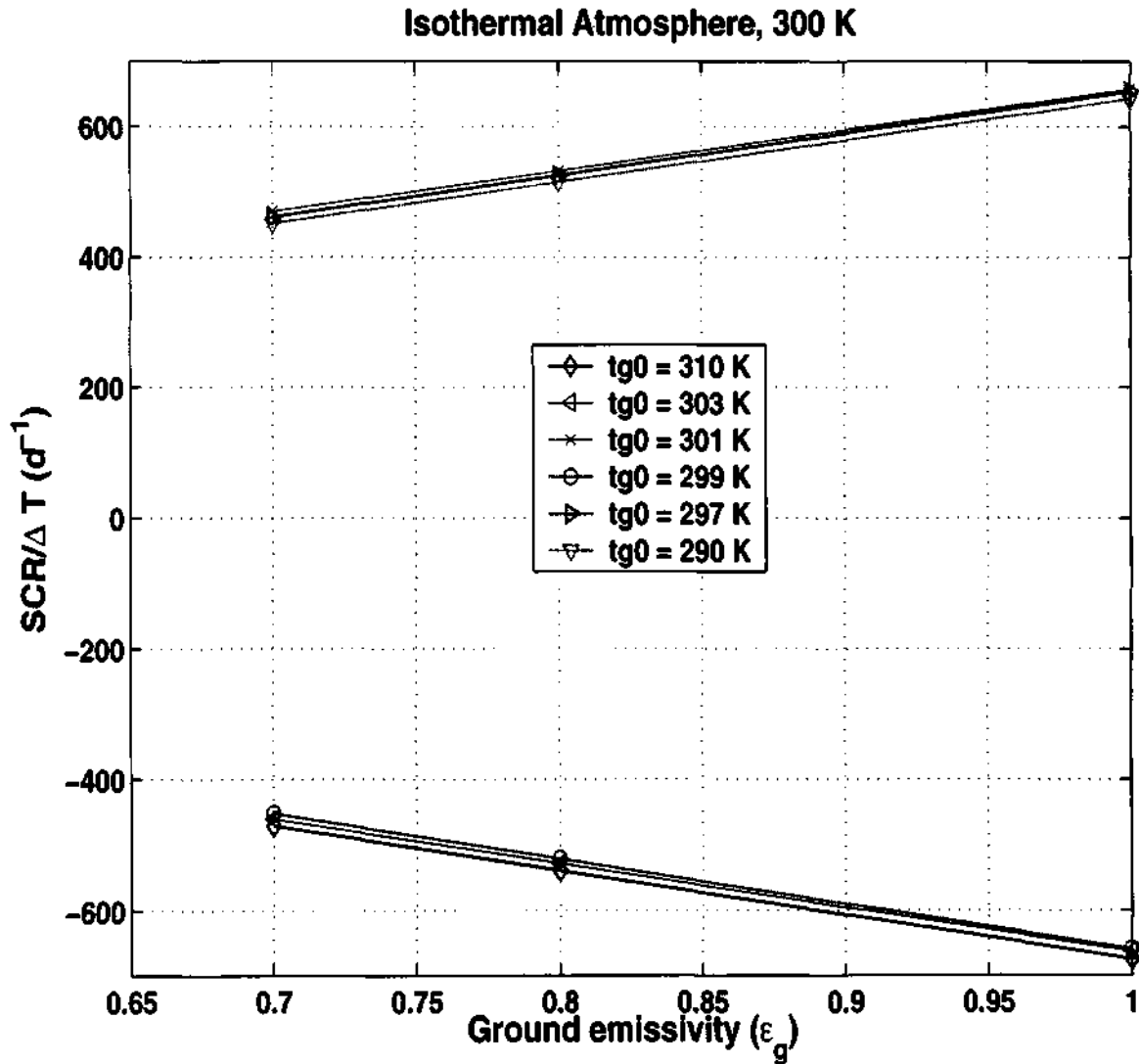


Figure 5.6: Variation of $SCR/\Delta T$ with ground emissivity.

appears that surface cooling is more sensitive to changes in ground temperature than to ground emissivity. Moreover, a black surface appears to produce larger cooling than a non-black surface when the ground temperature is decreased, as we have already inferred from Figure 5.7.

Figures 5.10 and 5.11 which show spectral cooling for an MLS atmosphere

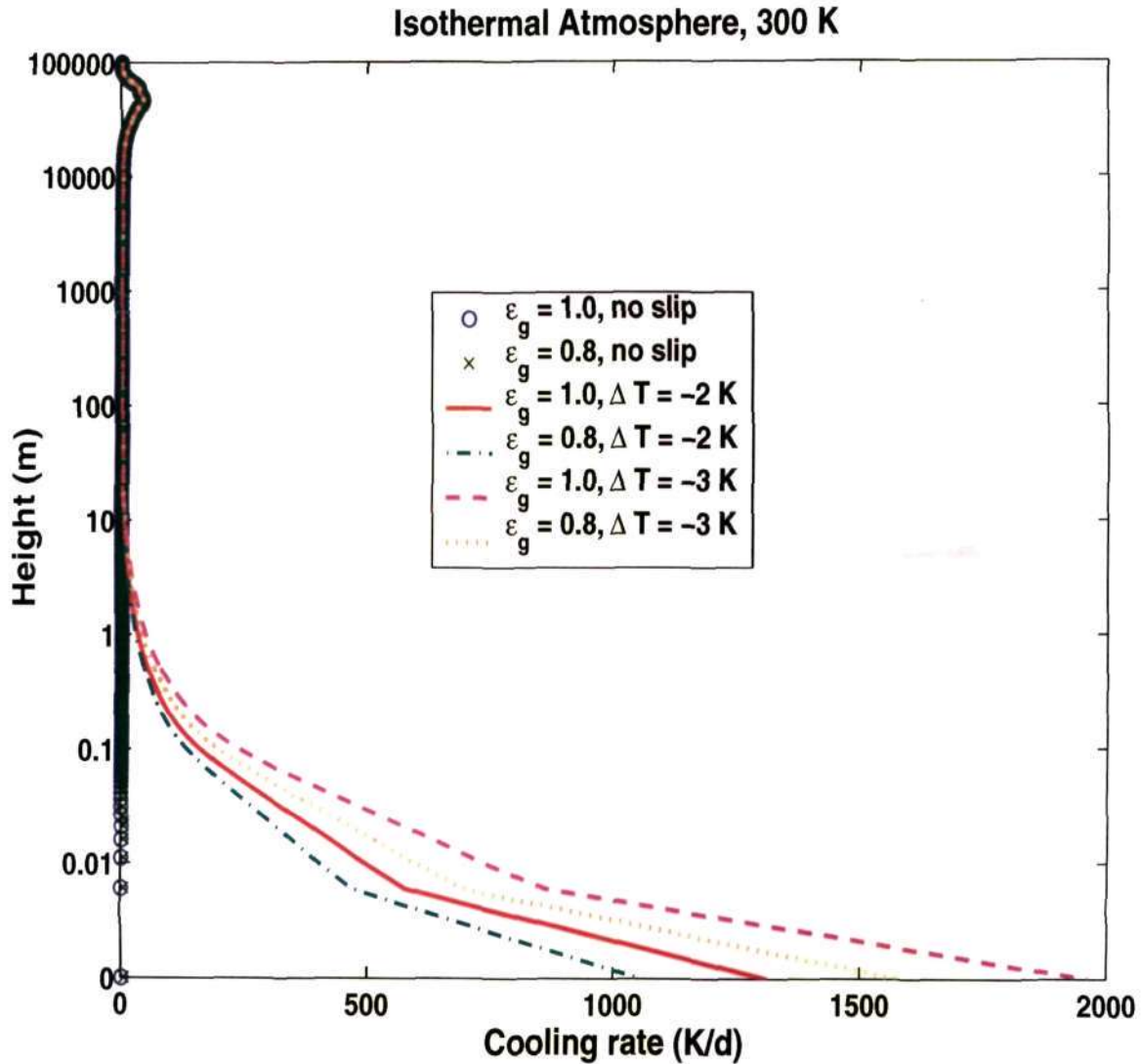


Figure 5.7: Variation of cooling rate with height for different temperature slip and ground emissivity.

with $T_g = 292$ K and $T_g = 291$ K which is less by 2 K and 3 K respectively from the standard value of 294 K. As in the previous cases ground temperature changes produce high cooling near the surface upto 100 m in all spectral regions except in the window region. Again the cooling rates are higher for $\epsilon_g = 1.0$ than $\epsilon_g = 0.8$. The major contribution for the increased cooling appears to come from either side

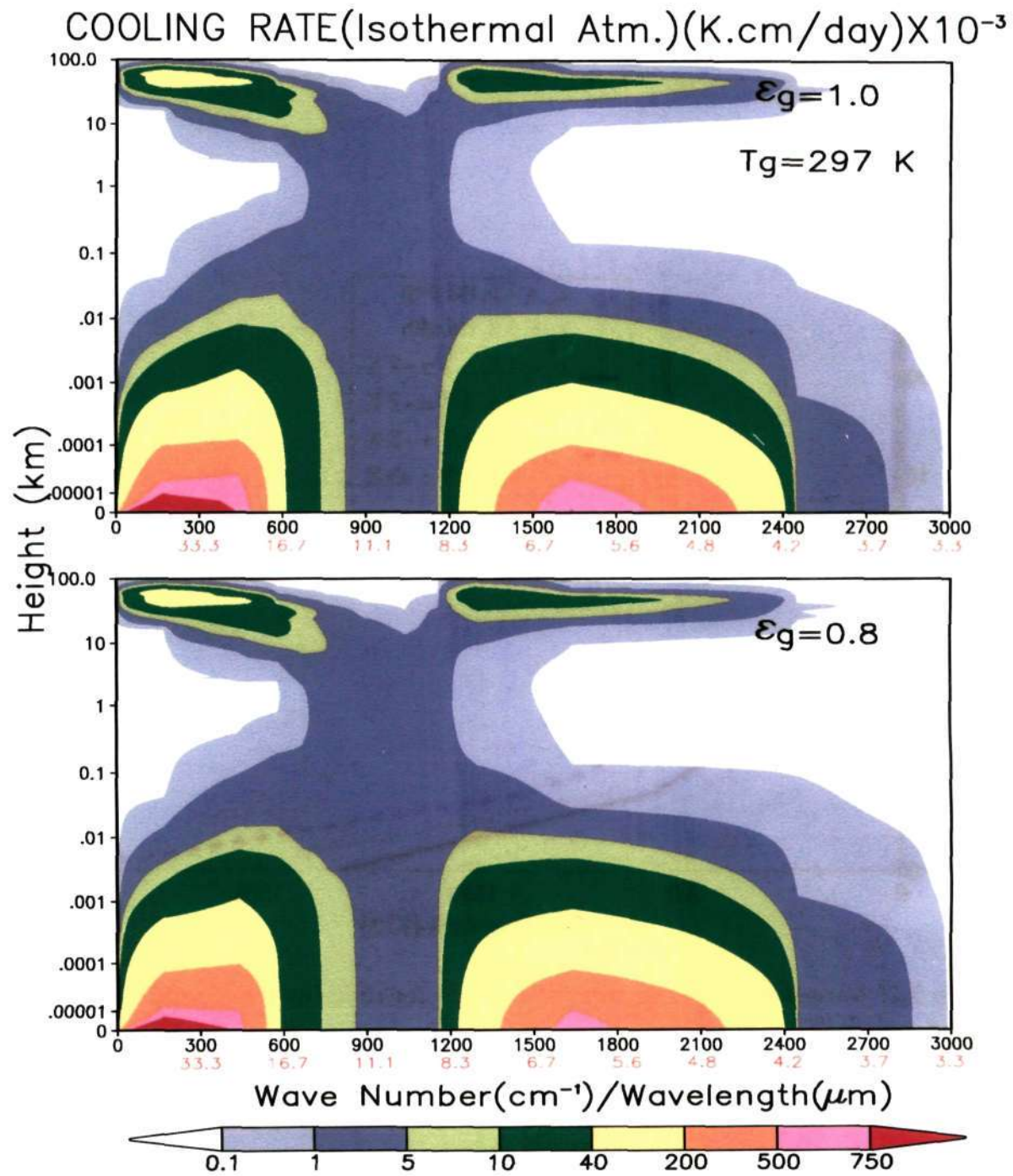


Figure 5.8: Spectral distribution of cooling rate for an isothermal atmosphere (300 K) with temperature slip of 3 K.

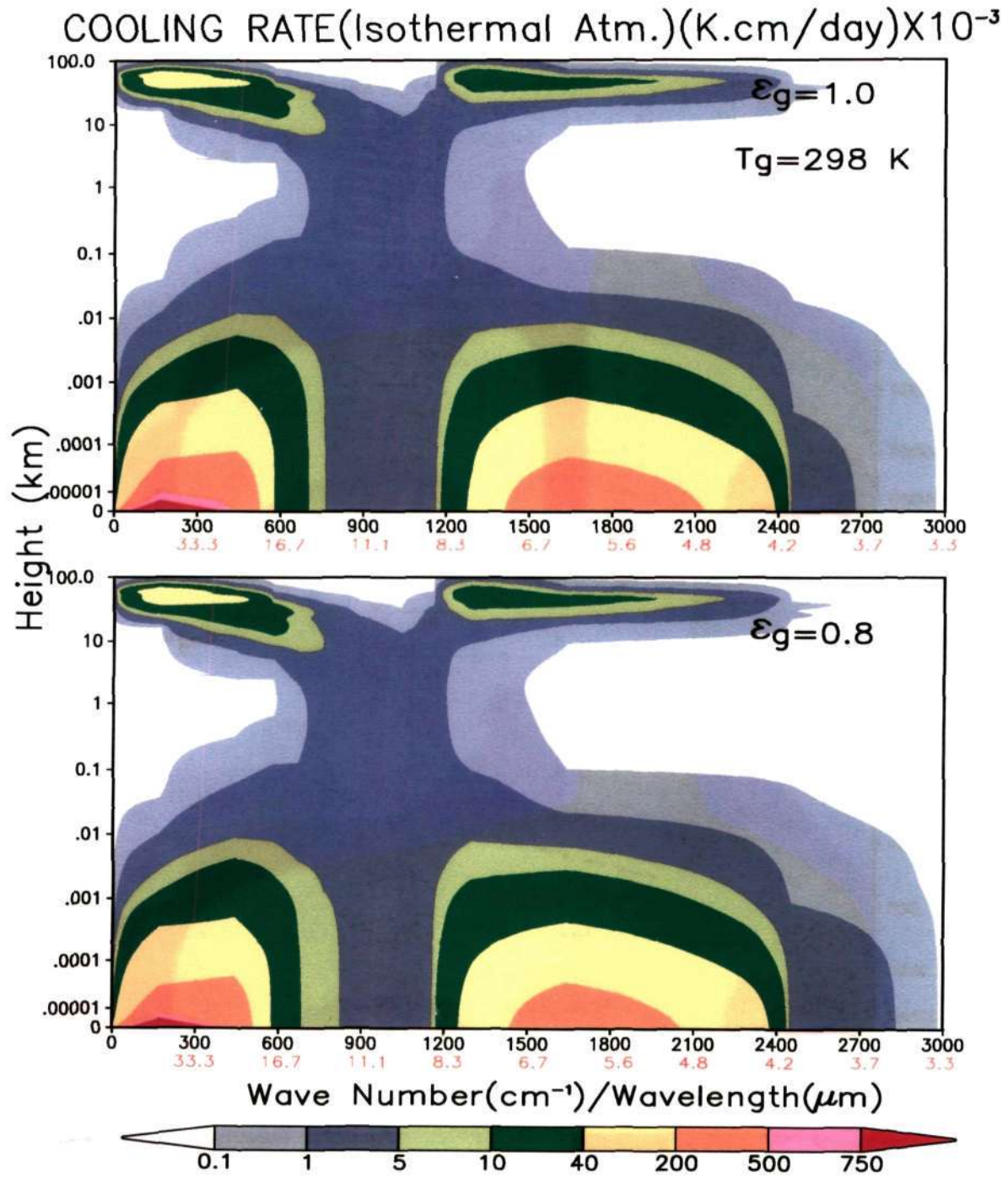


Figure 5.9: Spectral distribution of cooling rate for an isothermal atmosphere (300 K) with temperature slip of 2 K.

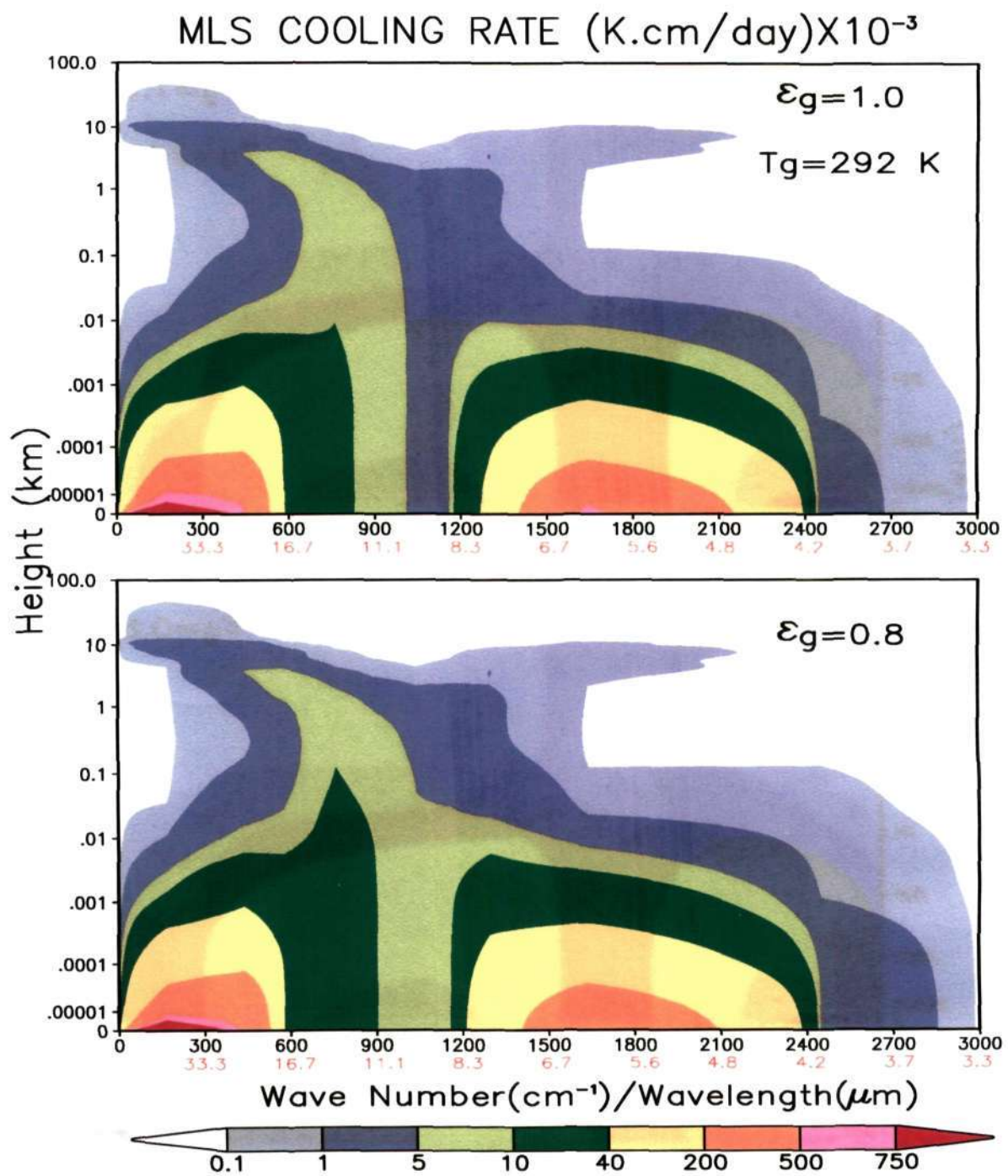


Figure 5.10: Spectral distribution of cooling rate for MLS atmosphere with temperature slip of 2 K.

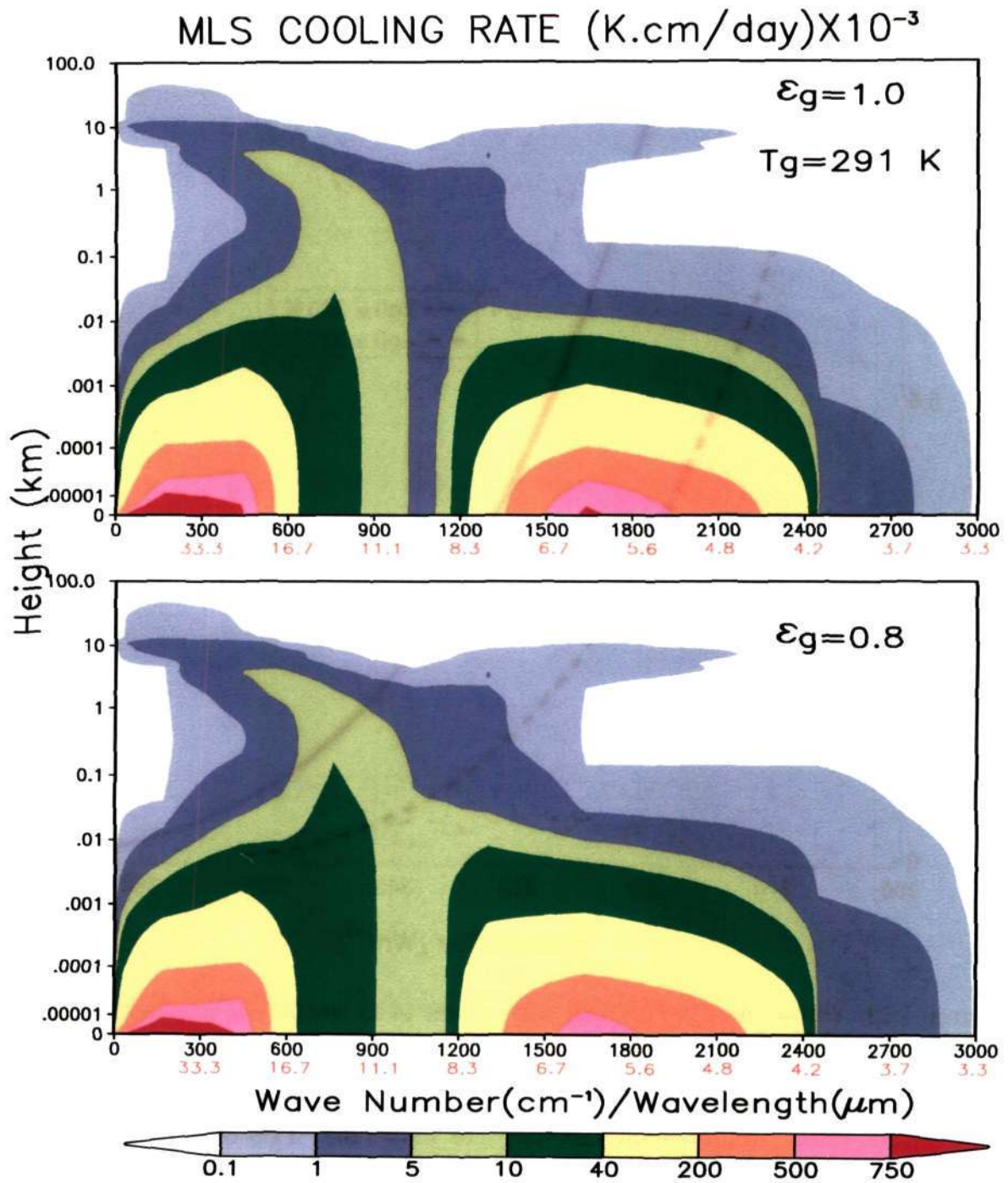


Figure 5.11: Spectral distribution of cooling rate for MLS atmosphere with temperature slip of 3 K.

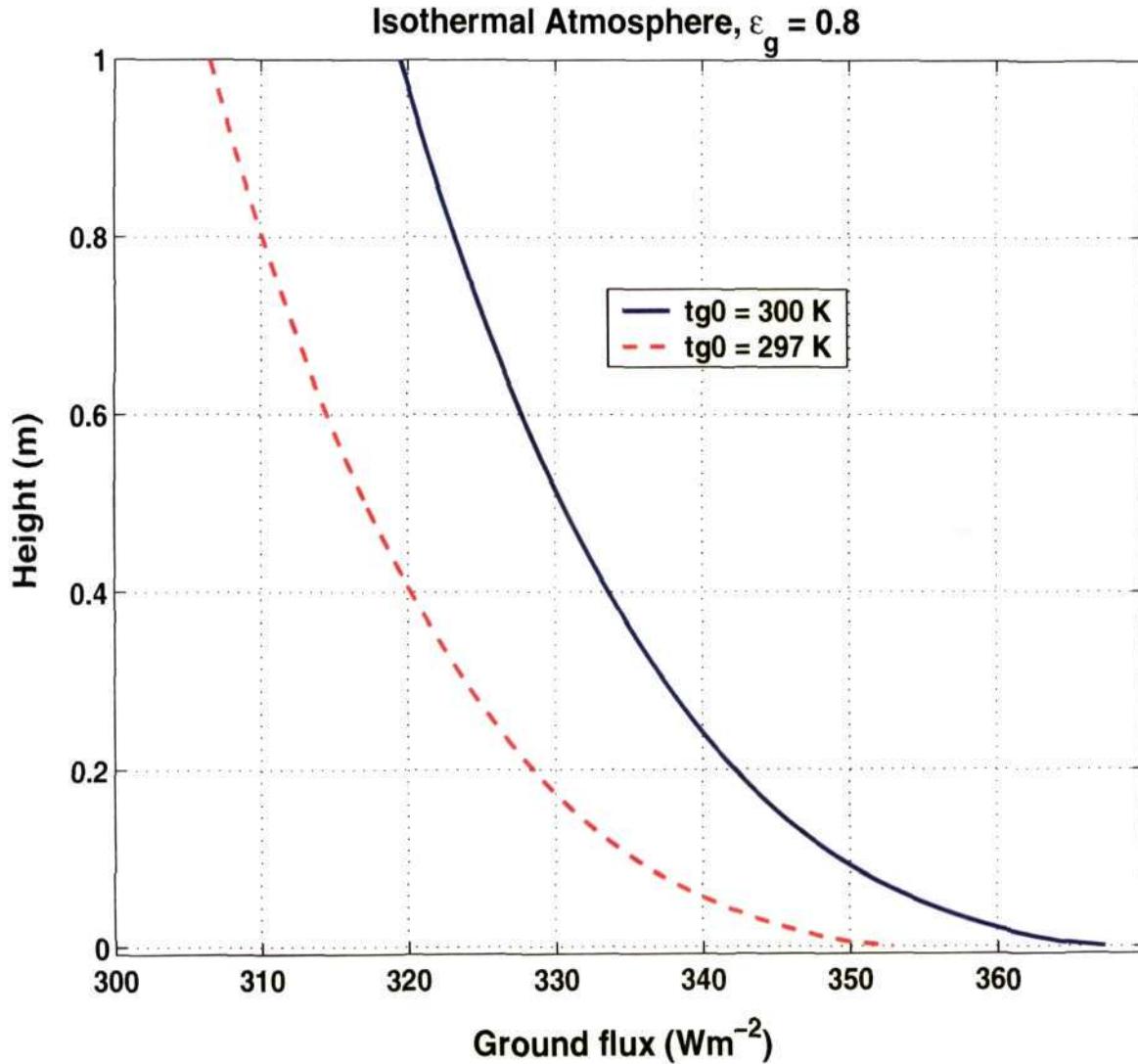


Figure 5.12: Variation of ground flux with height in an isothermal atmosphere (300 K) for ground temperatures 300 K and 297 K.

of the atmospheric window ($800\text{--}1200\text{ cm}^{-1}$ or $8\text{--}12\text{ }\mu\text{m}$). This can be inferred by comparing Figure 4.3 in Chapter 4 (which shows the standard case where T_g is not altered) with Figures 5.10 and 5.11.

Now let us examine in detail the origin of the high cooling rate with the introduction of a slip. In the experiments conducted for the case of isothermal atmo-

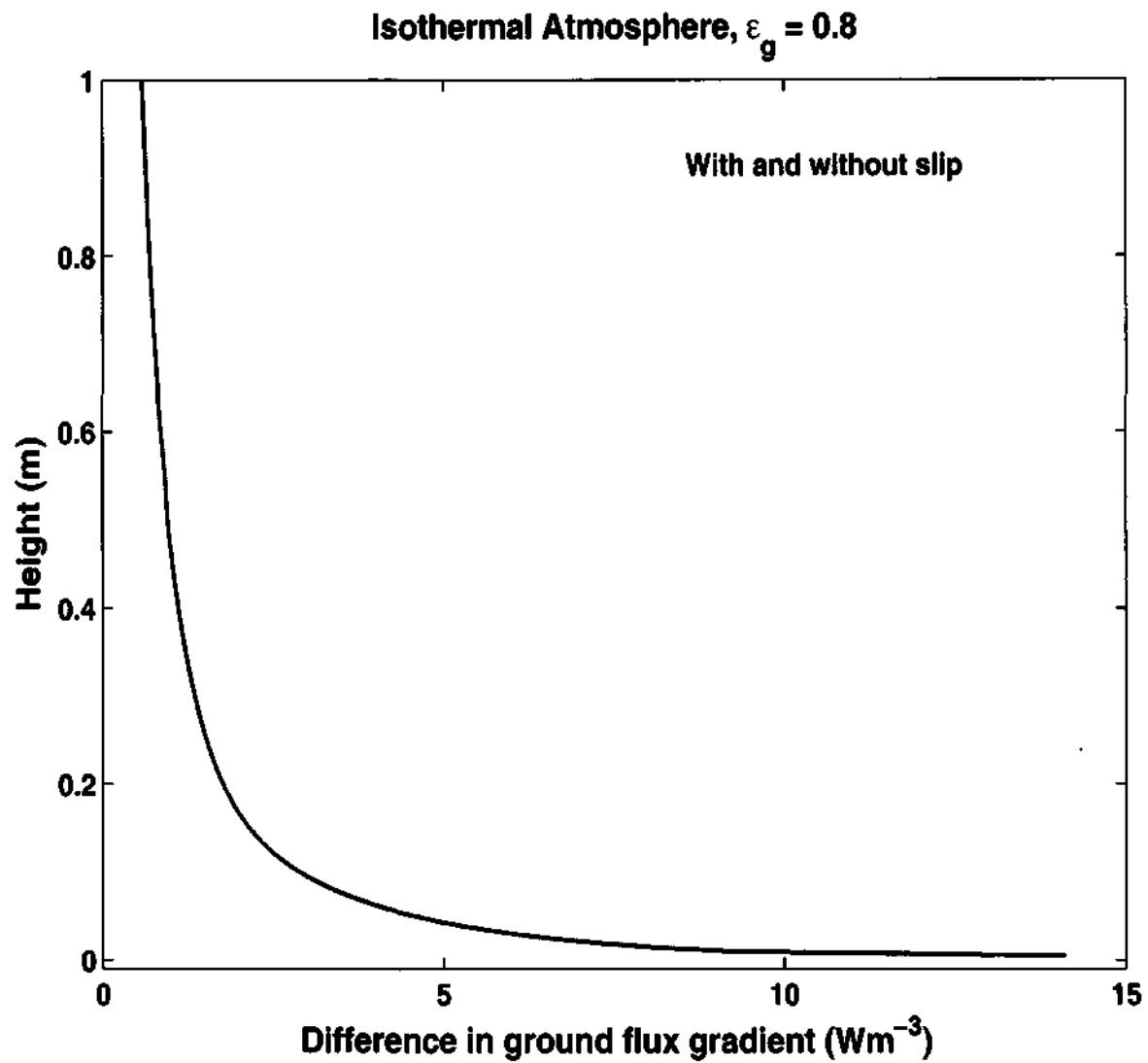


Figure 5.13: Difference in ground flux gradient (with and without temperature slip), ground temperatures being 300 K and 297 K.

sphere (300 K), with and without a slip, we found no changes in the total downward fluxes. Moreover the air emission term and the reflected component of the downward flux also remained the same. The only difference found were in the ground emission term. Figure 5.12 shows the variation in ground emission alone in the first 1 m. Figure 5.13 shows the difference in variation of ground emission gradient in the

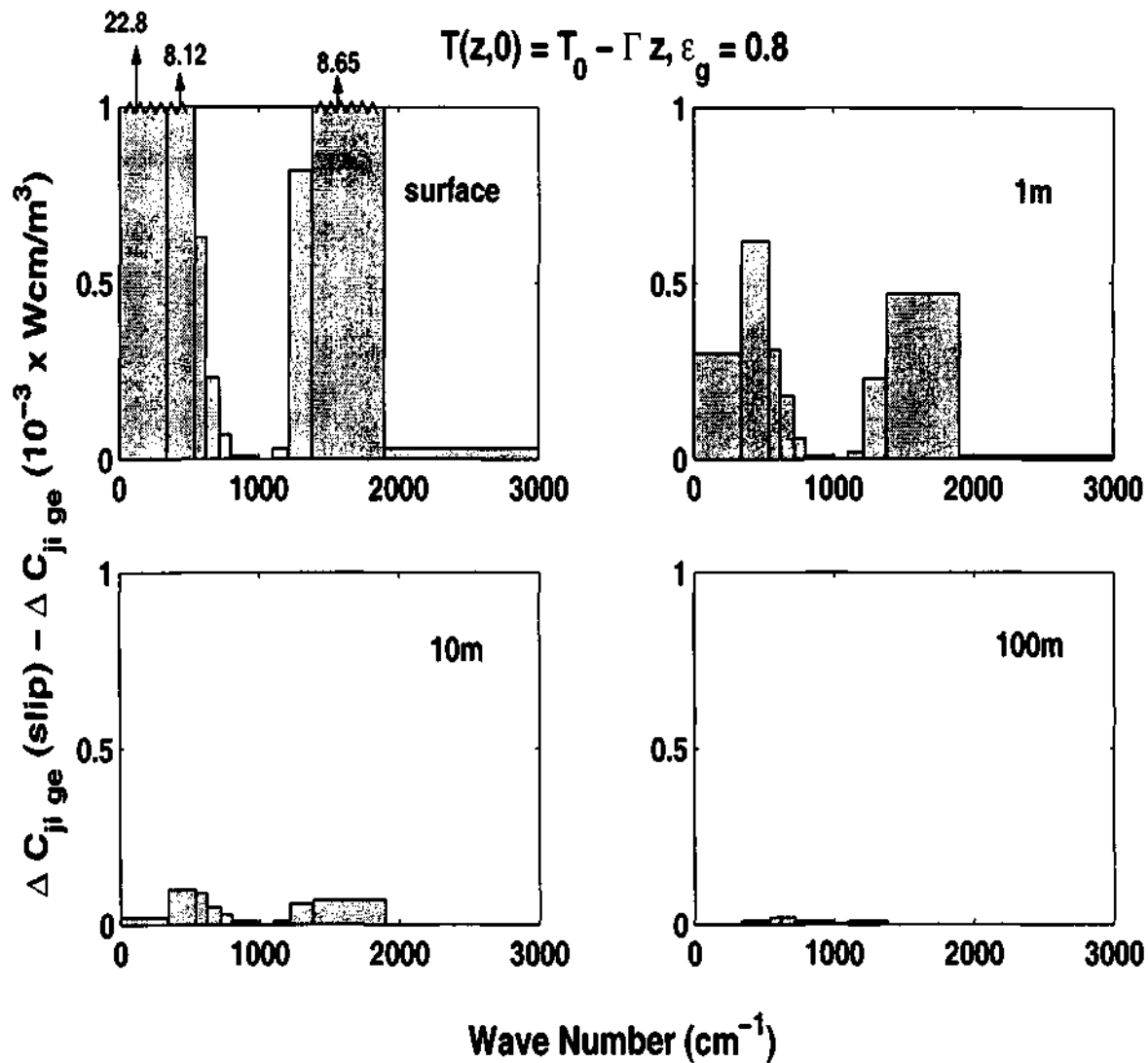


Figure 5.14: Spectral distribution of difference in ground emission gradient (with and without slip) for different heights, $T = T_0 - \Gamma z$.

same region. A huge gradient can be seen in the first 20 cm from the surface. The spectral variation of the same is shown in Figure 5.14. The major contributing bands are seen on either side of the atmospheric window, the first band being the largest contributor. Therefore it can be concluded that in the case of a discontinuity at the ground-air interface, most of the cooling originates due to the strong variation of the

ground emission term in the region close to the surface.

Results show that the cooling rate is highly sensitive to small changes in ground temperature. Slight tinkering of this input variable which produces an initial slip produces very large cooling rates. It also shows that huge temperature slips evolve in course of time. Therefore from the present analysis it follows that the ground temperature is the most influential parameter in determining near-surface cooling rates.

In the next Chapter, results of simulation of lifted temperature minimum with the present model are shown and discussed along with the LTM results obtained with an artificial slip.

Chapter 6

Simulation of Lifted Temperature Minimum with the Present Code

As stated in Chapter 1, one of the objectives of this work is to simulate the LTM using the present code. We have already reviewed the previous work related to the Ramdas layer and the VSN theory in Chapter 1. Here an attempt is made to simulate the Ramdas layer using the VSN physical model but replacing the infrared radiation scheme based on the flux emissivity method by the present code. The formulation of the problem and method of solution are discussed in detail by VSN. However a brief description of the VSN model is given below before we proceed to describe the present work.

6.1 VSN Model

Calm, clear nights with no advection, and a surface of bare soil, are considered in the VSN model. Wind profile, soil temperature variation and the humidity content of the air are incorporated into the model as parameters that can be prescribed. However, the soil temperature can, if necessary, be computed independently through a coupled air-soil model which is also formulated in VSN (1993). But it was shown that, for purposes of gaining insight into the phenomenon, it was adequate to use an approach where the ground temperature is prescribed as a function of time. This approach

has the advantage of providing a more immediate physical interpretation. Horizontal homogeneity is assumed so that the air temperature is a function only of time and of vertical distance z from the ground surface.

With these assumptions the governing equation for the problem, expressing energy balance, can be written as

$$\rho_a C_p \frac{\partial T}{\partial t} = \frac{\partial Q}{\partial z}, \quad (6.1)$$

where ρ_a is the density of air, C_p is the specific heat at constant pressure and T is the air temperature. Q is the total energy flux, split into three components,

$$Q = Q_m + Q_t + Q_r \quad (6.2)$$

where Q_m , Q_t and Q_r are the contributions from conduction, convection and infrared radiation respectively. Q_m is given by

$$Q_m = -K_m \frac{\partial T}{\partial z} \quad (6.3)$$

where K_m is the molecular conductivity of air. Q_t is given by

$$Q_t = -K_t \frac{\partial \theta}{\partial z}, \quad \theta = T + \Gamma z \quad (6.4)$$

where K_t is the eddy conductivity, θ is the potential temperature and Γ is the prescribed constant lapse rate in the free atmosphere. The eddy conductivity is taken to be

$$K_t = \rho_a C_p u_* k_* z \phi(\text{Ri}) \quad (6.5)$$

where u_* is the friction velocity, k_* is the Karman constant and $\phi(\text{Ri})$ is a stability function which, following Liou and Ou (1981), is taken as

$$\begin{aligned} \phi(\text{Ri}) &= 1.35(1 - 9\text{Ri})^{-1/2} \quad \text{for } \text{Ri} \leq 0, \\ &= 1.35(1 + 6.35\text{Ri})^{-1} \quad \text{for } \text{Ri} > 0, \end{aligned} \quad (6.6)$$

Ri being the Richardson number

$$\text{Ri} = \frac{k_*^2 g z^2}{u_*^2} \frac{\partial \theta}{\partial z}. \quad (6.7)$$

The inclusion of eddy diffusion by VSN (1993) allowed them to assess the role of turbulence in the phenomenon and to account for any residual turbulence left in the atmosphere.

The radiative flux Q_r is given by

$$Q_r = F^\uparrow - F^\downarrow \quad (6.8)$$

where F^\uparrow and F^\downarrow are the upward and downward radiative fluxes respectively. The radiative fluxes were modelled using the broadband flux emissivity method (Liou 1980, Liou and Ou 1983). In this model the fluxes are taken as

$$\begin{aligned} F^\downarrow &= \int_u^{u_\infty} \sigma T^4(u', t) \frac{d\epsilon}{du'} (u' - u) du', \\ F^\uparrow &= \left\{ \epsilon_g \sigma T_g^4(t) + (1 - \epsilon_g) F^\downarrow \right\} \{1 - \epsilon(u)\} \\ &\quad - \int_0^u \sigma T^4(u', t) \frac{d\epsilon}{du'} (u - u') du', \end{aligned} \quad (6.9)$$

where u is the water vapour mass path length given by

$$u(z) = \int_0^z \rho_w(z') \left\{ \frac{p(z')}{p(0)} \right\}^\delta dz', \quad (6.10)$$

$\rho_w(z)$ denotes the density of water vapour at level z , $p(z)$ is the pressure of air at level z and $u_\infty = u(\infty)$ is the total atmospheric path length. The exponent δ is chosen to be 0.9 following Garratt and Brost (1981). ϵ_g is the ground emissivity, $T_g(t)$ is the ground temperature and $\epsilon(u)$ is the broadband flux emissivity function of water vapour, which is taken as

$$\epsilon(u) = 0.0492 \ln(1 + 1263.5u) \quad \text{for } u \leq 10^{-2} \text{ kg m}^{-2}$$

$$= 0.05624 \ln(1 + 875u) \quad \text{for } u > 10^{-2} \text{ kg m}^{-2} \quad (6.11)$$

following Zdunkowski and Johnson (1966). With the contribution from molecular conduction, convection and radiation modelled along these lines, the problem is completed using the initial and boundary conditions,

$$\begin{aligned} T(z, 0) &= T_{g0} - \Gamma z \\ T(0, t) &= T_{g0} - \beta\sqrt{t} \\ \frac{\partial T}{\partial z}(\infty, t) &= -\Gamma. \end{aligned} \quad (6.12)$$

Details of the validity of these boundary conditions can be obtained from VSN (1993).

6.6 Validation of Code for Time Evolution

To make sure that the results from the present code for time evolution are reliable, it is useful, where possible, to validate it against an exact solution. In the present study, radiation and diffusion codes have been validated separately. The following two sub-sections give more details of the validation.

6.6.1 Validation of Radiation Code

To validate the radiation code, an isothermal atmosphere (300 K) was considered as the initial condition with $\varepsilon_g = 0.8$ and the rest of the initial parameters being the same as in the VSN model. A forcing term derived was used to correct the temperature changes during time evolution. Figures 6.1 and 6.2 show the error in temperature after five hours of evolution for two different heights. A maximum error of around 2.3×10^{-3} K was found at a height of ~ 5 cm.

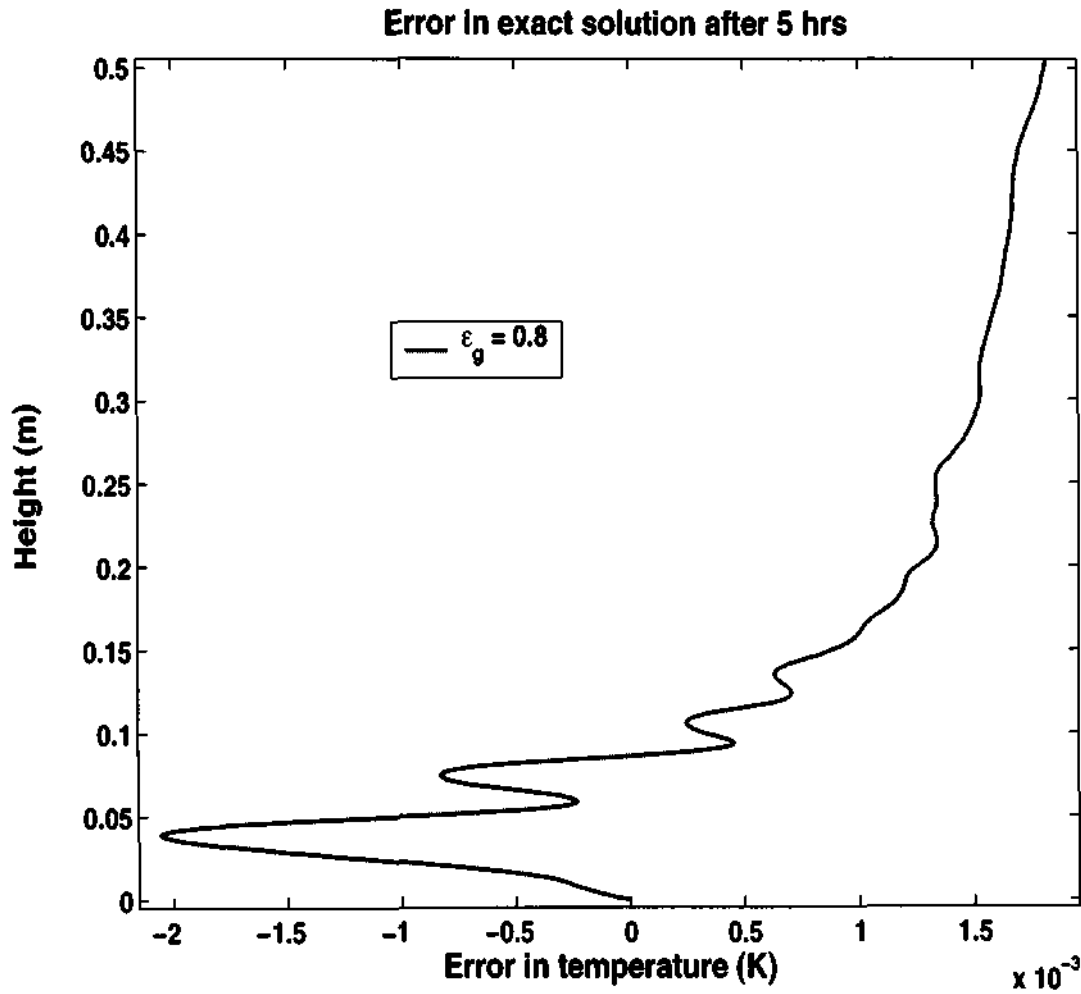


Figure 6.1: Error in the radiation code for an exact solution at $t = 5$ h.

6.6.2 Validation of Diffusion Code

The diffusion code was validated with an exact solution. The diffusion equation can be written as:

$$\frac{\partial T}{\partial t} = K_m \frac{\partial^2 T}{\partial z^2} + f(z, t), \quad (6.13)$$

where $f(z, t)$ is the forcing term.

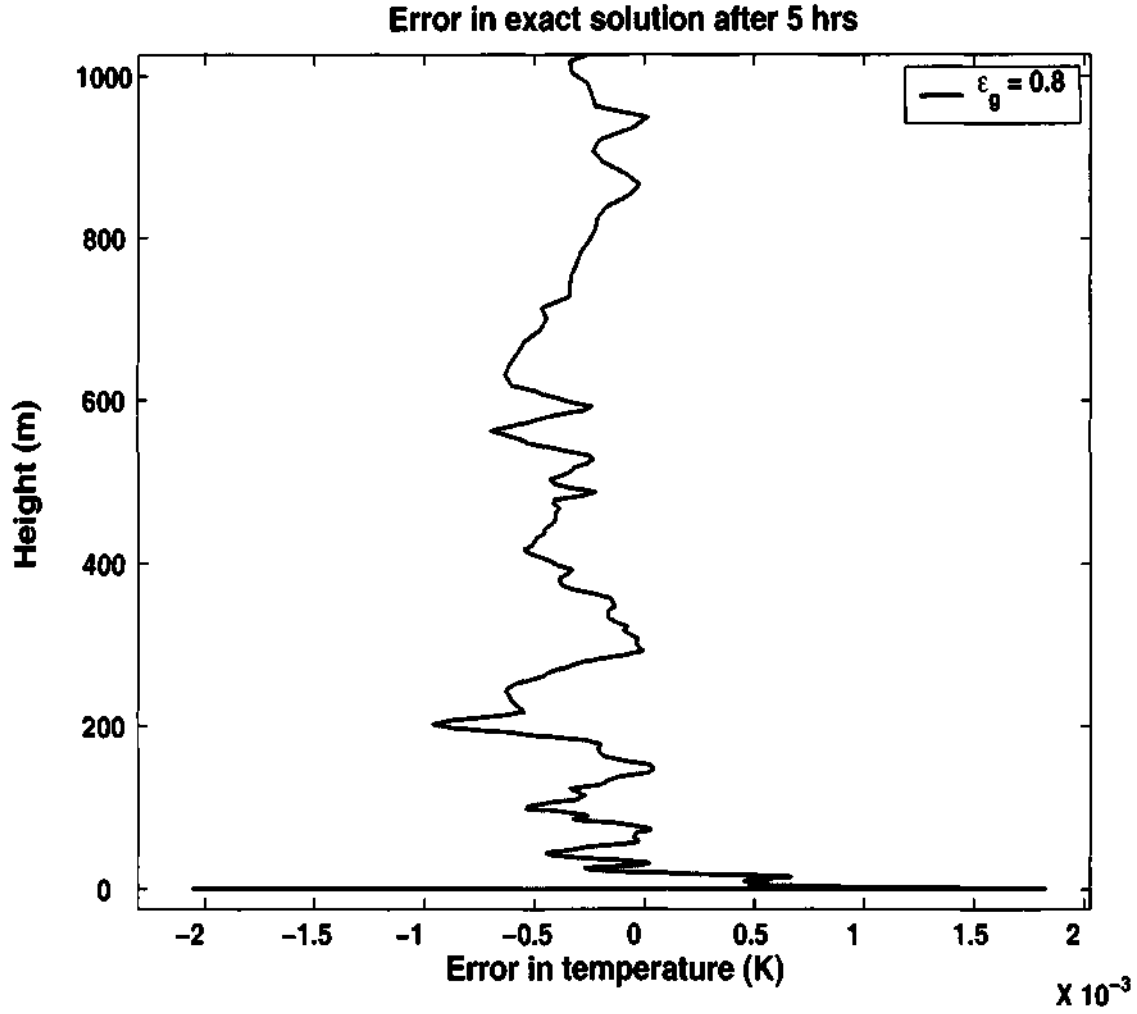


Figure 6.2: Variation of error in the radiation code upto a height of 1 km with an exact solution, $t = 5$ h.

The boundary conditions used are:

$$\begin{aligned} T(z, 0) &= e^{-z} \\ T(0, t) &= e^{-t} \\ \frac{\partial T}{\partial z}(0, t) &= 0. \end{aligned} \tag{6.14}$$

Here

$$\frac{\partial T}{\partial z}(L, t) = e^{-L-t}, \tag{6.15}$$

L is taken to be 2 km and $K_m = 10^{-5}$ m²/s. To satisfy the stability criterion $\Delta t \leq \Delta z^2/2K_m$ (Fletcher, 1988), a time step of 10^{-5} s was considered.

If we take

$$f(z, t) = -e^{-z-t} - K_m e^{-z-t} \quad (6.16)$$

the solution is

$$T(z, t) = e^{-z-t} \quad (6.17)$$

Figure 6.3 shows the difference between computation and exact solution after 10^6 time-steps. Errors in temperature are mostly seen in the first 15 m from the surface. The maximum error occurs at a height of around 5 m and the value is $\sim 6.5 \times 10^{-6}$ K.

6.2 Simulation with the Present Band Model

As convection is not a necessary condition for the formation of the LTM, it is ignored in the simulations, which were carried out for the pure radiation case and for both radiation and molecular diffusion, which are known to play major roles in the evolution of LTM (VSN, 1993). For the studies reported here, the present band model (which is described in detail in Chapter 2) for long wave radiative transfer calculations has been incorporated into the VSN model, replacing the broadband flux emissivity scheme. In the simulation of LTM, only water vapour absorption is considered, although carbon dioxide is included in the present code and can be considered if necessary. Unlike the flux emissivity model in which an empirical fit is made to the optical path length, the present model takes the absorption coefficient as a function of pressure, temperature, wave number and optical path length; there are fewer approximations, and the model is validated against line-by-line and ICRCCM results as already described in Chapter 3.

Figures 6.4 and 6.5 show the simulation results with the present model

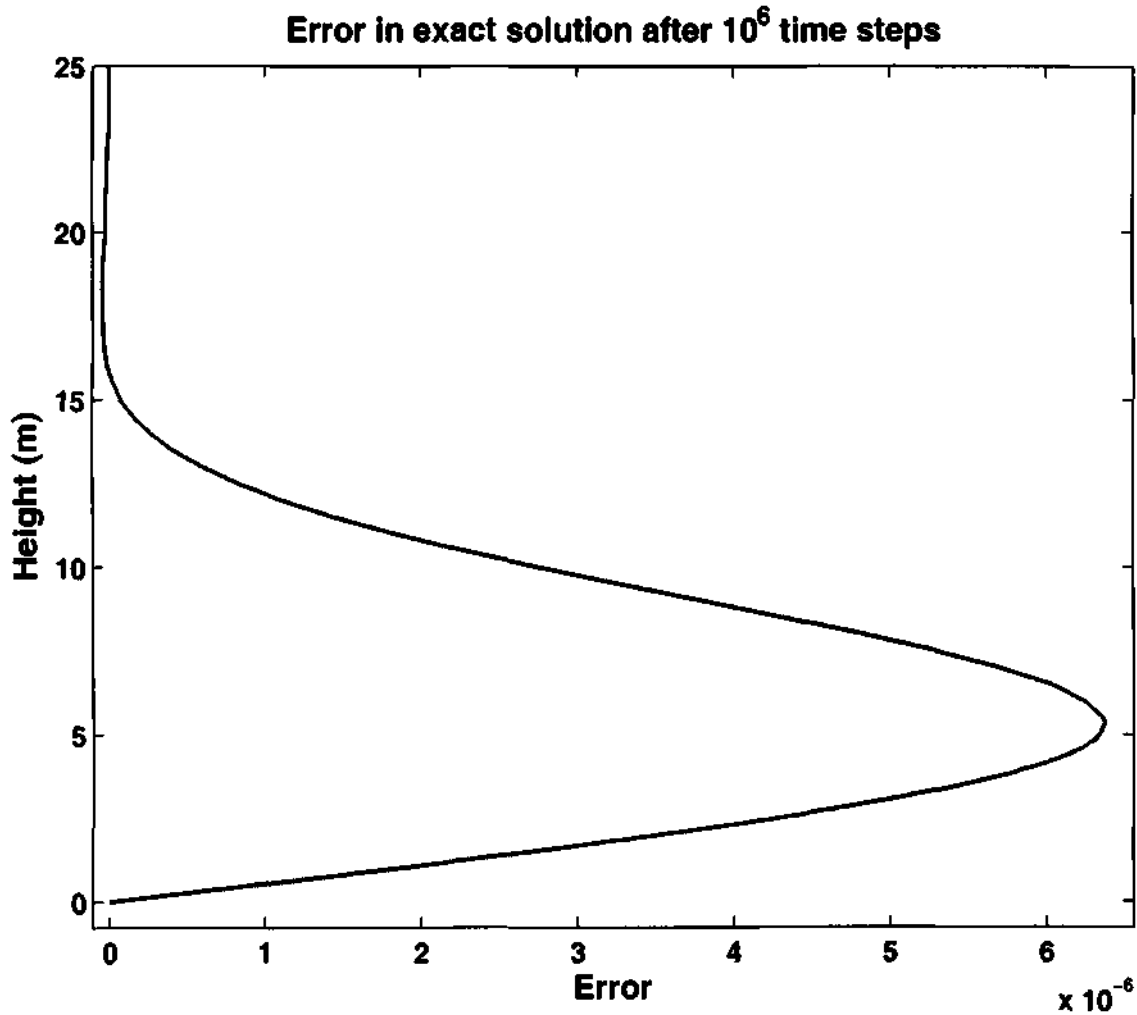


Figure 6.3: Error in diffusion code for an exact solution after 10^6 time steps.

for pure radiation with $\epsilon_g = 0.8$ and $\beta = 0$ and $2 \text{ K hr}^{-1/2}$ respectively. The flux emissivity model produces a slip of 7 K after 1 hour for $\epsilon_g = 0.8$ and $\beta = 0$ while the present band model produces 0.25 K as already seen in Chapter 5. For $\beta = 0 \text{ K hr}^{-1/2}$ the temperature slip does not appear to grow substantially. Even after 4 hours of evolution after sunset, the slip produced is just 0.42 K. When $\beta = 2 \text{ K hr}^{-1/2}$, the growth in temperature slip is slow and negative as can be seen in Figure 6.5. Therefore the large temperature slip seen from flux emissivity model is absent in the

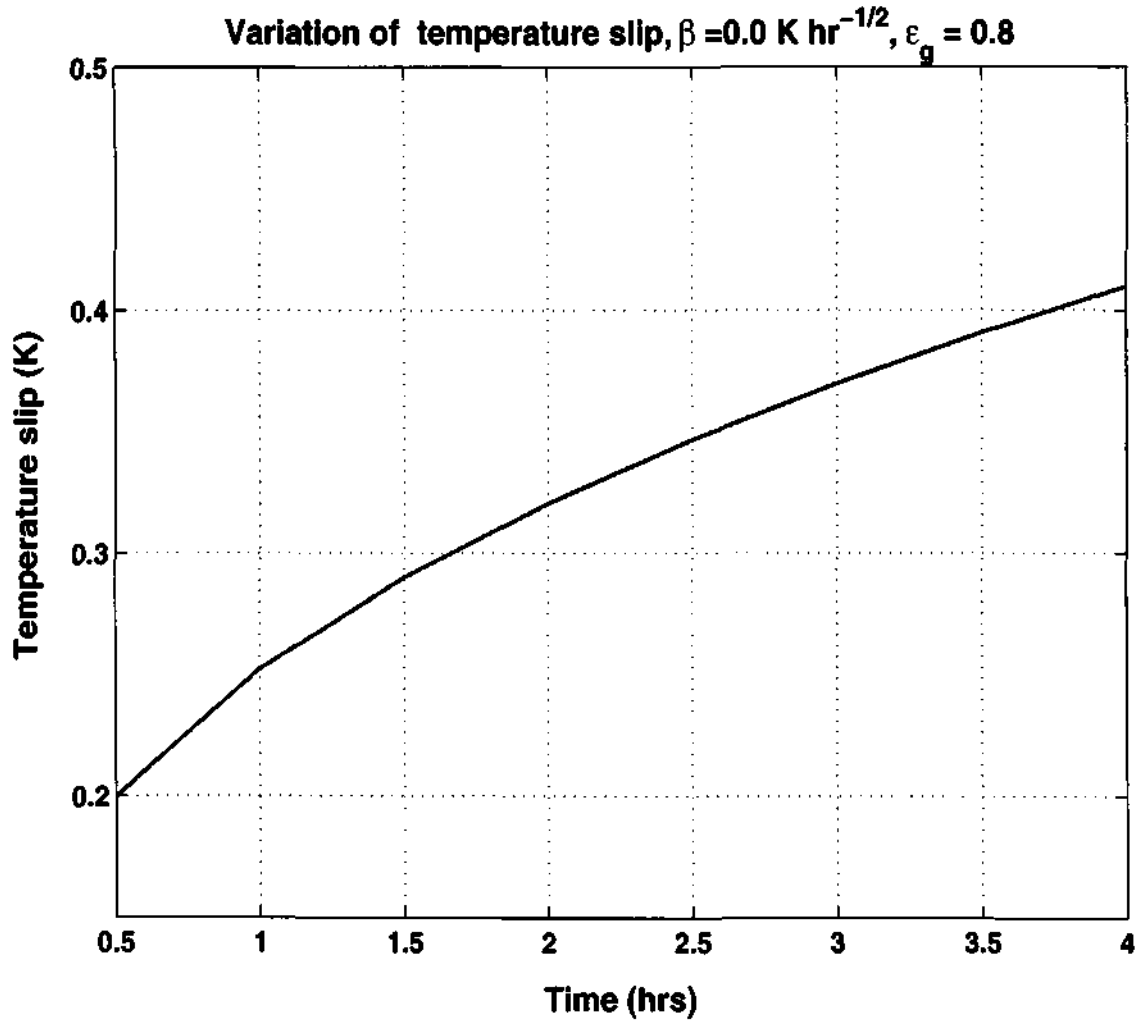


Figure 6.4: Temperature slip evolution for $\epsilon_g = 0.8$ and $\beta = 0.0 \text{ K hr}^{-1/2}$.

simulations with the present model.

Figures 6.6 and 6.7 show the results of simulation of time evolution of temperature and cooling rate with pure radiation for $\epsilon_g = 0.8$ and $\beta = 0$ respectively. In both cases time evolution was computed for a period of 1 hr. A minimum in the temperature profile is observed near the surface at around 50 cm which can be seen clearly in Figure 6.8. Such a minimum is due to the maximum cooling which occurs just above the surface (see Figure 6.9).

Figures 6.10 and 6.11 show the evolution of the temperature profile and

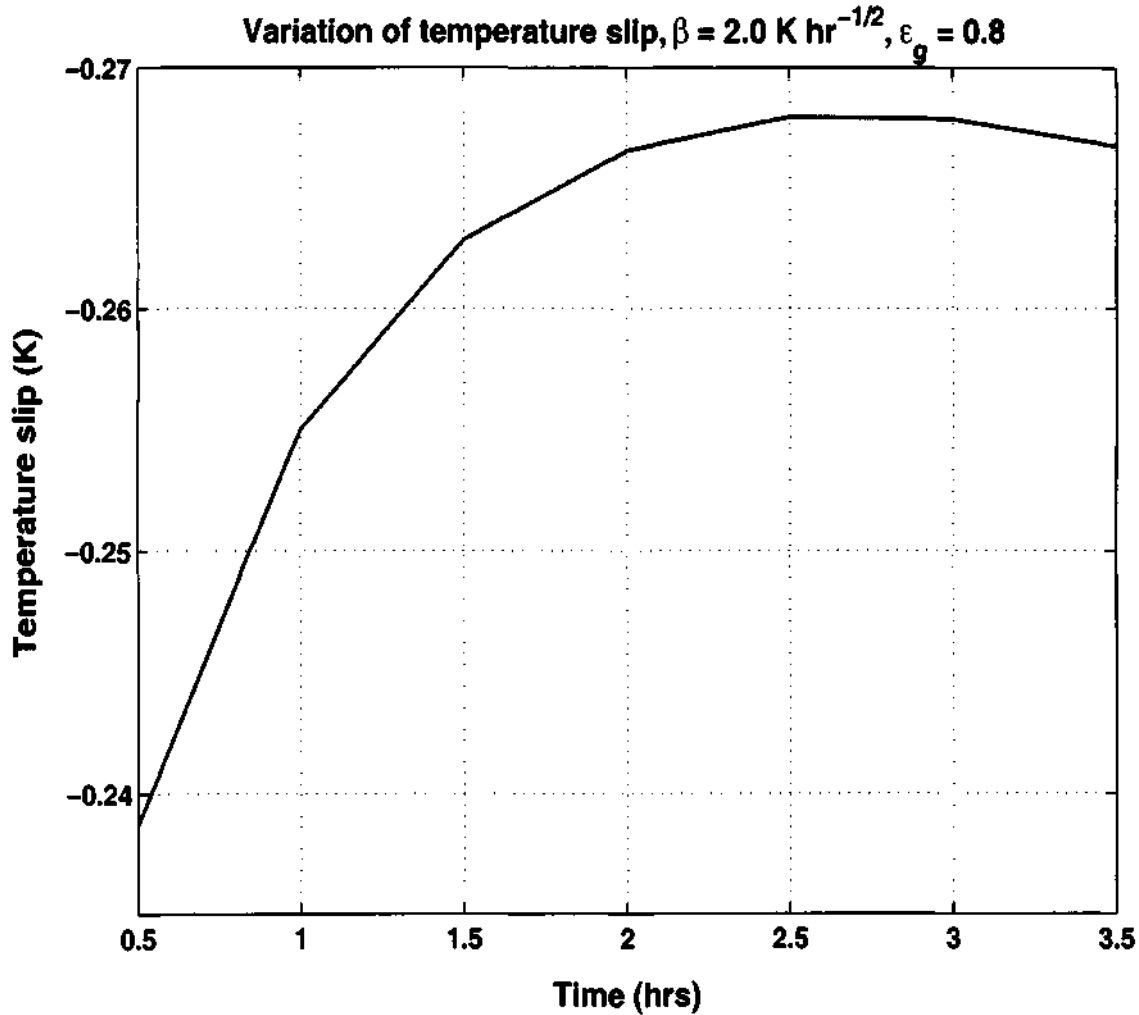


Figure 6.5: Temperature slip evolution for $\varepsilon_g = 0.8$ and $\beta = 2.0 \text{ K hr}^{-1/2}$.

cooling rate for four hours, with $\varepsilon_g = 0.8$ and $\beta = 0 \text{ K hr}^{-1/2}$ respectively, in an initial isothermal atmosphere. Again a temperature minimum which evolves with time can be seen. The minimum which was seen at a height of around 20 cm after 30 minutes from sunset is seen at height of 7.5 m at $t = 4 \text{ hr}$. Figures 6.12 and 6.13 show the temperature and cooling rate profiles respectively for the same case but plotted for a height upto 1 m.

Figures 6.14 and 6.15 show the temperature and cooling rate profile at $t = 1 \text{ hr}$ from sunset with $\varepsilon_g = 0.8$ and $\beta = 0 \text{ K hr}^{-1/2}$ for both radiation and

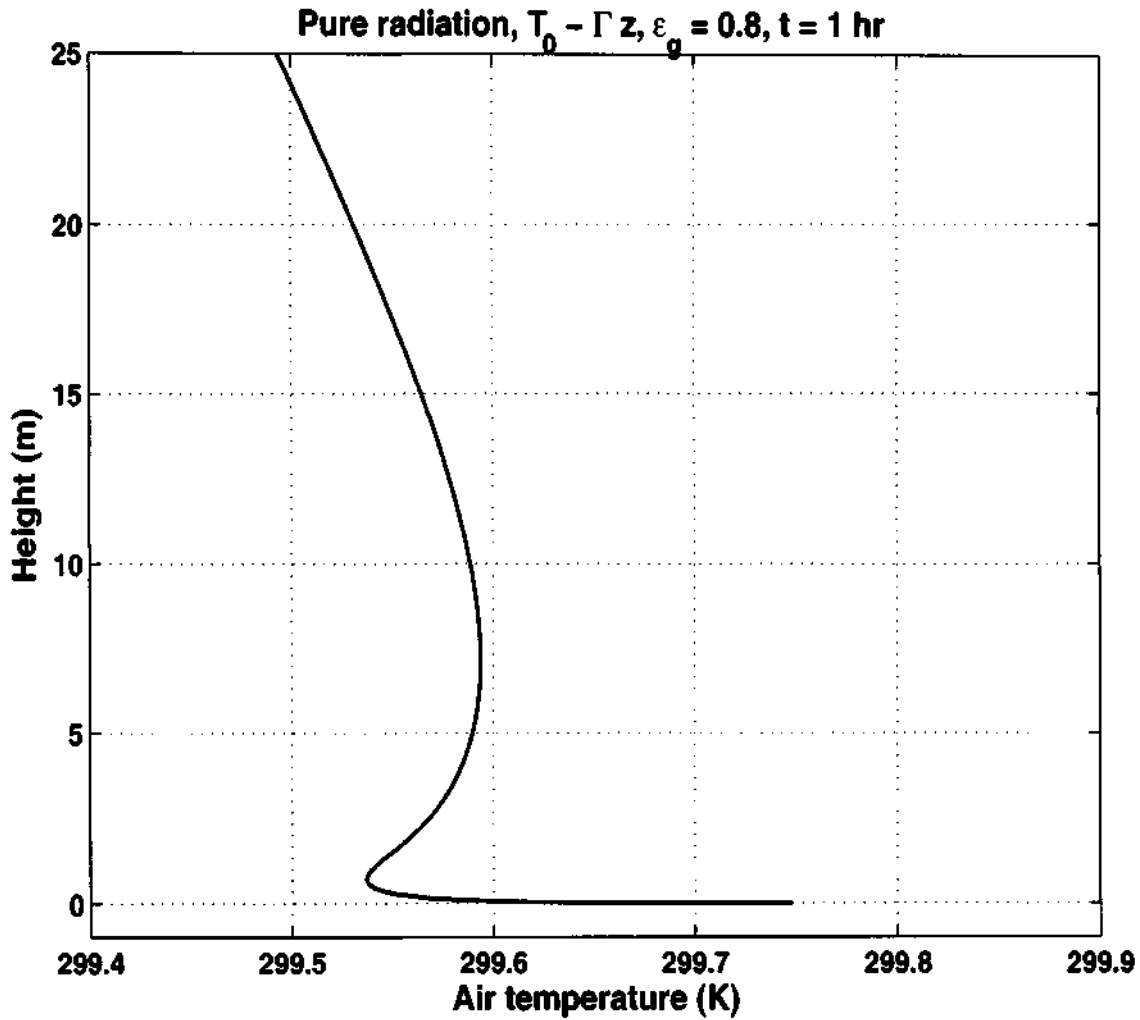


Figure 6.6: Temperature profile for a height a 25 m; pure radiation, $\varepsilon_g = 0.8$ and $\beta = 0.0 \text{ K hr}^{-1/2}$.

diffusion. An initial temperature profile of $T = T_0 - \Gamma z$ was assumed. A minimum in the air temperature is seen at a height of around 50 cm. The intensity of the minimum ($\Delta T = T_g - T_{min}$) is very weak (0.4 K) compared to that obtained from the flux emissivity model. Figures 6.16 and 6.17 show the temperature and cooling rate respectively for the same case but the height is limited to 1 m from the surface.

The effect of diffusion is shown in Figure 6.18 for the same initial conditions.

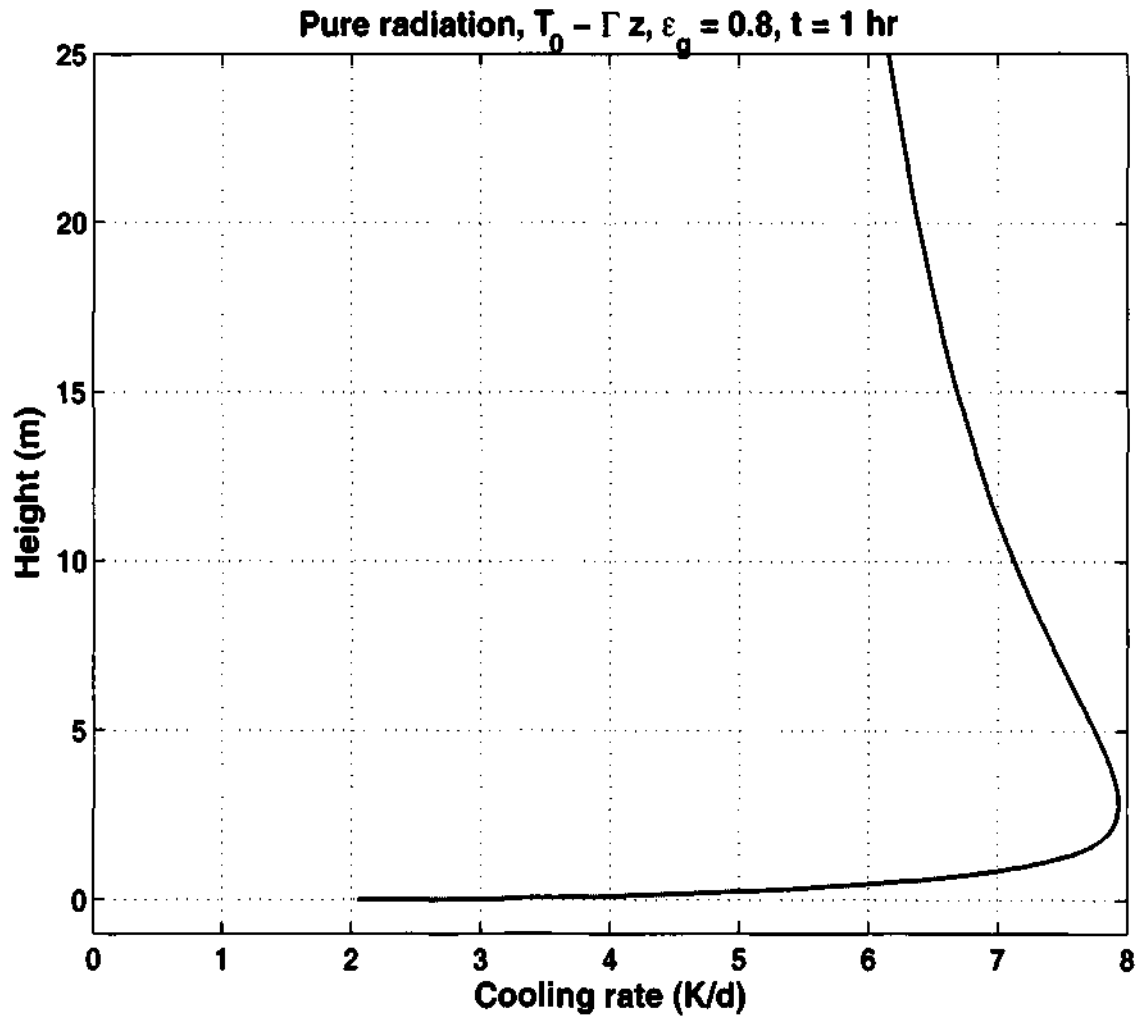


Figure 6.7: Cooling rate profile for a height a 25 m; pure radiation, $\varepsilon_g = 0.8$ and $\beta = 0.0 \text{ K hr}^{-1/2}$.

The pure radiation profile is now smoother and the effect of diffusion is noticeable up to a height of around 4 m, but the prominent effect is weak beyond a height of 1.5 m.

It is seen that the present band model does reproduce the lifted temperature minimum. The temperature slip produced by the present model is small, and its predictions for both intensity and height are lower than values typical of observation. It should be noted that flux emissivity model predicted the height and intensity in

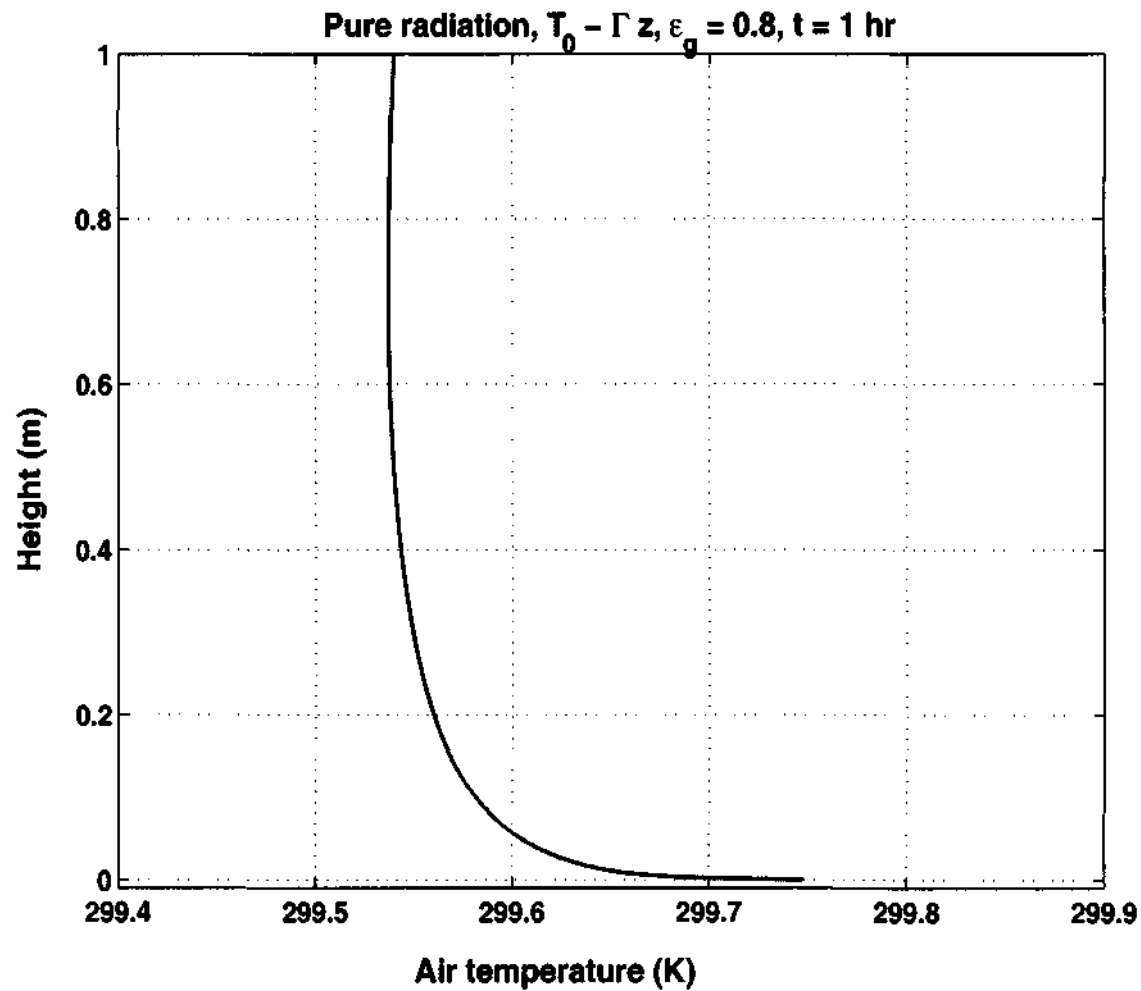


Figure 6.8: Temperature profile for a height a 1 m; pure radiation, $\epsilon_g = 0.8$ and $\beta = 0.0 \text{ K hr}^{-1/2}$.

close agreement with observations. At this juncture, it would be appropriate to discuss the origin of discrepancy in the simulated cooling rates/temperatures when the two different models are used.

The band model of Chou *et al.* (1993) is used in several numerical weather prediction and climate models. It has also been validated against line-by-line code and ICRCM results which are state of the art benchmarks for validating radiation

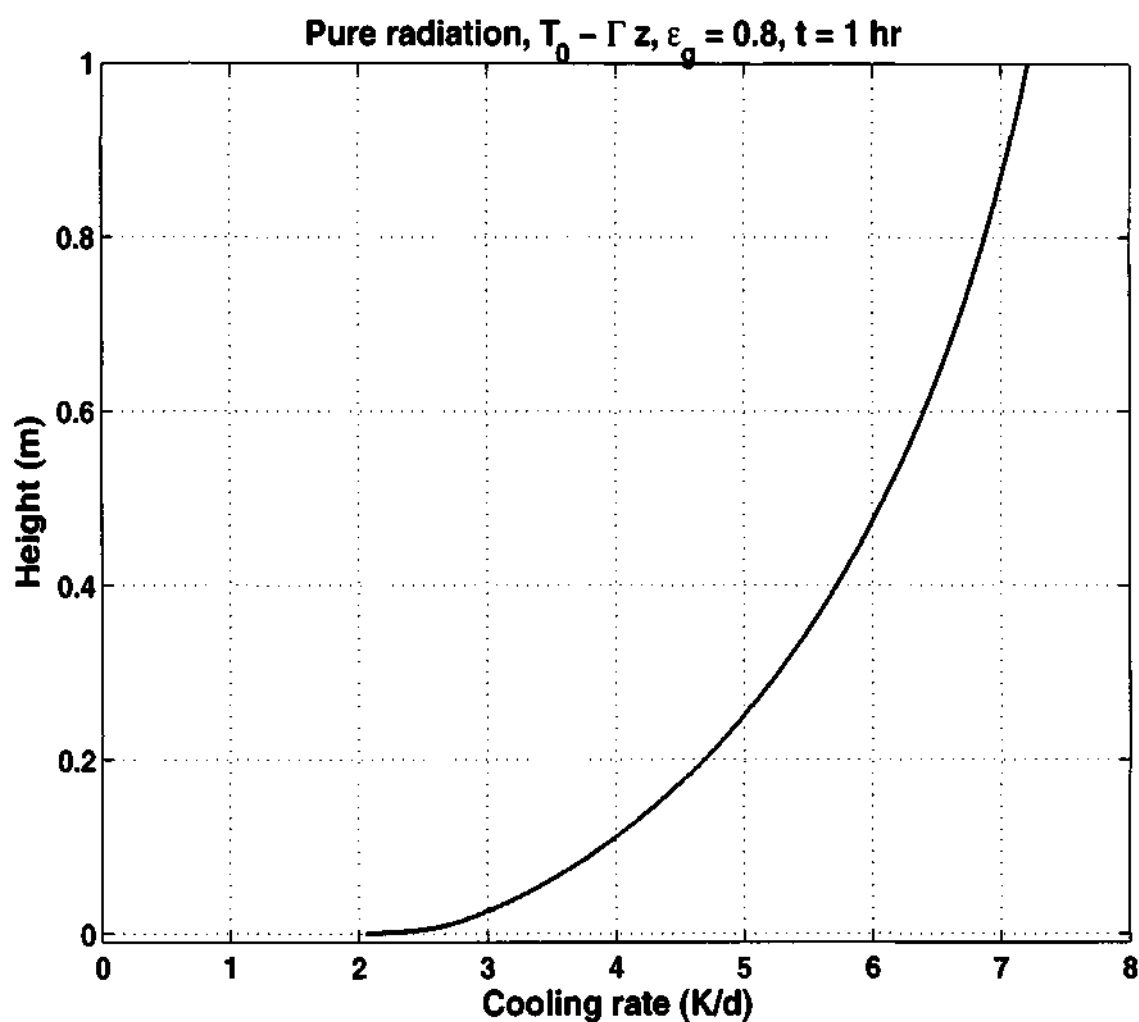


Figure 6.9: Cooling rate profile for a height a 1 m; pure radiation, $\varepsilon_g = 0.8$ and $\beta = 0.0 \text{ K hr}^{-1/2}$.

codes. The latest spectroscopic data for the absorption coefficients are used in these models. Even though the first grid point in Chou's model is at $\sim 250 \text{ m}$ from the surface, there is no reason to suspect the validity of the spectroscopic data in the first few metres from the surface.

According to Corradini and Severini (1975), computation of radiative cooling in the atmosphere based on flux emissivity method is "carried out by Brooks

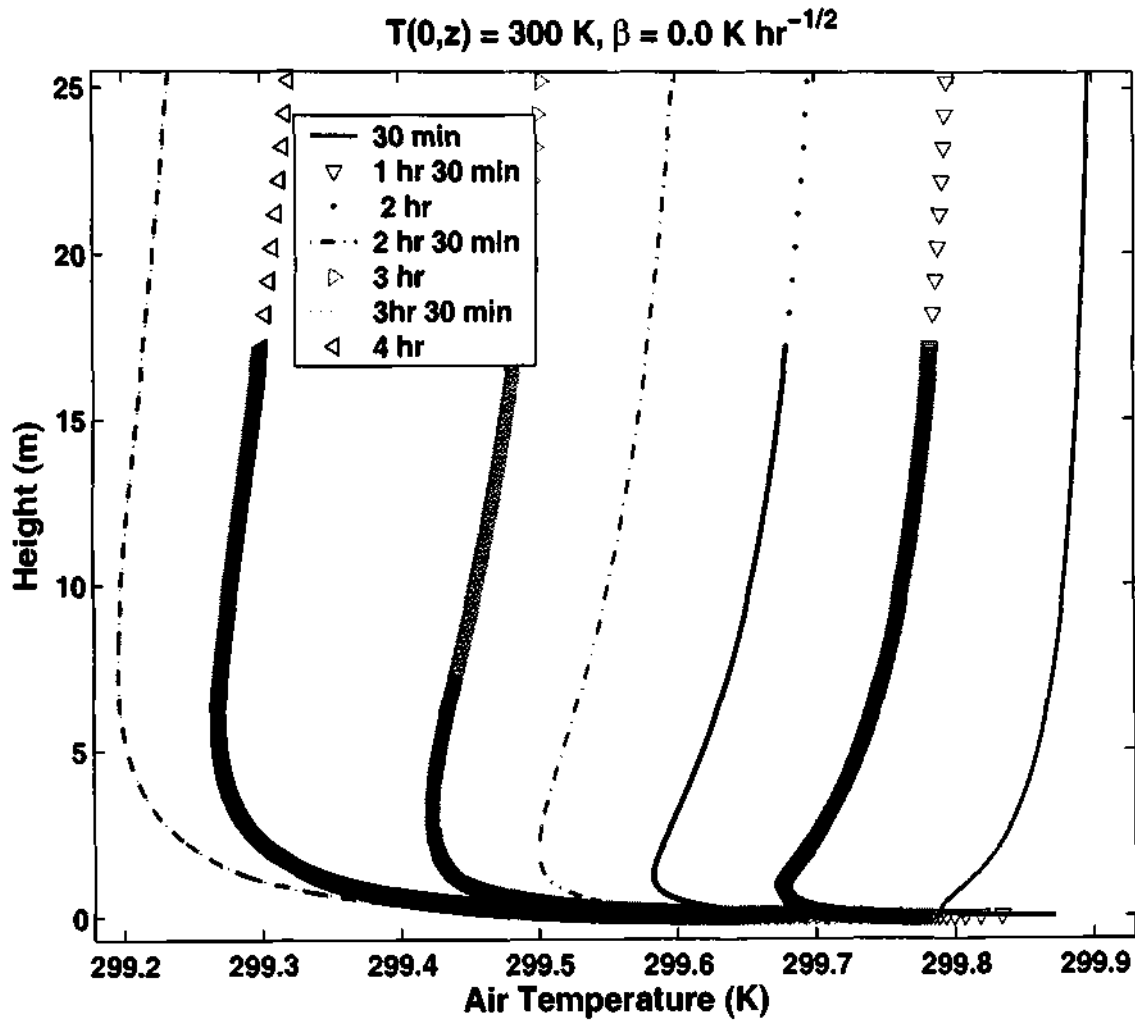


Figure 6.10: Temperature profiles at different time intervals for a height a 25 m; isothermal atmosphere, pure radiation, $\varepsilon_g = 0.8$ and $\beta = 0.0 \text{ K hr}^{-1/2}$.

method (1950) based on the use of empirical values of emissivity and corrected for the temperature discontinuity effect at the ground-air interface (Funk 1961, Hales *et al.* 1963, Elliot 1964, Zdunkowski and Johnson 1965).” Corradini and Severini carried out laboratory experiments to verify the cooling rate computed using the flux emissivity method in a 50 m^3 airtight, thermally insulated chamber, with relative humidity of less than 70 %. The inner walls were coated with aluminium foil and

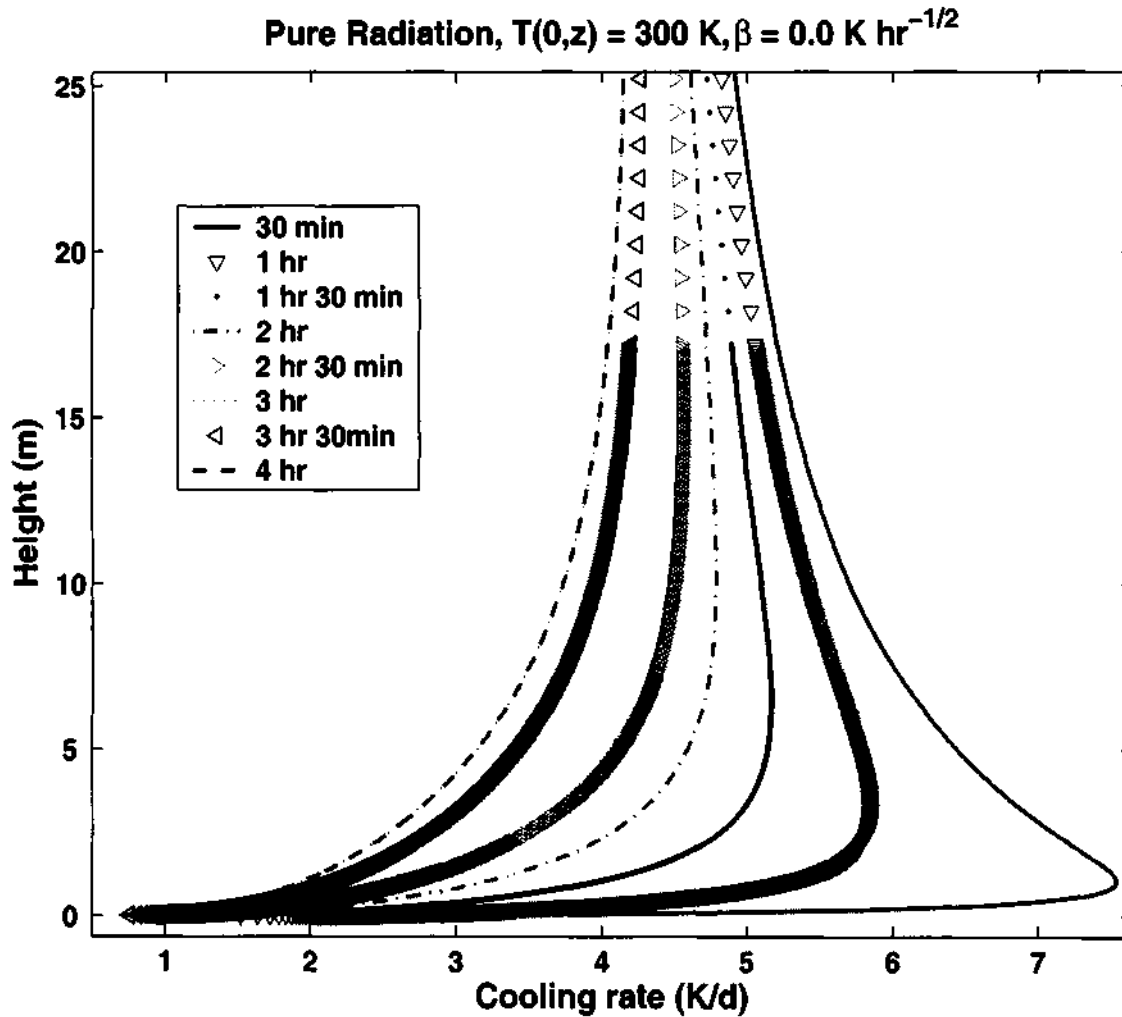


Figure 6.11: Cooling rate profiles at different time intervals for a height a 25 m; isothermal atmosphere, pure radiation, $\varepsilon_g = 0.8$ and $\beta = 0.0\text{ K hr}^{-1/2}$.

ensured a uniform temperature on each base. The lower base of the chamber was made of aluminium superimposed on a system of plates connected to a water-glycol circulation refrigerator plant, by which it was possible to vary the floor temperature. The surfaces of the ceiling and floor were coated with a thin layer of black paint. The absence of turbulent motions was assured by decreasing the floor temperature to a value lower than that of the overlying air. A discontinuity in temperature near the

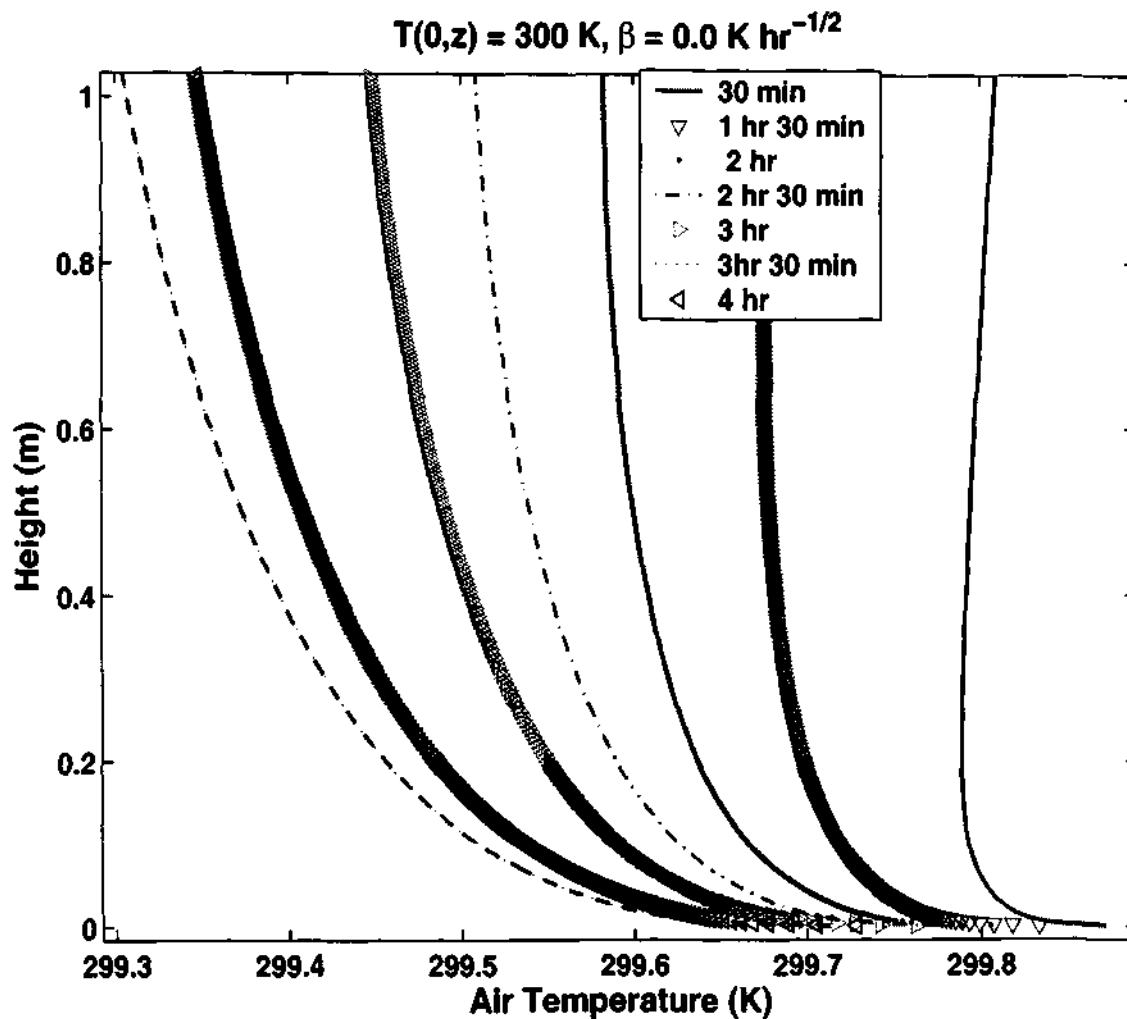


Figure 6.12: Temperature profiles at different time intervals for a height a 1 m; isothermal atmosphere, pure radiation, $\varepsilon_g = 0.8$ and $\beta = 0.0 \text{ K hr}^{-1/2}$.

surface was present. However, no explicit account of such a discontinuity is included in the flux emissivity method. Therefore it appears that the effect of the discontinuity in temperature is implicitly included in the flux emissivity method as well as in the experiments of Corradini and Severini (1975) that have been used in validating the scheme (Zdunkowski and Johnson, 1965). (The differences between observed and estimated cooling rate results are less than 10 %). The present band models do not take into account the discontinuity in temperature at the surface explicitly or implicitly,

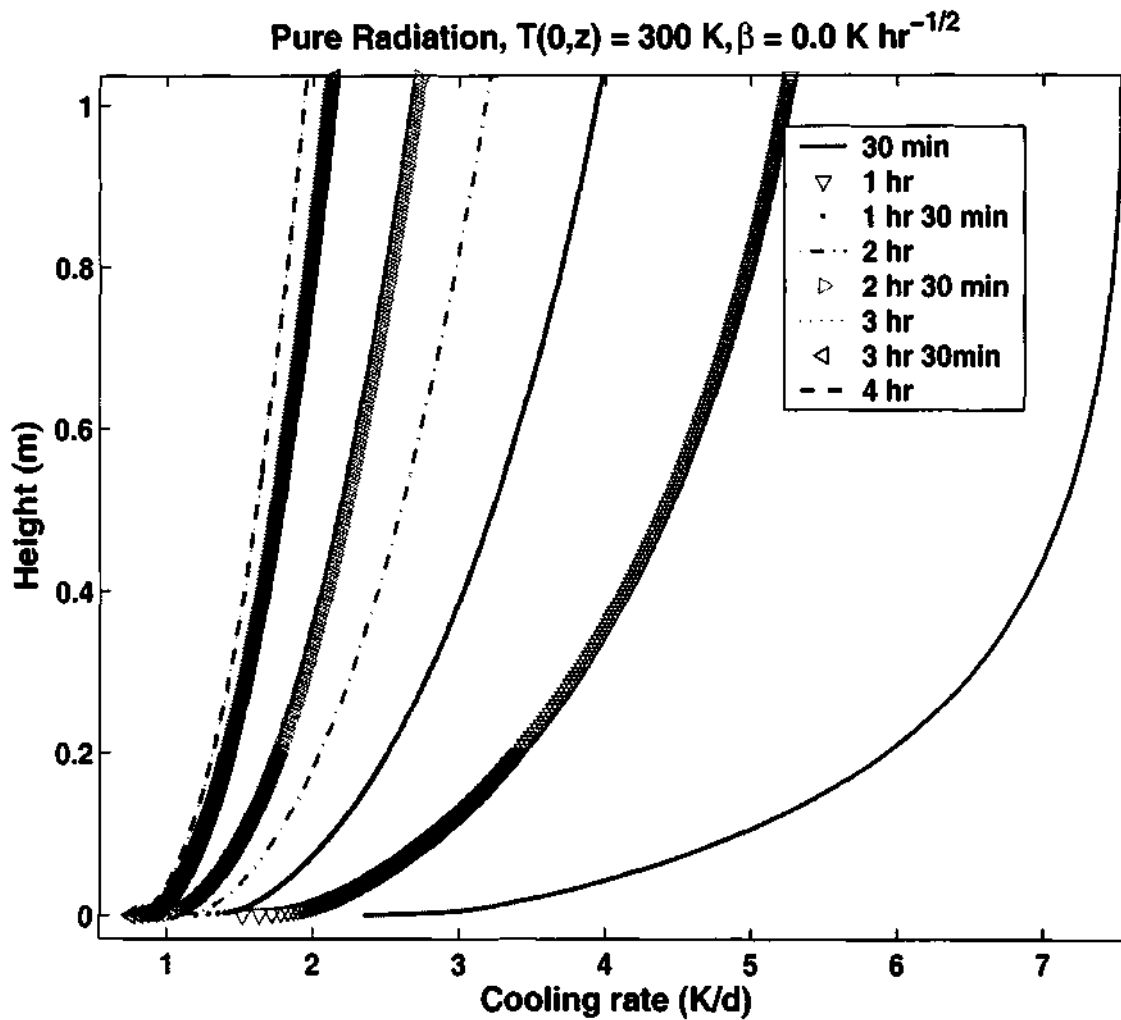


Figure 6.13: Cooling rate profiles at different time intervals for a height $a = 1\text{ m}$; isothermal atmosphere, pure radiation, $\epsilon_g = 0.8$ and $\beta = 0.0\text{ K hr}^{-1/2}$.

and this appears to be an unaddressed problem in the field of near-surface radiative transfer.

A new approach has to be evolved to circumvent this problem. In the previous Chapter, it is seen from Figure 5.3 that a small increase or decrease in ground temperature in an isothermal atmosphere can lead to high cooling or warming rates near the surface. A temperature slip of -3.1 K with ground temperature of 296.9 K produced a surface cooling rate of 1728 K/d , almost equivalent to that produced by

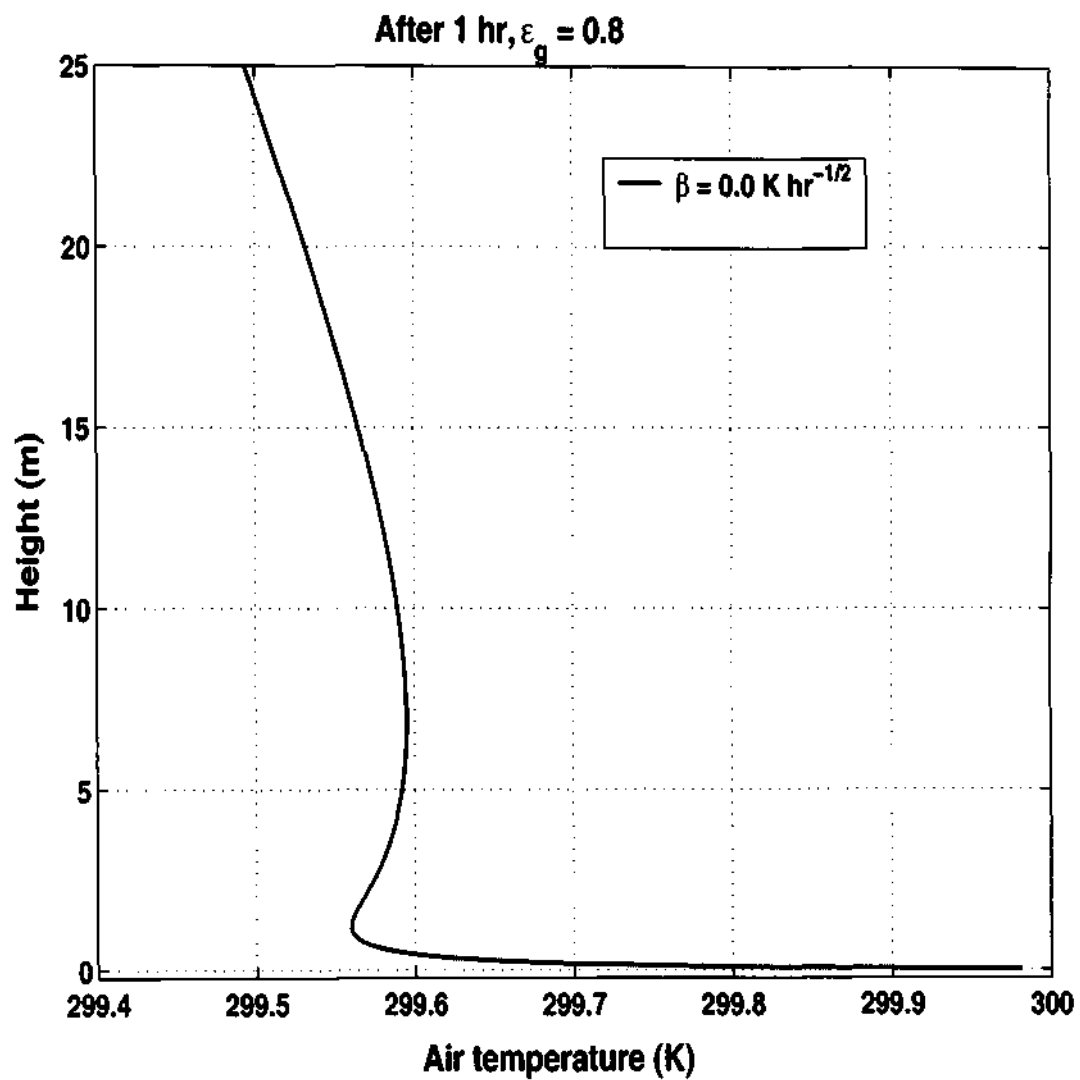


Figure 6.14: Temperature profile at $t = 1$ hr and upto 25 m with $\varepsilon_g = 0.8$ and $\beta = 0$ $\text{K hr}^{-1/2}$ for both radiation and diffusion.

a flux emissivity model (see Figure 5.3). A rational, accurate method of estimating the temperature slip should therefore be considered an integral part of a satisfactory scheme for computing near-surface longwave fluxes.

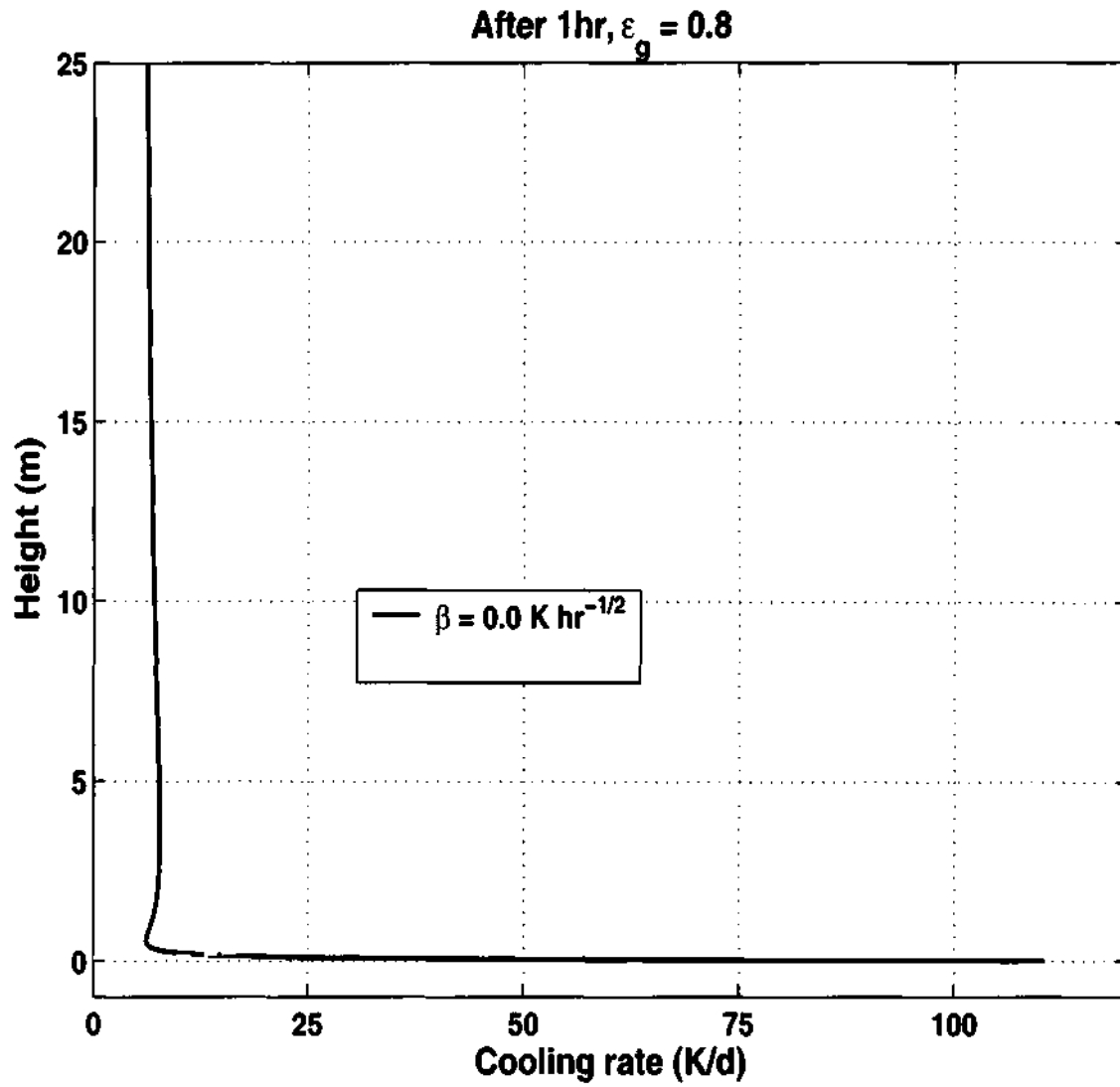


Figure 6.15: Cooling rate profile at $t = 1$ hr and upto 25 m with $\varepsilon_g = 0.8$ and $\beta = 0$ $\text{K hr}^{-1/2}$ for both radiation and diffusion.

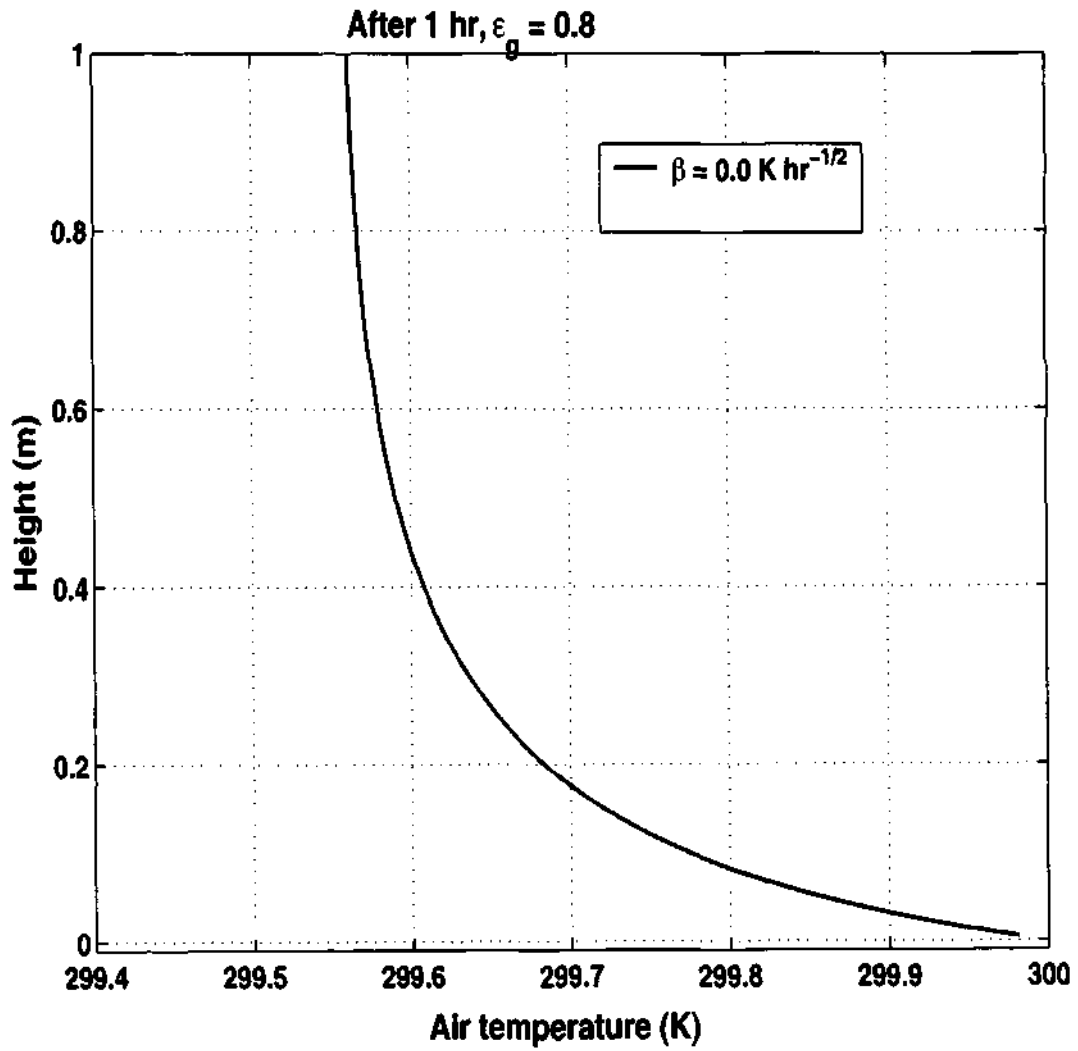


Figure 6.16: Temperature profile at $t = 1$ hr and upto 1 m with $\epsilon_g = 0.8$ and $\beta = 0$ $\text{K hr}^{-1/2}$ for both radiation and diffusion.

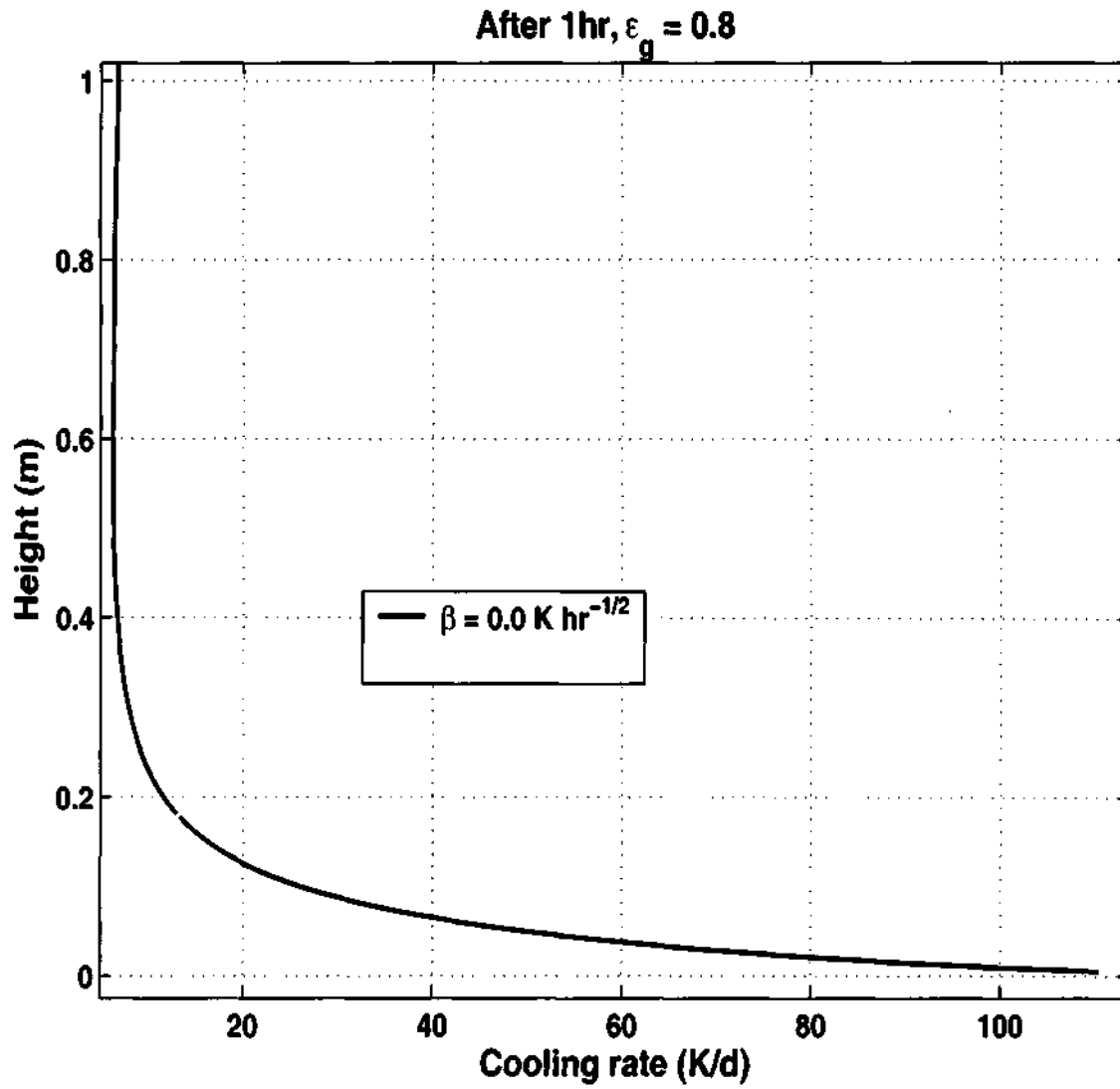


Figure 6.17: Cooling rate profile profile at $t = 1$ hr and upto 1 m with $\varepsilon_g = 0.8$ and $\beta = 0 \text{ K hr}^{-1/2}$ for both radiation and diffusion.

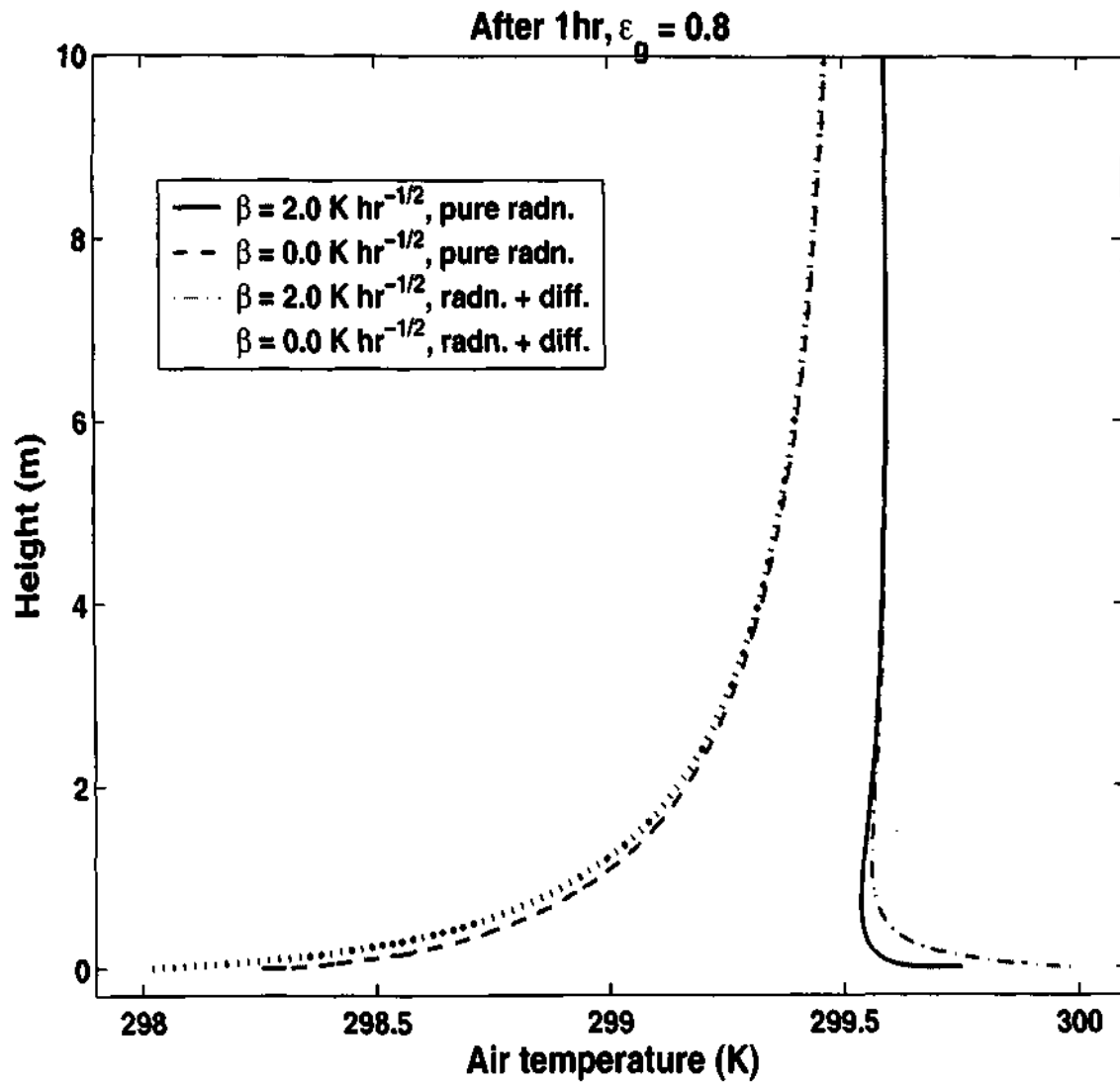


Figure 6.18: Temperature profiles at $t = 1$ hr and upto 10 m with $\epsilon_g = 0.8$ and $\beta = 0$ and $2 \text{ K hr}^{-1/2}$ with pure radiation and with radiation and diffusion.

Chapter 7

Conclusions

Due to inadequate vertical resolution, and the inaccuracy and instability associated with cooling rates generated near the surface by the longwave radiation codes currently in use in numerical weather prediction/climate models, there has been a need to develop a robust, flexible, accurate and stable model to study the near-surface thermal environment. Therefore a new infrared radiation code, based on the parameterization of Chou *et al.* (1993), has been developed in this thesis.

The present code adopts a new numerical approach to solve the particularly severe problem of vertical resolution. The new numerics enables precise computation of long-wave radiation fluxes and cooling rates, all the way from the surface to a height of 100 km. The new code is verified against an exact solution for an isothermal atmosphere, and validated both against line-by-line and ICRCCM results for several cases. The computing times for executing the current program are comparable (for given accuracy) to those demanded by other standard current codes. As the present radiation code has no restriction on the number of grid points and yields fluxes accurate to a prescribed tolerance limit, it consequently also provides cooling rates to a desired accuracy.

We have furthermore presented an analysis of the spectral and net distribution of the cooling rate for the MLS atmosphere. It is found that a decrease in surface emissivity ε_g from 1.0 to 0.8 increases the surface cooling rate from 4.47 to

37.54 K/d, and that the effect of surface emissivity extends to a height of almost 1 km. We also find that the greatest contributions to cooling near the surface come from bands on either side of the atmospheric window. Band 2 (wave-number range 340–540 cm^{-1} , or wavelength range 29.4 to 18.5 μm) is the single largest contributor to near-surface cooling ($> 50 \times 10^{-3}$ Kcm/d), followed closely by band 9 (1215–1380 cm^{-1} , 8.2 to 7.2 μm , contribution 45×10^{-3} Kcm/d); these bands are on either side of the atmospheric window region (8 μm –12 μm). The cooling in these two bands is approximately 50 times higher than that in the weakest band. There is a strong gradient of the cooling rate over the first few centimetres above the surface.

At different heights different bands contribute to the cooling rate, depending on the balance between the flux and absorption at each altitude. Bands 2 and 9 play a special role because they have sufficient absorption at frequencies where the ground radiation flux is significant; it is the combination of these two factors that results in the dramatically high cooling rates. As altitude increases and temperature falls, the flux spectrum peaks at longer wavelengths, where absorption still remains significant; consequently the contribution to cooling also moves to the longer waves.

When $\varepsilon_g = 1.0$, the large gradients of air and ground emission nearly cancel each other out, leaving a relatively small cooling rate which receives dominant contributions from bands 4 to 6 (wave-number range 620–980 cm^{-1} , or wavelength range 16.1–10.2 μm). At $\varepsilon_g = 0.8$ the ground emission is lower relative to the value at $\varepsilon_g = 1.0$, so the balance that prevailed between air and ground emission at $\varepsilon_g = 1.0$ is lost; but in addition the ground reflection is a substantial contributor to the cooling. Thus the predominant cause of the higher cooling when ground is not radiatively black is lower ground emission and higher ground reflection. The present code enables us to investigate in considerable detail the spectral energetics of long-wave radiative transfer that result in the extremely high cooling rates observed near ground. This should be of use in exploring the basic problem of interaction between radiation and

turbulence on the one hand, and (with the inclusion of effects of vegetation) the elucidation of the meteorological conditions that influence the health of agricultural crops – in particular the occurrence and possible control of frost.

Apart from water vapour which is one of the main absorption species, carbon dioxide has also been included in the present code. The addition of CO₂ results in a general decrease in the cooling rate everywhere in the atmosphere. At the surface the differences are appreciable, being 3.2 K/d and 1.21 K/d, i.e. 9 and 37 % of the total, for ground emissivity of 0.8 and 1.0 respectively.

A detailed survey of near-surface cooling rates and the effect of temperature slip was carried out. Results from the numerical experiments show that the cooling rate is highly sensitive to changes in ground temperature. The present code permits incorporation of a discontinuity in temperature at the surface, a feature that is not available in many of the currently available radiation codes. When surface is non-black ($\epsilon_g \neq 1.0$) or when the temperature discontinuity at the ground-air interface is large, near surface cooling rate can change dramatically. The present analysis indicates that the nocturnal boundary layer will be strongly affected by infrared cooling, especially in view of its sensitivity to ground emissivity and ground temperature.

Finally, it is shown that the present code is capable of simulating the lifted temperature minimum (LTM). The intensity and height of the predicted LTM are however weak. This is thought to be due to the extremely small temperature slip produced by the present analysis, confined to the atmosphere only. Significantly, the cooling rates are several times lower than values given by the flux emissivity model. A discontinuity in temperature has to be introduced into the band model to achieve large cooling rates.

It is therefore proposed that a more detailed and elaborate study has to be carried out to understand the dynamics involved in the temperature slip generation, so as to incorporate the mechanism into the present model satisfactorily. Thus, to

study the heat transfer near the surface, air has to be coupled with a detailed soil model involving thermal conduction. Moreover there is great need for more studies involving accurate physical observation of near-surface temperature and cooling rate to validate radiative transfer codes.

Appendix A

Calculation of Transmission Function

From (2.7) and (2.15) we obtain

$$\frac{\int_{\nu_j}^{\nu_{j+1}} F_\nu^\downarrow(0) \tau_\nu(u) d\nu}{F_j^\downarrow(0)} = \frac{-\int_{\nu_j}^{\nu_{j+1}} d\nu \tau_\nu(u) \int_0^{u_\infty} \pi B_\nu(T') [d\tau_\nu(u')/du'] du'}{-\int_0^{u_\infty} \pi B_j(T') T_j'(u') du'}$$

Dividing numerator and denominator above by $\pi B_j(T')$, and replacing T' in the Planckian by T_0 based on the argument given in the paragraph below (2.12), we obtain

$$\frac{\int_{\nu_j}^{\nu_{j+1}} F_\nu^\downarrow(0) \tau_\nu(u) d\nu}{F_j^\downarrow(0)} = \frac{\int_{\nu_j}^{\nu_{j+1}} B_\nu(T_0) \tau_\nu(u) [\tau_\nu(u_\infty) - \tau_\nu(0)] d\nu}{B_j(T_0) [\tau_j(u_\infty) - \tau_j(0)]}$$

Now from (2.4) and (2.18) it follows that $\tau_\nu(u_\infty) \simeq 0 \simeq \tau_j(u_\infty)$ and $\tau_\nu(0) = 1 = \tau_j(0)$.

Consequently we obtain the approximate result (2.17)

$$\frac{\int_{\nu_j}^{\nu_{j+1}} F_\nu^\downarrow(0) \tau_\nu(u) d\nu}{F_j^\downarrow(0)} \approx \frac{\int_{\nu_j}^{\nu_{j+1}} \pi B_\nu(T_0) \tau_\nu(u) d\nu}{\int_{\nu_j}^{\nu_{j+1}} \pi B_\nu(T_0) d\nu}$$

Appendix B

Derivation of Flux Equations

Let us consider the downward flux F^\downarrow without subscripts in (2.23),

$$F^\downarrow = cdk \int_u^{u_\infty} \pi B(T') e^{-dk(u'-u)} du'.$$

Treating F^\downarrow and T' as functions of u we get

$$\begin{aligned} \frac{dF^\downarrow}{du} &= cd^2k^2 \int_u^{u_\infty} \pi B_j(T') e^{-dk(u'-u)} du' - cdk\pi B_j(T) \\ &= dk[F^\downarrow - c\pi B(T)]. \end{aligned}$$

This in turn yields

$$\frac{dF^\downarrow}{dz} = dk \frac{du}{dz} [F^\downarrow - c\pi B(T)],$$

and from (2.19) we have

$$\frac{dF^\downarrow}{dz} = -A[c\pi B(T) - F^\downarrow],$$

which is equation (4.29) with A defined in (2.28). The equation for upward flux is obtained similarly.

Appendix C

Computation of Blackbody Fraction

The black body fraction $B_j(T)$ in (2.12) is evaluated in the following way. Define

$$\bar{F}(\xi) = \frac{1}{\sigma T^4} \int_0^{\xi} \pi B_\nu(T) d\nu;$$

then

$$B_j(T) \approx \left[\bar{F} \left(\frac{C_2 \nu_{j+1}}{T} \right) - \bar{F} \left(\frac{C_2 \nu_j}{T} \right) \right] \sigma T^4 \approx \epsilon_j \sigma T^4$$

where

$$C_2 = hc/K,$$

and h, c, K are the constants appearing in the Planck function. ϵ_j is the black body fraction for band j . The \bar{F} functions are computed using the method given by Lawson (1997) which is described in the next Section.

C.1 Lawson's Method

The total emissive power of a black body is found by integrating the Planck function.

$$B(T) = \int_0^\infty \pi B_\nu(\nu, T) d\nu = \sigma T^4.$$

The emissive power of a band of the spectrum from wavelength ν_1 and ν_2 is given by

$$B_j(\nu_1, \nu_2, T) = \int_{\nu_1}^{\nu_2} B_\nu(\nu, T) d\nu.$$

Emissive power of the band from 0 to ν_2 is the sum of the emissive powers of the bands from 0 to ν_1 and from ν_1 and ν_2 . Therefore,

$$B_j(\nu_1, \nu_2, T) = B_j(0, \nu_2, T) - B_j(0, \nu_1, T).$$

The black body fraction of the band from 0 to ν is,

$$F(0, \nu, T) = \frac{1}{\sigma T^4} \int_0^\nu \frac{2\pi C_1 \nu^5}{[\exp(C_2 \nu/T) - 1]}.$$

The two independent variables (ν, T) in the above equation can be reduced to one by setting $x = T/\nu$. We find that

$$F(0, \nu, T) = \bar{F}(\nu, T) = \frac{1}{\sigma} \int_0^{T/\nu} \frac{2\pi C_1}{x^5 [\exp(C_2/x) - 1]} dx.$$

The integral above can be simplified by making the substitution $x = C_2/z$. Therefore,

$$\bar{F}(T/\nu) = \frac{2\pi C_1}{\sigma} \int_\infty^{C_2\nu/T} \frac{z^5}{C_2^5(e^z - 1)} \left(\frac{-C_2}{z^2}\right) dz.$$

Changing the order of the limits,

$$\begin{aligned} \bar{F}(T/\nu) &= \frac{2\pi C_1}{\sigma C_2^4} \int_{C_2\nu/T}^\infty \frac{z^3}{e^z - 1} dz, \\ &= \frac{15}{z^4} \int_{C_2\nu/T}^\infty \frac{z^3 e^{-z}}{1 - e^{-z}} dz. \end{aligned}$$

Using binomial expansions

$$\begin{aligned} \bar{F}(T/\nu) &= \frac{15}{z^4} \int_{C_2\nu/T}^\infty z^3 e^{-z} (1 + e^{-z} + e^{-2z} + \dots) dz, \\ &= \frac{15}{z^4} \sum_{n=1}^\infty \int_{C_2\nu/T}^\infty z^3 e^{-nz} dz. \end{aligned} \tag{1.1}$$

Repeated use of integration by parts leads to

$$\bar{F}(T/\nu) = \frac{15}{\pi^4} \sum_{n=1}^\infty \frac{e^{-nz}}{n} \left(z^3 + \frac{3z^2}{n} + \frac{6z}{n^2} + \frac{6}{n^3} \right)$$

where $z = C_2\nu/T$.

Appendix D

Unit Conversion

D.1 Conversion of atm.cm to kgm^{-2}

Analogous to column mass, column number $N_i(1, 2)$ is defined as the number of molecules (of composition i , each with molecular mass M_i) in a cylinder of unit cross section:

$$N_i = \int_1^2 ds n_i = M_i(1, 2)/M_i = N_i(z_2, \theta) - N_i(z_1, \theta)$$

Although N_i has the MKS units of [molecules.m⁻²], it is more commonly expressed in units of atm.cm especially in atmospheric radiation calculations. This unit is the length of a column filled with the species of interest and compressed to standard temperature and pressure (STP), which are 273.16 K and 1013.25 mb, respectively. To convert from [molecules.cm⁻²] to [atm.cm], one divides N_i by Lochmidt's number, the air density at STP, $n_L = 2.687 \times 10^{19} \text{ cm}^{-3}$.

However, to convert atm.cm to kgm^{-2} , the following method can be adopted. Consider the case of carbon dioxide.

$$\begin{aligned} \text{atm.cm} \times \rho_{\text{CO}_2\text{STP}} &\equiv m_{\text{CO}_2} \text{ kgm}^{-2} \\ &\equiv (\text{atm.m}/100) \times \rho_{\text{CO}_2\text{STP}} \end{aligned} \quad (1.1)$$

where $\rho_{\text{CO}_2\text{STP}}$ is the density of carbon dioxide (1.977 kgm^{-3}) at STP. Therefore, to convert atm.cm to kgm^{-2} , one has to multiply by a factor of 1.977×10^{-2} and by a factor of 50.581 to convert from $(\text{atm.cm})^{-1}$ to m^2kg^{-1} .

D.2 Conversion of ppmv to kgm^{-3}

A convenient variable to describe deviations of the species height distribution from the hydrostatic case is the mixing ratio. This is defined either in terms of mass mixing ratio, $w_m^i(z) = \rho_i(z)/\rho(z)$, or the volume mixing ratio, $w^i(z) = n_i(z)/n(z)$, where $\rho(z)$ is the total density and $n(z)$ is the total concentration of the ambient atmosphere. We mostly deal with constituents with very small mixing ratios. Typically w is specified in parts per million by volume [ppmv] or parts per billion by volume [ppbv]. w is also sometimes called the molar fraction of species i . w_m^i is usually specified in [g.g⁻¹] (grams per gram).

Here conversion of ppmv to kgm^{-3} is shown taking carbon dioxide as an example.

$$\text{kgm}^{-3} \equiv 10^{-6} \times [\text{ppmv}] \times MW_{\text{CO}_2} / R.T \times P$$

where MW_{CO_2} is the molecular weight of CO_2 , R the gas constant, T the temperature and P the pressure. Substituting $P = \rho_{\text{air}} R / M_{\text{air}} T$,

$$\begin{aligned} &\equiv 10^{-6} \times [\text{ppmv}] \times MW_{\text{CO}_2} / MW_{\text{air}} \times \rho_{\text{air}}(z) \\ &\equiv 10^{-6} \times [300] \times 44 / 28.97 \times \rho_{\text{air}}(z) \end{aligned}$$

The molecular weights of carbon dioxide and air are 44 and 28.97 g respectively.

Appendix E

Comparison of Cooling Rates for Broadband Flux Emissivity and Band Models in an Isothermal Atmosphere with a Discontinuity at the Surface

In the following we shall consider the temperature profile

$$T(z) = T_0; \quad z > 0, \quad (\text{E.1})$$

$$= T_{g0}; \quad z = 0. \quad (\text{E.2})$$

for comparing the cooling rates between the broadband flux emissivity formulation (6.8)-(6.11) and the present band formulation (2.24). The reason for choosing this profile is simplicity in evaluating the integrals.

E.1 Flux emissivity

We first recall the flux emissivity function given in (6.11)

$$\begin{aligned} \epsilon(u) &= 0.0492 \ln(1 + 1263.5u) \text{ for } u \leq 10^{-2} \text{ kg m}^{-2} \\ &= 0.05624 \ln(1 + 875u) \text{ for } u > 10^{-2} \text{ kg m}^{-2}. \end{aligned}$$

Using the profile (E.1)-(E.2) in (6.9) radiative flux divergence is determined by the term

$$\frac{dQ_r}{du} = \varepsilon_g[\sigma T_{g0}^4 - \sigma T_0^4]\epsilon'(u) + \sigma T_0^4[(1 - \varepsilon_g)(1 - \epsilon(u_\infty))\epsilon'(u) + \epsilon'(u_\infty - u)]. \quad (\text{E.3})$$

E.2 Band emissivity

We have also seen from (2.18) that the j^{th} band transmission function τ_j in terms of its sub-bands τ_j^i can be written as

$$\tau_j(u) = \sum_{i=1}^{m_j} c_i^j \tau_j^i; \quad \tau_j^i = \exp(-dk_j^i u_j). \quad (\text{E.4})$$

The emissivity in each band is then

$$\epsilon_j(u) = 1 - \tau_j(u), \quad (\text{E.5})$$

and the radiative flux divergence is

$$\frac{dQ_r}{du} = \sum_j \frac{dF_j}{du}, \quad (\text{E.6})$$

$$\frac{dF_j}{du} = \varepsilon_g[\pi B_j(T_{g0}) - \pi B_j(T_0)]\epsilon_j'(u) + \pi B_j(T_0)[(1 - \varepsilon_g)(1 - \epsilon_j(u_\infty))\epsilon_j'(u) + \epsilon_j'(u_\infty - u)]. \quad (\text{E.7})$$

E.3 Discussion

It is to be noted that the vertical variation of the emissivities in the two models are very different. In the flux emissivity scheme the variation of emissivity is slow as it is a logarithmic function while in the band model it is an exponential as in a gray case. The emissivity attains a value of 1 in some bands at very low heights (for example, bands 1 and 9 reach unity at around 1 km). This is shown in Figures E.1

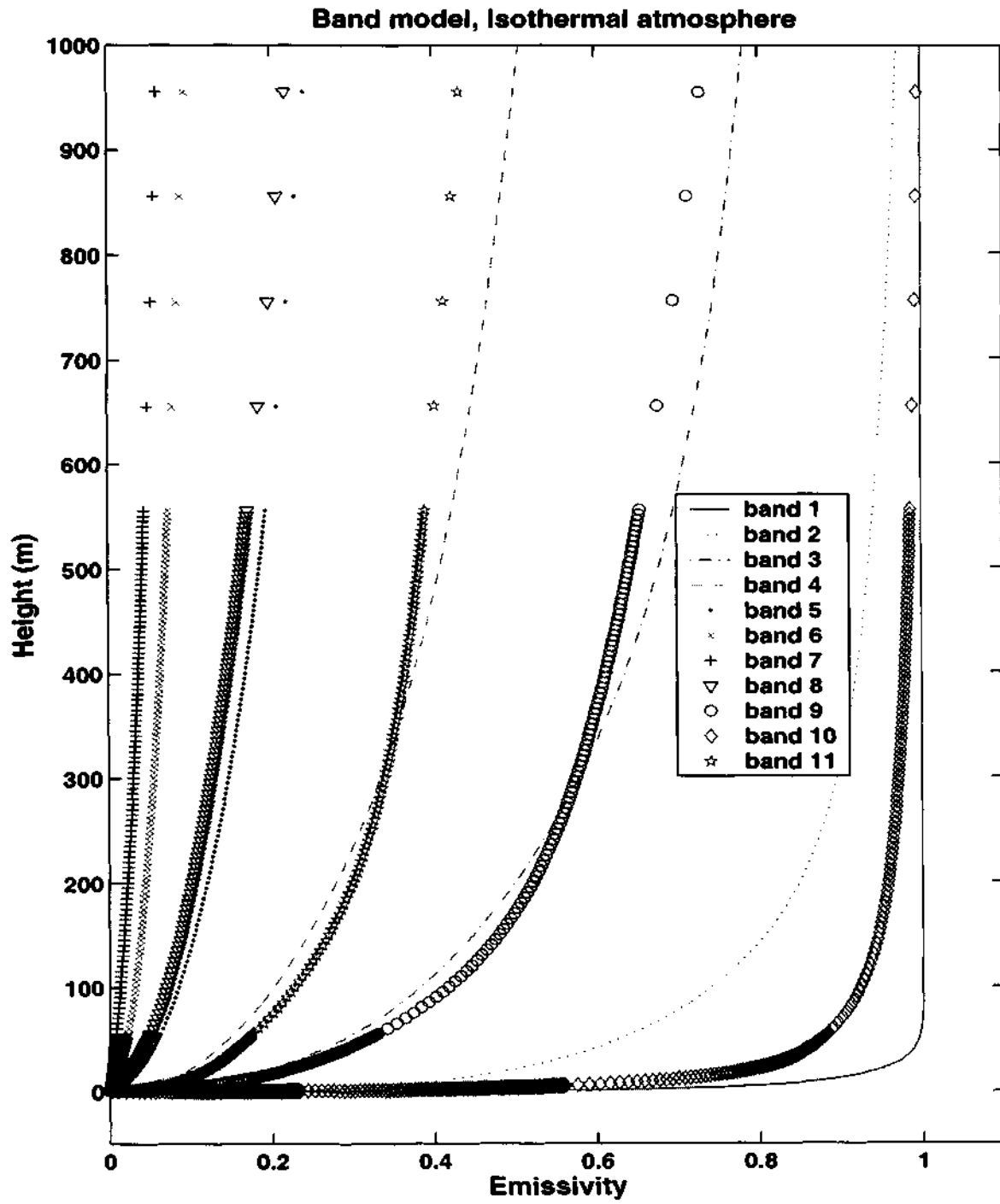


Figure E.1: Vertical variation of emissivity with present band model upto 1 km.

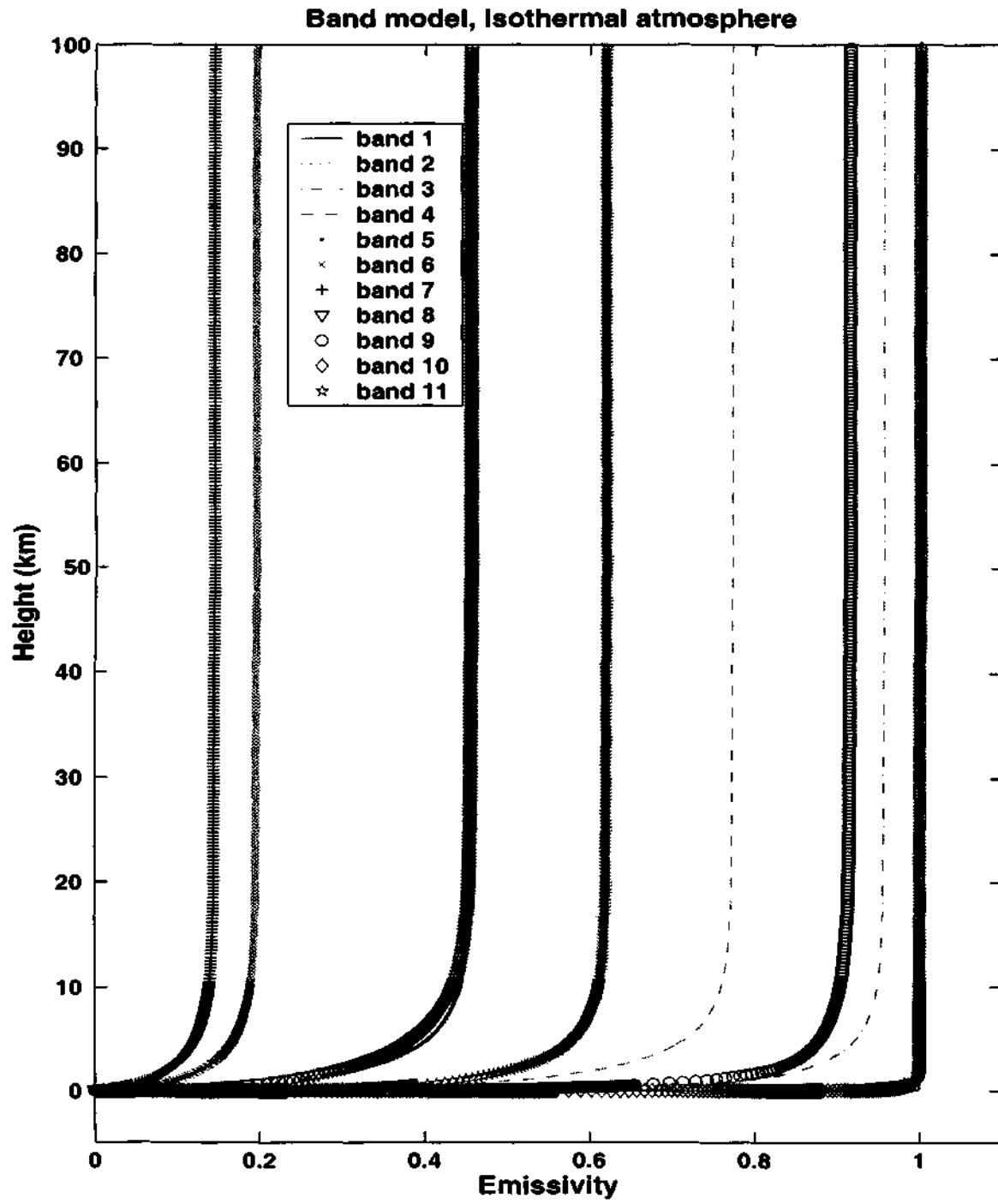


Figure E.2: Vertical variation of emissivity with present band model upto 100 km.

and E.2 where the variation of emissivity is shown for 1 km and 100 km respectively for different bands from the present band model.

Figures E.3 and E.4 show the vertical variation of emissivity upto 1 km and 100 km with the flux emissivity function.

In the cooling rate expression in (E.3) the second term dominates, whereas in the band model exactly the opposite is true, i.e., the first term dominates over the second term. Thus, even if $\varepsilon_g \equiv 1$, the band model will give a higher cooling rate compared to the flux emissivity model (see Figures E.5 -E.6). However, if $\varepsilon_g \equiv 1$ and $T_{g0} \leq T_0$, then the flux emissivity scheme is equivalent to a fully isothermal atmosphere but with a different $\bar{\varepsilon}_g$ because

$$\sigma T_{g0}^4 = \bar{\varepsilon}_g \sigma T_0^4$$

where

$$\bar{\varepsilon}_g = \sigma T_{g0}^4 / \sigma T_0^4$$

Now $T_{g0} \leq T_0$ ensures that $\bar{\varepsilon}_g \leq 1$. For $T_0 = 300$ K and $T_{g0} = 298$ and 297 K we have $\bar{\varepsilon}_g = 0.9736$ and 0.9606 respectively. If $T_0 > T_{g0}$, then $\bar{\varepsilon}_g > 1$ which is unphysical.

In Figure E.5 a comparison between the flux emissivity and the present band model is made for the cooling rates in a fully isothermal atmosphere ($T_0 = T_{g0} = 300$ K; (E.1)-(E.2)), at both $\varepsilon_g = 1.0$ and 0.8 upto 1 km. The same feature can be seen more distinctly in Figure E.6 where the height is limited to 1 m. Table E.1 shows the band emissivity values at u_∞ , its gradient at the surface and the product of blackbody fraction and gradient of emissivity at the surface.

On the other hand if $\varepsilon_g \leq 1$, there is a dramatic improvement in cooling rate for the flux emissivity scheme because the second term contributes appreciably as $1 - \varepsilon(u_\infty)$ can never be zero because of the logarithmic function, whereas in the band model it is zero or near zero (as seen in Table E.1) because of the exponentials.

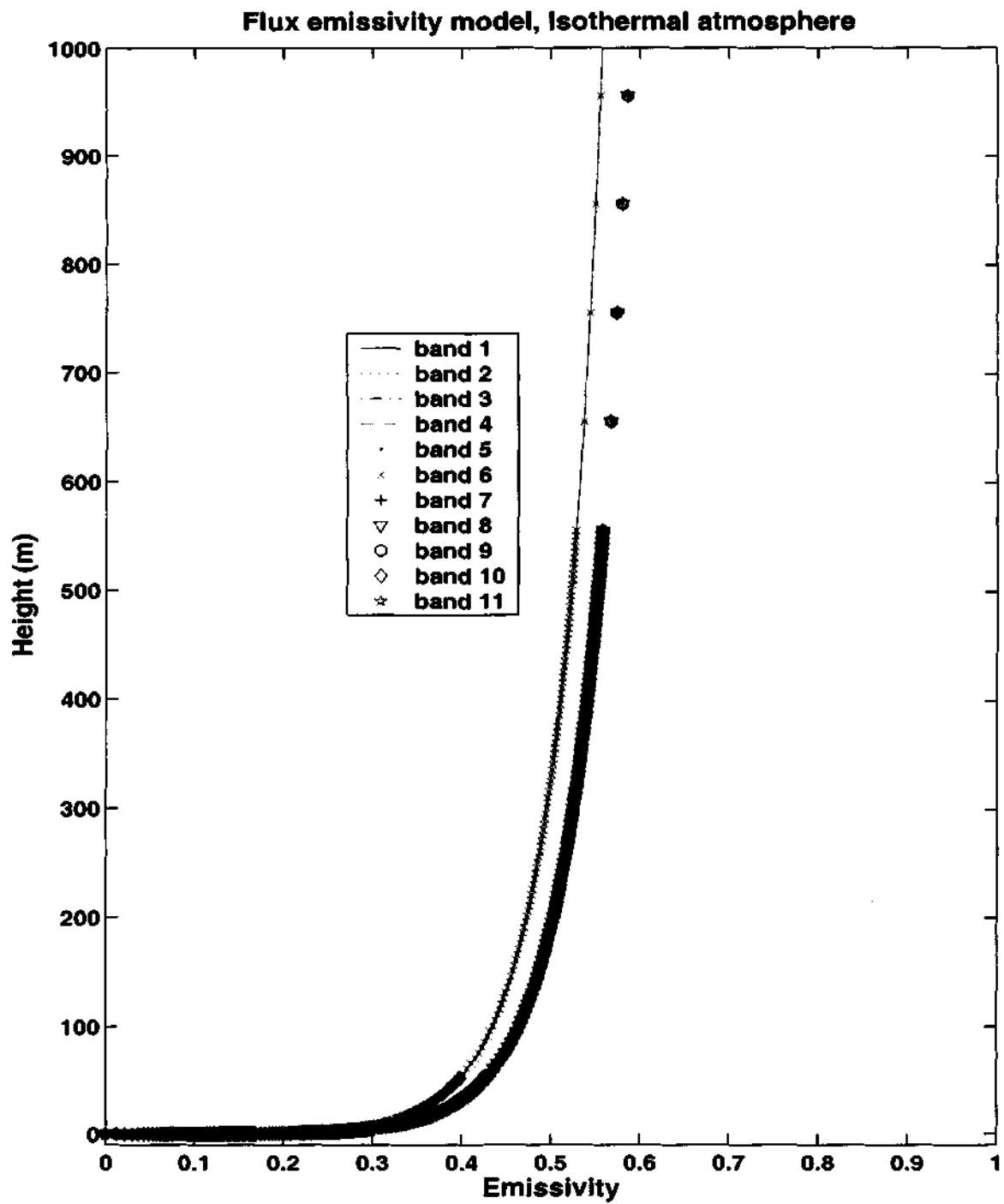


Figure E.3: Vertical variation of emissivity with flux emissivity model upto 1 km.

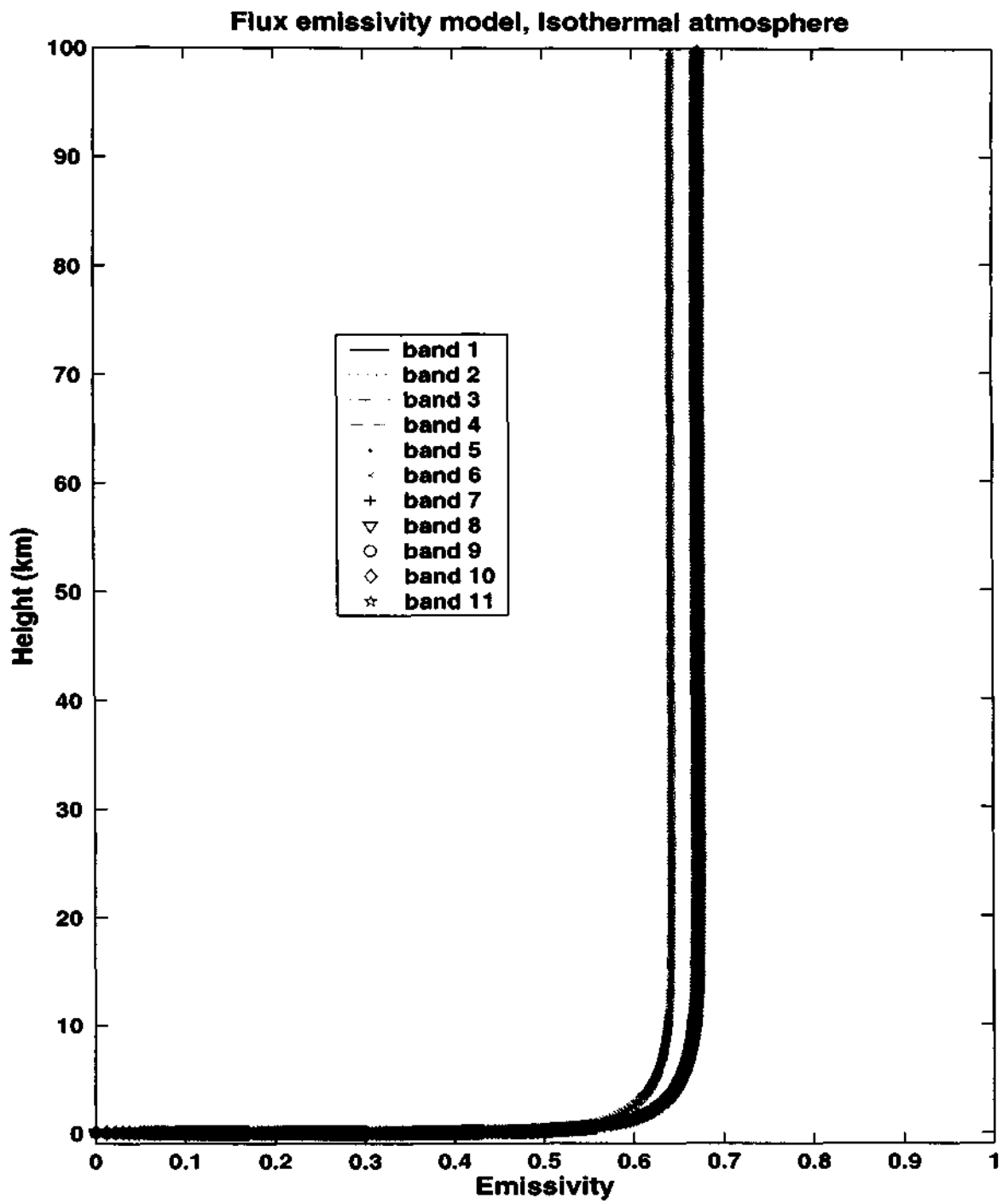


Figure E.4: Vertical variation of emissivity with flux emissivity model upto 100 km.

Table E.1: Values for band emissivity at 100 km, its gradient at the surface and the product of blackbody fraction and gradient of emissivity at the surface from the present code.

Band	$\epsilon_j(u_\infty)$	$\epsilon'_j(0)$	$(B_j(T)/\sigma T^4) \times \epsilon'_j(0)$
1	1.0000	830.77	95.700
2	0.9999	21.11	3.975
3	0.9560	1.0	0.0838
4	0.7728	0.31	0.0308
5	0.4559	0.0724	0.005553
6	0.1958	0.00835	0.0012241
7	0.1448	0.00191	0.0001444
8	0.4553	0.0489	0.000277
9	0.9151	2.95	0.1729
10	1.0000	84.13	6.5621
11	0.6197	1.28	0.0228
total		940.911	106.555

Table E.2 shows the variation of surface cooling for different ground temperatures with band and flux emissivity models. Here ϵ_g is taken to be 0.8. The rate of change of surface cooling rate with T_{g0} is larger for the band model. This can be seen more clearly in Figure E.7 where the data in Table E.2 is plotted. The two models give an identical cooling rate at $T_{g0} = 293.25$ K.

Figures E.8 and E.9 show the variation in cooling rate in an isothermal atmosphere with $\epsilon_g = 0.8$ and 1.0 respectively. In both the cases, large variations occur within the first 1m. Thereafter the cooling rates are close to zero. With $\epsilon_g = 0.8$ and $T_{g0} = 302$ K, the band model shows a warming (~ -1000 K/d) near the

surface while the flux emissivity scheme shows cooling (~ 1250 K/d). The changes in cooling rate with T_{g0} are larger for band the band model, as noted previously.

With $\varepsilon_g = 1.0$, the cooling/heating trend appears more or less symmetrical with respect to the ordinate for each model. As we have already seen in Figures E.5 and E.6 the cooling rates are close to zero for both models. However the band model tends to produce larger cooling/heating near the surface when the ground temperature is decreased/increased. In all cases ($\varepsilon_g = 0.8$ and 1.0), the effect of change in ground temperature is seen only within 10 m from the surface.

Table E.2: Values for cooling rate at the surface with band model and flux emissivity model for different ground temperatures; $\varepsilon_g = 0.8$, isothermal atmosphere.

T_{g0} (K)	band model (K/d)	flux emissivity model (K/d)
290	5084.13	4236.1
295	2575.59	3032.1
298	1041.86	2279.6
299	525.74	2023.7
300	7.14	1765.2
301	-513.95	1504.1
302	-1037.56	1240.0
305	-2623.69	433.3
310	-5319.45	-965.6

From the present analysis it follows that the main reason for the difference in cooling is the nature of functions used to compute them (exponential in the case of band model and logarithmic in the case of flux emissivity model). With a discontinuity at the air-ground interface the cooling rates produced by both the models are large. With $\varepsilon_g = 1.0$, for any ground temperature, cooling/heating rate values are

higher for band model. With $\epsilon_g = 0.8$, for small decrease in ground temperatures, cooling rates from flux emissivity model dominates but for ground temperatures lower than 293.25 K, band model dominated. For cases where $T_{g0} > T_0$, heating rates from band model are always larger compared to flux emissivity scheme. The above study reiterates the point that ground temperature is a very important factor and its accurate determination is very crucial in the estimation of near-surface cooling rates.

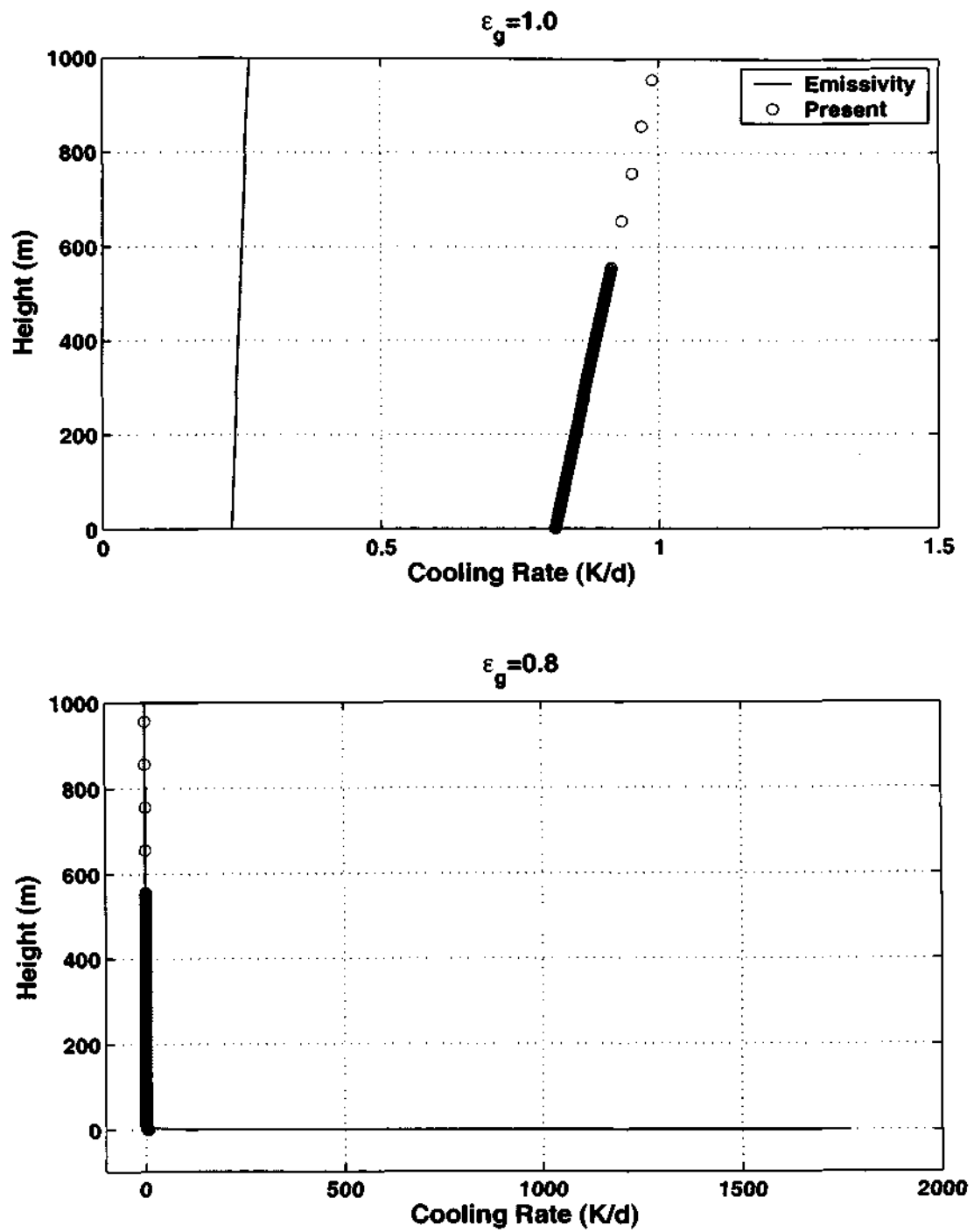


Figure E.5: Vertical variation of cooling rates with flux emissivity scheme and present band model for $\epsilon_g = 1.0$ and 0.8 upto 1 km; $T_0 = T_{g0} = 300$ K.

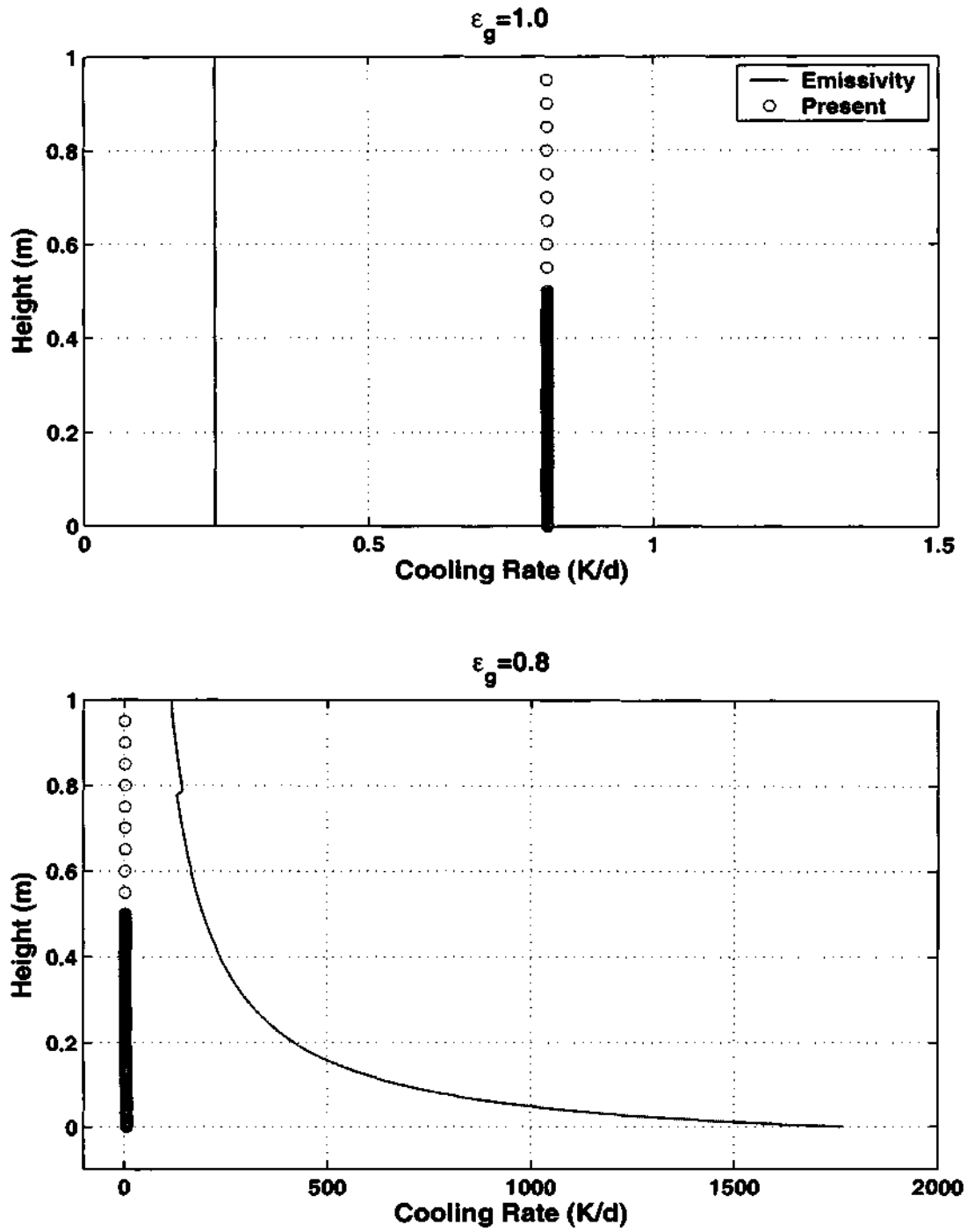


Figure E.6: Vertical variation of cooling rates with flux emissivity scheme and present band model for $\epsilon_g = 1.0$ and 0.8 upto 1 m; $T_0 = T_{g0} = 300$ K.

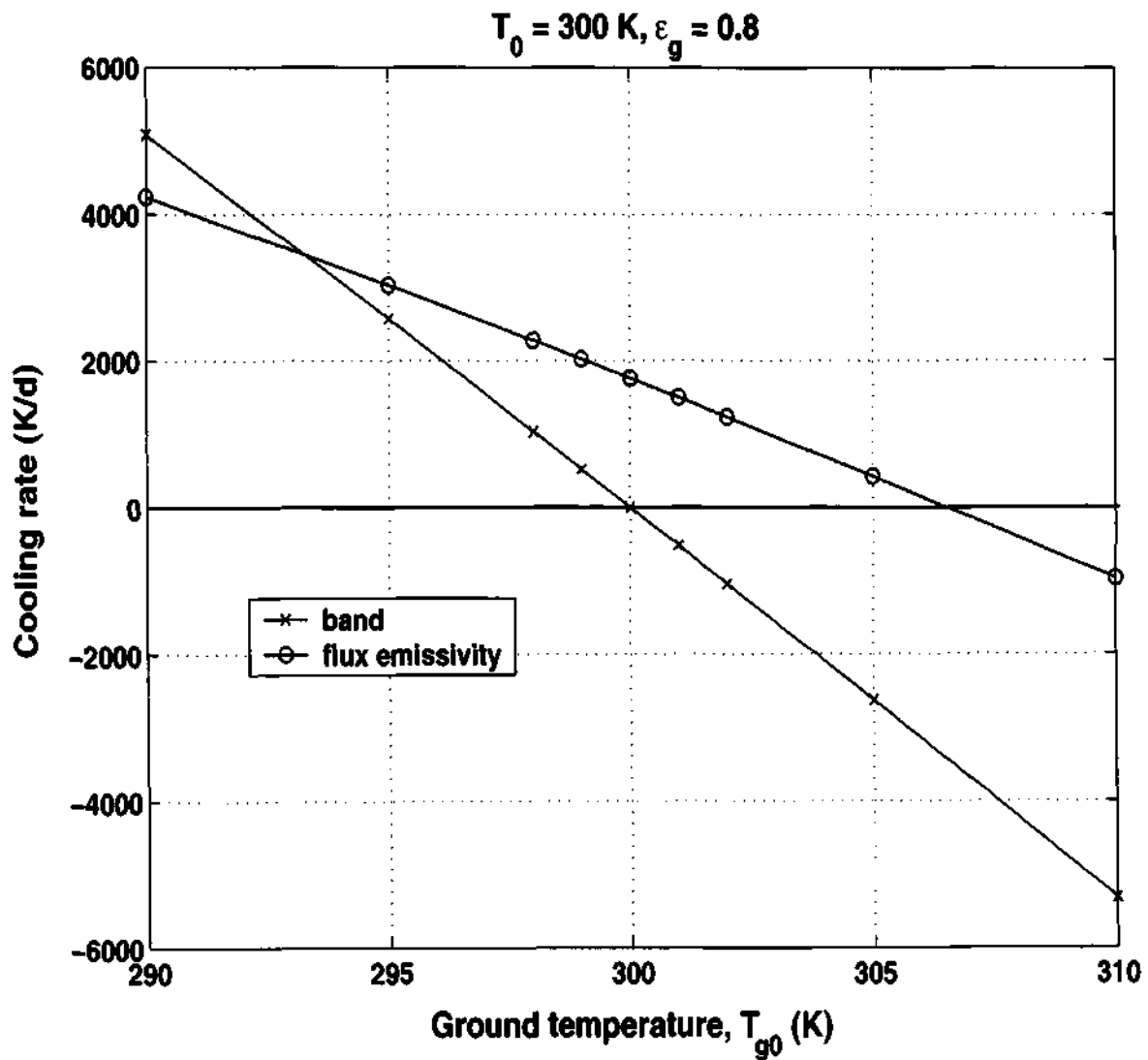


Figure E.7: Variation of surface cooling rate with different ground temperatures for flux emissivity scheme and band model, $\epsilon_g = 0.8$.

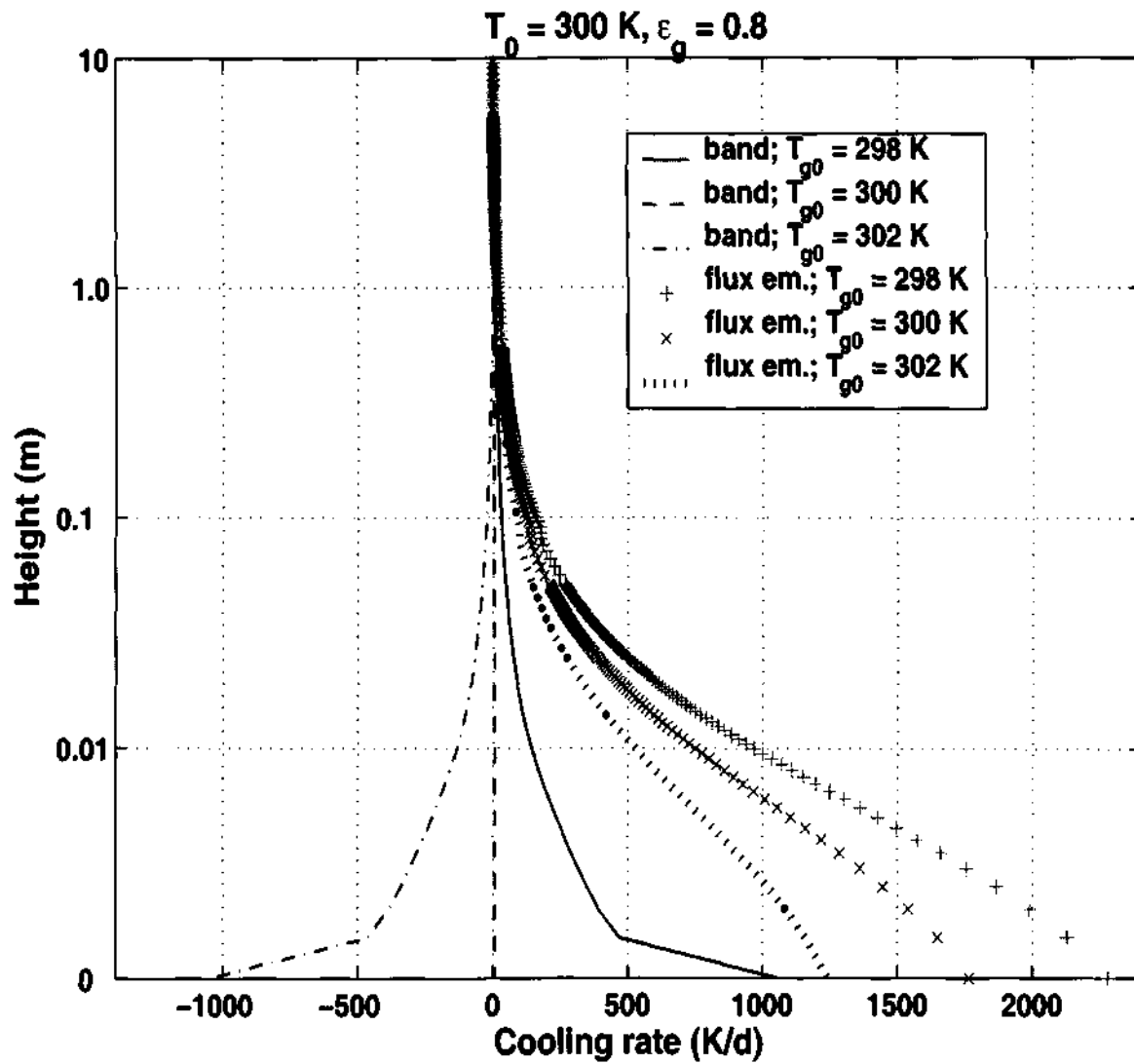


Figure E.8: Variation of cooling rate with different ground temperatures for flux emissivity scheme and band model; $\varepsilon_g = 0.8$.

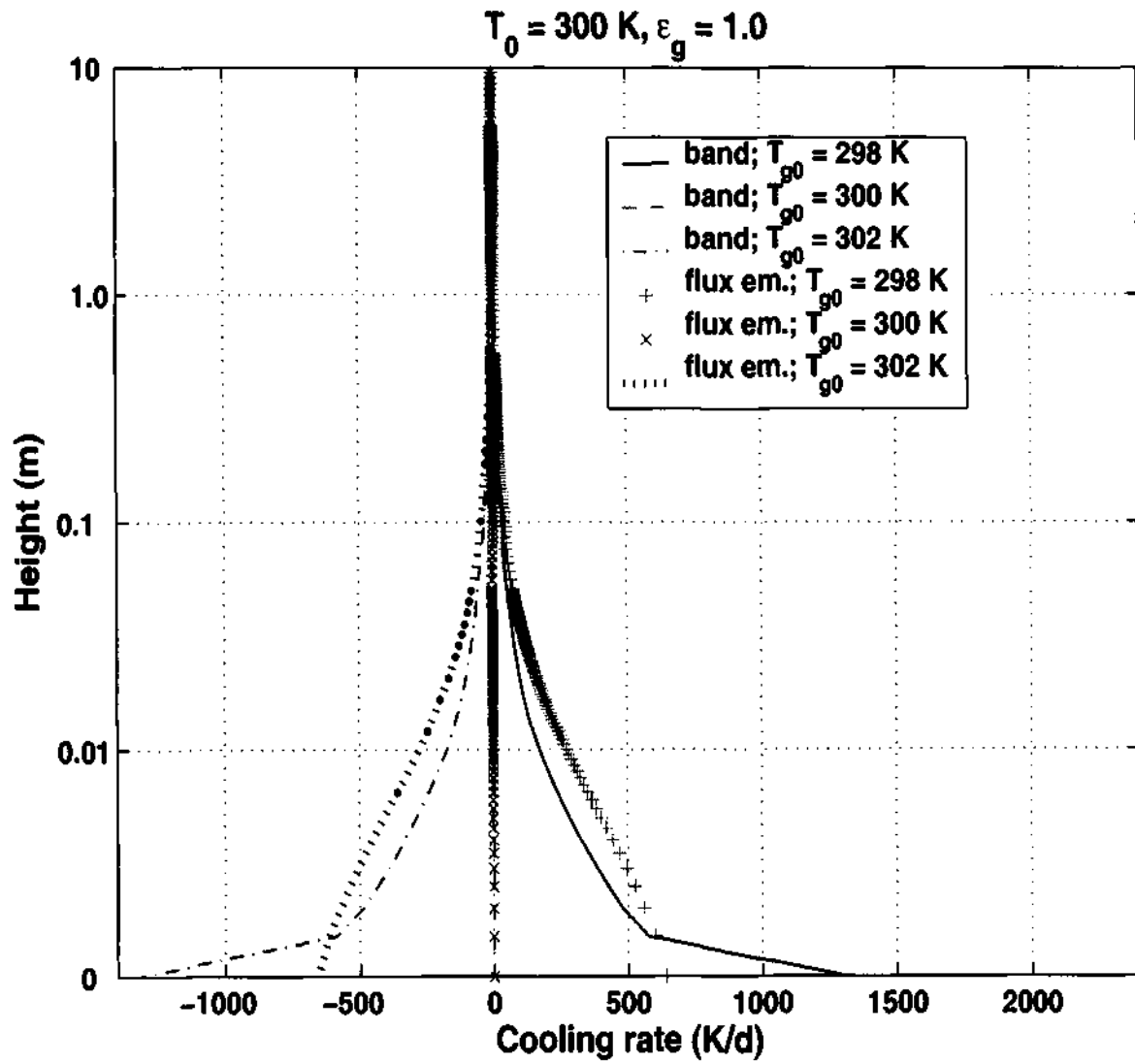


Figure E.9: Variation of cooling rate with different ground temperatures for flux emissivity scheme and band model; $\varepsilon_g = 1.0$.

References

- [1] Allan, R. P., 2000: Evaluation of Simulated Clear-sky Longwave Irradiance at the Surface using Ground-based Radiometric Observations. *J. Climate*, **13**, 1951-1964.
- [2] André, J.C., G. De Moor, P. Lacarrere, G. Therry and R. du Vachat, 1978: Modeling the 24 hour evolution of the mean and turbulent structures of the planetary boundary layer. *J. Atmos. Sci.*, **35**, 1861-1883.
- [3] Baer, F., N. Arsky, J. J. Charney, and R. G. Ellingson, 1996: Intercomparison of heating rates generated by global climate model longwave radiation codes. *J. Geoph. Res.*, **101**, D21, 26589-26603.
- [4] Becker, F., W. Ngai and M.P. Stoll, 1981: An active method for measuring thermal infrared effective emissivities: implications and perspectives for remote sensing. *Adv. Space Res.*, **1**, 193-210.
- [5] Brooks, D.L., 1950: A tabular method for the computation of temperature change by infrared radiation in the free atmosphere. *J. Met.*, **7**, 313-321.
- [6] Brunt, D., 1939: Physical and Dynamical Meteorology, 2nd ed., *Cambridge*, 286 pp.
- [7] Chou, M.-D., 1991: The derivation of cloud parameters from satellite-measured radiances for use in surface radiation calculations. *J. Atmos. Sci.*, **48**, 1549-1559.

- [8] Chou, M.-D. and A. Arking, 1980: Computation of infrared cooling rates in water vapour bands. *J. Atmos. Sci.*, **37**, 856-867.
- [9] Chou, M.-D., W.L. Ridgway and M.M.-H. Yan, 1993: One-parameter scaling and exponential-sum fitting for water vapor and CO₂ infrared transmission functions. *J. Atmos. Sci.*, **50**, 2294-2303.
- [10] Chou, M.-D., and L. Peng, 1983: A parameterization of the absorption in the 15 μm CO₂ spectral region with application to climate sensitivity studies. *J. Atmos. Sci.*, **40**, 2183-2192.
- [11] Chou, M.-D and M.J. Suarez, 1994: An efficient thermal infrared radiation parameterization for use in General Circulation Models- Technical Report Series on Global Modeling and Data Assimilation. *NASA Tech. Memo* 104606, **3**.
- [12] Chou, M.-D., M.J. Suarez, X.-Z. Liang, M.-H. Yan, 2001: A thermal infrared radiation parameterization for atmospheric studies. *NASA Tech. Memo.* 104606, **19**, 85 pp.
- [13] Clough, S.A., F.X. Kneizys, E.P. Shettle and G.P. Anderson, 1985: Atmospheric radiance and transmittance, paper presented at the Sixth Conference on Atmospheric Radiation, Am. Meteorol. Soc., Boston, Mass., 141-144.
- [14] Clough, S.A. and M.J. Iacono, 1995: Line-by-line calculations of atmospheric fluxes and cooling rates: Application to carbon dioxide, ozone, methane, nitrous oxide and the halocarbons. *J. Geophys. Res.*, **100**, 16519-16535.
- [15] Clough, S.A., M.J. Iacono and J.-L. Moncet, 1992: Line-by-line calculations of atmospheric fluxes and cooling rates: Application to water vapour. *J. Geophys. Res.*, **97**, 15761-15785.

- [16] Coantic, M. and B. Seguin, 1971: On the interaction of turbulent and radiative transfer in the surface layer. *Boundary Layer Meteorology*, **100**, 152 - 177.
- [17] Coantic, M. and O. Simonin, 1984: Radiative effects on turbulent temperature spectra and budgets in the planetary boundary layer. *J. Atmos. Sci.*, **41**, 2629-2651.
- [18] Corradini, C and M. Severini, 1975: Laboratory experimental check of radiative air cooling theory. *Quart. J. Roy. Meteor. Soc.*, **101**, 163-167.
- [19] Curtis, A.R., 1956: The computation of radiative heating rates in the atmosphere. *Proc. Roy. Soc.*, **A 236**, 148-156.
- [20] Duynkerke, P.G., 1999: Turbulence, radiation and fog in Dutch stable boundary layers. *Boundary layer meteorology*, **90**, 447-477.
- [21] Eliseyev, A. A., N.N. Paramonova, V.I. Privalov and Z.M. Utina, 2001: Experimental study of heat transfer in atmospheric surface layer. IRS 2000: Current problems in Atmospheric Radiation, W.L.Smith and Y.M. Timofeyev (Eds.), *Proceedings of the International Radiation Symposium, St. Petersburg, Russia, 24-29 July, 2000*, A. Deepak Publishing, 1081-1084.
- [22] Ellingson, R.G. and Y. Fouquart, 1991: The inter-comparison of radiation codes in climate models: An overview. *J. Geophys. Res.*, **96**, 8925-8927.
- [23] Ellingson, R.G., J. Ellis and S. Fels, 1991: The inter-comparison of radiation codes used in climate models: Long wave results. *J. Geophys. Res.*, **96**, 8929-8953.
- [24] Ellingson, R.G. and W.J. Wiscombe, 1996: The Spectral Radiance Experiment (SPECTRE): Project description and sample results. *Bull. Amer. Meteor. Soc.*, **77**, 1967-1985.

- [25] Elliot, W. P., 1964: The height variation of vertical heat flux near the ground. *Quart. J. Roy. Met. Soc.*, **90**, 260-265.
- [26] Elsasser, W.M., 1942: Heat Transfer by infrared Radiation in the Atmosphere. Harvard University Press, 43 pp.
- [27] Emanuel, K. A., and M. Zivkovic-Rothman, 1999: Development and evaluation of a convection scheme for use in climate models. *J. Atmos. Sci.*, **56**, 1766-1782.
- [28] Estournel, C. and D. Guedalia, 1985: Influence of geostrophic wind on atmospheric nocturnal cooling. *J. Atmos. Sci.*, **42**, 2695-2698.
- [29] Farrel, P.A., A.F. Hegarty, J.J.H. Miller, E. O'Riordan and G.I. Shishkin, 2000: Robust computational techniques for boundary layers. *Applied Mathematics*, **16**, Chapman and Hall/CRC.
- [30] Fedoseyev, A.I. 2001: A regularisation approach to solving the Navier-stokes equations for problems with boundary layer. *CFD Journal (II-16)*, Special Number, Proc. 8th ISCFD 1999, ZARM, Bremen, 317-324.
- [31] Fels, S. B., and M. D. Schwarzkopf, 1981: An efficient, accurate algorithm for calculating CO₂ 15 m band cooling rates. *J. Geophys. Res.*, **86(C2)**, 1205-1232.
- [32] Fletcher, C. A. J., 1988: Computational Techniques for Fluid Dynamics, **1**, Springer-Verlag, 409 pp.
- [33] Fouquart, Y., B. Bonnel and V. Ramaswamy, 1991: Intercomparing shortwave radiation codes for climate studies. *J. Geophys. Res.*, **96**, 8955-8968.
- [34] Funk, J. P., 1960: Measured radiative flux divergence near the ground at night. *Ibid.*, **86**, 382-389.

- [35] Funk, J. P., 1961: A numerical method for the computation of the radiative flux divergence near the ground. *J. Met.*, **18**, 388-392.
- [36] Garratt, J. R., 1992: The atmospheric boundary layer. Cambridge Atmospheric and Space Science Series. Cambridge University Press., 316 pp.
- [37] Garratt, J.R. and R.A. Brost, 1981: Radiative cooling effects within and above the nocturnal boundary layer. *J. Atmos. Sci.*, **38**, 2730-2746.
- [38] Garratt, J.R., A.J. Prata, 1996: Downwelling longwave fluxes at continental surfaces - A comparison of observations with GCM simulations and implications for the global land-surface radiation budget. *J. Climate*, **9**, 646-655.
- [39] Garratt, J.R., A.J. Prata, L.D. Rotstayn, B.J. McAvaney and S. Cusack, 1998: The surface radiation budget over oceans and continents. *J. Climate*, **11**, 1951-1968.
- [40] Goody, R.M., 1964: *Atmospheric Radiation, Part I, Theoretical Basis*. Oxford: Clarendon Press, 522 pp.
- [41] Gupta, S. K., 1989: A parameterization for longwave surface radiation from Sun-synchronous satellite data. *J. Climate*, **2**, 305-320.
- [42] Ha, K.-J. and L. Mahrt, 2003: Radiative and turbulent fluxes in the nocturnal boundary layer. *Tellus*, **55A**, 317-327.
- [43] Hales, J.V., W. Zdunkowski and D. Henderson, 1963: A study of the physical, thermodynamical and dynamical causes of low ceiling and visibilities. *International Weather Inc.*, Final Report Contract AF 19 (604), 7333.
- [44] Hartmann, D. L., 1994: Global Physical Climatology. *Academic Press*, 411 pp.
- [45] Holtslag, A.A.M. and H.A.R. De Bruin, 1988: Applied modelling of the nighttime surface energy balance over land. *J. Appl. Meteor.*, **27**, 689-704.

- [46] Hillger, D.W. and G.P. Ellrod, 2000: Detection of unusual atmospheric and surface features by employing principal component image transformation of GOES imagery. *10th Conference on Satellite Meteorology and Oceanography*. 14-18 January, Long Beach, CA, Amer. Meteor. Soc.
- [47] Kahle, A.B. and R.E. Alley, 1992: Separation of temperature and emittance in remotely sensed radiance measurements. *Remote Sensing of Environment*, **42**, 1-20.
- [48] Kealy, P. S., and S. J. Hook, 1993: Separating temperature and emissivity in thermal infrared multispectral scanner data: Implications for recovering land surface temperatures. *Geoscience and Remote sensing*, **31**, 1155-1164.
- [49] Kneizys, F.X., E.P. Shettle, L.W. Abreu, J.H. Chetwynd, G.P. Anderson, W.O. Gallery, J.E.A. Shelby, and S.A. Clough, 1988. Users Guide to LOWTRAN7, AFGL-TR-88-0177, Air Force Geophysics Laboratory, Bedford, Mass.
- [50] Kondo, J., 1971: Effect of radiative heat transfer on profiles of wind, temperature and water vapour in the atmospheric boundary layer. *J. Met. Soc. Japan*, **9**, 75-94.
- [51] Kondratyev, K. Ya., 1972: Radiation processes in the atmosphere. WMO Note 309.
- [52] Lacis, A. A. and J. E. Hansen, 1974: A parameterization for the absorption of solar radiation in the earth's atmosphere. *J. Atmos. Sci.*, **31**, 118-133.
- [53] Lake, J.V., 1956: The temperature profile above bare soil on clear nights. *Quart. J. Roy. Meteor. Soc.*, **82**, 187-197.
- [54] Lawson, D., 1997: A closer look at Planck's blackbody equation. *Phys. Educ.*, **32**, 321-326.

- [55] J. Lenoble, 1993. Atmospheric Radiative Transfer. *A. Deepak Publishing*, Hampton, 532 pp.
- [56] Liou, K. N., 1980: An Introduction to Atmospheric Radiation, Int. Geophys. Series., *Academic Press*, **25**, 392 pp.
- [57] Liou, K.-N., 1992: Radiation and Cloud Processes in the Atmosphere. Oxford University Press, 487 pp.
- [58] Liou, K.N., and S.C. Ou, 1981: Parameterization of infrared radiation transfer in cloudy atmospheres. *J. Atmos. Sci.*, **38**, 2707-2716.
- [59] McClatchey, R. A., W. S. Fenn, J. E. A. Selby, F. E. Volz, and J. S. Garing, 1971: Optical properties of the atmosphere, Rep. AFCr1-71-0279, Air Force Cambridge Res. Lab., Bedford, Mass., 85 pp.
- [60] Mlawer, E.J., S.J. Taubman, P.D. Brown, M.J. Iacono, S.A. Clough, 1997: Radiative transfer for inhomogeneous atmospheres: RRTM, a validated correlated- k model for the longwave. *J. Geophysical Res.*, **102**, 16663-16682.
- [61] Morcrette, J.-J., 1989: Description of the radiation scheme in the ECMWF model. *Tech. Memo.*, **165**, ECMWF, Research Department, Reading, U.K., 26 pp.
- [62] Morcrette, J.-J., 1991: Radiation and cloud radiative properties in the ECMWF operational weather forecast model. *J. Geophys. Res.*, **96D**, 9121-9132.
- [63] Morcrette, J.-J., S.A. Clough, E.J. Mlawer, M.J. Iacono, 1998: Impact of a validated radiative transfer scheme, RRTM, on the ECMWF model climate and 10-day forecasts, ECMWF Tech. Memo. No.252.
- [64] Morcrette, J.-J., and Y. Fouquart, 1985: On systematic errors in parameterized

- calculations of longwave radiation transfer. *Quart. J. Roy. Meteor. Soc.*, **111**, 691-708.
- [65] Morcrette, J.-J., E.J. Mlawer, M.J. Iacono, S.A. Clough, 2001: Impact of the radiation-scheme RRTM on the ECMWF forecasting system, ECMWF Newsletter No.91, 2-9.
- [66] Morcrette, J.-J., L. Smith, and Y. Fouquart, 1986: Pressure and temperature dependence of the absorption in longwave radiation parameterizations. *Beitr. Phys. Atmosph.*, **59**, 455-469.
- [67] Modest, M.F., 1993: Radiative Heat Transfer. Mc-Graw Hill, New York.
- [68] Moriyama, M and K. Arai, 1995: Iterative estimation of the earth surface temperature and emissivity, *Adv. Space Res.*, **16**, 117-120.
- [69] Narasimha, R., 1983: On 'compressed' log plots. *International Journal of Mechanical Engineering Education*, **11**, 207-214.
- [70] Narasimha, R., 1994: The dynamics of the Ramdas layer. *Current Science*, **66**, no. 1, 16-22.
- [71] Narasimha, R., 1997: Down-to-earth temperatures: the mechanics of the thermal environment, *Theoretical and Applied Mechanics 1996*, (ICTAM 96, ed. T. Tatsumi, E. Watanabe, T. Kambe), Elsevier Science, Amsterdam, 567-582 pp.
- [72] Nieuwstadt, F. T. M., 1984: The turbulent structure of the stable, nocturnal boundary layer, *J. Atmos. Sci.*, **41**, 2202-2216.
- [73] Oberkampf, W.L. and G.F. Blottner, 1998: Issues in computational fluid dynamics code verification and validation. *AIAA J.*, **36**, 687-695.
- [74] Oke, T. R., 1987: Boundary layer climates. 2nd ed., *Methuen, N.Y.*, 435 pp.

- [75] Olaguer, E. P., H. Yang, and K. K. Tung, 1992: A reexamination of the radiative balance of the stratosphere, *J. Atmos. Sci.*, **49**, 1242-1263.
- [76] Paltridge, G.W. and C. M. R. Platt, 1976: *Radiative processes in meteorology and climatology*. Amsterdam: Elsevier Scientific Publishing Company, 318 pp.
- [77] Phillips, N., J. Susskind, and L. Mc Millin, 1988: Results of a joint NOAA/NASA sounder simulation study. *J. Atmos. Oceanic Technol.*, **5**, 44-56.
- [78] Plokhenko, Y. and W. P. Menzel, 2000: The effects of surface reflection on estimating the vertical temperature-humidity distribution from spectral infrared measurements. *J. Appl. Meteor.*, **39**, 3-14.
- [79] Quinet, A. and J. Vanderborght, 1996: Clear-sky nocturnal temperature forecast and greenhouse effects. *J. Appl. Met.*, **35**, 401-415.
- [80] Ragothaman, S., R. Narasimha and A.S. Vasudeva Murthy, 2001: The dynamical behaviour of the lifted temperature minimum, *Il Nuovo Cimento*, **24**, 353-375.
- [81] Ragothaman, S., R. Narasimha and A.S. Vasudeva Murthy, 2002: Evolution of nocturnal temperature inversions - A numerical study. *Il Nuovo Cimento*, **25**, 147-163.
- [82] Raisanen, P., 1996: The effects of vertical resolution on clear-sky radiation: tests with two schemes, *Tellus*, **48 A**, 403-423.
- [83] Raisanen, P., 1999: Studies on the effects of vertical resolution and spectral resolution in GCM-type radiation schemes, *Department of Meteorology, University of Helsinki*, Report 48.
- [84] Ramanathan, V., 1976: Radiative transfer within the Earth's troposphere and

- stratosphere - a simplified radiative-convective model, *J. Atmos. Sci.*, **33**, 1330-1346.
- [85] Ramanathan, V., 1981: The Role of Ocean-Atmosphere Interactions in the CO₂ - Climate Problems. *J. Atmos. Sci.*, **38**, 918-930.
- [86] Ramanathan, K.R, and S. Atmanathan, 1932: The vertical temperature distribution of air temperature near ground at night. *Beit. Zur. Geophys.*, **37**, 116-117.
- [87] Ramanathan, K.R, and L.A. Ramdas, 1935: Derivation of Angstrom's formula and some general considerations regarding nocturnal cooling of air layers near ground. *Proc. Ind. Acad. Sci.*, **1**, 822-829.
- [88] Ramdas, L.A., and S.L. Malurkar, 1932: Theory of extremely high lapse rates of temperature very near the ground. *Ind. J. Phys.*, **6**, 495-508.
- [89] Raschke, K., 1994: On the nocturnal temperature minimum above bare soil in Poona (India), Report 94 AS 2, Centre for Atmospheric Sciences, Indian Institute of Science, Bangalore, India.
- [90] Rider, N. E., and G. D. Robinson, 1951: A study of the transfer of heat and water vapour above a short grass surface. *Quart. J. Roy. Met. Soc.*, **77**, 375-401.
- [91] Ridgway, W.L., Harshvardhan and A. Arking, 1991: Computation of atmospheric cooling rates by exact and approximate methods. *J. Geophys. Res.*, **96**, 8969-8984.
- [92] Ritter, B. and J.-F. Geleyn, 1992: A comprehensive radiation scheme for numerical weather prediction models with potential applications in climate simulations. *Mon. Wea. Rev.*, **120**, 303-325.
- [93] Roberts, R.E., J.E.A. Selby, and L.M. Biberman, 1976: Infrared continuum

- absorption by atmospheric water vapour in the 8–12 μ m window, *Appl. Opt.*, **15**, 2085–2090.
- [94] Rodgers, C.D., 1967: The use of emissivity in atmospheric radiation calculations. *Quart. J. Roy. Meteor. Soc.*, **93**, 43-54.
- [95] Rodgers, C.D. and C.D. Walshaw, 1966: The computation of infra-red cooling rate in planetary atmospheres. *Quart. J. Roy. Meteor. Soc.*, **92**, 67-92.
- [96] Rossow, W. B., and Y.-C. Zhang, 1995: Calculation of surface and top of atmosphere radiative fluxes from physical quantities based on ISCCP data sets: 2. Validation and first results. *J. Geophys. Res.*, **100**, 1167-1197.
- [97] Salerno, R. and G. Gianotti, 1995: A model for the evolution in rural areas of the temperature profile in the boundary layer and a comparison with measured data. *Boundary layer meteorology*, **73**, 255-278.
- [98] Salisbury, J.W., and D.M. D’Aria, 1992: Infrared (8-14 mm) remote sensing of soil particle size, *Remote Sensing of the Environment*, **42(2)**, 157-165.
- [99] Selby, J.E.A., E.P. Shettle, and R.A. Mc Clatchey, 1976: Atmospheric Transmittance from 0.25 to 28.5 m. Supplement LOWTRAN 3B, AFGL-TR-76-0258, AD A040701.
- [100] Shiskin, G.I. 1997: On finite difference fitted schemes for singularly perturbed boundary value problems with a parabolic boundary layer. *J. Math. Analysis and Applications*, **208**, 181-197.
- [101] Siegel, R. and J. Howell, 2002: Thermal radiation heat transfer. Taylor and Francis, New York and London, 864 pp.

- [102] Slingo, A., R. Brown and C.L. Wrench, 1982: A field study of nocturnal stratocumulus; III. High resolution radiative and microphysical observations. *Quart. J. Roy. Meteor. Soc.*, **108**, 145-165.
- [103] Sommeijer, B.P., L.F. Shampine and J.G. Verwer, 1998: RKC: An explicit solver for parabolic PDEs. *J. Comp. Appl. Math.*, **88**, 315-326.
- [104] Su, F.Y., 1973: Radiative slip between two adjacent absorbing-emitting gases and its application to air pollution. *J. Atmos. Sci.*, **39**, 317-320.
- [105] Sundaresan, S., S. Nagarajan, S.M. Deshpande and R. Narasimha, 1999: 2D lid-driven cavity at high Reynolds numbers: Some interesting fluid dynamical issues. *Lecture notes in Physics*, **515**, 231-236.
- [106] Stephens, G. L., 1984: Review: The parameterization of radiation for numerical weather prediction and climate models. *Mon. Wea. Rev.*, **112**, 826-867.
- [107] Swinbank, W.C., 1964: Longwave radiation from clear skies. *Quart. J. Roy. Meteor. Soc.*, **90**, 488-493.
- [108] Thomas, G.E. and K. Stamnes, 1999: Radiative transfer in the atmosphere and ocean, *Cambridge University Press*, New York, 517 pp.
- [109] Tjemkes, S.A., and P.G. Duynkerke, 1989: The nocturnal boundary layer: model calculations compared with observations. *J. Appl. Met.*, **3**, 161-175.
- [110] Tompkins, A. M. and K. A. Emanuel, 2000: Simulated equilibrium tropical temperature and water vapor profiles and their sensitivity to vertical resolution. *Quart. J. Roy. Meteor. Soc.* , **126**, 1219-1238.
- [111] Varghese, S., A.S. Vasudeva Murthy, R. Narasimha, 2001: A robust, accurate and flexible code for computing near-surface infrared radiation in the atmosphere.

- IRS 2000: Current problems in Atmospheric Radiation, W.L.Smith and Y.M. Timofeyev (Eds.), *Proceedings of the International Radiation Symposium, St. Petersburg, Russia, 24-29 July, 2000.*, A. Deepak Publishing, 445-448.
- [112] Vasudeva Murthy A.S., J. Srinivasan and R. Narasimha, 1993: A theory of lifted temperature minimum on calm clear nights. *Phil. Trans. R. Soc. London, A*, **344**, 183-206.
- [113] Wan, Z., and J. Dozier, 1996: A generalized split-window algorithm for retrieving land-surface temperature from space. *IEEE Transactions on Geoscience and Remote Sensing*, **34**, 892-905.
- [114] Warner, J. X., and R. G. Ellingson, 2000: A new narrow band radiation model for water vapor absorption. *J. Atmos. Sci.*, **57**, 1481-1496.
- [115] Weller, R. and S. Anderson, 1996: Surface meteorology and air-sea fluxes in the western equatorial Pacific warm pool during the Toga Coupled Ocean-Atmosphere Response Experiment. *J. Climate*, **9**, 1959-1990.
- [116] Weng, F., B. Yan and N. Grody, 2001: A microwave land emissivity model. *J. Geophys. Res.*, **106**, D 17, 20115-20123.
- [117] Wilber, A. C., D. P. Kratz and S. K. Gupta, 1999: Surface emissivity maps for use in satellite retrievals of longwave radiation. NASA/TP-1999-209362, 30 pp.
- [118] Wild M., A. Ohmura A, H. Gilgen and E. Roeckner, 1995: Validation of GCM simulated radiative fluxes using surface observations. *J. of Climate*, **8**, 1309-1324.
- [119] Wild M., A. Ohmura, H. Gilgen, E. Roeckner, M. Giorgetta and J.J. Morcrette, 1998: The disposition of radiative energy in the global climate system: GCM-calculated versus observational estimates. *Climate Dynamics*, **14**, 853-869.

- [120] Zdunkowski, W., 1966: The nocturnal temperature minimum above the ground. *Beitr. Phys. Atmos.*, **36**, 792-804.
- [121] Zdunkowski, W. and F.G. Johnson, 1965: Infrared flux divergence calculations with newly constructed radiation tables. *J. Appl. Met.*, **4**, 371-377.
- [122] Zhao W. Z., W.R. Kuhn and S.R. Drayson, 1994. The significance of detailed structure in the boundary-layer to thermal radiation at the surface in climate models. *Geophys. Res. Lett.*, **21(15)**, 1631-1634.
- [123] Zhong, W. and J.D. Haigh, 1995: Improved broadband emissivity parameterization for water vapour cooling rate calculations. *J. Atm. Sci.*, **52**, 124-138.